The University of Nottingham

UNITED KINGDOM · CHINA · MALAYSIA

Magnetron sputtered thin films and composites for automotive and aerospace electrical insulation

Benjamin Vincent Timothy Hanby

Thesis submitted to the University of Nottingham for the
Degree of Doctor of Philosophy,

May 2019

Declaration

I Benjamin V. T. Hanby, herby certify that this thesis has been composed by myself and that it is a record of my own work over the period from October 2015 to October 2018.

Except where specific reference is made to other sources or collaborators, the work presented in this thesis is the original work of the author. It has not been submitted, in whole or in part, for any other degree.

Benjamin V. T. Hanby

Acknowledgements

I would like to acknowledge the support of my supervision team David Grant, Miquel Gimeno-Fabra and Christopher Gerada for their wealth of knowledge, support throughout my studies and providing funding so I could complete this work. Special mention also goes to Bryan Stuart who pushed me to be my best.

I would like to thank staff at the university of Nottingham NMRC facility specifically Christopher Parmenter and Michael Fey for FIB lift out and TEM characterisation. Additional thanks go to Colin Grant of Bradford University and Jonathan Moffat of Oxford Instruments for carrying out AFM DB measurements on thin film samples.

I would also like to thank the following technical staff for training and advice on characterisation and preparation instrumentation through the course of my work: Nigel Neate, Hannah Constantin and Max Mason (all Wolfson), Martin Roe and Beth Steer (both NMRC) and Nick Botterill. Additionally I would like to thank Rory Screton, Graham Malkinson, Matthew Carrington and John Kirk for assistance with machining and rig development.

I would also like to thank my friends and colleagues for their support and for making my doctoral studies such an enjoyable experience.

Finally I would like to express my gratitude to Vilma, Mum, Dad and the rest of my family for unconditional proof reading and unwavering confidence in me throughout.

Abstract

Ceramics are highly prised as insulating materials because of their high stability under demanding conditions (thermal, chemical and radiological). However, the use of ceramics as wire insulation is currently limited to powder packed and relatively thick low voltage coatings. This work follows the development of sputtered Al_2O_3 and Al_2O_3, SiO_2 and Ta_2O_5 composite films as deposited onto copper. Copper disk studies will ultimately be translated onto Cu wire for a proof of concept study.

Initial Al_2O_3 deposition utilised RF or DC sputtering but this found to have low deposition rate (up to 16 nmh^{-1}) and to contain crystallite and metallic defects (up to 19.6 at. % Al^0) respectively. These issues were addressed by introducing pulsed DC (PDC) deposition conditions, producing films with no crystalline or metallic defects (up to 146 nmh^{-1}). The dielectric strength of PDC films measured by AFM time dependant dielectric breakdown was 310 ± 21 Vμm^{-1}, higher than that of the DC deposited films which had a dielectric strength of between 165 ± 19 and 221 ± 20 Vμm^{-1}. A dielectric strength of 310 Vμm^{-1} is suitable for applications with a voltage rating below 150 V and is also a good platform for the production of higher quality coatings. The mechanical properties of the films did suffer from a lower amount of blending at the interface, DC pull off strength was 25.8 ± 9.8 - 72.3 ± 5.6 MPa with the PDC pull off strength being 55.7 ± 2.9 MPa). Wires coated with such PDC Al_2O_3 showed promise with full circumference coating, however, short circuiting was apparent in the wires potentially caused by micro cracking induced either during or post deposition.

The use of multilayer composites consisting of the aforementioned PDC Al_2O_3 and RF SiO_2 or RF Ta_2O_5 resulted in significant gains with respect to the material's electrical properties. The films deposited with 2 layers of each PDC Al_2O_3 and the RF addition performed best in terms of dielectric strengths of 513 ± 18 and 466 ± 86 Vμm^{-1} for Ta_2O_5 and SiO_2 composites respectively. The success of the 2x2 layer configuration resulted from a compromise between the number of RF layers and their thickness. The mechanical properties did, however, suffer as a result of increased intrinsic stress caused by the use of multilayers of materials with varying expansion coefficients, reducing pull off adhesion strength to a maximum of 34.4 ± 4.4 MPa, where ideally the pull off adhesion would be above 80 MPa.

Heat treatment of these coatings resulted in decreased adhesive properties, with a maximum pull off adhesion strength of 20.1 ± 0.9 MPa being apparent. Most of the electrical properties remained the same or were decreased by heat treatment, however the dielectric strength of the SiO_2 composites improved by an average of 12 % resulting in a maximum dielectric strength of 517 ± 24 $V\mu m^{-1}$ due to a reduction in the defect density in the films. Conversely the electrical properties of Ta_2O_5 composites suffered greatly following heat treatment with a maximum dielectric strength of 358 ± 31 $V\mu m^{-1}$. This was theorised to result from Cu migration from the substrate and the potential for Ta_2O_5 to crystallise at temperatures close to 500 °C.

Coating of Cu wires with PDC alumina was shown to be possible, with coatings of various interlayer and coating thickness. Characterisation showed that the wire coating rig enabled the whole circumference of the wire to be coated with alumina. Tensile testing resulted in transvers cracking followed by longitudinal cracking above an applied strain of 1.5 and 4.0 % respectively. Following heat treatment the copper substrate softened and resulted in delamination failures in the coatings during tensile testing. Electrical testing of the wires was inconsistent due micro cracking in the wire coatings.

It has been shown that the use of mixed material composites sputtered by PDC and RF sputtering have potential as high dielectric strength insulating materials, improving upon the base Al_2O_3 believed to be a result of passivation of structural and compositional defects. Additionally, it has been shown that physical vapour deposition in conjunction with a modified sample holder can be utilised for coating of bare copper wire with the potential to act as isolative coatings.

Table of Contents

1 **Introduction** 1
1.1 Dielectric coatings 1
1.2 Market for Insulation and cable materials 1
1.3 Historical wire insulation solutions 3
1.4 Current wire insulation solutions 4
1.5 Magnet wire insulation solutions 7
1.6 Summary of issues with current wiring systems 8
1.7 Coating production methods 8
2 **Aims and Objectives** 11
3 **Literature Review** 12
3.1 Physical Vapour Deposition 12
3.2 Electrical breakdown in dielectrics 24
3.3 Conduction mechanisms in thin films 29
3.4 Mechanical properties and adhesion of thin films 33
3.5 Sputtering of ceramic thin film candidates 38
3.6 Alumina 38
3.7 Silica 43
3.8 Tantalum Pentoxide 46
3.9 Diamond like carbon 48
3.10 Boron nitride 49
3.11 Glasses 53
3.12 Other candidates 53
3.13 Composite materials 53
3.14 Reel to reel coatings 60
3.15 Literature summary 62
4 **Materials and Methodology** 64
4.1 Thin film deposition 64
4.2 Structural characterisation 73
4.3 Electrical measurements 81
4.4 Mechanical Properties 84
5 **Results: DC and RF sputtering** 90
5.1 RF materials characterisation 90
5.2 DC Material characterisation 95
5.3 Time dependant study on DC deposited films 112
5.4 Summary 119

6 Results: PDC deposited films 120
6.1 Duty cycle and frequency optimisation 120
6.2 PDC-60 characterisation 124
6.3 PDC-60 structural characterisation 125
6.4 PDC-60 electrical characterisation 126
6.5 PDC-60 mechanical characterisation 130
6.6 Reproducibility of PDC-60 films 132
6.7 Summary 134
7 Results: Multilayer composite materials 135
7.1 Initial Al_2O_3 SiO_2 multilayer materials 135
7.2 Al_2O_3, SiO_2 and Ta_2O_5 multilayer films 137
7.3 Reproducibility of Ta_2O_5 composites 149
7.1 Summary 150
8 Results: Reel to reel coating of wires..151
8.1 Trial deposition 151
8.2 Coating without chain drive 152
8.3 Coating with chain drive 155
8.4 Optimised wire coatings 158
8.5 Summary 173
9 Results: Heat treatment of sputtered films................................174
9.1 Heat treatment of PDC films 175
9.2 Heat treatment of multilayer films 177
9.3 Mechanical properties 188
9.4 Heat treated Al_2O_3 coated wire 192
9.5 Summary 198
10 Discussion 199
10.1 RF, DC, BDC and PDC films 200
10.2 Multilayer composite films 219
10.3 Wire coating 233
11 Conclusions..238
12 Future work..240
13 References...242

List of Figures

Figure 1.1: *Schematic and image of the windings in a brushless single-phase brushless DC motor [11].* *2*

Figure 3.1: *Schematic of the regions of a typical glow discharge between a cathode and anode with a low pressure working gas [62].* *13*

Figure 3.2: *Principles of sputter deposition, based in the TEER UDP-650. The target is being sputtered using Ar, which is ionised by the application of a potential difference over the target and chamber which acts as the anode. The Ar ions then bombard the target releasing secondary electrons and target neutrals, as shown in the high resolution section. Bombarding species may also become embedded in the target. It is also important to note that target poisoning due to the reactive gas can become an issue in reactive deposition, whereby charge builds up on non-conductive regions of the target leading to arc events [63].* *14*

Figure 3.3*: a) Sputtering yield with relation to atomic number when sputtering with 400 eV* Ne^+ *ions, reproduced from [60]. b) Target power and resulting film thickness after 20 min coating from a Ti target, reproduced from [65].* *16*

Figure 3.4:*Relationship between sputtering rate and reactive gas flow rate reproduced from [78]*... *18*

Figure 3.5: *Schematic of the voltage sequence in bipolar pulsed DC sputtering, showing the cycling used to alleviate charging on the surface dielectric materials. Taken from [90].* *20*

Figure 3.6: *Helical path of an electron in perpendicular electrical and non-uniform magnetic fields reproduced from [98].* *21*

Figure 3.7: *Magnetron configurations and the resulting plasma density (top row). Closed and mirrored field magneton arrangements (bottom row), all as shown by Kelly and Arnell [100].* *23*

Figure 3.8: *Images of catastrophic breakdown sites on a) alumina thin film produced using sol-gel methodology and b) anodised* Ta_2O_5 *(mid grey) on sputtered Ta (light grey) [49,111].* *26*

Figure 3.9: *Relationship between breakdown voltage and breakdown mechanism with time and the different mechanisms which occur relative to both (reproduced from [110]).* *27*

Figure 3.10: *Energy level diagrams for MIM based electrical systems. Included are thermionic mechanisms: Schottkey (top) and Pool-Frenkel emission (bottom) and tunneling mechanisms: Fowler-Nordheim (top) and Direct tunneling (bottom) [104].* *31*

Figure 3.11: *Cracking and buckling in Mo and MoRe sputtered thin films, cracking and buckling have been shown. As shown by Jörg et al. [167].* *37*

Figure 3.12: *A breakdown crater in polycrystalline alumina [175].* *39*

Figure 3.13: *Graphite like structure of hexagonal boron nitride.* *50*

Figure 3.14: *Modified roll to roll deposition system as used by Tamagaki et al. to coat flexible glass substrates [274]* *60*

Figure 4.1: *(left) TEER UDP-650 rig top down configuration used during thin film deposition and substrate preparation. Magnetron (Mag) 2 is equipped with RF power and a Cu Target and Mag 3 is equipped with DC and PDC power and an Al target. (right) 3D render of the TEER-UDP650 showing magnetron and sample holder placement.* *65*

Figure 4.2: *Schematic of PDC alumina RF multilayer materials. Showing nomenclature as relating to film structure.* *69*

Figure 4.3: *Process graph for 4x4* Al_2O_3 Ta_2O_5 *composite film shows the extensive blending stages used to ensure a cohesive film.* *70*

Figure 4.4: *(left) Render of the wire coating apparatus as loaded into the TEER UDP650, showing on and off reels as well as the chain drive, (top right) plan view of the coating apparatus as loaded into the TEER-UDP650 and (bottom right) schematic of the copper wire as coated using the sputtering apparatus.* *71*

Figure 4.5: *Diffraction of X-rays as they interact with the atoms within a crystal structure.* *74*

Figure 4.6: *Removal of core shell photo electrons by X-rays as in XPS.* *76*

Figure 4.7: *Interaction of surfaces with an electron beam, showing the interactions which result in SEM, TEM and EDX detectable phenomena.* *77*

Figure 4.8: *Simplified beam diagrams for bright (left) and dark field (right) TEM imaging modes.* .. *79*

Figure 4.9: *Schematic for in house electrical probe breakdown testing apparatus.* *82*

Figure 4.10: *Pull off adhesion schematic, showing the procedure as well as representations of adhesive and partial and complete interfacial failures.* *85*

Figure 4.11: *Major scratch test failure mechanisms with respect to substrate and coating hardness, re-processed from [157].* *86*

Figure 4.12: *Scratch testing depicting 1) test parameters 2) cohesive film failure (cracking) 3) further cohesive failure with partial film removal and 4) adhesive failure and complete film delamination.* . . 87

Figure 4.13: *Test specimens and failure motif during micro-tensile testing of wire. Arrows indicate direction of force applied to each end of the specimen.* 89

Figure 5.1: *FTIR spectra for 8 hour (RF 1) and 19 hour (RF 2) RF deposited alumina (Cu disk substrates) using a target holder target separation of 55 and 120 mm respectivley.* 91

Figure 5.2: *Backscattered electron SEM cross sections of RF thin films as deposited onto borosilicate cover slides with thickness of 217 nm (RF 2 deposited for 19 h with a target separation of 100 ± 0.5 mm) and 117 nm (RF 1 deposited for 8 hours with a target separation of 55 ± 0.5 mm).* 91

Figure 5.3: *Diffraction pattern for RF deposited alumina on a Cu disk (RF 1 8h and RF 2 19 h). Diffraction peaks result from the copper substrate which were matched to PDF 01-085-1326.* 92

Figure 5.4: *Light microscope images of pull off failure images of RF 1 (complete interfacial delamination) and RF 2 (partial interfacial delamination) as deposited onto Cu disks.* 93

Figure 5.5: *(left) XRD diffraction patterns for RF* SiO_2 *and* Ta_2O_5 *films deposited onto silicate glass substrate. (right) FTIR spectra for* SiO_2 *and* Ta_2O_5 *RF sputtered films as deposited onto copper foil.* 93

Figure 5.6: *Secondary electron SEM cross sectional micrographs of* SiO_2 *and* Ta_2O_5 *films as deposited onto Cu disks at 100 W RF power for 8 h.* 94

Figure 5.7: *XPS survey spectra for 8 h RF deposited* SiO_2 *and* Ta_2O_5 *films as deposited on Cu disk substrates. High resolution spectra for Ta_4f and Si_2p photoelectron emissions are fitted with constituent peaks depending on the spin and charge of the ejected electron.* 95

Figure 5.8: *DC (top) and BDC (bottom) layer configuration see experimental section for more details.* 95

Figure 5.9: *FTIR spectra and peak positions for Al-O bonding in DC and BDC* Al_2O_3 *films as deposited onto Cu foil. Samples were deposited onto Copper foil to achieve sufficient ATR crystal contact.* 95

Figure 5.10: *XRD diffraction data for DC and BDC Alumina films. Diffraction peaks were attributed to the metallic Aluminium ICDD-PDF-00-004-0787 whilst the amorphous hump present between 20 and 40 2θ° was attributed to the combined structure of the film and glass substrate.* 96

Figure 5.11*: XPS spectra containing DC and BDC alumina films as deposited onto Cu disks. Peak deconvolution for BDC-60 is also included to show the shoulder position, with the dashed black curves representing* Al^{3+} *and* Al^{0}*components as labelled.* 97

Figure 5.12: *Thickness of* Al_2O_3 *films determined using SEM micrographs of sputtered alumina films, as deposited onto copper substrates and mounted in conductive resin to obtain a cross section. High resolution images of the interlayer section have been inset in the top right of each image.* 99

Figure 5.13: *(top row) TEM analysis of BDC films showing layer configuration and short range order (circled) and finally EDX mapping for Al, Cu and O. (bottom row) TEM micrographs displaying short range order and cracking seen in the films respectively. Striations running through the material can be seen in the EDX analysis as well as the micrographs on the bottom row.* 100

Figure 5.14: *Applied voltage plotted against leakage current density for DC and BDC films as deposited on Cu substrate and tested using the in house breakdown testing equipment.* 102

Figure 5.15 *AFM electrical breakdown of films deposited for 12.5 min, DC films deposited with a bias voltage of -10, -45 and -60 V (left) and BDC films deposited with a bias voltage of -10, 45 and -60 V (right). Current voltage measurements for this data were carried out using AFM DB methods on a 30x30 µm array.* 103

Figure 5.16: *summary of the dielectric breakdown strength values obtained for DC and BDC films measured using in house probe based methods and AFM DB methods with respect to the substrate bias.* 104

Figure 5.17: *Current leakage plotted against applied field for DC and BDC films as deposited for 12.5 min onto Cu disks. Inset are Fowler-Nordheim plots with multiple linear regions highlighted in each case (indicating multiple tunnelling barriers).* 105

Figure 5.18: *Pores found in BDC-45 and BDC-60 films with 3D view and graphical pore profile. Pore profiles were generated for the area within the black squares using the Gwyddion AFM analysis package.* 106

Figure 5.19: *Failure modes in pull off adhesion tests a) DC-10 interfacial delamination b) BDC-60 partial film delamination c) BDC-45 failure in adhesive. The remaining Al appears light in the EDX maps. Average adhesive failure values are given in the table below with standard error as well as a summary of failure modes from each sample.* 108

Figure 5.20 *Scratch test failure modes and adhesion for DC films produced at a)-10 b)-45 and c) -60 V substrate bias and BDC films produced at d) -10, e)-45 and f) -60 V substrate bias.* L_{c1+2} *indicates chevron, arc tensile and combination cracking,* L_{c3} *indicates the onset of adhesive failure through buckling and* L_{c4} *onset of complete film delamination.* 110

Figure 5.21: *Summary bar charts of pull off adhesion and scratch test failure loads for DC and BDC films deposited under varying sample bias conditions as indicated.*..111
Figure 5.22: *FTIR spectra for Al_2O_3 films deposited onto Cu disks for sequentially longer periods of time all with -60 V bias, the peak positions have been indicated with dashed lines..* 112
Figure 5.23: *XRD diffraction patterns for films deposited with varying time to produce films of different thickness. Diffraction peaks were attributed to metallic Aluminium (ICDD-PDF-00-004-0787) whilst the amorphous hump present between 20 and 40 2θ° was attributed to the combined structure of the film and glass substrate*...113
Figure 5.24: *Table of average thickness values for DC films as deposited onto borosilicate glass slides (above). Cross sectional SEM (Backscattered electron) micrographs of DC films deposited onto borosilicate cover slips for different time scales below (Below). d) Shows secondary electron image included to show pinholes which were located in DC12-6 samples (bottom right).* 114
Figure 5.25: *XPS Spectra for Al_2P electrons in DC deposited alumina films on Cu disks. Deconvolution is used to indicate the position of the Al^0 shoulder at ca. 72 eV. Note that for the deconvolution shown for DC3-60 the dotted line represents Al^{3+} and the solid green line represents Al^0.* 115
Figure 5.26: *Light microscope images of pull off adhesion failure sites for time dependant alumina films. The most common failure modes were partial interfacial delamination as seen for DC3-60 and complete interfacial failure for DC6-60 and DC12-60.* 117
Figure 5.27: *scratch testing carried out on time dependent coatings as deposited onto Cu disks (descending 30 min, 60 min and 120 min) note extensive buckling delamination on D12-60 sample. L_{C1+2} and L_{C3} failures have been indicated in each case with the attributed mechanism given in the subsequent table.*..118
Figure 6.1: *FTIR spectra for films deposited onto Cu foil using pulsed DC deposition with varying frequency and duty cycle (as indicated in the legend).*..121
Figure 6.2: *SEM (secondary electron) cross section images of pulsed DC films deposited for 240 min with a -60 V substrate bias onto Cu substrates. The pulse frequency and duty cycle were as follows: a) 50 kHz 24%, b) 50 kHz 40%, c) 150 kHz 22.5%, d) 150 kHz 40%, e) 201 kHz 24% and f) 201 kHz 40%. Additionally to this a table including the thickness and deposition rate of each coating is seen below* 122
Figure 6.3: *XPS Al_2P peaks for films as deposited onto Cu substrate with varying pulse frequncy (kHz) and duty cycle as indicated in the legend*...124
Figure 6.4: *XPS of PDC-60 thin film as deposited onto copper indicating no Al^0 in the surface layer of the film, due to the absence of a shoulder at 70 eV which was seen in DC and BDC films.*..............125
Figure 6.5: *a) TEM (SEM inset) micrographs of PDC-60 as deposited onto Cu, with cross sections showing film thickness, interlayer and structure. b) TEM EDX analysis is included to show the consistency of the oxygen distribution and lack of striations in the films.* 126
Figure 6.6: *Current leakage density graph for PDC-60 as deposited onto 5mm Cu disks, with measurements made using the in house probe based method based upon ASTM D3755-14.*............127
Figure 6.7: *Elctrical testing for PDC-60 as deposited onto 10 mm Cu disks, measured using AFM DB with 5x5 μm (left) and 30x30 μm (right) arrays.*...127
Figure 6.8: *Table displaying dielectric strength with respect to film thickness. Cross sectional backscattered electron SEM micrographs used to determine film thickness and breakdown voltage for PDC-60 as deposited onto 10 mm Cu disks to thicknesses of a) 107 nm and b) 215 nm respectively. Also included below each micrograph is the current voltage data for each sample.*................................128
Figure 6.9: *Leakage current density plot for PDC-60, 200 nm samples as deposited onto Cu disk with inset Fowler-Nordheim plot with red highlighted linear region.* 129
Figure 6.10: *Light micrographs of the prevalent pull off failure mechanisms in PDC Al_2O_3 (all indicate some degree of partial interfacial failure).*...130
Figure 6.11: *Scratch failure for PDC-60 Films as deposited onto Cu Disk, displaying cohesive and adhesive failures with combination cracking (L_{C1+2}) and buckling (L_{C3}) respectivley. The maximum scratch load was 15 N, with scratch length of 3 mm.* 131
Figure 6.12: *FTIR, XRD and XPS spectra of PDC alumina as deposited onto Cu foil, borosilicate glass slide and Cu disk respectively.*...132
Figure 6.13: *Light microscope images of pull off adhesion failure sites for PDC films. Al EDX of the pull off site is included to show the presence of Al on the pull off stub.*...133
Figure 6.14: *Light microscope images of scratch tests for PDC films deposited to Ca. 200 nm onto Cu disks showing L_{C1} and L_{C2} failure in the high magnification image.*..133
Figure 7.1: *Multilayer film layer configuration for additional information see methodology section.* 135

Figure 7.2: *(top) Table showing xps Si_2P peak positions and Si:O ratios. (bottom) a) FTIR, b) XRD and c) XPS data for silica alumina multicomponent films as deposited onto Cu foil (FTIR), borosilicate glass slides (XRD) and Cu disks (XPS) using initial multilayer deposition techniques.....................136*

Figure 7.3: *Cross sectional secondary electron SEM of Al_2O_3, SiO_2 multilayer as deposited onto Cu Disk...137*

Figure 7.4: *FTIR spectra for Ta_2O_5 (left) and SiO_2 (right) multilayer materials as deposited onto copper foil. Spectra for the RF single Absorbance bands have been marked. 138*

Figure 7.5: *XRD diffraction patterns for multilayer films of ca. 200 nm thick deposited onto glass substrates and 8 hour deposited RF films, with Ta_2O_5 Al_2O_3 composites (left) and SiO_2 Al_2O_3 composites (right). 138*

Figure 7.6: *High resolution XPS spectra for multilayer composite films as deposited onto Cu disks, for Ta_4F (left) and Si_2P (right) photoelectrons. Fitting is indicated in the key next to each set of spectra. The subsequent table includes binding energies and atomic ratios. 139*

Figure 7.7: *Deconvolution results of XPS O_1S peaks for SiO_2 composites as deposited onto Cu disks. Included below is the deconvolution spectra showing the Si^{4+} peak shoulders. 140*

Figure 7.8: *Cross sectional secondary and backscattered (inset) SEM micrographs of Ta_2O_5 (top row) and SiO_2 (bottom row) multilayer materials as deposited onto Cu disks. Average thickness values are given in the table below...141*

Figure 7.9: *Scratch test images depicting the archetypal failure modes in Ta_2O_5 (left) and SiO_2 (right) multilayer films as deposited onto Cu disks...143*

Figure 7.10: *Pull off adhesion sites showing a) and d) partial interfacial delamination in Ta_2O_5 1x1 and SiO_2 2x2 composites respectively and complete interfacial delamination for Ta_2O_5 4x4 and SiO_2 1x1 composites in b) and c) respectively. Where available EDX maps showing Al and Cu apparent on the stubs following testing are included below the pull off site. 144*

Figure 7.11: *Summary of the mechanical adhesion testing data for PDC composite materials, with pull off adhesion displayed on the left and scratch test critical failures on the right................................145*

Figure 7.12: *Plot and table of AFM breakdown voltage and dielectric breakdown for Ta_2O_5 and SiO_2 multilayer composites deposited onto Cu disks. Layer structure and film thickness are included (and was used to calculate the dielectric strength). N represents the total measurements that resulted in breakdown (out of 16). 146*

Figure 7.13: *AFM DB current, applied field plots, for Ta_2O_5 composites deposited onto Cu disks. Layer configuration is indicated on the top of each graph. 147*

Figure 7.14: *AFM DB current, applied field plots, for SiO_2 composites deposited onto Cu disks. Multilayer configuration is as indicated on the top of each graph..148*

Figure 7.15: *FTIR spectra for Ta-O and Al-O bonding, XRD and XPS Ta_4F results for reproduced Ta_2O_5 multilayer films deposited onto Cu foil, borosilicate glass slides and Cu substrates respectively. 149*

Figure 8.1: *Secondary electron SEM micrographs and EDX mapping of the cross section of an Al coated Cu wire, coated using the trial deposition apparatus. 152*

Figure 8.2: *Force extension plots for 2 A 0.5 RPM Al with thickness of ca. 300 nm. Note slipping in test 1 resulted in dips in the plot. 153*

Figure 8.3: *Light micrographs of untested (top) and tensile tested (bottom) Al coated copper wire. Bare copper is seen in the bottom images following testing, as a result of delamination of the wire coating. 154*

Figure 8.4: *FTIR spectra for wires coated with 1 layer of alumina using the methodology stated in section (4.1.5) with one Al_2O_3 coating run. An Al interlayer was deposited on the wire at 1.5 rpm. The legend indicates the measured sites across the wire..154*

Figure 8.5: *Micrographs of Al (left) and Al_2O_3 (right with Al interlayer) coated Cu wire with inset high magnification micrographs displaying delamination with visible Cu in both cases. 156*

Figure 8.6: *Cross sectional secondary electron SEM micrographs of Al_2O_3 coated wire with an Al interlayer deposited at 1.5 rpm followed by 0.5 rpm reactive PDC Al_2O_3 coating from two opposite sides of the wire...156*

Figure 8.7: *FTIR spectra taken from around the circumference of the Al_2O_3 film as deposited onto Cu wire (T=top, L=left, R=right and B=bottom sides) at a distance of 55 mm with no substrate bias at 0.5 rpm. 157*

Figure 8.8: *Light microscope images of Cu wires coated in PDC Al, deposited at increasing reel to reel speed to modify the coating thickness as indicated above the micrographs. Defects in the wires have been circled in each instance. 158*

Figure 8.9: *Light microscope images of the surface of Al_2O_3 coated Cu wires with varying rotation speed during interlayer deposition (indicated above the image). (top) With as received bearings, (bottom) with step machined away from the bearing grooves.* 159

Figure 8.10: *A table of thicknesses followed by secondary electron SEM micrographs from the cross section of Cu wires coated with a single Al interlayer with a deposition speed as indicated above each column and one layer of Al_2O_3, deposited at 0.5 rpm. Images are taken clockwise around the samples going down the columns.* 160

Figure 8.11: *Cracking in Cu wires coated with an Al interlayer deposited at 1.5 rpm and 1 layer of PDC Al_2O_3 deposited at 0.5 rpm. It can be seen that transverse cracking is followed by combination cracking during tensile testing at loads above 125 MPa. Note tensile stress was applied in the direction horizontal to the page.* 161

Figure 8.12: *FTIR Al-O peak positions for coated wire, measured around the circumference of same samples, coated with an Al interlayer with speed as indicated and a single layer of Al_2O_3. Associated spectra from around the wire are included below.* 162

Figure 8.13: *FTIR Al-O peak positions for coated wire, measured around the circumference of same samples, coated with an Al interlayer as indicated and 3 layers of Al_2O_3. Associated spectra are included below.* 163

Figure 8.14: *Cross sectional back scattered SEM (with secondary electron inset) images of wire coated with 3 passes of Al_2O_3 on top of an Al interlayer deposited at the speed indicated. Images are taken from around a cross section of the corresponding wire moving around in a clock wise fashion down the columns.* 165

Figure 8.15: *Light microscope images of Cu wire bias cleaned at -150 V for two winds and coated with an Al interlayer at 1.5, 3.0 or 4.5 rpm and then coated with 3 Al_2O_3 layers deposited at 0.5 rpm. Cu which is visible through the coating is more prevalent in the 3.0 and 4.5 rpm interlayer coatings. Top row taken from the top side, 2nd row images from the inside of the wire as wound onto the on reel, 3rd row from the outside and the 4th row taken from the bottom of the wire.* 166

Figure 8.16: *Coating crack formation (secondary electron SEM images) on Cu wires. The coatings consist of an Al interlayer deposited at 1.5, 3.0 or 4.5 rpm followed by 3 layers of Al_2O_3 deposited at 0.5 rpm. Inset are the minimum failure stress and strain for each test group. Note tensile stress was applied in the direction horizontal to the page. A longitudinal crack has been highlighted in the top right tile.* 167

Figure 8.17: *Crack density - resulting from tensile testing - for Cu Wire coated with 3 layers of Al_2O_3 at 0.5 and an Al interlayer deposited at 1.5, 3.0 or 4.5 rpm.* 168

Figure 8.18: *FTIR spectra for Cu wire coated with 1 layer of Al at a speed of 1.5 rpm and 5 layers of Al_2O_3 deposited at 0.5 rpm. Where measurements were taken around a sample T (top), B (bottom), L (left) and R (right).* 169

Figure 8.19: *Light micrographs of Cu wire coated with 1 Al layer deposited at 1.5 rpm and 5 layers of Al_2O_3 each deposited at 0.5 rpm. Where a) is the top b) is the inside, c) is the bottom and d) is the outside of the wire respective to the off reel of the coating apparatus.* 169

Figure 8.20: *Cross sectional SEM of Cu wire coated with one layer of Al at 1.5 rpm and 5 layers of Al_2O_3 at 0.5 rpm showing the thickness around the wire. Backscattered electron micrographs are displayed with secondary electron images inset.* 170

Figure 8.21: *Maximum and minimum range for cracking failure seen in multilayer Al_2O_3 (deposited at 0.5 rpm) coated wire with an Al interlayer (Deposited at 1.5 rpm). Data was generated by finding the maximum and minimum possible onset of failure from SEM micrographs. (Below)Tensile test failure sites for Cu wire coated with an Al interlayer deposited at 1.5 rpm and 5 layers of PDC Al_2O_3 deposited at 0.5 rpm. Note tensile stress was applied in the direction horizontal to the page* 171

Figure 8.22: *Crack density in Al_2O_3 coated wires with an Al interlayer deposited at 1.5 rpm with varying layers of Al_2O_3 applied at 0.5 rpm (1x, 3x and 5x).* 172

Figure 9.1: *FTIR spectra for thermally treated PDC thin films as deposited onto copper foil.* 174

Figure 9.2: *FTIR, XRD and Al_2P high resolution XPS spectra for PDC thin films deposited onto Cu foil, borosilicate glass coverslips and Cu disk respectively, all having a post deposition heat treatment at 500 °C.* 175

Figure 9.3: *Pull off test light micrographs showing typical pull off partial interfacial delamination for heat treated PDC films as deposited onto Cu disks. Al EDX of the pull off stub has been included to the bottom right of each sample, note that high amounts of Al seen around the side of the sample result from the Al stub holder.* 176

Figure 9.4: *Scratch test failure mechanisms for heat treated PDC films as deposited onto Cu disks. L_{C1} indicates the onset of tensile cracking and L_{C2} indicates the onset of buckling.* 176

Figure 9.5: *a) AFM DB dielectric breakdown measurements of heat treated PDC alumina films deposited onto Cu disks as carried out using AFM DB. b) Cross sectional secondary electron SEM of heat treated PDC films as mounted in resin. 177*

Figure 9.6: *Images of SiO_2 and Ta_2O_5 multilayer films as deposited onto Cu disks before (left) and after heat treatment (right) at 500 °C. Layer configuration is as indicated on the left of the images.........178*

Figure 9.7: *FTIR spectra for Ta_2O_5 (left) and SiO_2 (right) multilayer composites as deposited onto copper foil. Peak positions have been indicated using the dashed lines. 179*

Figure 9.8: *XRD diffraction patterns for Ta_2O_5 composite (top) and SiO_2 composite (bottom) materials with varying layer configuration as deposited onto borosilicate glass slides. Dashed lines are used to indicate potential peaks resulting from the interlayer. 180*

Figure 9.9: *XPS high resolution spectra for Ta_4F and Si_2P in Ta_2O_5 and SiO_2 319multilayer composites deposited onto Cu disks, followed by heat treatment at 500 °C. The table contains peak position data as well as Si_2P deconvolution data and Ta:O and Si:O ratios. 181*

Figure 9.10: *Deconvoluted O_1S spectra, peak positions and % contribution, for heat treated SiO_2 composite films as deposited onto Cu disks. Layer configurations are indicated in the top left and peak assignments are indicated in the first spectra..182*

Figure 9.11: *XPS spectra for Cu_2P$^{3/2}$ and Cu_2P$^{1/2}$photoelectrons from Ta_2O_5 (left) and SiO_2 (right) multilayer composites as deposited onto Cu disks and heat treated at 500 °C for 1 h. Peaks have been identified, including satellites at a higher binding energy and are indicated using a dashed line. The table below displays the Cu at.% in the composites. 183*

Figure 9.12: *Cross sectional secondary electron SEM images of heat treated Ta_2O_5 composites (top row) and SiO_2 composites (bottom row) with inset backscattered electron images...........................184*

Figure 9.13: *Graphical and tabulated AFM breakdown voltage and dielectric strength values for heat treated Ta_2O_5 and SiO_2 multilayer composites as deposited onto Cu disks. Composite thickness and the number of test sites achieving breakdown (N) are also shown...185*

Figure 9.14: *AFM DB current plotted against applied field for heat treated Ta_2O_5 composite films as deposited onto Cu disks. The layer configuration is as indicated at the top of each graph...............186*

Figure 9.15: *AFM DB current plotted against applied field for heat treated SiO_2 composite films as deposited onto Cu disks. The layer configuration is as indicated at the top of each graph...............187*

Figure 9.16: *Surface roughness (Ra, taken from 4 μm^2 surface maps) values given for multilayer and heat treated multilayer films as deposited onto Cu disks. 188*

Figure 9.17: *Scratch test failure for heat treated composite materials as determined by light microscopy, high magnification images for the identification of failure mechanisms have been included. 189*

Figure 9.18: *Illustrative adhesive light microscope failure sites for heat treated Ta_2O_5 and SiO_2 multilayer composites as deposited on Cu disks, with Al and Cu EDX maps of the associated pull off stub below. Included below is a plot of average failure strength (MPa) for as deposited and heat-treated multi-layer composite samples...191*

Figure 9.19: *FTIR average peak position and spectra for heat treated films as deposited onto Cu wire cleaned at -150 V bias and with a 1.5 rpm Al interlayer with 1, 3 or 5 layers of Al_2O_3 deposited at 0.5 rpm. 192*

Figure 9.20: *Optical microscope images taken from sites around the circumference of the Cu wires as bias cleaned at - 150 V and coated with a 1.5 rpm Al interlayer with 1, 3 or 5 layers of Al_2O_3 deposited at 0.5 rpm. Below the corresponding columns are high magnification images of transverse cracking found on the inside of the 3 layer Al_2O_3 coating and on the outside of the 5 layer Al_2O_3 coating......193*

Figure 9.21: *Back scattered electron (secondary electron inset) SEM micrographs for heat treated coated wires with 1, 3 and 5 layers of Al_2O_3 deposited on top of an Al interlayer deposited at 1.5 rpm. Images are taken from sites around a cross section of wire mounted in conducting resin................195*

Figure 9.22: *Stress strain curves for the tensile testing of non-heat treated and heat treated Cu Wires coated with 3 layers of Al_2O_3 and an Al interlayer deposited at 1.5 rpm. With imaging of cracking and delamination failure modes and the average stress and strain at which they were observed. Note that depressions in the data relate to losses during imaging and tensile stress was applied in the direction horizontal to the page..196*

Figure 9.23*: Crack density in heat treated Cu wires coated with an Al interlayer at 1.5 rpm and 1,3 or 5 layers of Al_2O_3 deposited at 0.5 rpm. 197*

Figure 10.1: *Schematic to describe charge trapping and de-trapping in reactive DC sputtered Al_2O_3 films. In stage one electrons can flow from the electrode into defects in the material structure causing an increase in current. Stage two shows the negative charge that has built up in a defect repelling the addition of further charge. It is these actions cycling, which cause the oscillations in the current prior to breakdown. 209*

Figure 10.2: *Schematic showing the reasoning behind the improved breakdown characteristics of the PDC films, TEM micrographs showing short range order in the DC/BDC films and the lack of such order in PDC films are inset. Defects shown in DC sputtered films were potentially a route to their premature electrical breakdown.* *213*
Figure 10.3: *Effect of multilayers for capping and barrier properties in resisting current flow and disrupting breakdown paths in thin ceramic composites. Defects are shown to be passivated in the films having a multilayer configuration. The dielectric strength is highest for the 2x2 films and the maximum dielectric strength for each layer configuration given in the bottom right of each illustration.* *226*

List of Tables

Table 1.1: *Historical wire insulation solutions 4*
Table 1.2: *Electrical properties of selected polymeric materials........ 5*
Table 1.3: *Composition of Ceramawire ceramic wire coating 7*
Table 3.1: *Measurement methods used to determine dielectric strength of* Al_2O_3 *films and typical dielectric strength values obtained. 28*
Table 3.2: *linear plot relationship for conduction mechanisms and plots of their current voltage properties [104,132–134]. 32*
Table 3.3: *Stress in various sputter deposited films, in relation to working gas pressure........ 33*
Table 3.4: *Assorted electrical data for selected alumina thin films deposited through various sputtering routes 42*
Table 3.5: *Selected electrical properties of silica thin films as deposited by various sputtering methods. 45*
Table 3.6: *Dielectric strength of* Ta_2O_5 *sputtered films deposited using various techniques. 47*
Table 3.7: *Summary table indicating the suitability of the explored materials for thin film electrical applications considering a number of different properties. +++ represents the most promising attributes and – represents a negative property with respect to the material acting as an insulator as deposited onto copper. 59*
Table 4.1: *Deposition parameters for RF deposited thin film materials sputtered onto copper substrates. 66*
Table 4.2: *Deposition parameters for BDC and DC alumina films, with a constant sample target separation of 55 ± 1 mm and a rotation speed of 5 RPM. 67*
Table 4.3: *PDC film deposition parameters, note that the duty cycle varies within samples deposited at the same pulse frequency with a constant sample target separation of 55 ± 1mm and a rotation speed of 5 RPM........ 68*
Table 4.4: *Multilayer sputtering parameters for* Al_2O_3, Ta_2O_5 *and* SiO_2 *composites as deposited onto Cu foil and disks as well as borosilicate cover slides. 69*
Table 4.5: *Sputtering and drawing parameters for aluminium and alumina coated wires. Note that one of the wire interlayers was used prior to all subsequent* Al_2O_3 *regardless of the number of* Al_2O_3 *layers, the interlayer speed will be added to the start of the sample name for instance 1.5 rpm 3x........ 72*
Table 5.1: *Ahession strength and failure mechanisms for RF deposited alumina films RF 1 and RF 2 as deposited onto Cu disks........ 92*
Table 5.2: *Component positions and % concentration for the de-convoluted Al_2P photoelectron emmisions. Al:O ratios for deposited films were calculated from the O_1S and Al_2P relative peak areas in CASA XPS software. See* ***Figure 5.11*** *for the peak deconvolutions for Al_2P photo electron emission of DC, BDC and PDC films. 98*
Table 5.3: *Breakdown strength and dielectric strength of DC and BDC films as deposited onto 5 mm Cu disks and measured using the in house probe based methods. 101*
Table 5.4: *AFM DB summary where N is the number of tests out of 16 which broke down below the 150 V limit of the power supply. Dielectric strength calculated from breakdown voltage (V) and thickness. 104*
Table 5.5: *Average AFM surface roughness Ra (nm) for DC and BDC alumina films as deposited onto CU disk, as averaged from five 400* μm^2 *scans with standard error values included (nm). 107*
Table 5.6: *XPS peak positions and Al:O ratios for reactively sputtered DC alumina films deposited for different lengths of time (as indicated in the sample name) onto Cu disks........ 115*
Table 5.7: *Average AFM surface roughness summary for time dependant DC films as deposited onto Cu disks. 116*
Table 5.8: *Direct pull off stub adhesion failure strength (MPa) and failure modes for time dependant DC films........ 116*
Table 6.1: *FTIR peak positions for pulsed DC alumina films as deposited onto Cu foil with varying pulse frequency and duty cycle (as designated in the film column). 121*
Table 6.3: *XPS Al_2P binding energy and Al:O ratio assessed using casa XPS for pulsed DC films as deposited onto Cu disks........ 123*
Table 7.1: *FTIR peak positions for alumina silica composite films (with 2 to 4 layers) as deposited onto Cu foil for maximum ATR crystal contact........ 136*
Table 7.2: *Average surface roughness values (Ra) for multilayer composite films as deposited onto Cu disks. Average taken from 3 2x2* μm *areas as analysed by Gwyddion AFM analysis software 142*

Table 7.3: *Critical failure loads (N) and failure modes for multilayers deposited onto Cu disks as identified using light micrographs. Whereby conformal cracking has been abbreviated.*..................142
Table 7.4: *Average adhesive pull off strength (MPa) and failure mechanism for Ta_2O_5 and SiO_2 multilayer films as deposited onto Cu disks.*..........144
Table 8.1: *Average, minimum and maximum coating thickness and in sample variation for Cu wires coated with 1 layer of Al (speed indicated in the left column) and 3 layers of Al_2O_3 deposited at 0.5 rpm.*..........164
Table 8.2: *Minimum and maximum cracking failures perpendicular and parallel to the direction of tensile stress for Cu wire samples coated with 3 layers of Al_2O_3 at 0.5 rpm on top of an Al interlayer as outlined in the table.*..........168
Table 8.3: *Critical bending radii as calculated for Al_2O_3 coated copper wires with various interlayer and coating thickness.*..........172
Table 9.2: *AFM average surface roughness (Ra) for heat treated multilayer films as deposited onto Cu disks.*..........188
Table 9.3: *Average failure strength for heat treated (500 °C) multilayer films as deposited onto copper disks, with corresponding failure mechanisms for each sample.*..........190
Table 9.4: *Average coating thickness for heat treated Al_2O_3 coated wires with a 1.5 rpm Al interlayer. Also included is the lowest and highest average thickness.*..........194
Table 9.5: *Maximum and minimum failure stress and strain for tensile failure in heat treated Al_2O_3 coated wires with an Al interlayer deposited at 1.5 rpm.*..........197
Table 9.6: *Critical bending radii calculated using critical stress from tensile testing on wires deposited with a 1.5 rpm interlayer and varying layers of Al_2O_3.*..........198
Table 10.1: *FTIR Al-O phonon peak positions, SEM cross sectional thickness and XPS Al:O ratio and Al^0 content for RF, DC and PDC Al_2O_3 thin films.*..........207
Table 10.2: *Summary of the AFM DC properties of DC, BDC and PDC Al_2O_3 films as deposited onto Cu disks and heat-treated in the case of PDC films.*..........214
Table 10.3: *Summary of the pull off and scratch adhesion of DC, BDC and PDC Al_2O_3 films as deposited onto Cu disks and heat treated in the case of PDC films.*..........217
Table 10.4: *Compositional, electrical and mechanical properties of as deposited and heat treated SiO_2 and Ta_2O_5 composite films.*..........232

1 Introduction

1.1 Dielectric coatings

Dielectric materials are key for many components used in the electronic industry, such as transistors and capacitors, as they can provide electrical insulation and charge storage whilst maintaining thermal conductivity [1,2]. Thin ceramic materials are already well accepted in the microelectronics industry with tantalum pentoxide a stalwart of capacitor technology, where it is utilised as a dielectric layer between the anode and cathode, in widely available tantalum capacitors [3].

One of the biggest uses of insulating materials is as magnet wire insulation, which is used heavily in motor windings. Wire insulation comes in many forms and can be composed of many kinds of materials such as polymers and ceramics. It is often selected with a specific application in mind, taking into account environmental and operational factors.

1.2 Market for Insulation and cable materials

The market for wire insulation is driven by three main industries: construction, power and communication. This is a market completely dominated by poly vinyl chloride (PVC) and poly olefins consisting up to 85 % of the market according to estimates made by *Frost and Sullivan* in 2012, with the market for electrical insulating materials set to be worth 9.58 billion (USD) by 2021 [4,5].

These markets become especially important when considering the recent drive towards “more electrical aircraft” (MEA); for example the need to develop insulation to facilitate a higher number of windings which can be used to modify the electric field, for example an increase in the energy density of 4 pole permanent magnet motor from 286.5 to 573 kJm^{-3}, resulted in the output power and starting torque increasing by 25-30 % [6]. Other research focuses on the use of creative winding motifs to increase motor efficiency and power density, by improving the copper fill factor to *ca.* 90% such as in the orthocyclic patterns discussed by *Stenzel et al.* [7,8]. The wires have the potential to help replace pneumatic and hydraulic systems with electrical power transmission in the form of cabling and windings. An increase in thermal stability of insulators would also help to facilitate an increased packing density and potentially a reduced weight because a smaller core could be used to accommodate the same currents (because the thinner wire has a higher resistance meaning more heat would be generated for the same applied current) [9]. Kilometre lengths of coated wire would be needed to utilise these benefits in every motor winding, see ***Figure 1.1***. The amount of wire depends on the number and the volume of windings, fill factor and wire thickness, once these parameters are known the wire length can be calculated.

Magnet wire in electric motors and actuators is of particular importance when considering the growing number of electric vehicles (EV), because of their key role in motor windings. The EV market is projected to grow to 150 million units by 2030 with one of the most telling predictions made by the international energy agency being the complete electrification of two wheel vehicles by 2055 [10].

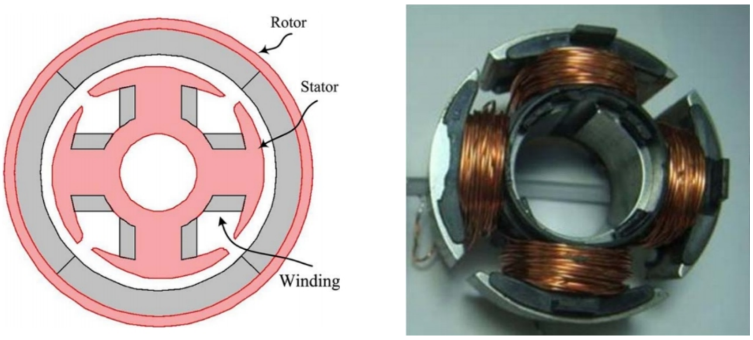

Figure 1.1: *Schematic and image of the windings in a brushless single-phase brushless DC motor* [11].

There are also many other challenges in MEA, such as the design and selection of the most suitable type of motor as discussed by *Hashemnia and Asaei*, [12]. This study showed that the type of motor implemented needs a number considerations with respect to cost/ efficiency and model of motor for instance, brushless DC motors can offer higher efficiencies because the lack of a brush, however, they typically cost twice as much as brushed DC motors and whilst high efficiency motors (IE2) have a larger starting cost than a low efficiency motor (IE1), for example *Torrent et al.* have shown that an IE2 motor running at 300 W could save more than 800 €/year compared to an IE1 motor [13].

Consideration towards the bulk wire material has led in most cases to the use of Cu, because of its low resistivity (1.68x10^{-8} Ωm) [14]. Whilst materials such as Al, Ag and C could provide alternative cores: cost (for instance to wind the electric motor of a Toyota Prius with Ag would cost $4,118, compared to Cu $572) and higher electrical resistivity (with Al 2.65 x10^{-8} Ωm) are amongst a number of properties seen to be obstructive. Composites are also an attractive option for decreased resistivity at higher temperatures (for instance Cu carbon nano tube composites can have average conductivity 20% higher than Cu) [15,16].

1.3 Historical wire insulation solutions

Since the development of electrical systems such as the dynamo, developed by Faraday in 1821 and the introduction of Volta's Voltaic cell ways to isolate current have been sought, in order to prevent short circuiting, damage and injury. Early solutions included the use of impregnated papers as well as fabrics modified with organic varnishes. The shortcomings of these methods soon became apparent such as their bulk, susceptibility to moisture and tendency to stick to themselves in storage became clear. Silk was employed to address these shortcomings, being wound in a helical pattern around the wire [17,18]. Currently textile coatings are rarely applied and are used primarily for decorative purposes.

Rubber insulation was also commonly implemented in the early part of the 20th century, a number of different fillers were subsequently used alongside rubber. Kerite was one such material, developed by *A. G. Day,* who combined it with rubber to produce insulation with improved moisture and temperature resistance (capable of running at 1.1 kV) [19]. Rubber insulation was the only polymeric insulating material used until the 1930's when it was replaced by synthetic polymer materials due to dielectric strength and cost improvements, including polyvinyl chloride (PVC –often used with an outer coating of nylon) and polyimides such as Kapton® which has improved thermal resistance properties, see ***Table 1.1*** for some typical properties of historically employed electrically isolating materials [19].

Table 1.1: *Historical wire insulation solutions*

	Example Materials	**Cons**	**dielectric strength ($V\mu m^{-1}$)**	**Thermal stability (°C)**	**ref**
Textiles/ papers	*silk, cotton, flax etc.*	• *Bulky* • *Moisture sensitive*	*51.13*	*155*	[20,21]
	Paper/ boards	• *Poor properties without impregnation*	*120*	*105*	[21,22]
Minerals	*Sand, mica, asbestos*	• *Bulky* • *Difficult to form* • *Terminals needed* • *Moisture sensitive* • *difficult to repair*	*/*	*1000*	[23]
Manmade insulation	*Bakelite, modified rubber*	• *Brittle* • *Hazardous chemical synthesis*	*9.8-16*	*230*	[24]

1.4 Current wire insulation solutions

Wiring insulation is often selected from commercially available materials and not specifically tailored from research. The insulation solutions typically employed in different wiring systems vary depending on electrical, mechanical and structural requirements. Systems need to be rated for purpose; for instance domestic electrical insulation for AC 230 V at 50 Hz requires a minimum resistance of 1 MΩ. Above 1 kV a typical guide is that 1 MΩ resistance needs to be added for every additional kV [25]. The breakdown voltage must also be considered and rated accordingly to the required operating voltage.

ASTM D1676 “Standard Test Methods for Film-Insulated Magnet Wire” contains many material characterisation methods which should be used in order to test the electrical properties of wire insulation and provide proof of its suitability. The main methods set out in this standard are wide ranging but include AC breakdown methods utilising wire pairs to determine insulation dielectric strength [26]. The following subsections consider current polymer, composite and ceramic insulation solutions.

1.4.1 Polymers

Wires are commonly coated with polymeric materials, such as PVC and polyimide, brand name Kapton®, commonly used where a relatively high temperature stability up to 300 °C is required. Magnet wire is normally supplied as enamelled, and despite the name this coating is actually a thin coating of polymer (such as polyimides, polyestherimides and polyamide-imides) with a thickness in the region of around 20 μm [27].

Key considerations of polymers include degradation and thermal stability because of arc tracking in aged insulation. Arc tracking is an event caused by the creation of a conductive pathway in insulation due to carbonisation of the polymer material. This pathway then allows the creation of a potential difference between multiple wires. This can result in short circuiting and potentially an arc can then be sustained between these wires resulting in further damage to the insulation [28]. This kind of breakdown in polyimide films has been an issue in the past and was researched by NASA and the FAA among other groups, who showed that the use of polyimide laminated with SiO_x and fibreglass meant that "disastrous flashover" didn't occur, where it did in polyimide films [28]. Breakdown of this kind has been overcome with the application of composite materials, summarised in the following section. Another down side of widely used polymer insulation is that it limited to low temperature operating conditions below 300 °C as shown in ***Table 1.2*** along with other selected properties.

Table 1.2: *Electrical properties of selected polymeric materials.*

	Dielectric Strength ($V\mu m^{-1}$)	*Dielectric Constant at 1 MHz*	*Volume Resistivity* (Ωcm)	*Max. Operating temp.* (^oC)	*Ref.*
u-PVC	*14*	*2.7-3.1*	10^{16}	*75-105*	[29]
Polypropylene	*30-40*	*2.2-2.6*	10^{16}-10^{18}	*128-126*	[29,30]
Polyethylene	*27*	*2.2-2.35*	10^{15}-10^{18}	*80*	[29]
Polyimide	*22*	*3.4*	10^{18}	*249*	[29,30]

1.4.2 Composite insulation

Composite insulation materials such as multi layered materials and materials containing ceramic fillers have been used to enhance coating properties. Current wire insulation solutions often contain multiple layers of insulation, consisting of multi sheathed polymer materials, such as polyimide/fluoropolymer composites (such as tufflite 2000) or the polyimide/SiO_x/fiberglass composite mentioned earlier, for their arc track resistance [31]. Polyimide is utilised in many of these wires especially those that require higher operating temperatures (260 °C and below) [32].

Nano-filler inclusion (< 10 wt% and < 100 nm particle size, otherwise known as micro-composites) into polymer insulation provides a number of improvements in thermal, electrical and mechanical properties over traditional polymers. The addition of alumina trihydrate fillers can be used to achieve improved arc tracking resistance, for example by adding 130 phr of the alumina trihydrate a *ca.* 60 s increase in arc resistance time to 420 s was achieved in high temperature vulcanised silicone rubber [33]. The thermal stability of hydrogenated butadiene rubber was increased from 460 to 484 °C with the inclusion of 16 phr sepiolite [34].The addition of ceramic fillers has also been explored to increase the thermal conductivity of polymeric materials, the addition of 40 wt% silica nanoparticles to epoxy has been shown to increase the thermal conductivity from ca. 0.22 to 0.29 WmK^{-1} [35]. Specifically with respect to improvement in electrical breakdown the addition of exfoliated BN nano sheets to a polymer matrix, as shown by *Xie et al.* can be used to improve breakdown strength (with 6 wt% exfoliated sheets and 5 wt% $BaTiO_3$ a breakdown strength of 400 $V\mu m^{-1}$ was achieved, which was 40 % higher than the $BaTiO_3$ and polymer alone). This is because of the sheets high resistivity and fine dispersion acting as an effective barrier to charge conduction [36]. A review by *Zhang et al.* has explored the benefits of composites with respect to both thermal conductivity and electrical insulation. The work concluded that a high loading (> 30 vol.%) of ceramic was needed to take advantage of improved properties. For example the thermal conductivity of epoxy composites increased from 3.60 to 13.46 WmK^{-1} when Al_2O_3 loading was increased from 55 to 70 vol.%, however, with some fillers chemical modification is required to negate an increase in conduction when added to the composite [37,38].

1.4.3 Ceramic coated wires

Commercial ceramic coatings applied to wires are available, such as those produced by Ceramawire, who use a large combination of oxides within their coatings as listed in ***Table 1.3***. These coatings are applied to Ni and Ni coated copper wire for applications such as coil or stator winding, with maximum temperature and voltage handling of 540 °C and 150 - 200 V (wire gauge dependant) respectively and a minimum warrantied bending radius of 7 times the wire diameter [39].

Table 1.3: *Composition of Ceramawire ceramic wire coating*

Component	***% By Weight***
Lead Oxide	*30.0-50.0*
Titanium Oxide	*15.0-25.0*
Silicon Dioxide	*15.0-25.0*
Magnesium Dioxide	*8.0-15.0*
Boron Oxide	*1.0-5.0*
Nickel Oxide	*1.0-3.0*
Manganese Dioxide	*1.0-3.0*
Cobalt Oxide	*0.5-2.0*
Aluminium Oxide	*0.5-2.0*

Other ceramic coated wires are available, with similar wires produced by Compagnie Générale des Plastiques; both products can suffer from poor moisture handling, low voltage rating (similar to the ceramawire with a maximum 150 V), and both have a similar maximum continuous operating temperature of 500 °C [40].

1.5 Magnet wire insulation solutions

With a climate which is shifting towards electrifying power transition systems, magnet wire is set to play a huge role in power transmission. Magnet wire is named as such because it is used to convert electrical to magnetic energy, hence is used extensively, specifically in components containing windings such as electric motors. These wires consist of a copper core with an “enamelled” coating which consists of a layer of resin varnish. These coatings are usually formed of various polyimide polymers and have evolved from earlier textile coatings as discussed previously [41]. High temperature stability (> 300 °C) in insulating materials is of high importance for improving insulation lifetime and applicability for high temperature environments, such as in the wires discussed in the previous section, which have maximum operating temperatures of 540 °C.

Solderable magnet wires were developed in which the insulation is decomposed at the soldering temperature, leaving bare copper. Materials such as polyurethane which decomposes at 360 °C are incorporated into composites for this reason. *Payette* showed that increasing the amount of urethane groups improved the solderability, a reduction in imide groups was also found to improve solderability to the detriment of the thermal stability, where the modified coatings typically had a maximum thermal rating of 155 °C [42].

1.6 Summary of issues with current wiring systems

Polymeric coatings are the most commonly used insulation, whether in the form of an extruded or varnished material. Chemical resistance and inertness can be achieved by modifying the use of different polymers and multilayers [37]. However, there is a lack of commercially available polymeric coatings which can provide reliable insulation above *ca.* 260 °C, which is somewhat limiting in the design aspect of high temperature devices. Thus, a coating which is stable at high temperatures is crucial for further development of high temperature stable apparatus.

1.7 Coating production methods

The following section will explore the established methods for wire coating as well as some of the research conducted on wire coating for electrical and other applications.

1.7.1 Polymer coated wire

Typically polymer insulation has been applied using extrusion techniques whereby the wire is drawn through extruded polymer following annealing of the Cu to remove work hardening after drawing. Control systems are used to make sure of consistent coating thickness and quality [43]. Often multiple polymer layers are needed as discussed previously, such as the combination of nylon and polyimide for arc protection. Polymers can also be dip coated requiring the use of appropriate concentrations where an increased concentration results in increased viscosity and coating thickness (typically of the order of 1μm), whereby film uniformity is dependant on drainage, solvent evaporation and drying [44].

Magnet wire insulation can be applied in a number of ways. Tapes and sheets are utilised by companies such as DuPont ^{TM} by combining heat sealable Kapton $^{®}$ films which are wound helically around the wire with fluoropolymer adhesive [45]. *Ait-Amar et al.* also outline the typical coating process of drawing wire through trays containing varnish dissolved in solvents. However, such processes are described as heavily polluting as well as energy intensive. *Ait-Amar et al.* explored the potential of polyester and polyester acrylate films deposited through solvent free methods as magnet wire insulation. They found that a composite insulation produced wires with a breakdown voltage of *ca.* 8000 V comparable to the commercially available (polyester-imide/polyamide-imide) wires, showing the potential for new coating methods [27].

1.7.2 Ceramic coated wire

Methods for applying ceramic insulation include packing, dip coating and other solution based methods. Packed insulation of MgO and to a lesser extent SiO_2 and Al_2O_3 are used in highly demanding environments. The properties which facilitate include high temperature stability up to 1000 °C, ionisation resistance (where $MgO.nAl_2O_3$ insulation can strongly resist the formation of defects under energetic particle bombardment, e.g. no defects were found under irradiation with 1 MeV electrons) and combustibility resistance due to the high thermal stability [23,46]. Mineral insulated cable generally consists of a metal sheath which contains conductors packed into the appropriate insulator. Bulk ceramics can also be formed using a herring bone conformation using pressing and joined along the length of a wire. Whilst this provides ample electrical insulation and a certain degree of flexibility (determined by the size of the rings) this solution is extremely bulky and limited in use to vacuum environments.

Chemical methods can also be used for the production of insulating coatings. Coating of tapes of various composition in reel-to-reel systems has been studied by a number of groups using sol-gel processing. Whereby the tape is drawn through appropriate precursors and solvents, resulting in relatively thick coatings (> 50 µm) of various oxide components (including ZrO_2, MgO, Y_2O_3 and CeO_2) being required to achieve a reasonable breakdown voltage of above 500 V [47,48]. Benefits of this kind of technique include its relatively low cost when compared to vacuum deposition methods, ease of implementation of multilayers and doped structures (without necessarily needing large amounts of material) and ease of implementing a reel to reel system. However, films produced through sol-gel and dip coating processing suffer from porosity which is one of the major breakdown routes in ceramic insulators and whilst this is a bonus in some applications such as in filter materials it can be seen as detrimental to isolative films because of breakdown and pre-breakdown conduction [49,50]. An additional issue with sol-gel coating is that the production of precursor materials can be time consuming, for instance production of TiO_2 powder by *Liang et al.* required the hydrolysis of tetrabutyl titanate and required 12 h to form the TiO_2 sol [51].

Other methods for deposition had been considered for coating of wires, such as chemical vapour deposition (CVD), which can be assisted in many ways such as with a plasma or highly ionised pulsed magnetron sputtering (HiPMS). However, the expense of additional equipment (a HiPIMS power supply can cost three times more than a DC power supply of a similar power) and relatively low deposition rate (deposition efficiencies for HiPIMS range between up to 40 % of conventional magnetron sputtering) were seen as additional barriers to coating and thus such methods were not considered further [52–54].

Cost is often cited as a draw back for the use of plasma/ sputtering based technology, however, a continuous process could be utilised to coat kilometre sections of wire relatively quickly, creating a high through put process. This combined with the use of inexpensive starting materials (such as aluminium and copper targets) and reactive sputtering could also keep the cost of raw materials down. The improved structure and electrical properties of PVD films results in a higher dielectric strength, whilst lower thickness also allows potential improvements in flexibility as shown by the higher fracture strain in the thinnest RF sputtered ZnO:Al films deposited by *Mohanty et al.* [55].

2 Aims and Objectives

The aims of this study are to produce highly isolating ceramic films, which adhere well to copper and offer a potential increase in thermal stability and packing density compared to commercially available insulation. Ideally for use in motor windings and actuators for electrical vehicles.

To achieve this aim a number of key objectives were considered:

1. Investigation of different approaches to sputtering Al_2O_3 onto copper by examining the potential selection of: power supply options (RF, DC and pulsed DC) and the tuning of deposition parameters (including optical emission intensity, deposition bias and film substrate interface), in order to optimise Al_2O_3 films so that they possess suitable electrical properties including a dielectric strength above 500 $V\mu m^{-1}$ and would also be adherent to copper.
2. Explore the potential of multilayers of PDC Al_2O_3 and different RF sputtered ceramics, to further enhance the dielectric strength of the sputtered coatings by up to 50 %.
3. Develop a processing route through which suitable coatings will be applied to copper wire substrate, to produce wires suitable for winding applications.
4. Examine the role of temperature on adhesive and electrical properties through heat treatments on these films. This will help assess the films potential as high temperature insulation coatings above the traditional limit of 300 °C and to observe any change in properties upon annealing.

3 Literature Review

3.1 Physical Vapour Deposition

Physical vapour deposition (PVD) is a term used to describe a variety of techniques whose basic principle is to use physical methods (such as plasma) to vaporise atoms of a desired material which are then allowed to condense onto a substrate. This method allows the deposition of films from <1 nm ranging up to 2 μm, of any material which can be used to produce a suitable target.

3.1.1 Sputtering

The origins of sputtering lie in the creation of the first glow emission in vacuum chambers. Very early development of plasma was credited to *Faraday* in 1853, whereby passing a current through a low pressure working gas created a glow discharge [56]. Other early work on plasma was carried out by *W. Crookes* who experimented with discharges in vacuum tubes as discussed in his lecture “On Radiant Matter” [57,58]. In its infancy, and possibly the first documented use of plasma as a method for deposition, sputter deposition was used by *Grove* in 1852 to coat polished silver surfaces [59–61]. All of these discharges consist a state of matter (Plasma) whereby electrons in a low pressure gas are liberated from their atom creating a positively charged atom with an electronically neutral state of matter overall.

The typical profile for a plasma discharge between a cathode and anode, confined within a glass tube with a low pressure working gas is shown in ***Figure 3.1*** [62]. It is also important to note here that there is the potential for different kinds of discharge depending on the working gas pressure and the applied current. Of such discharges arc evaporation is also another physical method, which can be used for coating and involves using a higher discharge current.

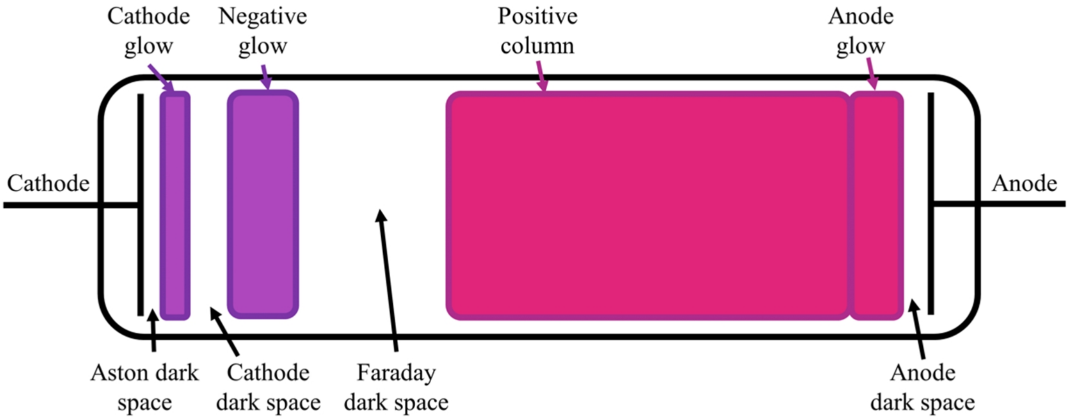

Figure 3.1: *Schematic of the regions of a typical glow discharge between a cathode and anode with a low pressure working gas* [62].

Great improvements have been made upon the base technique with the improvement of vacuum technology and implementation of magnetrons, solenoids and varying power supply options among other techniques. Sputtering processes and the improvement of deposition equipment will be discussed in the following section.

3.1.1.1 Sputtering Theory

At its core sputtering technology relies on the use of an inert gas plasma to remove target atoms by momentum transfer. In the plasma atoms of the working gas (usually argon) become ionised by a voltage applied between the target and substrate, causing the plasma glow and are accelerated towards the target. Target atoms are then sputter ejected as neutrals through momentum transfer with these ions and can condense on a substrate [63].

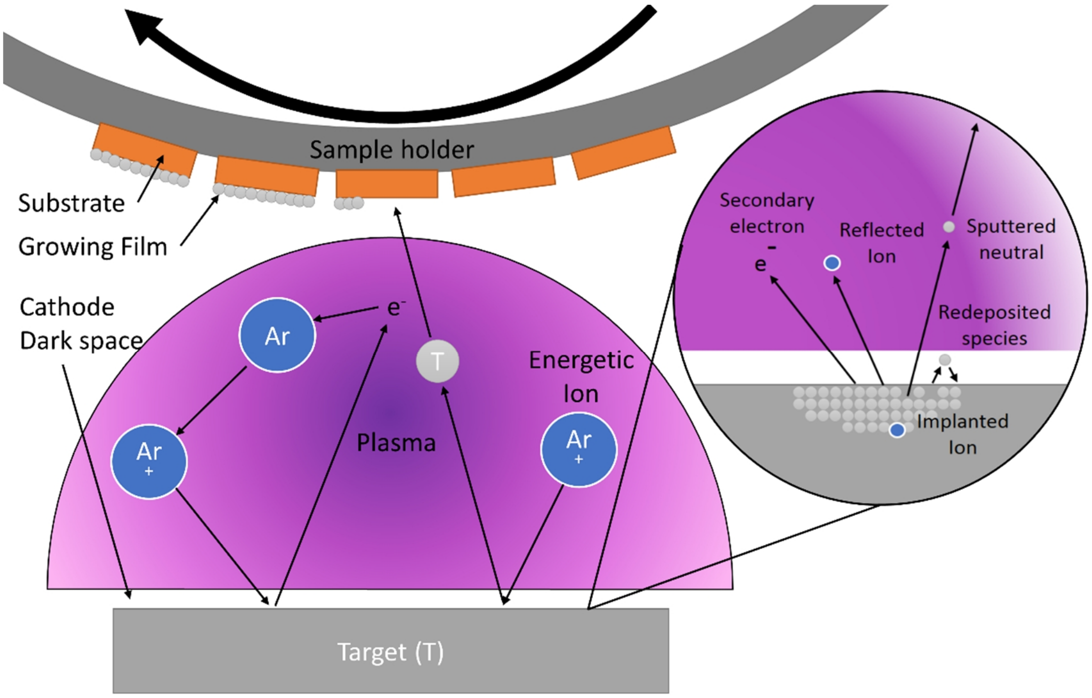

Figure 3.2: *Principles of sputter deposition, based in the TEER UDP-650. The target is being sputtered using Ar, which is ionised by the application of a potential difference over the target and chamber which acts as the anode. The Ar ions then bombard the target releasing secondary electrons and target neutrals, as shown in the high resolution section. Bombarding species may also become embedded in the target. It is also important to note that target poisoning due to the reactive gas can become an issue in reactive deposition, whereby charge builds up on non-conductive regions of the target leading to arc events* [63].

There are a number of phenomena which can occur at the target surface as outlined by Mattox amongst others [63,64]; including sputtering, implantation, reflection and re-deposition, see ***Figure 3.2*** for a schematic of these phenomena at the target surface.

3.1.1.2 Sputtering Parameters

As a result of the physical processes occurring at the target and film surfaces it can be seen that the processing parameters will play a large role in the properties of the resulting film. The main effect of modifying a parameter is to modify the energetics of the sputtered and sputtering particles. For instance chamber pressure, non-reactive gas species and flow rate (determining the number of collisions) have the potential to reduce the energy of sputtered particles resulting in films of decreased density as well as decreased thickness because of lower energy and fewer sputtered particles reaching the substrate [65]. These effects are the result of processes such as thermalisation, where the energy of vaporised material is lowered to that of the ambient gas and scattering, where at higher pressures ions can undergo physical and charge exchange collisions. It is for these reasons that the substrate target distance is also key [63].

The target material and its surface binding energy plays a role in sputter yield; see ***Figure 3.3a)*** for reference to the variance in sputtering yield for selected elements with respect to atomic number [63]. The shape and size of the target will also play a part in film properties such as the increased plasma density offered by a hollow cathode source, forming denser coatings through a higher level of ionisation [66]. Specific material phases and structure such as grain structure can also effect sputtering. It is worth noting that Ar is often the sputtering gas of choice because it is of a suitable mass that it results in sufficient momentum transfer to sputter a large range of materials, the cost compared to other noble gases is another attractive aspect of Ar [59,63]. An increase in target power will also lead to an increase in deposition rate and an increased plasma density, leading to improved crystallinity due to the higher energy sputtered species, as shown by research on the effect of target power and Ar pressure on sputtered Ti films by *Kavitha et al.,* see ***Figure 3.3b)*** for thickness power relationships [65].

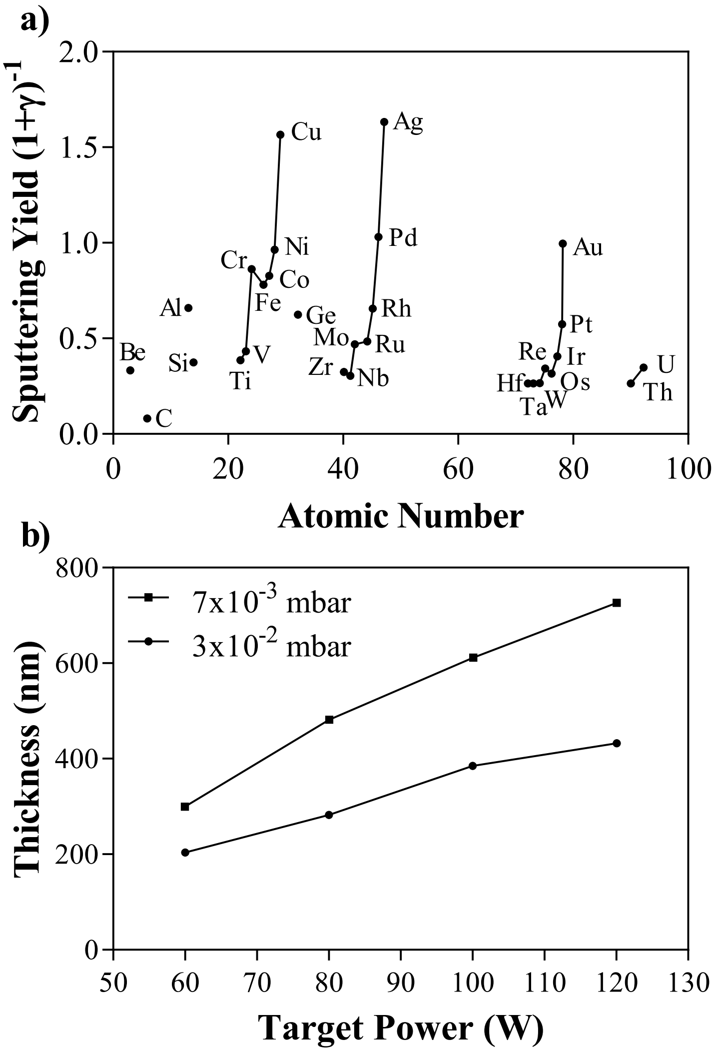

Figure 3.3*: a) Sputtering yield with relation to atomic number when sputtering with 400 eV Ne$^+$ ions, reproduced from* [60]. *b) Target power and resulting film thickness after 20 min coating from a Ti target, reproduced from* [65].

Substrate biasing and sample heating are other optional parameters which some equipment can utilise. Biasing of the substrate is a powerful addition which can modify film composition and structure. The applied bias has the effect of bombarding the growing film with energetic particles which can modify the growing film in a number of ways such as heating, atomic peening, sputtering and contaminant desorption [67–69]. A large number of benefits can be achieved through this ‘ion bombardment’ such as improvements in intrinsic stress as seen by *Cemin et al.* for sputtered Cu films where grain growth was modified by bias application [70]. *Kovac et al.* also showed an improvement in defect density with the application of a suitable substrate bias on Al-Sc sheets [71]. Studies by *Kelly et al.* found that a high substrate bias was conducive to the formation of stoichiometric alumina [72]. Heating is also another route to inducing morphology changes as it can be used to increase adatom kinetic energy resulting in an increased film density [65]. This can be beneficial to a film's protective qualities as demonstrated by the improved leakage current density with increasing substrate bias for TiO_2 films deposited by *Chandra Sekhar et al.* ($1x10^{-6}$ to $1.41x10^{-7}$ Acm^{-2} when a bias of 1.5 V was applied)[73]. Increasing the energy of sputtered species through ionisation has also been shown to be useful in creating crystalline films, such as in HiPIMS [74].

3.1.1.3 Reactive sputtering

According to *Mattox* the first meaningful use of reactive sputtering was when *Berry* deposited Ta_2N films from a Ta target in an N atmosphere [63]. The process facilitates deposition of compound materials from metallic targets by the addition of a reactive gas into the inert gas plasma. The sputtered target atoms will react with the reactive species to form a compound. However, this does not exclusively occur at the substrate surface [75]. This leads to one of the complications of reactive sputtering with direct current (DC) power resulting in arcing at the target as charge builds up at the poisoned sites. These problems are often mitigated by using radio frequency (RF) or Pulsed DC sputtering enabling the sputtering of insulators and selective preferential sputtering of poisoned regions [63,76,77].

Generally because of the low atomic mass of the reactive gas (i.e. O_2 or N_2) they are ineffective for sputtering so they are used in combination with a heavier sputtering gas such as Ar [63]. Reactive sputtering, however, is a sensitive method since small additions of reactive gas can lead to a change in the state of the target (i.e. metallic or poisoned) meaning a means for gas control is crucial. The flow of gas is typically controlled by mass flow, however, a hysteresis behaviour can be seen whereby the sputtering rate is dependent on the reactive gas flow rate, because of the cycle on the target surface between poisoned/ compound and metallic modes, see ***Figure 3.4*** [78].

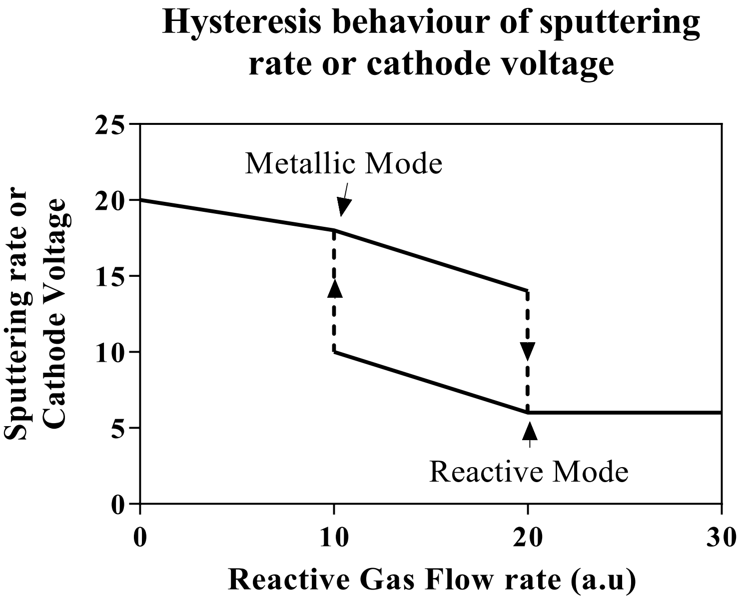

Figure 3.4:*Relationship between sputtering rate and reactive gas flow rate reproduced from* [78].

Gas flow can also be controlled by using an optical emissions monitoring system (OEM, also known as optical emission spectroscopy) as demonstrated by *Schiller et al.* who carried out pioneering work showing that optical emission can be used in a feedback loop to maintain a desired stoichiometry [79]. Monitoring of this kind relies on the observation of a certain emission wavelength determined by the sputtered material, whereby the addition of a reactive gas will decrease the intensity and thus can be used in conjunction with a feedback loop to constantly control reactive gas flow. The selection of the desired emission line is outlined by *Chen et al.* for TiO_x sputtering [80]. This removes the need for constant manual adjustment to the gas flow rate, to achieve reasonable deposition rates. The OEM relies on the control of the plasma emission intensity, which is changed through the addition of a reactive gas, where the plasma intensity when sputtering in 100% Ar is used as a calibration [72,81,82].

Reactive sputtering is not limited to nitride ceramics, it can be used to deposit oxides, oxynitides and diamond like carbon films (whereby a hydrocarbon species is used whilst sputtering from a graphite target to promote the production of sp^3 C materials) among other materials [83–85].

3.1.1.4 Power supply options

Conventional DC deposition relies on the delivery of DC power to a metallic sputtering target and is the simplest sputtering technique, this is the kind of power which was used in early diode sputtering. DC sputtering has found use for metallic films with high deposition rates which are dependent on the target material. DC deposition can also be utilised to reactively sputter non-metallic material from a metallic target, with sputtering rates lower than the pure target material, caused by target poisoning [63,86]. However, as mentioned previously target arcing becomes a problem (with respect to target, power supply life time and coating quality) once the target becomes poisoned by the reactive gas, see section (3.1.1.3) [87].

Pulsed DC deposition – developed in the early 1990's - is more suited to the deposition of ceramic materials than reactive DC sputtering because of the target charge neutralisation and reduction in the build-up of target poisoning offered, as a result of periodic reversal of applied voltage [88]. Unlike when utilising RF sputtering, it is possible to control the frequency and duty cycle at which the power is pulsed when using pulsed DC power, see ***Figure 3.5***. The duty cycle and the pulse frequency, typically between 20 and 60 kHz, can be controlled in order to optimise arc free deposition time [87]. The pulsing of the supplied power allows the preferential sputtering of contaminant material from the target surface as the bias is reversed during the deposition, allowing any surface charges to be neutralised and thereby preventing arcing. This also has the effect of creating a higher potential difference between the poisoned surface and results in the preferential sputtering of this material, meaning that the surface contaminants can be controlled [89].

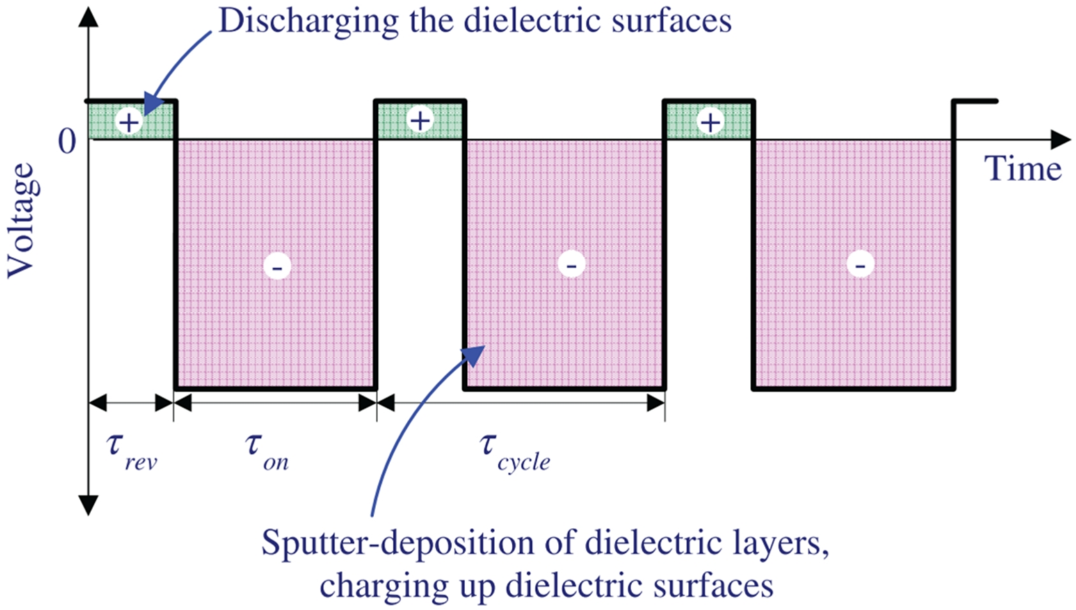

Figure 3.5: *Schematic of the voltage sequence in bipolar pulsed DC sputtering, showing the cycling used to alleviate charging on the surface dielectric materials. Taken from* [90].

HIPIMS methodology uses a pulsed profile as with pulsed power sputtering, however, it is differentiated by the use of extremely short pulses (*ca.* 100 µs, to avoid arcing during deposition) at high power with peak powers up to 100 MW [77,91]. These high power pulses produce a highly dense plasma, with a much higher degree of ionisation in the sputtered material, because of the self-sputtering which takes place at the target [92,93]. This dense plasma is useful for creating highly dense defect free films. The benefits of ion bombardment resulting from the higher amount of ionisation have been discussed previously, see section (*3.1*). The downside of this technique is the start-up cost coupled with the potentially low deposition rate [94].

Radio frequency (RF) deposition is a technique which requires the use of a RF power supply in conjunction with a matching unit to supply power to a target. This method of sputtering was developed in the 1960's by *Davidse and Maiseel* for sputtering dielectric materials [95]. RF power is delivered at radio frequencies, typically 13.5 MHz. RF deposition is commonly used to deposit ceramics from compound targets, because during sputtering the target is alternatively bombarded with electrons and ions [91,95]. Despite sputtering from compound targets materials can still benefit from the inclusion of a reactive gas (during sputtering or as a conditioning stage), with regards to stoichiometry and structure, such as improved stoichiometry of Al_2O_3 deposited using RF reactive sputtering from a ceramic target as noted by *Bhatia* [96].

However, there are drawbacks to RF power, including high equipment cost and low deposition rates when compared to DC deposition. The use of compound targets also needs to be considered because of potential for preferential sputtering, varying surface binding energy and the effect of different target power on such, such as the increase in Al liberation seen when sputtering from an Al_2O_3 target at higher powers as sputtered by *Reddy et al.* [88,97].

3.1.2 Magnetrons

Magnetrons are magnetic arrays which are placed behind the sputtering target and are used to contain the secondary electrons close to the target (electrons move in a helical path due to the non-uniform magnetic field lines). The helical path causes electrons to have a longer free path, thus they have the potential to ionise more of the working gas close to the target see ***Figure 3.6*** *and* ***Equation 1***. It has been shown that the deepest erosion occurs at the point where the magnetic field lines are parallel to the target surface [98].

Equation 1: *Velocity of electron in perpendicular magnetic and electric fields as shown in* ***Figure 3.6****.*

$$V_d = E * B$$

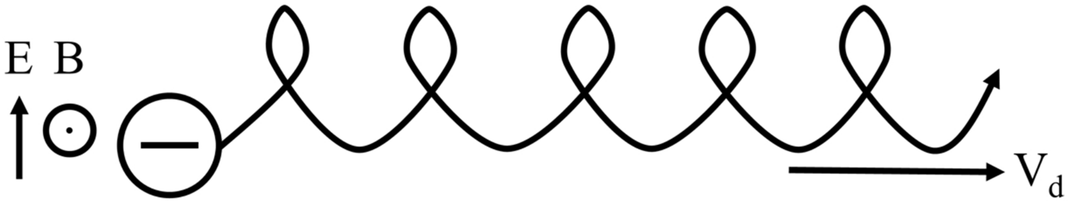

Figure 3.6: *Helical path of an electron in perpendicular electrical and non-uniform magnetic fields reproduced from* [98].

Magnetron implementation has allowed considerable advantages over conventional diode sputtering and they have become an integral component in sputtering equipment, especially in industry because of improved deposition rates. It is important to note that magnetrons do decrease the target utilisation when compared to standard diode sputtering, because of the increased target erosion directly below the high intensity plasma region due to the confined electrons.

3.1.2.1 Varieties of magnetron

The magnetron sputtering method was developed by a number of researchers as a response to poor deposition rates in diode sputtering, relying on the control of electron motion near the sputtering target. Early work by GE among others to control the electron density in many fields was followed by *Chapin* who patented a closed field planar magnetron for sputtering applications [77,99].

One of the major benefits of magnetron sputtering is that the target can be cooled (as well as the chamber) allowing the temperature to be moderated. This cooling benefits the growing films because it inhibits diffusion of the target materials, allowing stoichiometry to be maintained when sputtering compounds or alloys.

The fixed magnet configuration can be changed to provide a number of different magnetron options, including balanced and unbalanced magnetrons. The difference in these two is increased ion current density at the target on an unbalanced magnetron, caused by an increase in the strength of the magnets in the outer ring relative to the inner pole, see ***Figure 3.7*** for a schematic of the magnetron systems, noting the magnet sizes [100]. Work by *Constantin and Miremad* in the deposition of decorative coatings showed the importance of the unbalanced magnetron on the decorative and mechanical properties [101].

It is also important to note that in multi magnetron systems the plasma density can be controlled even further by modifying the magnet arrangement of adjacent magnetrons. In closed field configurations the magnets are opposite polarities and in the case of mirrored arrangement the polarities are the same. A closed field reduces the losses of electrons to the chamber and increases the plasma density at the substrates [100]. More recently flat magnetrons have been developed by which a higher percentage of the target material can be utilised, before the target must be changed, with a patent granted to *Clarke* of Tegal for a flat magnetron design [102].

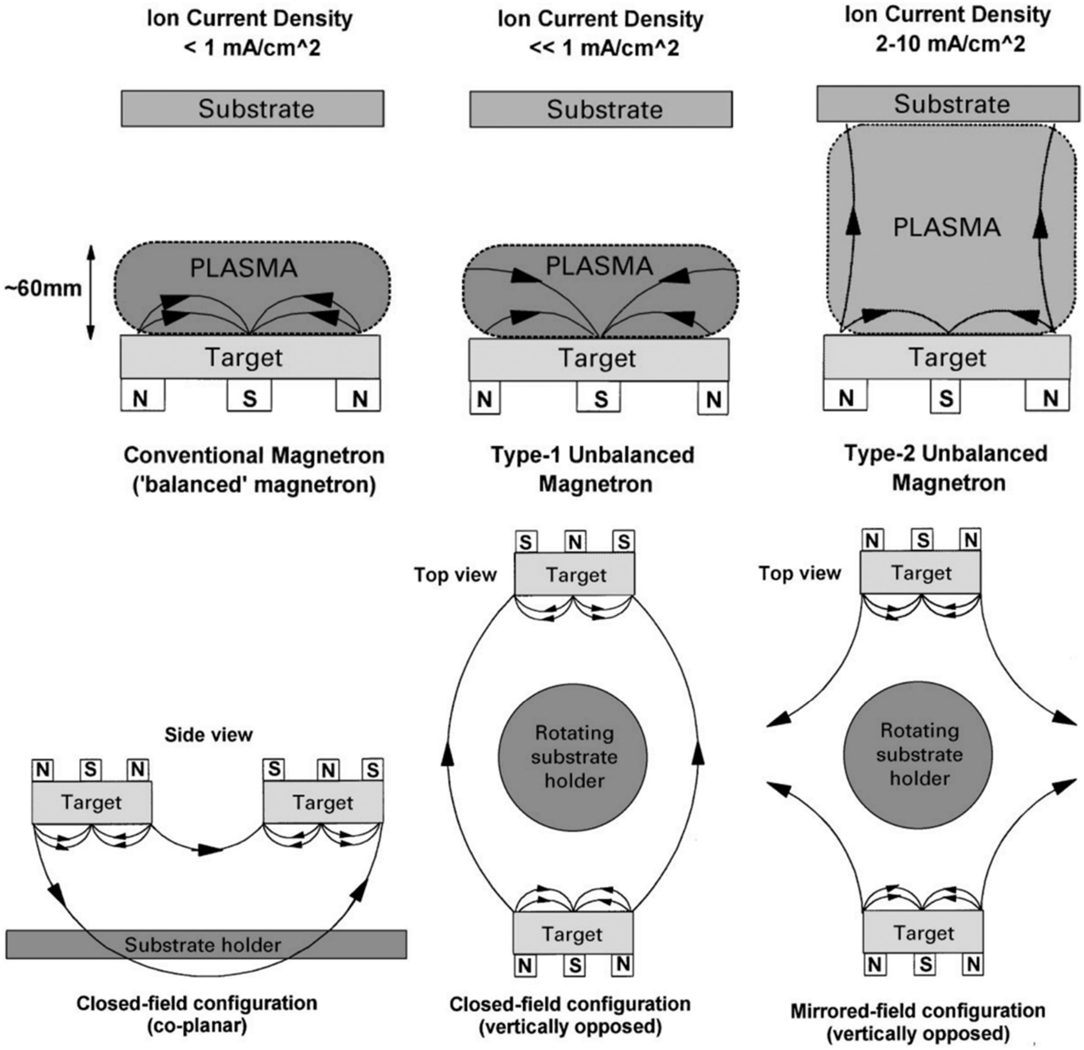

Figure 3.7: *Magnetron configurations and the resulting plasma density (top row). Closed and mirrored field magneton arrangements (bottom row), all as shown by Kelly and Arnell* [100].

3.2 Electrical breakdown in dielectrics

Electrical breakdown in dielectric materials occurs once the material’s insulating properties deteriorate to the point where the material becomes a conductor. This will occur if a voltage above that of the breakdown voltage is applied and may result in soft (where the material can recover) or hard breakdown (where material is completely broken down and will not recover) [103]. There are a number of mechanisms for conduction in normally insulating materials, which can be grouped into two categories: bulk and electrode limited mechanisms. Bulk limited conduction is dictated by the material properties and electrode limited conduction is determined by the electrode dielectric interface. There may be a number of conduction mechanisms operating at one time [104]. A more comprehensive discussion of the electrical conduction in thin films will follow an appreciation of the breakdown mechanisms in dielectrics. Hence the following section will look at the factors which lead to breakdown within dielectric materials.

Intrinsic breakdown is considered wholly related to the material and is the absolute maximum field that can be applied before breakdown will occur, where the only influences are the intrinsic material properties and the temperature [105]. The intrinsic breakdown of a material relies on the evolution of charge carriers, which occurs when the species gain energy from the applied voltage at a greater rate than it can lose it [106]. When a low voltage electric field is applied energy gained by charge carriers is lost relatively easily through phonon collisions. Under a large enough applied electric field an electron has the potential to ionise the lattice. At this point more charge carriers are created and an **avalanche** can occur breaking bonds in the material [50,105,107].

Extrinsic factors still play a large role in initiating breakdown (because measurement systems are not ideal), factors such as surface defects, including chemical impurities and voids in the film and variation in the material structure as well as differences in the measurement configuration [105]. For instance, breakdown in polymer insulation can also occur through arc tracking events caused by the production of carbonised tracks which can conduct electricity as seen in a study of the pyrolysis of polyimide by *Stueber and Mundson* [28]. The carbonisation of some materials depends on the service time as well as the atmospheric conditions. The following section will explore a number of other breakdown mechanisms driven by external factors.

Defects within the dielectric material such as crystal faults/grain boundaries, porosity and contamination are potentially a route to breakdown in the material, acting as charge traps or as sites for ionisation among other things [50,108]. These sites can cause premature breakdown and is why careful consideration should be given to the material production method to avoid such defects [109].

Electromechanical breakdown relies on the maximum electrical stress a material can withstand before breakdown. Mechanical instability will occur when the thickness decreases by 40% (thinning is caused by build-up of charge on opposing sides which causes an attraction). The breakdown occurs when the materials mechanical properties cannot compensate for such attractive forces [110]. As a result of the mechanical properties required, electromechanical breakdown is restricted to a number of low strength and high ductility polymers such as polyethylene [111].

Thermal electronic breakdown occurs due to heating caused by the passage of current and dielectric losses. Once the level of heat generated is above the heat that can be emitted then the material will begin to undergo thermal breakdown, thus this kind of breakdown takes a longer time to initiate, see ***Figure 3.9*** [112]. *Sawa* has expanded upon the mechanisms of thermal breakdown of polymeric dielectrics which included: field impulse breakdown caused by field dependant electric conduction and filamentary thermal breakdown [113].

Chemical/ electrochemical breakdown is caused by the action of the operating environment on the material, such as the action of solvents, for example in the process of Al anodization as discussed by *Tajima* the anodizing electrolyte dissolves the film, producing a porous film, leading to premature breakdown [110,114]. **Treeing and tracking** are essentially the stepped breakdown of materials between impurities/ voids within the material. Failure of this ilk is usually caused by long exposure to electronic stresses and contamination, such as those that cause arc events as discussed for polyimide insulation [28,110].

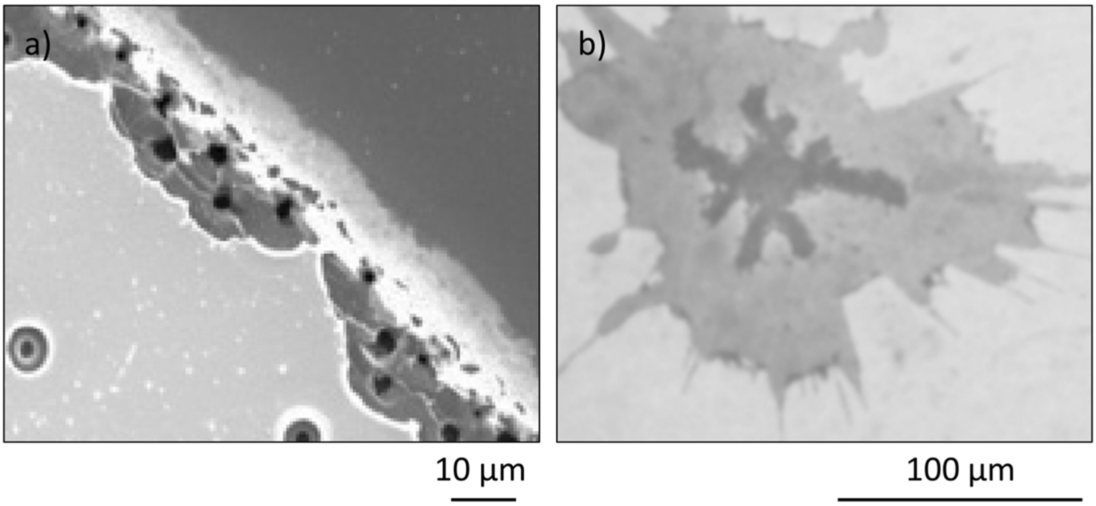

Figure 3.8: *Images of catastrophic breakdown sites on a) alumina thin film produced using sol-gel methodology and b) anodised* Ta_2O_5 *(mid grey) on sputtered Ta (light grey)* [49,111].

The breakdown of polymeric insulation is always considered catastrophic, where all instances of catastrophic breakdown are considered electronic/thermal in nature because of carbonisation (in the case of polymers), melting or vaporisation of the dielectric material [115]. Breakdown spots in the film can often be characterised through light or scanning electron microscopy, as seen in sol-gel Al_2O_3 films seen by *Yao et al.* , see ***Figure 3.8*** [49].

As evidenced by this section routes to increasing the dielectric strength often include improving structure and decreasing the defect density, resulting in less weak spots in the film which could result in lower breakdown [108,109]. Other routes such as composites as discussed in the introduction will be discussed further in section (*3.13*).

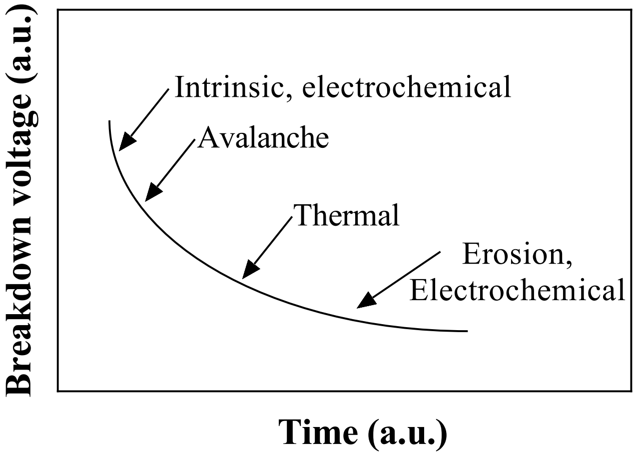

Figure 3.9: *Relationship between breakdown voltage and breakdown mechanism with time and the different mechanisms which occur relative to both (reproduced from* [110]*).*

3.2.1 Breakdown (dielectric strength) measurements

Breakdown measurements can be made by applying an electric field across the sample, with a voltage greater than that needed to initiate a current flow, as discussed above. This can and often does include the measurement of current voltage characteristics prior to breakdown. From these voltage characteristics it is also possible to calculate a materials resistance at specific DC voltages using Ohm's law. These results can also facilitate characterisation of the conduction mechanism.

Breakdown voltages of thin films have been measured extensively for many kinds of materials and the results are usually expressed in the form of dielectric strength the breakdown voltage per unit thickness see ***Equation 2***, with values often expressed in Vμm^{-1} [50].

Equation 2*: Dielectric strength (E_{BD}) as calculated from breakdown voltage (V_{BD}) and film thickness d.*

$$E_{BD}(Vm^{-1}) = \frac{V_{BD}(V)}{d(m)}$$

Dielectric strength has been measured in a number of different ways, often utilising a multi probe system and a high voltage power supply for analysis. Often a resistor is placed in series in the circuit to prevent damage to the power supply on eventual breakdown, voltage over such a resistor can also be used to calculate the current flow [116]. It can be seen in the literature that the probe selection can have an effect on the measurement values and consistency depending on the material preparation, size and probe material are of great importance, for the roles they play in interaction with defects and space charge injection, see ***Table 3.1*** [117]. For instance a smaller probe contact area has been shown to result in a lower breakdown strength, because of the more localised charge density, for example a *ca.* 50 $V\mu m^{-1}$ decrease in dielectric strength of acrylic elastomers was seen with a decrease in probe radius from 1.0 from 2.5 mm when an initial stress of *ca.* 10 MPa was applied) [118]. *Groner et al.* have utilised mercury probes for well-defined area of measurement on Al_2O_3 films [119]. AFM instruments have also been used to measure the conduction and breakdown properties of thin films, some as thin as 10 nm, as studied by *Ganesan et al.* [103,120]. Inherent benefits of these AFM measurements include ability to avoid extrinsic defects and provide consistent local area measurements in tuneable arrays. See ***Table 3.1*** for a summary of methods used to measure breakdown strength on different batches of alumina.

Table 3.1: *Measurement methods used to determine dielectric strength of Al_2O_3 films and typical dielectric strength values obtained.*

Probe type	***method***	***Film thickness (nm)***	***Dielectric strength ($V\mu m^{-1}$)***	***Ref.***
(0.004 cm^{-2}) Hg probe	*ALD*	*12*	*530*	[119]
(0.25 cm^{-2}) Cu contact	*Sputtered*	*2000*	*80*	[116]
(0.13 cm^{-2}) Al Contact	*Sputtered*	*1000*	*620*	[121]
(0.008 cm^{-2}) Au contact	*Sol-gel*	*216*	*276*	[122]
C-AFM	*ALD*	*2* *0.4*	*1000* *2000*	[120]

3.3 Conduction mechanisms in thin films

Conduction in insulating materials is a widely studied topic and a number of reviews have been produced focusing on conduction mechanisms in insulators and oxide materials. Conduction properties depend heavily upon the measurement system (electrode substrate interaction) and material purity and structure [104,106,123]. The following is a review of the conduction mechanisms that have been commonly attributed to insulating materials. It is important to note here that in ultra-thin films conduction can be attributed to direct tunnelling because the material is not thick enough to eliminate the probability that the electron can exist on the other side of the potential barrier [124]. ***Figure 3.10*** displays diagrams of selected conduction mechanisms.

3.3.1 Electrode limited mechanisms

Electrode limited mechanisms result from the interaction between the dielectric surface and electrodes, where the most important parameters are: the barrier height between the two materials and the rate at which electrons can be supplied by the electrode. The most well-known mechanisms include:

- **Schottky emission**, whereby electrons are injected from the electrode into the conduction band of the dielectric. These electrons gain sufficient energy through thermal excitation (leading to an increased probability of electrons being in a higher energy state). Thus testing over a range of temperatures can be used to help demonstrate a temperature dependence. Often this mechanism is responsible for conduction in dielectric materials at high temperature. Measurements of RF sputtered Ta_2O_5 films by *Atanassove et al.* indicated that below a field of 1.3 $MVcm^{-1}$ Poole-Frenkel or Schottky emission were the driving conduction mechanism [125]. *Atanassova et al.* also reiterated the importance of using thermal testing for more accurate mechanism differentiation.
- **Fowler-Nordheim (FN)** tunnelling relies on electrons tunnelling through the triangular potential barrier between the electrode and insulator. The electron may penetrate this barrier when the applied field is high enough. Measurements made at low temperature can be used to negate the effect of thermally excited electrons on the current. Fowler-Nordheim conduction is

often seen at high applied fields such as in 12 nm thick Al_2O_3 and thermally grown SiO_2 films as seen by *Groner et al.* and *Lenzlinger and Snow* respectively [119,126].

- **Direct tunnelling** as mentioned previously is a mechanism which relies on the thickness of material being extremely low, creating a potential barrier small enough that electrons can tunnel through the whole barrier. Often seen in ultrathin films less than 40 nm [104]. This differs from FN tunnelling because the direct tunnelling doesn't rely on an applied voltage for electrons to tunnel through the barrier, see ***Figure 3.10*** for the difference in tunnelling barriers for FN and direct tunnelling mechanisms.

3.3.2 Bulk limited mechanisms

Bulk limited conduction mechanisms in thin films depend entirely upon the rate at which electrons can flow through the material, which is determined by the intrinsic material properties (such as purity and crystal structure). Among these mechanisms the following are some of the most prominent:

- **Poole-Frenkel Emission** is a mechanism where electrons within the material (which are held at traps) are thermally excited into the conduction band of the material. Poole-Frenkel is a common conduction mechanism seen to be the dominant in many films, such as in Boron Nitride (BN) and Ta_2O_5 at high applied fields [127–129].
- **Space charge limited conduction (SCLC)** is a mechanism that is composed of a number of different conduction regimes. Initial conduction in the material at low field is attributed to ohmic conduction, where the leakage current is proportional to applied voltage, this is followed by the traps filled limit, where the current is proportional to square of the applied voltage until the charge traps are filled. The final relationship obeyed is known as Child's law where the current is proportional to the applied voltage because conduction at this point is governed by space charge, which limits the amount of additional charge carriers which can be injected. This kind of conduction has been seen in cobalt phthalocyanine at high fields by *Malik and Adbel-Latif* [130].
- **Ohmic conduction** is caused by the movement of free electrons in the conduction band and or holes in the valence band. Due to the large bandgap of

insulators there are very few electrons in the conduction band promoted from valence or discrete energy levels. This conduction method is seen to be particularly important in the low resistance state in resistive switching devices and is seen in films composed of cobalt phthalocyanine at low applied voltages [130,131].

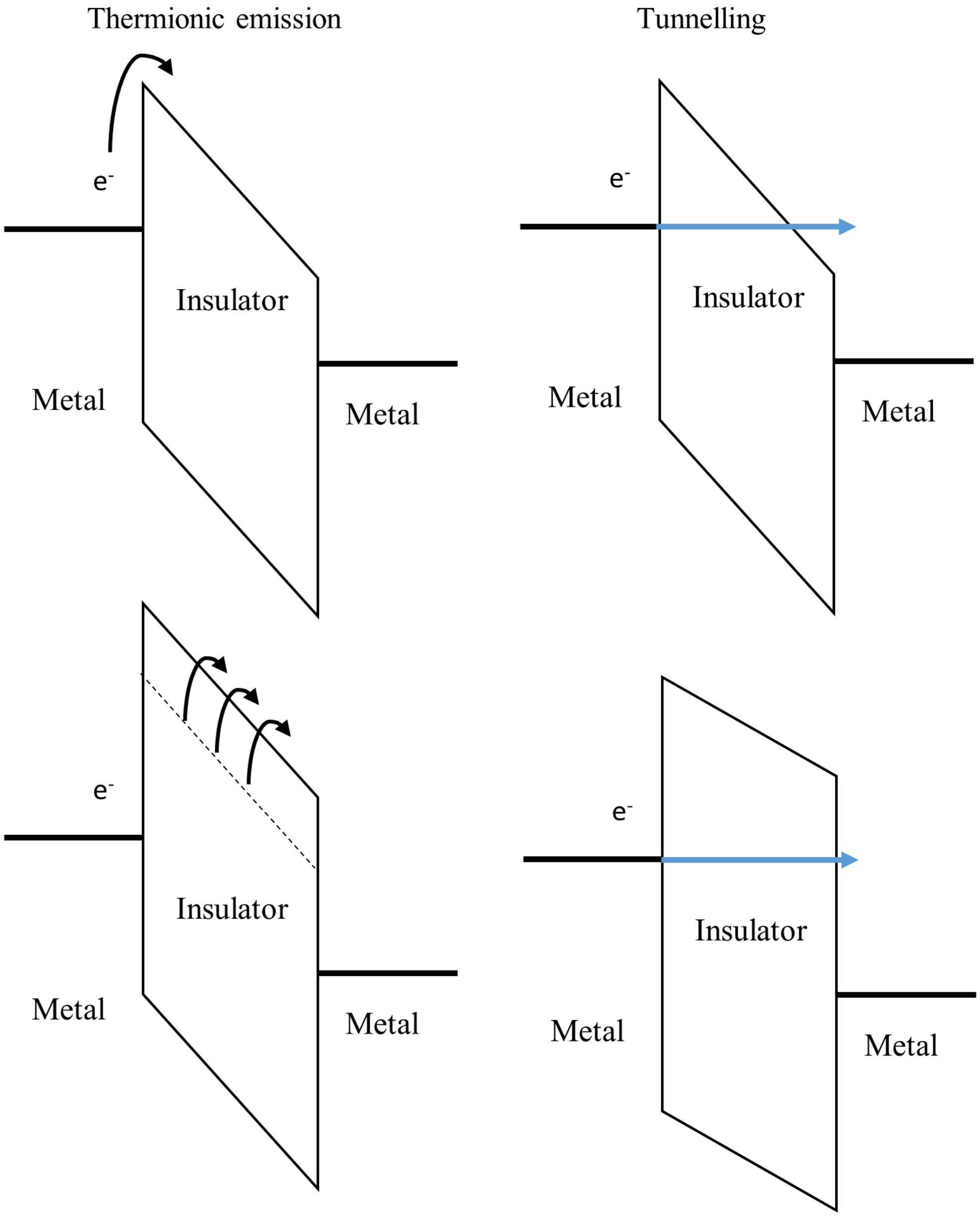

Figure 3.10: *Energy level diagrams for MIM based electrical systems. Included are thermionic mechanisms: Schottkey (top) and Pool-Frenkel emission (bottom) and tunneling mechanisms: Fowler-Nordheim (top) and Direct tunneling (bottom)* [104].

3.3.2.1 Mechanism determination

Plotting graphs of the current and voltage characteristics can be used to determine the relationship between the material and the conduction mechanism at different applied fields [104,132]. For instance linear relationship between 1/E and $\ln(J/E^2)$ could indicate FN tunnelling as discussed by *Chaneliere et al*, usually occurring at high applied fields [133]. ***Table 3.2*** identifies the graphical relationships for the most common conduction mechanisms.

Table 3.2: *linear plot relationship for conduction mechanisms and plots of their current voltage properties* [104,132–134].

Mechanism	***Plot***
Fowler-Nordheim	$(\ln(J/E^2))$ vs (E^{-1})
Schottky	$(Ln(J))$ vs $(E^{1/2})$
Poole-Frenkel	$(\ln(J/E))$ vs $(E^{1/2})$
SCLC	*(Ohmic conduction)* *(Childs law)*
Ohmic conduction	(J) vs (E)

Determination of thermal dependence of the voltage current characteristics can help to differentiate between electrode limited and bulk limited mechanisms, however, the attribution can often be difficult as discussed by *Ezhilvalavan and Tseng* who explored the conduction mechanisms of various Ta_2O_5 materials [135]. Additional graphical analysis such as data fitting, can be combined with measurements at varying temperatures to differentiate between electrode and bulk limited mechanisms as well as divulging information such as the tunnelling or thermionic barrier heights. It is also important to note that other film properties may be useful for the full electrical characterisation, for instance dielectric constant can also be useful for differentiation between electrode and bulk limited conduction mechanisms [104,136].

3.4 Mechanical properties and adhesion of thin films

This section will focus on the adhesion of sputtered films onto metal substrates and analysis of different adhesion metrics. The mechanical properties of thin films vary considerably from that of their bulk counterparts and are linked very closely to the deposition mechanism, as well as the relationship between the substrate and film. It is these factors which determine the intrinsic and extrinsic stress in the films (intrinsic stress results from the coating methods and extrinsic stress relates to the differences in thermal expansion coefficients) [137]. An idea of the differences in stress between some deposited films can be gained by FTIR measurements as demonstrated by *Haanappel et al.* who used saw peak shifting in CVD Al_2O_3 films [138]. Some typical values for the stress in sputter deposited films are given in ***Table 3.3***. The stress evaluation was generally measured by observing the variation in curvature of the sample following coating in combination with Stoney's formula, which is used to relate the curvature to the average film stress.

Table 3.3: *Stress in various sputter deposited films, in relation to working gas pressure.*

Film	***Deposition method***	***Stress measurement method***	***Pressure (mTorr)***	***As deposited stress (MPa)***	***Ref.***
Cu	*DC Sputtered*	*Optical beam bending*	*3.8* *45*	*-150* *150*	[139]
Ta	*DC Sputtered*	*Surface profilometry*	*3.8* *7.5*	*-1000* *1100*	[140]
SiO_2	*RF sputtered*	*Optical beam bending*	*5.0* *20*	*-90* *-310*	[141]
Al_2O_3	*RF sputtered*	*Light selection profilometry*	*30*	*-190* *-33*	[142]

The design of the desired system is important with respect to the adhesion of the films and the use of interlayers and careful surface preparation should be considered where good adhesion is not inherent to the coating system. Interlayers have been utilised by many groups, specifically when binding metals and ceramics. Ti is a popular choice because reactive metals that form stable oxides have been shown to exhibit good adhesion to other oxides. For instance *Ramos and Viera* showed that an increase in critical failure in Al_2O_3 coatings on high speed steel could be achieved by using a Ti interlayer, additionally it was suggested that Ti was suitable for this system because of its potential to react with oxygen from the substrate and the coating [143,144]. It is also important to note that interlayers can be used to template the growth of crystalline films, such as the use of CrO for sputtering α-Al_2O_3 instead of amorphous films for cutting tools [145,146].

The adhesion of thin coatings is of key importance when considering an isolative coating with specific importance in the flexibility and durability of the resulting wire before delamination becomes an issue. There are a number of reasons increased thickness of the coating can modify mechanical behaviour. With increasing thickness the effect of any ion bombardment of the sample becomes less when depositing onto insulating substrates (if using a DC bias) and thus results in a lower amount of mobility during film growth, because the film acts as a barrier to the plasma flux. This effect manifests because of the charging of the surface of the growing film/substrate (as it is bombarded) and thus it is beneficial to use a pulsed substrate bias [147]. Another reason for decreased adhesion properties with increasing thickness is the increase in internal stress, as seen by *Detor et al.* who showed an increase in average stress of beryllium films (sputter deposited at 10 mTorr Ar) from *ca.* 0.2 to 0.48 GPa with a thickness increase from 0.5 to 2.0 μm. A specific mechanism was difficult to assign in this case and the increase was ascribed to a thickness dependence on properties such as grain size, surface roughness, substrate heating, in-plane crystallographic texture and impurities. The negative impact of increasing film thickness is one reason why a high dielectric strength is important for an electrically insulating thin film.

Sputtering allows tailored deposition which can mitigate cracking and delamination upon flexural testing, namely by mediating thickness and mitigating thermal expansion variation and high internal stress, which is beneficial for flexural properties [148,149]. As seen in ALD deposited Al_2O_3 onto polymer the critical bending radius increases from 2.59 to 12.02 mm with a coating thickness from 5 to 80 nm [150]. Increasing the thickness has the effect of increasing the residual stress, meaning that the mechanical properties decrease and cracking upon bending will occur more easily. The application of an elastic top layer has also been shown to help reduce cracking in brittle films. Work by *Musil et al.* showed that by using materials with a high elastic recovery and a hardness: Young’s modulus ratio ≥ 0.1 as a top layer cracking could be prevented in Zr-Si-O sputtered films [151]. This last advantage is particularly important for maintaining mechanical properties when coating flexible substrates such as that required for copper wires and tapes.

Multilayer systems also require attention when considering their mechanical properties, the adhesion between the layers and any extra intrinsic and extrinsic stress introduced by mismatches in thermal expansion or material matching. For example the mismatch in silicon and insulator materials results in generation of residual stress as the system cools from the deposition temperature to room temperature [152]. Multilayers have been explored extensively as wear resistant coatings such as those discussed by *Holleck and Schier*, who explored the use of PVD TiC/TiN based multilayers, showing that additions of intermediate layers could improve hardness by (*ca.* 2810 to 3140 HV0.005 for TiC and 100 layers of TiN-TiC respectively) [153]. The improvements seen were the result of a number of effects including crack deflection, reduced stress and nanoplasticity. Other multilayer systems have also been used to improve hardness and wear resistance in Ag/Cu composite films (when compared to Ag or Cu alone) [154].

3.4.1 Determination of critical loads in thin film coatings

The use of **scratch testing** for the determination of adhesion has developed from work performed by *Heavens and Benjamin* and *Weaver*, [155,156]. *Bull et al.* have comprehensively analysed the effect of scratch testing on many materials and have explored the failure mechanisms which are associated with reaching critical load points [144,157]. Scratch testing is also commonly coupled with acoustic emission in order to determine the load required to initiate critical loads. Scratch testing on thin films can give an indication of the adhesion strength as well as the failure modes which can give a better understanding of the interfacial and bonding properties. For example, poorly adhered Al_2O_3 films have critical adhesive failure loads as low as 5 N (with sever spallation seen) [143]. The failure mechanism is typically a result of compressive (in front of the indenter) or tensile (behind the indenter) deformation of the films. In the case that adhesion is poor - for example thin films on a ductile substrates - both tensile and compressive failures can occur, contrasting to failure occurring within the coating for well adhered films [144]. For instance, low resistivity (12-14 μΩcm) Mo films deposited by *Scofield et al.* showed poor adhesion due to compressive stress, but noted an improvement resulting from an increase in Ar pressure (whereby films passed a qualitative tape pull test above 2 mTorr Ar) [158]. The critical load of a coating system is also impacted by the coating thickness, this is because a lower load is required to deform the substrate when a thinner coating is used. For example, a three times increase in the thickness of a CVD Al_2O_3 coating resulted in a two fold increase in the critical scratch failure load to *ca.* 120 mN [159].

Direct pull off testing is a technique where a stub is adhered (this can be done by using epoxy or solder) to a coating system and then pulled off perpendicular to the sample surface, the force required to remove the stub can be converted to a pressure using the stub size. The pull off sites can be analysed further for information on the failure site, for example failure at substrate, at an interface within the film system, cohesive failure within the coating or failure within the epoxy. This technique is limited by the strength of the adhesive and by alignment issues [160,161]. For example, pull off testing was carried out by *Suzuki et al.* who argued that in the case of metal oxides and nitrides deposited onto glass the bond strength was dependant on the chemical bonding in the metal oxide interlayer [162]. This was a result of a mixed layer which led to greater improvement in adhesion with increasing thickness.

Tensile and flexural properties of thin films are also dependant on the deposition method and preparation of the sample as well as the thickness and morphology of the deposited film. For instance tensile testing can be carried out on free standing films, as evidenced by *Huang and Spaepen* who tested a range of electron beam evaporated materials (*ca.* 3 μm thickness), measuring strain using an optical diffraction method, giving reliable Young's modulus and strain behaviour data [163]. Micro tensile testing work on free standing films by *Cheng et al.* showed that a decrease in the failure strains and Young's moduli in micro Al and Cu compared to larger specimens [164]. However, when depositing onto a substrate, the properties of the substrate will dominate and other methods are required for assessment of the failure mechanisms and failure stress/strain. When a ceramic film is deposited onto a ductile metal substrate transverse cracking perpendicular to the direction of travel will form, followed by longitudinal cracking/ buckling during tensile testing, similar cracking patterns are observed when brittle metallic films are deposited onto flexible substrates, as displayed in ***Figure 3.11*** [165]. For instance, anodic alumina films were deposited onto ductile Al-5%Mg by *Xie and Tong* who discussed the forces acting at the interface and film during tensile testing [166]. They reasoned that during application of tensile stress the coating must undergo elastic deformation as the substrate deforms to maintain continuity which gives rise to interfacial shear stress. This shear stress allows transfer of the tensile force into the film until the coating fracture strength is reached.

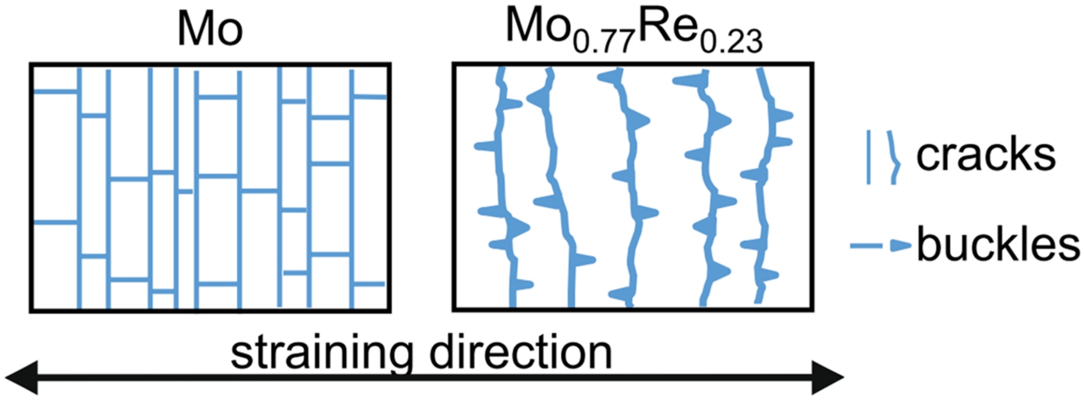

Figure 3.11: *Cracking and buckling in Mo and MoRe sputtered thin films, cracking and buckling have been shown. As shown by Jörg et al.* [167].

It has been shown in work by *Jen et al.* utilising work by *Suo et al.* on coated foils that the critical strain can be used to calculate the bending radius of the coating. Showing that 5 nm Al_2O_3 films deposited using atomic layer deposition onto polymeric substrates (Polytetrafluoroethylene) can achieve bending radii as low as 2.59 mm (before de-adhesion) [150,168].

The mechanical properties of the films also rely heavily on the surface preparation prior to film deposition. This includes the cleanliness of the samples (free from contaminants especially grease), surface roughness and surface composition. It has been shown that contaminants and loose surface oxides can lead to a decrease in adhesive strength. For example Cu films deposited onto Al_2O_3 by *Lim et al.* showed improved adhesive strength with solvent cleaning (5.4 to 6.1 MPa) and was further improved with heating and bias etching stages (up to a maximum of 16.9 MPa) . Degreasing and sample biasing have both discussed with respect to their improvement of adhesive properties, because of the removal of surface contaminants [143,169–171].

As well as effecting adhesion surface roughness can affect the structure and density of a growing film [170].

3.5 Sputtering of ceramic thin film candidates

The control which can be exercised over film properties by varying the sputtering parameters (as highlighted in the previous section), makes it an ideal technique for depositing flexible insulating coatings capable of achieving high breakdown strength. For that to be achieved, the coatings require low defects and good adhesive properties to prevent premature and uneven breakdown.

This section of the review will focus on specific cases of materials which are strong candidates for use as isolative thin films.

3.6 Alumina

3.6.1 Bulk material

Bulk alumina is a very well-studied material which comes in a number of allotropes depending on the material formation. Alumina is often produced from raw materials such as Bauxite which contains high amounts of aluminium hydroxide (using the Bayer process) [172]. Once obtained alumina can be formed into components, such as the herringbone insulation discussed earlier, through processes including sintering. Bulk alumina is commonly used for high temperature crucibles and also in the production of aluminium [173].

The mechanism of breakdown in crystalline alumina is described by the electromechanical model. This is because of the brittle nature of the ceramic the propagation of defects caused by electrical stresses can act as initiators to breakdown. Breakdown likely starts at surface pits formed by grain pull-out [174]. The breakdown strength of polycrystalline alumina is proportional to the purity and inversely proportional to the film thickness and electrode radius. Breakdown in poly crystalline alumina results in a crater, which is formed at the site of breakdown, it is suggested by *Tabli et al.* that the crater is formed prior to breakdown, as seen in ***Figure 3.12*** [175].

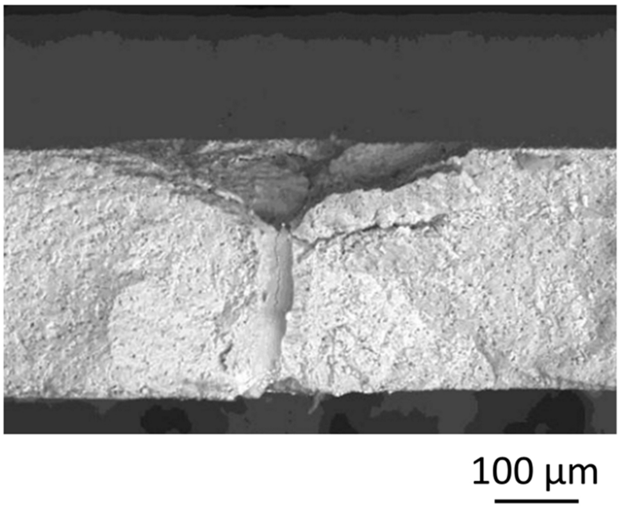

Figure 3.12: *A breakdown crater in polycrystalline alumina* [175].

Thin films of alumina have been sputtered as early as the 1960's through means such as the reactive sputtering route carried out by *Frieser* [176]. Since then alumina has been sputtered using a number of methods, as illustrated in the following sections.

3.6.2 RF sputtered films

Generally alumina thin films deposited using RF techniques are amorphous in nature, however, after vacuum annealing at 500 °C certain crystalline phases (theta θ, delta δ and chi χ) become apparent in XRD analysis, as shown by *Reddy et al.* [177]. However, no crystalline peaks have been observed in samples annealed at 300 °C. RF sputtered alumina films can suffer irreversible expansion caused by heating and contraction during argon evolution at temperatures above 850 °C [178]. Irradiation can be used to alter surface properties such as micro surface roughness whereby treatment with energetic He^+ modifies the electrical and optical properties (where bombardment increased the refractive index by a maximum of 1.15 times) [179]. Deposition rates for RF alumina have been reported for fixed substrates at 40 nm min^{-1} with a target power of 800 W and a substrate target separation of 25 mm [95].

Mechanical properties of RF sputtered alumina films have been studied variously with respect to their mechanical strength and wear resistance [143,180]. Al_2O_3 has been shown to have poor adhesion to copper without the use of an interlayer, this results from mismatching thermal expansion coefficients of 5.4×10^{-6} and 1.7×10^{-5} for Al_2O_3 and Cu respectively, this mismatch causes residual stress evolution upon cooling from the processing temperature, thus work has been done to improve this situation. Critical scratch adhesion failure of RF sputtered Al_2O_3 films onto steel were shown to improve from 10 to 30 N when a Ti/TiN interlayer was implemented [143]. An improvement in the adhesion of Al_2O_3 Cu systems was also found when using Ni/Ti interlayers in tensile testing by *Järvinen et al.* [181]. The interfacial layers in these studies work because they utilise materials with thermal expansion coefficients between that of the substrate and the coating which reduces the residual stress in the films following coating.

The dielectric strength of RF alumina has been explored by *Vuoristo et al.* showing breakdown strengths of up to 50 $V\mu m^{-1}$ could be produced [182]. The use of oxygen within the sputtering gas mixture has been shown to improve the dielectric strength by decreasing the Al:O ratio, because even in RF sputtered films randomly distributed aluminium rich weak spots can exist. The addition of extra oxygen helps to passivate such weak spots, increasing the breakdown strength. Films sputtered at 500 W Ar+5 % O_2 at 0.5 Pa gave films with a breakdown strength of close to 300 $V\mu m^{-1}$, it is also noted, however, that the addition of O_2 leads to a decrease in sputtering rate due to poisoning effects [96,182,183].

3.6.3 Reactive DC sputtering

Reactive DC deposition of Al_2O_3 is carried out by sputtering Al in an Ar-O_2 atmosphere facilitating high deposition rates of up to 23 nm min^{-1} with a target sample separation of 130 mm [184]. OEM control is an effective way to ensure the desired stoichiometry is achieved through the thickness of a coatings. For stoichiometric Al_2O_3 the plasma intensity needs to be tuned to at least 25 % of the initial intensity of the 396 nm emission line at 100 % Ar as shown by *Kelly et al.* [76]. As with RF Al_2O_3 coatings the adhesive properties of DC deposited alumina films have been shown to improve with the inclusion of a metal interlayer Ti or Ni [181].

DC sputtered Al_2O_3 films have been shown to have dielectric strength in the range of up to 120 $V\mu m^{-1}$ when measured at 200 °C [182]. This work suggests that DC films are generally inferior to RF films with respect to dielectric strength, but the potential for a much increased deposition rate, and therefore a higher throughput process, means that the technique still has value. It was shown these poorer electrical properties were a result of structural defects.

3.6.4 Reactive Pulsed DC sputtering

The implementation of OEM control combined with pulsed DC power has been shown to produce good quality Al_2O_3 films. The pulsing of the power supply during film deposition is used as a means to stop the build-up of Al_2O_3 on the target surface, which leads to arcing, and causes defects in the form of crystallites within in the deposited film. This method has successfully been used to form alumina films in many cases with tuning of the pulse parameters used to generate the fewest arc events [185]. Dielectric strengths as high as $620\ V\mu m^{-1}$ were produced for films produced by *Bartzsch et al.* using pulsed DC sputtering from a double ring magnetron [121].

Pulsed power deposition has been applied to produce dense defect free alumina thin films. *Carreri et.al* have produced highly insulating alumina films (breakdown strengths of up to $1500\ V\mu m^{-1}$) through the use of the power supply controls which minimised the expulsion of macro particulate from the target during arcing events (a result of the equipment’s ability to switch off power extremely quickly within 1 µs in the event of an arc, combined with the equipment’s ability to limit current spikes during arcing limiting the energy to the arc spot. The control imparted through the mid frequency cycling which resulted in low arc counts and arc control resulted in materials with very low levels of defects and high breakdown strengths [186].

As discussed in section (3.3) the dielectric strength depends heavily on the number of defects in the material structure [187]. Conduction in amorphous alumina thin films has been attributed to multiple mechanisms including Shottkey and Poole-Frenkel conduction as determined by *Zhu et al.* and *Kolodzey et al.* , see section (3.3) for an explanation of the conduction mechanisms [131,188]. See ***Table 3.4*** for a summary of the electrical properties of Al_2O_3 films sputtered using different methodologies.

Table 3.4*: Assorted electrical data for selected alumina thin films deposited through various sputtering routes*

	Carreri et al.	***Bartzch et al.***	***Vuoristo et al.***	***Voigt et al.***
Sputtering method	*Reactive MF +arc handling*	*Reactive PDC*	*RF*	*RF/ Reactive RF*
DC resistivity (Ωcm)	*/*	$2x10^{16}$	*/*	$2.5x10^{11}$
Dielectric strength ($V\mu m^{-1}$)	*1500*	*510*	*50-150*	*<100*
Dep. Rate ($nmmin^{-1}$)	*<67*	*65*	*27-77*	*/*
Ref.	[186]	[121]	[182]	[189]

3.7 Silica

Bulk silica is a very diverse material and exists naturally in a number of forms produced geologically most commonly as quartz, however silica can also be formed by bio-mineralisation, in organisms such as diatoms. Bulk silica is often used for the production of silicon, for making glass and ceramics and as fillers in some polymers [190].

3.7.1 Sputtered Thin films

Sputtered silica films have excellent dielectric properties, including high resistivity (up to 10^{17} Ωm) and a large bandgap *ca.* 9eV [121]. Silica films can be grown through oxidation of silicon wafers/substrates as well as through other physical and chemical methods [191]. Insulating silica films play a number of roles in the electronics industry [192]:

- Surface passivation by providing environmental protection or electrical/compositional stabilisation.
- Isolation layers, diffusion masking films [191].
- Gate layers in field effect transistors.
- Packaging to prevent the loss of dopant from doped oxide layers and protection from moisture or chemical attack.

As with alumina, amorphous silica films have been deposited using a variety of different sputtering techniques which will be discussed next.

3.7.1.1 RF deposition

As alluded to silica films can be deposited using RF (from a silica target or with silicon and oxygen to make reactive RF) or reactive DC or PDC (from a silicon target with oxygen reactive gas) sputtering methods. RF reactive sputtering has the potential to improve the surface morphology and stoichiometry of silica films, producing smoother surfaces which are less likely to absorb water [193]. *He and Xu* showed that reactive RF sputtering (from a pure Si target) had the potential to produce films with a stoichiometric composition when the ratio of $[O_2]/[Ar]$ was above 0.075, and also noted that the resistivity and breakdown strength of the films increased with an increase in oxygen pressure (a maximum breakdown strength of 330 Vμm^{-1} was achieved) [194]. Deposition of silica materials using reactive magnetron sputtering has also been realised by *Jun et al.* who showed films could achieve breakdown strength of up to 561 Vμm^{-1}, making it an attractive insulating film material. This maximum breakdown voltage was achieved for films produced at a temperature of 300 °C with an oxygen fraction of 0.15 and a sample bias of 150 V. The Si target was sputtered at 200 W RF, 3 mTorr pressure, 300 °C, 25.0/4.4 sccm Ar/O_2 [195].

RF sputtering of SiO_2 targets has also been shown to produce stoichiometric films, without the addition of oxygen [193]. Reactive sputtering can also be realised with silica targets, as the addition of oxygen can improve wear resistance whilst not affecting film stoichiometry [191]. The improved mechanical properties can be explained because of the reduced defect count in the films, which also explains the improvements in the breakdown strength from 161 to 561 Vμm^{-1} when a substrate bias of 150 V and heating at 300 °C were used. The introduction of oxygen reduces the number of dangling bonds, pores (through the coating thickness), vacancies and non-stoichiometric sites in the films. Further to this it was found that the resultant breakdown strength was not affected by substrate biasing [195].

3.7.1.2 DC/PDC sputtering

DC sputtering of SiO_2 thin films has been achieved in transition mode (sputtering between a fully metallic or fully oxidised target, by voltage monitoring) by *Ohsaki et al.* who sputtered from a Si target in an Ar/O_2 gas mixture, showing that SiO_2 could be deposited at relatively high rates such as 900 nm min^{-1} at a power of 1170 W [196]. However, careful control of the voltage is needed to achieve stable arc free deposition, making the method difficult to achieve. However, surprisingly OEM controlled deposition of SiO_2 has not been reported widely. Reactive PDC sputtering has been carried out by *Bartzch et al.* who achieved high breakdown strengths for bipolar pulsed DC sputtered Al_2O_3 films (510 Vμm^{-1}). They also found that substrate bombardment improved the dielectric strength of the SiO_2 films (430-620 Vμm^{-1}) when an RF substrate bias was applied to the growing films [121].

3.7.2 Summary of SiO_2

Alternatives methods exist for depositing silica thin films such as vacuum evaporation, CVD and sol-gel transitions to name a few methods. Silicon oxynitrides (such as $SiO_{0.60}N_{0.93}$) have been produced for their increased dielectric constant (with respect to SiO_2 alone) [197]. Silicon oxynitride has also presented itself as a candidate with films prepared by low pressure CVD, as they had breakdown strengths in the region of 1000 Vμm^{-1}, which is markedly improved on values for silica alone [198].

Table 3.5: *Selected electrical properties of silica thin films as deposited by various sputtering methods.*

	Deposition technique		
Property	*RF*	*Reactive RF*	*Reactive PDC*
DC Resistivity (Ωm^{-1})	*9.6x10^{13}*	*/*	*6.3x10^{16}*
Dielectric strength (Vμm^{-1})	*330*	*570*	*560*
Ref	[194]	[195]	[121]

An improvement in the mechanical properties of thin film SiO_2 was shown when an increase in substrate temperature during sputtering was used, increasing the critical tensile strain by up to 75%. This improvement was attributed to removal of thermal compressive residual stress, which could be a route to improving film properties in post treatment, if films suffer from poor adhesion [199].

Conduction mechanisms in thin film silica have also been explored by a number of groups and has been attributed to Fowler-Nordheim tunnelling in variously produced film conductor configurations such as metal-insulator-metal and metal-oxide-semiconductor systems [134,200,201]. The breakdown mechanism in silica films has been attributed to impact ionization/recombination models, whereby charge carriers gain sufficient energy to remove electrons from the lattice and initiate an avalanche breakdown [134].

Sputtered composite materials have been produced by *Martinez-Perdiguero et al.* by PDC sputtering from Al and Si targets. They showed that 8 layers of stacked alumina and silica were able to significantly reduce the leakage current from a maximum of ca. 2 to <0.5 mAcm^{-2} (for SiO_2 and a 4 layer SiO_2-Al_2O_3 structure respectively) as discussed further in section (*3.13*) [116].

3.8 Tantalum Pentoxide

Bulk tantalum pentoxide is a ceramic material with high chemical inertness which also boasts exceptional dielectric constants (such as 23 and up to 27.6 for anodic films) and high band gaps and dielectric strength (up to 4.36 eV and up to 600 $V\mu m^{-1}$ for anodic and RF films respectively) [135,202,203]. As a result Ta_2O_5 is used in the electronics industry for capacitors and dynamic random access memory (DRM) [133]. Besides its high desirability in optic and electric devices Ta_2O_5 offers biocompatibility which means it also has potential application in medical devices. Ta_2O_5 thin films heated above 600 °C results in the formation of βTa_2O_5 [204].

3.8.1 Thin Films

Tantalum pentoxide thin films are of great interest mainly because of their high dielectric constant (23 compared to 6 of Al_2O_3), which makes them suitable for thin film capacitors and other applications. As well as this high dielectric constant Ta_2O_5 has high dielectric strength of up to 600 $V\mu m^{-1}$, and band gap of up to 4.36 eV for pulsed DC films, also making it suitable as an insulator [203]. Ta_2O_5 thin film capacitors are of interest in computing, finding use in resistive random access memory, because of the resistive switching properties of the films which would allow the material to act as “atomic switches” [205].

Formation methods for Ta_2O_5 thin films were explored thoroughly in a review by *Chaneliere et al.* showing that films can be formed through a large range of methods including oxidative, CVD, PVD, atomic layer deposition and sol-gel methodology. The electrical properties of the thin films have a dielectric constant above 20 with dielectric strengths estimated to be between 1 and 600 $V\mu m^{-1}$ [133].

3.8.1.1 RF deposition

RF deposition of tantalum from a tantalum pentoxide target was carried out in 1983 by *Oehrlein et al.* achieving a breakdown strength between 300 and 400 $V\mu m^{-1}$ [204]. Higher breakdown voltages for RF deposition of films between 56 and 60 nm thick have been produced yielding a breakdown strength of 600 $V\mu m^{-1}$ as shown by *Seki et al.* [206]. RF produced films also show extremely low leakage current when annealed in oxygen. Post treatment of crystalline Ta_2O_5 films has also been used to improve the leakage current with annealing in gas such as O_2 and N_2O [135]. Reactive RF deposition using a TaO target has been accomplished by *Corbella et al.* who used an oxygen ratio up to 16%, the resulting deposition rate was linked strongly to the O_2 flow rate and the films exhibited a dielectric strength of up to 110 $V\mu m^{-1}$ [207].

3.8.1.2 DC/PDC sputtering

DC sputtering of Ta_2O_5 is typically carried out by controlling the reactive gas flow directly [208]. No OEM tuning or set points were found in the literature which could be used for OEM control of reactive DC sputtering of Ta_2O_5. Despite this, amorphous tantalum pentoxide films have been produced by *Sethi et al.* in 2007 and achieved a breakdown strength of 400 $V\mu m^{-1}$, using pulsed DC sputtering in combination with 16 % O_2 to generate the oxide films [209].

3.8.2 Summary of Ta_2O_5 films

Studies show that conduction in thin film amorphous Ta_2O_5 is potentially a result of Schottky or Poole-Frenkel mechanisms, the latter described as a mechanism by *Corbella et al* in reactive RF deposited films [136,207]. Breakdown strengths have been shown to have quite a range with results being as high as 600$V\mu m^{-1}$ for RF sputtered samples, see ***Table 3.6***. The adhesive properties of Ta_2O_5 thin films to other ceramics however are not well studied.

Table 3.6: *Dielectric strength of Ta_2O_5 sputtered films deposited using various techniques.*

	Deposition technique		
	RF	***Reactive RF***	***PDC***
Dielectric strength ($V\mu m^{-1}$)	*600*	*100*	*400*
Ref.	[206]	[207]	[209]

3.8.2.1 Composites

Multilayer tantalum alumina composites have been formed by a number of groups in order to achieve materials with high dielectric constant (above 8.9 seen for pure Al_2O_3 and up to 16 for 42% Ta_2O_5 inclusion in layers) and leakage current as low as 10^{-10} and $<10^{-7}$ Acm^{-2} for Ta_2O_5 and layered composites respectively [210]. Chemically produced Ta_2O_5/Al_2O_3 composites have been studied by *Ezhovskii and Klusevixh*, who showed the electrical properties to be linked to the relative amounts of each oxide and the thickness of the layers with tantalum increase directly linked to increase in permittivity (films composed of *ca.* 80 and 50% Ta_2O_5 had dielectric constants of 18.1

and 13.7 respectively) [211]. RF Sputtered composites have been produced for a number of materials including TiO_2 specifically with a view to improving the mechanical properties of optoelectronic thin film devices [212]. The use of these Ta_2O_5 composites shows the promise of the material as a component in high dielectric breakdown films.

3.9 Diamond like carbon

Diamond like carbon (DLC) is a term which refers to films of carbon based material which resemble diamond in chemical structure and composition. Early DLC coatings were deposited by PVD methods (glow discharges) by *Schmellenmeier* in 1953 [213]. Since the discovery of DLC major strides have been made and DLC coatings are now utilized as hard, anti-corrosion and low friction coatings in a wide variety of industries including: aerospace, electronics, machining industries [214,215].

Further to this DLC films have been produced through other CVD and PVD techniques which allowed further development of material properties. Reactive sputtering has mainly been utilized to form DLC films because of the high level of control over system parameters which can be achieved. The main production route for these materials is to sputter from a graphite target, with the inclusion of a hydrocarbon reactive species such as methane or acetylene as a reactive gas [216,217]. The selected gas and flow can affect the eventual material properties. The versatility of the sputtering technique means that DLC can be sputtered with varying amounts of sp^3 and sp^2 hybridization, for insulating films high levels of sp^3 are critical, whereas higher films with a high sp^2 content can offer useful wear resistant properties [215].

3.9.1 RF sputtering

As well as producing DLC films through the use of hydrocarbons RF sputtering has been used to deposit from graphite targets, producing hydrogen free DLC films [218]. However, these films typically suffer from a lack of sp^3 hybridized carbon and would still require a hydrocarbon feedstock to increase the amount of sp^3 carbon. Generally RF deposited films have good electrical properties with high dielectric strength above 700 $V\mu m^{-1}$ which was found to decrease with increasing gas content [219].

3.9.2 Summary of DLC films

The adhesion characteristics of DLC are often such that a complex bonding motif is required, as evidenced by *Jones et al.* who used the Ti-TiN-TiC-DLC motif to promote adhesion of DLC films to Ti [220]. Given that the current work will focus on a copper substrate development of a new set of interlayers to promote adhesion could also be required. This means that implementation of the material for an insulator could be hampered by the requirement for a thick interlayer which is not necessarily insulating. Additionally the potential for poor mechanical properties, caused by the very low thermal expansion coefficient $1.0\text{x}10^{-6}$ °C^{-1}, is seen as an obstacle to keeping coating thickness low, because grading between the many layers would be required to keep intrinsic stress low. Prevention of sharp boarders was shown by *Pei et al.* to improve elastic modulus, tensile yield and tensile elongation (by a minimum of 1.3 times) in ZrCu/Cu multi-layered films because of the reduced stress and mismatches at the interfaces [221].

The need for a highly specialised adhesion layer, the hydrocarbon feedstock required to produce materials with a high level of sp^3 hybridisation and the potential for inclusion of sp^2 centres, were seen as detrimental to using DLC as a possible accompaniment (multilayer/ composite) to sputtered Al_2O_3 which requires O_2 feedstock in the same coating rig.

3.10 Boron nitride

Boron nitride (BN) is commonly found in 2 crystalline phases, hexagonal and cubic forms (analogous to graphite and diamond respectively). BN materials have been formed through high temperature processing of suitable reagents such as sodium borates and ammonia, or nitrogen and boron as well as vapour deposition techniques which will be discussed further in this section [222]. BN is typically a white colour caused by defects and impurities (intrinsically BN is transparent) further synthesis methods have been covered in a review by *Paine et al.* [223]

Hexagonal boron nitride (h-BN) has properties that could lend their strength to electrical insulation with a high band gap and large breakdown strength. Using thermal annealing amorphous BN can be converted into h-BN, which has a similar structure to graphite as seen in ***Figure 3.13***. However, the electrical properties of h-BN differ considerably from graphite, with h-BN capable of insulation having a dielectric strength of 1200 Vµm^{-1} [224].

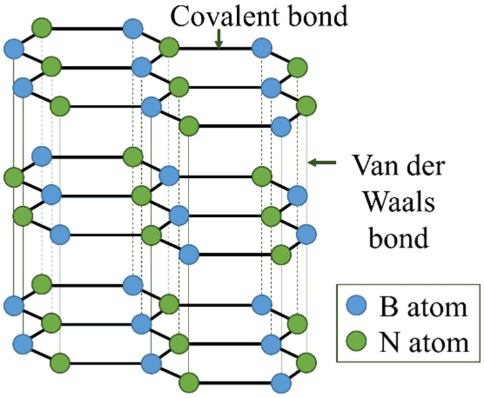

Figure 3.13: *Graphite like structure of hexagonal boron nitride.*

Cubic boron nitride (c-BN) is an extremely hard material (hardness of 50-60 MPa in sputtered films) being only bettered by diamond, thus offering high wear resistance. c-BN also has high thermal stability up to 1100°C and chemical inertness to ferrous metals, hence it is regularly applied to cutting tools [225,226]. However, the high internal stress in deposited films due to high ion bombardment is a cause for concern with regards to film adhesion and cracking.

3.10.1 Thin Films

3.10.1.1 RF deposition

BN thin films have been formed using sputtering methods as far back as the 1970's and 1980's with RF sputtering being commonplace. In 1976 *Puchevrier et al.* formed films using cathodic sputtering in a nitrogen atmosphere [227]. Formation of amorphous BN using RF plasma consisting of Ar and N_2 was carried out by *Wiggins et al.* who found that by increasing the amount of N_2 in the gas mixture the amount of excess boron decreased whilst also increasing the band gap from 3.3 to 5.6 eV; furthermore stoichiometric films with high band gap were grown in 25-100% N_2.[228] Other methods have also been successful in producing mixed films including plasma jet methods with extremely high deposition rates of up to 40 µm min^{-1} [229]. In 2009 h-BN was formed by *Jin-Xiang et al.* using RF sputtering from an h-BN target with a band gap comparable to that of single crystal h-BN (5.86 eV) [230]. RF sputtering was used by *Yu et al.* to form dense films, finding that films produced at an Ar pressure of 2 mTorr were dense, stoichiometric and also exhibited micro hardness comparable to other deposition methods. Films consisting of c-BN were also produced by *Seidel et* *al.* by applying a highly negative substrate bias during reactive cathode sputtering [231]. More recently RF deposition has been performed to generate BN with a higher content of c-BN. *Zhang et al.* used two stage RF deposition with a bias etching stage between RF deposition periods depositing onto Si(100) wafer in order to form films containing more cubic phase fraction whilst also minimising stress, as additional annealing of these films helped to reduce residual stress indicated by shifting towards the bulk value for c-BN in FTIR data [127]. *Ding et al.* deposited films using a pulsed substrate bias and a sample heater. The main findings were that c-BN content increases with substrate bias up to 150V (with sputtering rates adversely effected above this voltage), 75% c-BN content films were sputtered at 800 W target power, 400 ^{o}C substrate temperature, 150 V substrate bias and 20 % N_2 [232]. Despite this work the breakdown properties of RF sputtered BN are scarce. One of the main benefits of cubic boron nitride over the hexagonal allotrope is the larger band gap (6.36 ± 0.03 compared to 5.96 ± 0.04 eV respectively), [233]. The mechanical properties of the cubic phase are also strikingly different with h-BN exhibiting lower hardness (60 MPa, hence it's applicability as a solid lubricant) compared to c-BN (ca. 80 GPa) [234,235].

3.10.1.2 DC/PDC deposition

DC deposited films produced from boron metal targets are not as well reported as RF methods because of difficulties caused by nitride poisoning on the target surface reducing sputtering rate and effecting film quality (surface arcing due to the insulating nature of the BN on the target could cause droplet ejection as for the Al_2O_3 as discussed previously (*3.6.3*)) . *Jensen et al.* formed h-BN in 1995 by using nitrogen as the sputtering and reactive gas during deposition [236]. Reactive DC sputtering was also carried out by *Schzitze et al.* from conducting B_4C targets, however the level of c-BN in these films was relatively low at 14 % [226]. PDC sputtering has been used by *Yang et al.* to produce c-BN films which contained carbon again utilising a conducting B_4C target. This work showed films produced in this manner can reach high c-BN content (95 %) by careful control of substrate bias and heating to increase the number of c-BN nucleation sites [237]. Generally, however, films deposited this way form BCN films which have a lower breakdown strength (340 Vμm^{-1} compared to the possibility of up to 2000 Vμm^{-1} discussed previously) and thus is not so desirable [238].

3.10.1.3 BN composites

BN has been applied in composites with many polymers (such as epoxy, polymethylsiloxane and rubbers), mainly through the introduction of particles into the structure. This is often achieved by exfoliating the BN and then mixing with the polymer but it has also been achieved through polymer filling of a ceramic backbone structure. These composites are favoured for use in electrical insulation with high thermal conductivity (up to 1.34 $Wm^{-1}K^{-1}$) whilst maintaining flexibility, and thus are looked at as a solution for cooling in advanced electronic applications, however there are downsides to BN addition including a reduction in volume resistivity from $> 50x10^{14}$ to $6.3x10^{14}$ Ωcm (caused by the addition of defects following the addition of 50 wt.% h-BN) [239,240]. BN composite materials have also been produced through sputtering, with materials such as WBN and $BNSiO_2$ composites, having been deposited with a view to decrease the wear rate (from ca. $6.0x10^{-8}$ to $2.2x10^{-8}$ $mm^3N^{-1}mm^{-1}$ at 0 and 38 at.% B respectively), whereby the properties were modified through the tweaking of B content [241]. There are no cases of sputtered BN and Al_2O_3 composites in the literature. This could be a result of the anisotropy in the thermal expansion coefficients of BN, in the a and c directions the coefficients of thermal expansion are $-2.7x10^{-6}$ and $3.8x10^{-5}$ °C^{-1} respectively [242–244].

3.10.2 Summary of BN films

RF sputtering would be the most desirable way to sputter BN films from an isolative standpoint because of the better control of stoichiometry granted by the BN target. BN has a number of attractive properties including high thermal conductivity and high hardness, however, challenges in obtaining a single phase material could be a hindrance to using the material for a number of reasons: grain boundaries and defects associated with lattice mismatches (which could potentially be detrimental to dielectric and mechanical properties) and intrinsic stress (introduced by anisotropy in thermal expansion and lattice mismatches) [127]. Difficulties would also arise when combining with Al_2O_3 for the same reasons as discussed for DLC (*3.9.2*), which revolve around the aforementioned increase in intrinsic stress.

3.11 Glasses

Glass materials have been employed as insulation materials as far back as the 1850's primarily for the isolation of overhead electrical and communication lines [245]. Following this glasses have been used as electrical insulation for wires, typically applied in a braided configuration often used for high temperature applications [246].

Because the composition of thin film glasses is so wide, they have been utilised in areas such as biomedical applications and within the electronics and architectural industries (such as in TV screens or in architectural glass) but have not been used extensively for electrical insulation [247]. Sputtered glass (barium alumina silicate, corning 7059) was, however, used by *Probyn* to produce thin film capacitors which were able to achieve a dielectric strength of 200 Vμm^{-1} for very thin films (ca. 20 nm) produced with a sputtering rate of 40 nm min^{-1} on a static sample holder [248].

The low deposition rate associated with the limitations of an RF power supply and the composition determination combined with preferential sputtering effects on the composition (a *ca.* 18% increase in the mol.% of P_2O_5 was seen by *Stuart et al.* with a 6.6 times increase in Ar pressure, which was still *ca.* 10 mol.% lower than the target composition) are seen as prohibitive to the use of glasses as insulators in this work [247].

3.12 Other candidates

The range of insulating ceramics is broad and includes materials such as ZrO, TiO_2, and Y_2O_3 which can all be sputtered using RF, or reactive DC sputtering as discussed previously with dielectric strengths of up to 500 Vμm^{-1} [249]. However, they have downsides, such as crystallisation temperatures as low as 275 °C for ZrO based films and inherent crystallinity in as deposited TiO_2 materials. These properties would lead to problems with electrical insulation at higher temperatures or with thermal cycling due to increased current leakage at grain boundaries and potentially also issues with adhesion as the films crystallise. These properties are seen as barriers to the application of alternatives such as TiO_2 and ZrO in composite ceramic insulation [250–252].

3.13 Composite materials

As touched upon earlier, composite materials are an attractive solution to deficiencies apparent in currently available materials because of the combination of properties which are possible. Composite materials can come in the form of doped materials and multi-layer materials which can be used to combine properties in different ways. Specific examples of alumina, tantalum pentoxide and silica composites will be discussed towards the end of this section.

3.13.1 Multilayer and inclusion materials

Multilayer coatings are used for a number of reasons including the tuning of thermal, electrical, diffusive and mechanical properties and are a common way to combine desirable materials properties. These coatings can also be produced using many deposition techniques such as dip coating, polymer extrusion, CVD, and PVD which will be specifically discussed further in this section.

Advantages of multilayer coatings include the combination of multiple desirable properties in conventional polymer wire coatings. For example as mentioned previously that the combination of polyimide and various silica components or fluoro polymers can be used to completely stop “catastrophic flashover” events [28,31]. Many routes to improve fire resistance have also been shown (mainly focused on surface charring). For instance *Beyer* showed an increase in thermal stability from 452.0 to 493.5 °C, by incorporation of layered 5 wt.% clay structures, into melt blended ethylene-vinyl acetate [253]. Improved corrosion resistance of copper in a neutral medium was imparted by *Balaji and Sethuraman* by combining electroplating and a dense surface protective sol-gel coating [254]. *Ma and Lei* showed that including 15 wt.% layered double hydroxide modified with perfluorooctane sulphonate into polyimide coatings increased the corona resistance time 10 fold to 150 min. The glass transition temperature was also increased by *ca.* 1.5 times by applying with the same addition as above. However, the addition of the modified double hydroxide did decrease the breakdown strength, where a 10 wt.% addition resulted in a decrease from 224 to 168 Vμm^{-1} [255].

Layering in polycarbonate and polyvinylidene fluoride-hexafluoropropylene materials has been shown to improve dielectric strength, a result of the formation of treeing patterns which help prevent breakdown as shown by *Mackey et al.* [256]. In the study the materials were chosen for their high breakdown voltage and high dielectric constant *ca.* 650 Vμm^{-1} and 10 at 1 kHz respectively [257]. Multi layering materials is also interesting from the point of view that conduction can be tailored. For instance conduction in core shell structures can be tailored through the use of conductive particles, showing the potential for polymer composites in energy storage applications [258]. Additions of Al_2O_3 to Ta_2O_5 can also be used to fabricate films with extremely high dielectric constant up to 42.8 for metalorganic solution deposited materials [259].

Multilayer ceramics have been explored as a route to high volumetric efficiency in capacitors. With a view to improving dielectric strength of such materials, layer thickness and the number of layers can be modified in order to tune the properties. Whilst it is clear that increasing the total thickness results in a larger amount of defects (such as the decrease in dielectric strength from 1000 to 488 $V\mu m^{-1}$ seen in 5.0 and 49.4 μm thick films), the effect of changing the thickness of individual layers and the number of layers in a structure is more difficult to determine [260]. The barrier effect plays a large role in any improvements seen in certain multilayer materials (because of the suppression of treeing and charge migration through a material), however, the efficacy of the barrier on preventing breakdown depends on composition, position, thickness and interfaces [256,261].

3.13.2 PVD multilayer coatings

Multilayer PVD films can easily be created by using a multi cathode system or by alternating reactive motifs (modifying the reactive gas concentration or species). The use of equipment which has the capacity to rotate, or a system with multiple sources can also be used to make layered films which can potentially blend into one another. Work by *Knotek et al.* has discussed the benefits of these different multi component deposition techniques for improved wear properties because of the mixed crystals in multicomponent films which permit higher strength and hardness [262]. The benefits of multilayer and multicomponent films include improved dielectric strength, reduced leakage current, increased dielectric constant and increased corona resistance, improvements to other properties such as increased thermal conductivity can also be achieved.

PVD multilayer coatings have been used for a wide range of applications as well as improving wear resistance, of particular interest is the improvement of corrosion properties. This could have much wider implications as “removing” defects can lead to improved leakage current and potentially increase breakdown strength by making a conductive pathway harder to create. Hence the use of multilayer PVD films in electrical applications will be discussed in the following section.

3.13.3 PVD deposited composites for electrical application

Multilayers have been used extensively in electrical applications especially in capacitor technology to combine multiple materials. The use of multilayers/ interfacial layers when using Ta_2O_5 is important in reducing the leakage current through capacitor devices, for example *Hori* showed a maximum of 10^{-4} and a minimum of 10^{-8} Acm^{-2} leakage current density in annealed Ta_2O_5 films with and without an interfacial SiO_2 layer. Leakage in capacitors becomes a problem because of crystallisation following annealing which is often used to increase the dielectric constant above 20. Such current limiting multi/interfacial layers discussed by *Hori* can be created through annealing in O_2 on a silicon suitable substrate or by using modified deposition techniques [263]. Reducing grain boundaries, in the case of crystalline materials, or structural/ stoichiometric defects is key to improving leakage current and breakdown strength. Work based on HfO_2-SiO_2 sputtered thin film transistors showed improvements in leakage current, which decreased by more than one order of magnitude to a minimum of 10^{-10} Acm^{-2} with the application of a moderate substrate bias (10 W RF) [264].

Al_2O_3 and SiO_2 multilayers were deposited using pulsed magnetron sputtering by *Martínez-Perdiguero et al.* to a thickness of 2 μm. The multilayer films showed improved leakage current reaching a minimum of 10^{-8} A and the breakdown voltage improved from 40 to >140 $V\mu m^{-1}$ with respect to Al_2O_3 alone. Further improvements to the electrical properties were also made following annealing the multilayer structure at 500 °C, which could be a result of a reduction in the amount of defects as seen in other studies [116,265,266].

The addition of Al_2O_3 layers to Ta_2O_5 in atomic layer epitaxy deposited films as explored by *Kattelus et al.* showed a decrease in leakage current by several orders of magnitude (from greater than $1x10^{-2}$ to less than $1x10^{-8}$ Acm^{-2}), suitable for memory applications [267]. Multi component systems produced by sputtering have also shown benefits to the leakage current in Ta_2O_5 and HfO_2 systems whilst still maintaining a relatively high dielectric strength, whereby additions of Al_2O_3 and SiO_2 and modification of deposition parameters can offer improved leakage current.

The improvements in leakage current for multilayer materials could also potentially result in improved breakdown strength. Thus making multi-layering an attractive technique for improving electrical properties in thin films, by combining high breakdown strength RF films with high breakdown strength pulsed sputtered films with a higher deposition rate. Blending and heat treatments can also be employed to maintain mechanical properties.

3.13.4 Doping materials

Another route to modifying film properties is to use doping, which is often seen in sol-gel film production, whereby additional material is incorporated into a coating [268]. Doping is used extensively in the semiconductor industry for instance in transistors and can be used to tune the band gap or add discrete energy levels.

Doping in sol-gel technology has been used to improve electrical properties of ceramics. Doping of sol-gel produced alumina films with lanthanum metal has been carried out by *Zou et al.* finding that the introduction of 10% La decreased leakage current three fold as well as increasing the breakdown strength (from ca. 310 to 393 $V\mu m^{-1}$) [269]. The breakdown strength increase resulted from La trapping and scattering charge. The La also causes a more compact structure because of its larger radius resulting in decreased ion mobility.

3.13.5 Doping during PVD deposition

Doping can be achieved using PVD, by reactive sputtering or through the use of composite targets or co sputtering with suitably fast rotation. For instance, reactive and co-sputtering techniques were combined by *Ortega et al.* to produce AgN ZnO composites with improved semiconductor properties compared to ZnO alone (the best electrical properties being a low resistivity of 8.56×10^{-3} Ωcm and a high hole concentration of 3.17×10^{19} cm^{-3}) [270]. Dopants are often used to produce films which are highly conductive because the additional species have the potential to create electron carriers through p, n and dual doping. For instance doping of RF sputtered ZnO films with up to 10 at.% Al produced films with a resistivity as low as 3.84×10^{-4} Ωcm [271]. Sputtered films have also benefited from improved corrosion resistance, improved thermal stability and conductive properties through doping [241,272,273]. Whilst doping in sputtered films has been used for many applications as mentioned above, no reports of doping for improved isolative properties (breakdown strength/ resistivity) have been found.

3.13.6 Nano composites

As discussed previously (*1.4.2*), nanocomposites can be utilised in order to improve the thermal conductive properties of polymer coatings. However, the use of nanocomposites can also be used to aid in decreasing current leakage. Boron nitride nano sheets were utilised by *Xie et al.* in order to decrease the leakage current in polyvinylidene fluoride materials. For example when up to 6-8 wt.% was dispersed within the matrix the breakdown strength was 400 $V\mu m^{-1}$ [36].

3.13.7 Conclusion on the potential for composites

The use of multilayer sputtered materials, consisting of the ceramics as discussed above, has the potential to improve film properties with regards to the potential to passivate structural defects. The use of other materials with high breakdown strength such as SiO_2 or Ta_2O_5 could offer a multilayer composite with improved leakage current and potentially improved corrosion resistance. Composites of this nature could also be annealed in order to improve mechanical properties as shown with SiO_2-Al_2O_3 films. The use of tantalum pentoxide could offer the benefits seen using doping of sol-gel produced films and of multilayer constructs if a blending stage is incorporated. This would create a graded structure where the Ta_2O_5 initially dopes the Al_2O_3. Silica multilayer films would combine the properties of the two materials which can be sputtered to achieve a high breakdown strength, similarly to Al_2O_3. The use of multilayers would also be a route to utilising relatively cheap Al_2O_3 layers with more expensive materials which could potentially see improved electrical properties. Whilst doping is a route to improving breakdown strength as evidenced with the use of the La + Al_2O_3 sol-gel preparation, difficulties in obtaining consistent composition and structure using this method were seen as barriers to application [269]. A summary of the key attributes which were considered when designing an insulating system for copper for the discussed materials is included in ***Table 3.7***. The decision to choose Al2O3, SiO2 and Ta2O5 reflects the assignments in this table.

Table 3.7: *Summary table indicating the suitability of the explored materials for thin film electrical applications considering a number of different properties. +++ represents the most promising attributes and – represents a negative property with respect to the material acting as an insulator as deposited onto copper.*

Material	*Band Gap*	*Dielectric strength*	*Mechanical properties*	*Thermal conductivity*	*Ease of deposition*
Al_2O_3	+++	+++	++	+	++
SiO_2	+++	+++	+	+	++
Ta_2O_5	++	++	++	+	++
DLC	+++	+++	-	-	-
BN	++	++	-	+++	-

3.14 Reel to reel coatings

Roll to roll coatings utilising sputtering as the coating source have been explored by a number of groups but generally focuses on coating a single side. Currently reel to reel coating is of much interest in the production of flexible electronics and groups have deposited sputtered coatings onto flexible glass, while flexible polymer structures have been coated using sputtering or electroplating [274,275]. See ***Figure 3.14*** for a reel to reel coating system schematic.

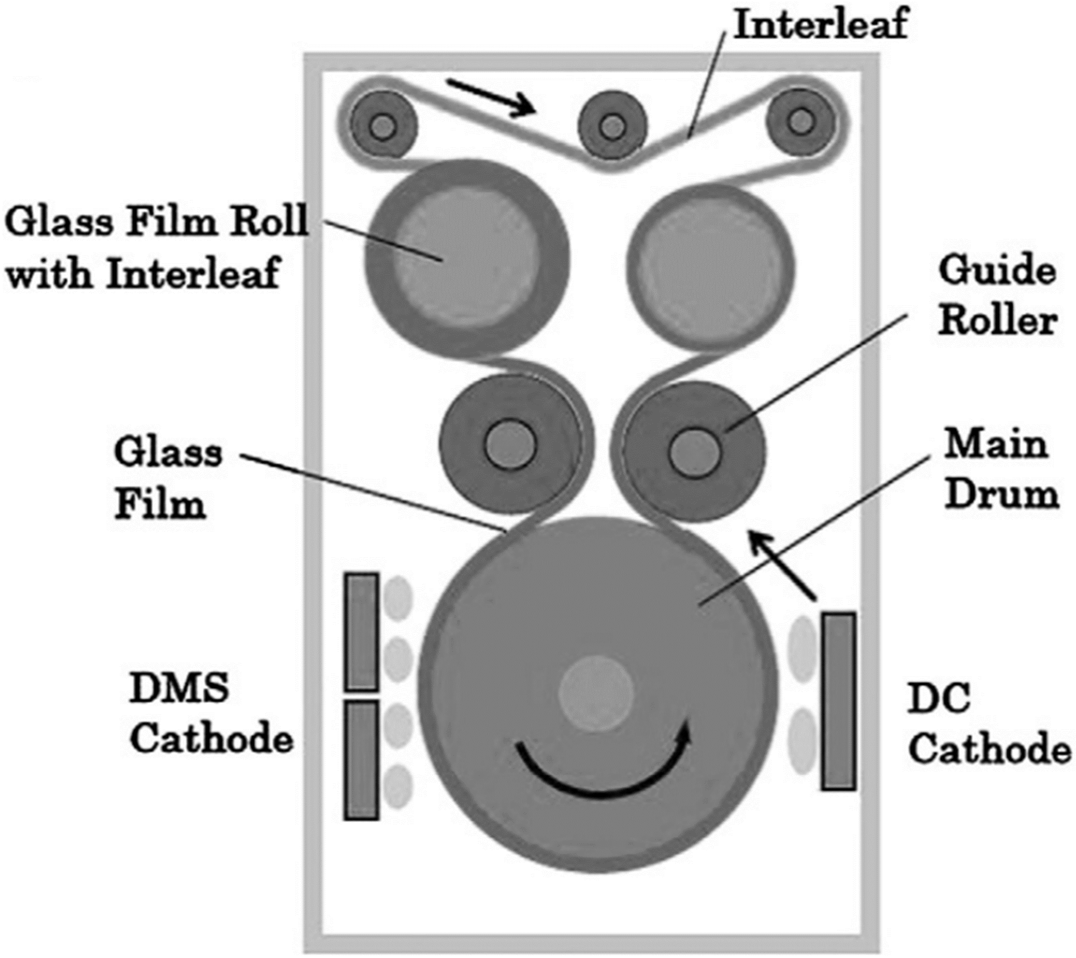

Figure 3.14: *Modified roll to roll deposition system as used by Tamagaki et al. to coat flexible glass substrates* [274].

The use of multiple or hollow cathode magnetrons could be used to facilitate the coating of wire, and are often used to coat complex 3D objects. Hollow cathode magnetrons are also utilised for their high plasma density and ability to deposit dense films [276]. A multi pass system could also be utilised to fully coat both sides of the substrate, with multiple layers, however, no examples were found concerning the coating of wire using this method in the literature.

3.14.1.1 Coated Wires and tapes

Coating of wires - as discussed previously in (*1.5*) - is often carried out using polymer materials and extrusion. However, other coating processes do exist for instance, electro plating can be used to deposit a metal coating, and sol-gel processing can be utilised for organic and inorganic coatings [47,277]. These methods generally work by passing the wire through a solution depending on the chemistry and the anode cathode configuration in the case of electroplating.

Celik et al. produced a number of coated wires and tapes and showed that upon increasing the number of dips the breakdown voltage decreased through crack covering and a thicker coating [47]. However, the sol-gel materials produced in the study were extremely thick (2 to 5 μm) and offered relatively low crystalline transition temperature (400 to 550 °C) which would be detrimental to the electrical properties at high temperature, resulting in breakdown strengths at a maximum of *ca.* 220 $V\mu m^{-1}$ for ZrO_2 coatings. Similar results have been found in a number of other studies on sol-gel produced coatings and also noted other limitations within the technique; namely mechanical problems, rigidity resulting from coating thickness and thermal treatment causing cracking, resulting from trapped organic species [278].

No reports of wire sputter coated using ceramic were found as cost is often cited as a prohibitive factor in excluding PVD methods for coating wire. However, if a high throughput system can be developed to deposit a coating which is thermally stable enough with a large enough dielectric strength to permit a decrease in wire thickness, the weight and space saved could potentially impact many industries including automotive and aerospace.

3.15 Literature summary

This literature review has identified a number of potential deposition techniques within PVD sputtering (specifically looking at the power supply options) which have the potential to produce thin insulating films; films which could offer higher thermal stability than current commercially available insulation. Ceramics have been sputtered extensively and literature exists with characterisation data on electrical and mechanical properties of such thin films.

Alumina has been shown to be an excellent candidate for electrical isolation with PDC sputtered materials exhibiting a maximum dielectric strength of 620 $V\mu m^{-1}$ [121]. SiO_2 also has a high dielectric strength and can be RF sputtered with a high breakdown strength of up to 570 $V\mu m^{-1}$ as shown by *Jun et al.* and has already shown possibilities for use in a multilayer material with other ceramics including Al_2O_3 [116,195]. Ta_2O_5 is a high band gap material and can be easily deposited in an amorphous form with a high breakdown strength up to 400 $V\mu m^{-1}$ using RF sputtering, as achieved by *Sethi et al.* [209]. Thus SiO_2 and Ta_2O_5 would make ideal partners to Al_2O_3 where the use of a blended interlayer could facilitate good adhesion in multilayer systems.

DLC coatings also show good potential but issues with film adhesion and the reactive gas composition resulting in the materials exclusion from testing at the current time. BN and other ceramics/ glasses as discussed in sections (*0*),(*3.11*) and (*3.12*) could offer properties suitable for thin insulation but issues with sputtering rate, reactive gas composition, target composition, material structure and crystalline transitions meant they were not implemented in this work.

The importance of deposition technique has been shown and that a trade-off between film quality and deposition rate is an important aspect with respect to stoichiometry and structure. The use of OEM control has also been shown to be critical to both film quality and deposition rate and should be used where reactive sputtering is applied. DC, PDC and RF sputtering all have potential to produce isolative coatings and can be combined to produce quality films with sufficient electrical properties whilst also considering deposition rate. These coatings would be particularly useful in aerospace and automotive applications given the drive towards electrification of various systems, especially those connected to motor and cable technology. The use of interlayers such as Ti and Ni have been explored. However, because Al also oxidises rapidly it will be considered as an interlayer in this work.

Multilayer composites offer the potential to improve mechanical and electrical properties, hence combining a number of materials is seen as a route to improving the electrical properties isolative coatings. Doping has also been shown to lead to improved properties, however, insertion of multilayers is seen as a more practical route when depositing using magnetron sputtering as there is less requirement to make precise custom targets. Structural and compositional defects in thin films can potentially be capped, through the use of multilayers and have been shown to improve the dielectric strength of Al_2O_3, SiO_2 through incorporation SiO_2 layers [116,279]

Reel to reel applications already exist within sputtering where one of the main aims is to produce flexible electronics. The review has highlighted a lack of literature detailing the deposition onto wires in a reel to reel process that utilises planar magnetron sputtering as the deposition technique. It has however, provided information about the design of such systems for large rolls of ribbon and design of systems which use other deposition methods such as sol-gel deposition. Whilst the coating of copper with alumina has been explored (*Vuoristo et al.*) reel to reel coating of Cu wires using PVD has not been explored and is thus an area with potential for development [182].

Following this section, details of the experimental procedure have been included, focusing on the deposition of thin film ceramics and the characterisation of such, exploring their structural, electrical and mechanical properties for their suitability as isolative coatings.

4 Materials and Methodology

This section will focus on sample preparation and manufacture of thin film coatings, before expanding upon the methods used to assess coating structure and composition and the electrical and mechanical testing of the coating systems.

4.1 Thin film deposition

Thin films were deposited using a TEER UDP-650 coating rig equipped with OEM, ENI RPG-50 power supply and a custom reel to reel multilayer wire coating system, see ***Figure 4.1***. The wire coater was specifically designed for this project to coat both sides of a wire and provide flexibility with regards to the layer structure and thickness of the deposited films. A central shaft which is used for sample rotation was utilised in order to drive the spool rotation and coat the samples, whilst also supplying a bias to the substrate.

Copper disks (20mm, 10mm and 5 mm diameter, 2mm thick, >99.9%) were punched using a fly press from CW004A-H065 Cu sheet ordered from Smith's metal. Disks were polished using sequentially higher grit silicon carbide paper (P240-P4000) with water as a lubricant, followed by polishing on a MD-Chem polishing pad (Struers®) utilising colloidal silica (particle size 0.06 µm). Disks were then sonicated in acetone and IMS for 10 min each before being dried with pressurised air. Samples were loaded into the rig using double sided Kapton® tape. The rig was pumped down to a vacuum of at least $3x10^{-5}$ Torr. Once vacuum was achieved the substrates were bias etched at -150 V under pulsed conditions (250 kHz with a 500 ns pulse width) for 20 minutes prior to deposition. Bias etching was carried out on the sample holder within the rig with power supplied by an Advanced Energy Pinnacle Plus power supply.

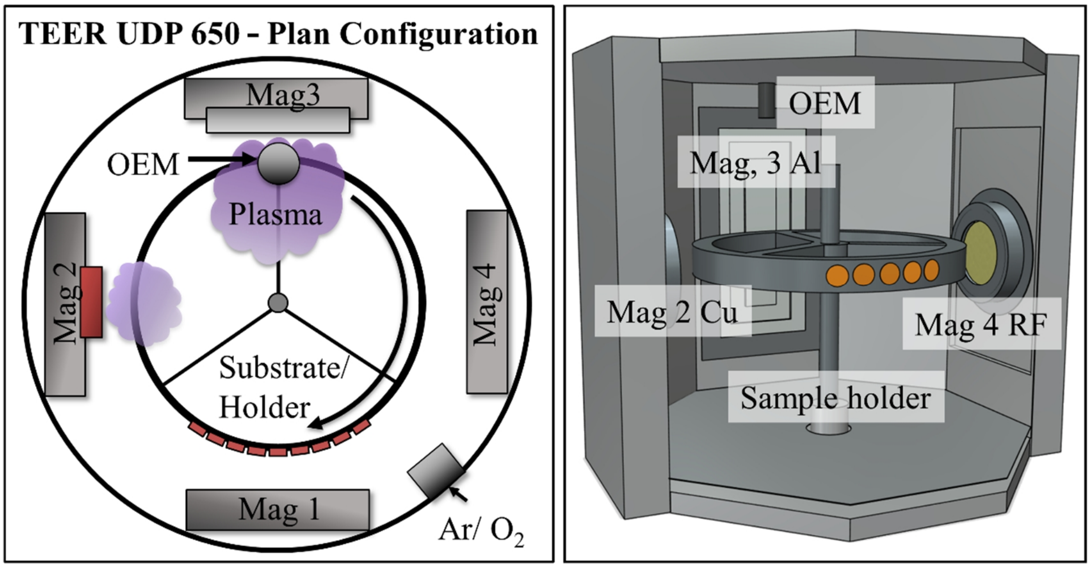

Figure 4.1: *(left) TEER UDP-650 rig top down configuration used during thin film deposition and substrate preparation. Magnetron (Mag) 2 is equipped with RF power and a Cu Target and Mag 3 is equipped with DC and PDC power and an Al target. (right) 3D render of the TEER-UDP650 showing magnetron and sample holder placement.*

4.1.1 RF deposition

RF deposition was carried out using the TEER UDP-650 equipped with an Advanced Energy Dressler CESAR RF power supply and matching unit programmed to deposit at a frequency of 13.5 MHz. Pulsed DC substrate bias was applied using an Advanced Energy DC Pinnacle power supply in all subsequent coatings (the same as used for substrate etching). The default target position (RF 1, RF SiO_2 and Ta_2O_5) had a target to sample separation of 55 ± 0.5 mm and sample 2 (RF 2) had a target sample separation of 120 ± 0.5 mm. See ***Table 4.1*** for additional deposition parameters. The rig was pumped down to a minimum of $3x10^{-5}$ Torr and had a sample rotation speed of 5 RPM. The same initial vacuum, rotation speed and etching stages were maintained for subsequent DC, Blended DC (BDC) and PDC depositions.

Table 4.1: *Deposition parameters for RF deposited thin film materials sputtered onto copper substrates.*

Sample	***Coating time (min)***	***Sample bias (V)***	***Al_2O_3 target power (W)***	***Ar gas flow (sccm)***
RF 1	*480*	*-60*	*100*	*40*
RF 2	*1140*	*-60*	*100*	*40*
RF SiO_2	*480*	*-60*	*100*	*140*
RF Ta_2O_5	*480*	*-60*	*100*	*140*

Note that RF2 samples were produced with no substrate cleaning to observe the effect of substrate cleaning the films adhesive properties.

4.1.2 DC deposition

DC samples were prepared using an OEM turn down of 23% at constant Ar gas flow of 23 sccm, target separation (55 ± 0.5 mm) and a coating time of 90 min. An Advanced Energy DC Pinnacle power supply equipped with the rig was used for DC deposition. All depositions used a sample rotation speed of 5 RPM. ***Table 4.2*** contains all additional DC and BDC deposition parameters.

Table 4.2: *Deposition parameters for BDC and DC alumina films, with a constant sample target separation of 55 ± 1 mm and a rotation speed of 5 RPM.*

Sample	***Coating time (min)***	***Sample bias (V)***	***OEM set point time/ (min)***	***Al target current (A)***
DC-10	*90*	*-10*	*5*	*6*
DC-45	*90*	*-45*	*5*	*6*
DC-60	*90*	*-60*	*5*	*6*
DC3-6	*60*	*-60*	*5*	*6*
DC6-6	*30*	*-60*	*5*	*6*
DC12-6	*120*	*-60*	*5*	*6*
BDC-10	*90*	*-10*	*10*	*6*
BDC-45	*90*	*-45*	*10*	*6*
BDC-60	*90*	*-60*	*10*	*6*

The OEM was calibrated to 100 % whilst pure aluminium was sputtered in Ar. Once the set point was reached and the interlayer was deposited, O_2 was then added according to the OEM feedback loop to achieve 23 % of the original intensity. This turn down was carried out over a set amount of time before deposition of alumina began to form a blended interface.

The interlayer between DC and BDC films varied as follows: DC films had an Al interlayer sputtered for 5 min prior to a 5 min OEM ramp down to 23 % from 100%. BDC films had a blended Cu/Al layer followed by 5 min Al deposition and a 10 min 100 to 23 % OEM ramp down. The blended BDC layer was created by ramping the Cu power from 60 to 0 W (RF) over 5 min whilst the Al target was ramped from 0 to 6 A (DC).

4.1.3 PDC deposition

A pulsed power supply (ENI RPG50 with arc handling capabilities) was equipped to magnetron 3 of the TEER UDP-650, in order to allow a pulsed deposition motif. Various pulsing parameters were trialled in order to deposit stably without arcing. Parameters are outlined in ***Table 4.3*** and the caption includes constant parameters. The interlayers and OEM ramping techniques employed for PDC films were the same as for DC sputtered films deposited previously.

Table 4.3: *PDC film deposition parameters, note that the duty cycle varies within samples deposited at the same pulse frequency with a constant sample target separation of 55 ± 1mm and a rotation speed of 5 RPM.*

Sample	***Coating time (min)***	***Sample bias (V)***	***OEM set point time/ (min)***	***Al target current (A)***	***Ar gas flow (sccm)***	***Pulse freq. (kHz)***	***Duty cycle (%)***
PDC-60	*240*	*-60*	*5*	*4*	*140*	*50*	*40.0*
	240	*-60*	*5*	*4*	*140*	*50*	*24.0*
	240	*-60*	*5*	*4*	*140*	*150*	*40.0*
	240	*-60*	*5*	*4*	*140*	*150*	*22.5*
	240	*-60*	*5*	*4*	*140*	*201*	*40.0*
	240	*-60*	*5*	*4*	*140*	*201*	*24.0*

PDC coatings deposited with 150 kHz and a 40% duty cycle were selected as the most appropriate and thus subsequent Al_2O_3 PDC depositions utilised these parameters and was subsequently named PDC-60.

4.1.4 Multilayer films

PDC films were combined with RF deposited films of SiO_2 and Ta_2O_5. The position of the RF layers are outlined in ***Figure 4.2***. PDC Al_2O_3 layers were deposited using the same deposition parameters as PDC-60 above. Layered film deposition was carried out by using RF deposition of ceramic materials from compound targets. A maximum 100 W RF power was applied to the ceramic targets whilst maintaining the similar gas pressure and substrate bias used for PDC depositions. Total sample thickness was maintained at 200 nm throughout the multilayer sample production. With *ca.* 150 nm of PDC Al_2O_3 and *ca.* 50 nm of additional RF material split between the assigned number of layers. The interlayer used in BDC films was also carried through and the process involved the same Cu to Al blending stage prior to reaching the Al OEM set point and also included the 10 min Al to Al_2O_3 blending stage.

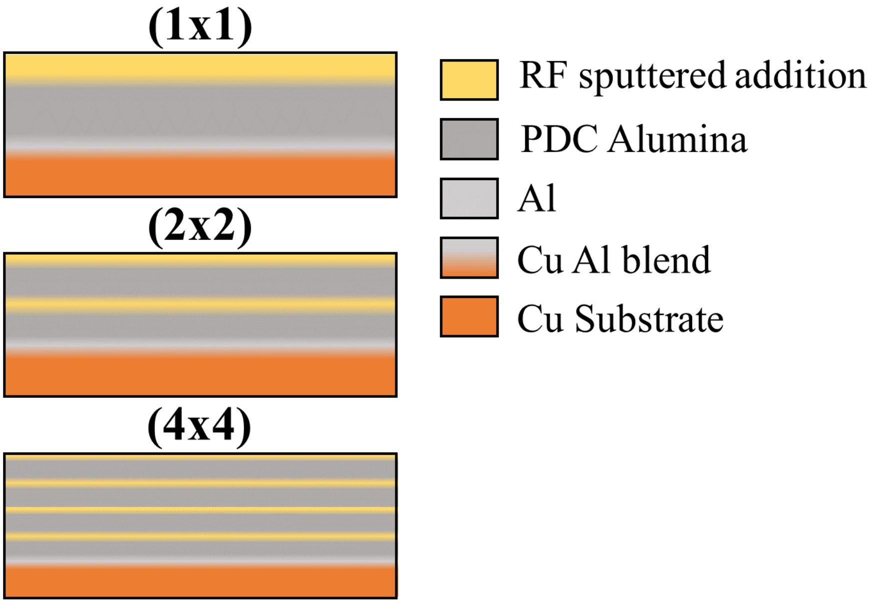

Figure 4.2: *Schematic of PDC alumina RF multilayer materials. Showing nomenclature as relating to film structure.*

Ramping of the RF (SiO_2 or Ta_2O_5) target 15 min prior to deposition was used to improve adhesion, ramping of the PDC target was not used past the initial film deposition. Fused SiO_2 (purity > 99 %) and Ta_2O_5 (99.99 %) targets of 57 mm ø were utilised for RF components. See ***Table 4.4*** for deposition parameters used following interlayer deposition.

Table 4.4: *Multilayer sputtering parameters for Al_2O_3, Ta_2O_5 and SiO_2 composites as deposited onto Cu foil and disks as well as borosilicate cover slides.*

Sample	***Al_2O_3 per layer (min)***	***Ta_2O_5 per layer (min)***	***SiO_2 per layer (min)***	***RF target power (W)***	***Ar Gas Flow (sccm)***	***Pulse Freq. (kHz)***	***Duty Cycle (%)***
1x1	*133.3*	*30.9*	*155.4*	*100*	*140*	*150*	*40*
2x2	*66.7*	*15.5*	*77.2*	*100*	*140*	*150*	*40*
4x4	*33.3*	*7.3*	*38.6*	*100*	*140*	*150*	*40*

Note that Ta_2O_5 and SiO_2 sputtering times were varied in order to obtain the same layer thickness in both sets of composites. See ***Figure 4.3*** for an example process graph used for the multilayer composites.

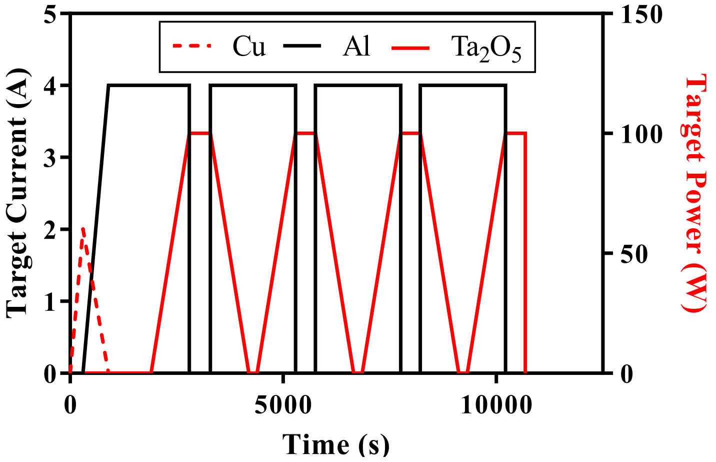

Figure 4.3: *Process graph for 4x4 Al_2O_3 Ta_2O_5 composite film shows the extensive blending stages used to ensure a cohesive film.*

4.1.5 Wire coating

For the experiments on wire coating the bespoke winding rig was designed and fabricated, fixing into the existing TEER UDP-650 chamber by attaching to the rail fixings (typically used for the 2 dimensional coating attachment) see ***Figure 4.4***.

Wire specific pre-treatment was carried out as follows: 3 m long Cu wire samples were sonicated in acetone followed by IMS for 15 min each. Samples were then wound onto the coating apparatus and the chamber was pumped to a vacuum > $3x10^{-5}$ Torr. A bias etch was applied to remove any surface contaminants at a rotation speed of 0.5 rpm for 2 cycles (with one cycle referring to the complete movement of wire from one reel to the other see ***Figure 4.4***). The bias etch was ultimately carried out as for the disk samples with a pulsed bias of - 150 V to remove unwanted surface contaminants whilst not damaging the wire. The Al target was also cleaned (behind the shield) at 0.2 A during the bias etching stage.

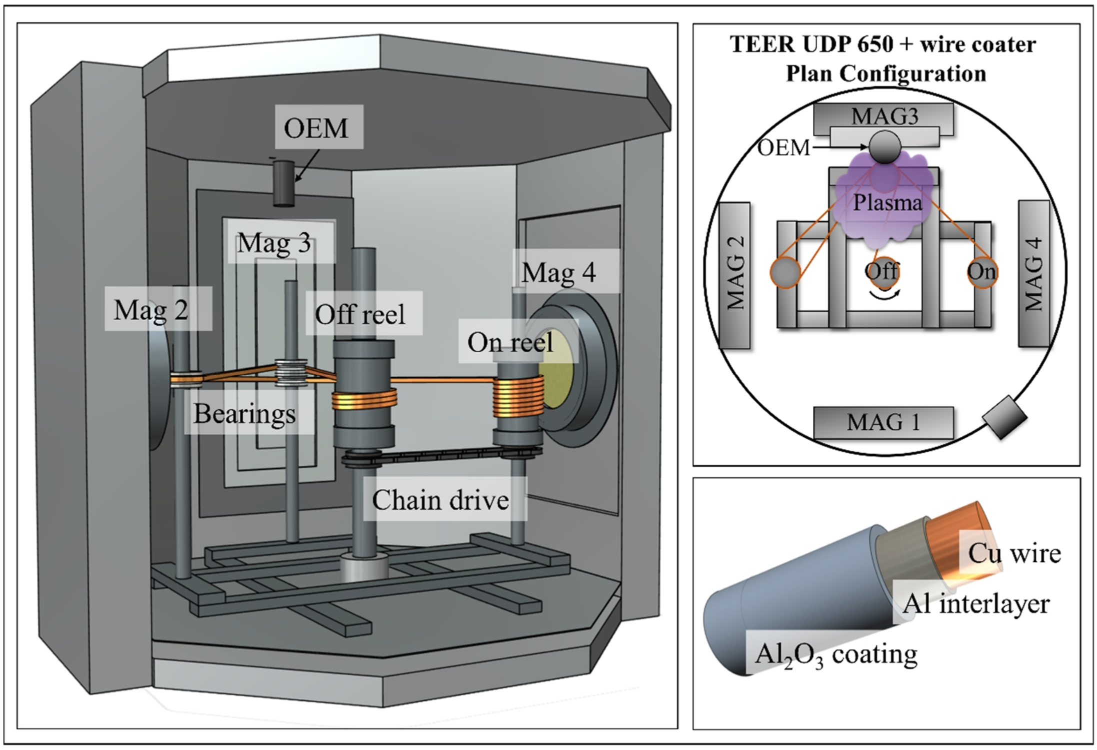

Figure 4.4: *(left) Render of the wire coating apparatus as loaded into the TEER UDP650, showing on and off reels as well as the chain drive, (top right) plan view of the coating apparatus as loaded into the TEER-UDP650 and (bottom right) schematic of the copper wire as coated using the sputtering apparatus.*

Wires were coated using Pulsed DC power for aluminium interlayer and subsequent alumina layers. The initial parameters for the coated wires were as follows: a base layer of aluminium was deposited at 4 A (150 kHz 40% duty cycle using a 1.5, 3.0 or 4.5 rpm rotation speed). Subsequently an Al_2O_3 layer was applied at the 23% OEM turn down as used for the PDC Al_2O_3 disk samples. A rotation speed of 0.5 rpm was used for all Al_2O_3 coating steps. A number of different passes were utilised in order to achieve varying alumina thickness. Additional passes were achieved by reversing the main shaft rotation allowing the chain to drive the second reel. A substrate target separation of 10 mm was used for the deposition of optimised coatings onto the wires. Sample specific layer sputtering times have been included in ***Table 4.5***.

Table 4.5: *Sputtering and drawing parameters for aluminium and alumina coated wires. Note that one of the wire interlayers was used prior to all subsequent Al_2O_3 regardless of the number of Al_2O_3 layers, the interlayer speed will be added to the start of the sample name for instance 1.5 rpm 3x.*

Sample	***Al_2O_3 Passes***	***Sample Bias (V)***	***Al target Current (A)***	***Ar Gas Flow (sccm)***	***RPM***
Interlayer	*/*	*-40*	*4*	*140*	*1.5, 3.0, 4.5*
1x	*1*	*-40*	*4*	*140*	*0.5*
3x	*3*	*-40*	*4*	*140*	*0.5*
5x	*5*	*-40*	*4*	*140*	*0.5*

4.1.6 Heat treatments

Heat treatments were carried out in an attempt to improve interfacial mixing in the composite films as well as remove defects and stress incorporated into the films during the initial deposition process. PDC Al_2O_3 and multilayer samples as deposited onto Cu disks, foil and borosilicate glass slides were heat treated at 500 °C for 60 min in a Carbolite HRF 7/22 furnace with a Eurotherm 808 controller. Heating and cooling rates were 10.8 and 1.4 $°Cmin^{-1}$ respectively. Once samples were cool the base copper of samples required for electrical testing was cleaned using 1200 grit silicon carbide paper to expose the copper electrode. Coated wire samples were heat treated in the same manner, for further mechanical testing.

4.2 Structural characterisation

It should be noted here that the errors displayed for results produced using all of the following techniques is the standard error mean.

4.2.1 Fourier transform infrared spectroscopy

Infra-red (IR) spectroscopy is based on the interaction of covalent bonds with infra-red radiation. Common modes of interaction include bending and stretching. IR spectroscopy usually focuses on the mid IR range (600-2000 cm^{-1}), however, there are options to study near and far IR. Depending on the type of bond and absorbance mode a different energy of radiation is absorbed. Whilst FTIR is usually used for organic compounds the technique is also suitable for some ceramic materials depending on the nature of the bonding [280].

The use of an attenuated total reflectance (ATR) module, can allow the use of solid materials not typically suitable for transmittance measurements (with an interaction depth of between 0.5 and 1.0 μm). This technique relies on absorbance of radiation by the sample, thus good surface contact with the ATR crystal is absolutely crucial. Total internal reflectance within the crystal creates an evanescent wave which penetrates into the sample, at energies where the evanescent wave is absorbed the beam will be attenuated, this attenuation is then used to create the spectrum [281].

4.2.1.1 Sample preparation and parameters

Fourier Transform Infrared Spectroscopy (FTIR) was carried out using a Bruker Tensor FTIR instrument equipped with ATR attachment consisting a diamond mirror and ZnSe lens. IR absorbance between 500 and 4000 cm^{-1} wavenumbers was measured with a resolution of 2 cm^{-1} using 64 scans. Following background scans samples were analysed by pressing the coating surface in contact with the ATR diamond (Films were deposited onto copper film, to allow adequate ATR crystal contact). FTIR analysis using opus software - of all films was carried out to confirm Al-O bonding.

4.2.2 X-ray diffraction

X-ray diffraction (XRD) is a powerful tool which can be used for material and phase identification as well as for more in depth modelling of structure for single crystals. This technique relies on the interaction of X-rays with the crystalline phases within a material. X-rays are generated by irradiating a copper filament with high energy electrons, as electrons are expelled from the inner shell the relaxation of electrons into the vacancy is accompanied by the release of an X-ray photon. The X-rays are fired at the surface of the sample through a pre sample monochromator [282].

The Bragg equation can be used to calculate the 2θ angle from the d spacing, the X-ray wavelength and the angles between incident rays see ***Figure 4.5*** and ***Equation 4.1***. The Bragg equation, when satisfied by an integer, identifies the angles at which constructive interference will take place and thus angles that will result in a peak of increased intensity.

Equation 4.1: *Braggs law*

$$n\lambda = 2d\sin\theta$$

Crystallite size can also be determined using this method, by treating the peak width with the Scherrer equation, where L is the crystallite size, λ is the X-ray wavelength and k is a constant related to the crystallite shape (***Equation 4.2****)* [283]. Modifications of this equation exist in order to generate results with less error attributed. The X-ray amorphous/ amorphous nature of a material can also be confirmed by presence of an amorphous hump in the diffraction pattern.

Equation 4.2: *Scherrer equation*

$$L = \frac{k\lambda}{\beta cos\theta}$$

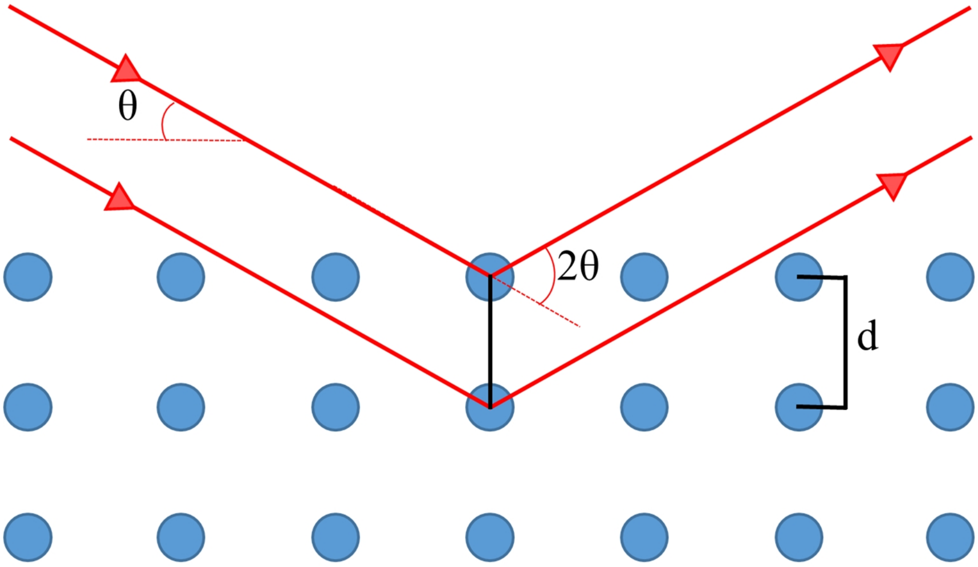

Figure 4.5: *Diffraction of X-rays as they interact with the atoms within a crystal structure.*

For the analysis of thin samples particularly films and also powders a glancing angle scan can be used to diminish signal generated from the substrate. This kind of scan positions the X-ray source at a shallow angle moving only the detector

4.2.2.1 Procedure

Films to be analysed with XRD were deposited onto borosilicate glass coverslips (Agar scientific L46R19-5 19 mm ø cover glasses) to avoid signal from the underlying copper substrate. Samples were affixed planar to the top of the sample holder and levelled flat with the top of the sample holder, to avoid peak shifting due to improper alignment. A Bruker D8 advanced (Cu Kα source at 40 kV and 35 mA) was used for glancing angle scans at 1.2 °, scanning between the 2θ values of 15 and 80 ^{o} using a step size of 0.04 ^{o} with a dwell time of 12 s. Phase identification was carried out using EVA software with a PDF Database.

4.2.3 X-ray photoelectron spectroscopy

X-ray photoelectron spectroscopy (XPS) is a powerful technique which allows the compositional analysis of the top 10 nm layer of a sample [284]. This technique allows the quantification of elemental composition as well as the analysis of the electronic states through peak deconvolution. This technique is based upon the ejection of photoelectrons from the surface layers of atoms which is caused by X-ray bombardment as seen in ***Figure 4.6*** [282].

The binding energy of the photoelectron can be calculated by using the energy of X-ray source used and the kinetic energy of the unbound electron as measured by the instrument ***Equation 4.3*** [285]. The kinetic energy of the ejected electrons depends on the strength with which they are bound, thus the orbital from which the electrons are released can be determined. This means that shifts in peak position can be used to account for variance in oxidation states.

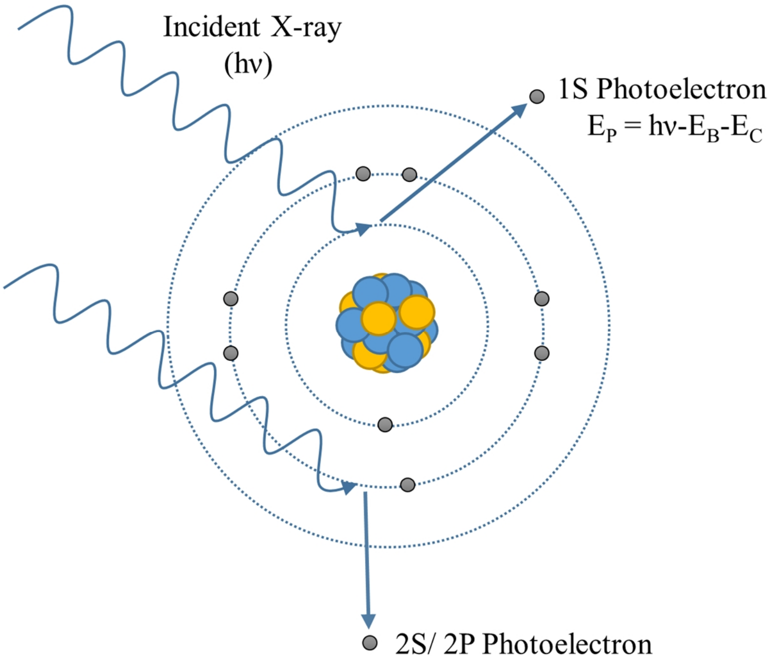

Figure 4.6: *Removal of core shell photo electrons by X-rays as in XPS.*

Equation 4.3: *calculation of Electron binding energy in XPS generated photoelectrons*

$$E_B = E_{Photon} - (E_{Photoelectron} + E_{corr})$$

4.2.3.1 Preparation and analysis

Prior to analysis samples were stored in Al foil, to avoid contaminants, organics or atmospheric particulate which could affect the surface composition. XPS of coating surface was conducted using a VG scientific Escalab Mark II with an AlKα non-monochromatic source. The X-ray source was operated at the following parameters: 12 kV, 4.6 A and 20 mA. Survey spectra consisting of 2 scans was collected between 0 and 1200 eV using a step size of 1.0 eV and dwell time of 0.2 s. The survey was followed by high definition scans which used a step size 0f 0.2 eV and dwell time of 0.4 s with 5 scans for O_1S, Al_2P, Si_2P, Ta_4d and C_1S photoelectron emissions (The positions of which were determined by the survey scan).

Casa XPS was used for elemental quantification, peak deconvolution and oxidation state analysis. All spectra were calibrated with respect to C_1S photoelectron emission at 284.8 eV. Gausian-Laurentz peak fitting for Al_2P consisted of fitting the Al^{3+} peak followed by fitting of the peak shoulder for Al^0, note that Si_2P^{4+} and Si_2P^{1+} peaks were also fitted to Si_2P peaks in SiO_2 composites. A Shirley baseline was applied to peaks prior to all fitting operations.

4.2.4 Electron microscopy

4.2.4.1 SEM

Scanning electron microscopy (SEM) utilises an electron beam focused by electromagnets to scan an area on the sample surface, able to resolve artefacts in the nm range. Resolution is heavily dependent on the electron generation method, for instance a higher resolution is achieved using a Field emission gun when compared to a more traditional tungsten filament, as well as the sample type and conductivity [286].

The interaction of these electrons causes a number of different phenomena, perhaps most importantly secondary electron emission, electron backscattering and the production of characteristic X-rays when electrons are removed from the inner shells within the material see ***Figure 4.7***. Secondary electrons (SE) are the most common mode used for observing a samples topography and are generated by inelastic collisions relatively close to the surface. Backscattered electrons (BSE) are electrons from the beam which are reflected from the atoms within the material (Elastic collisions) thus are heavily influenced by atomic weight and are useful in determining compositional differences. The characteristic X-rays are detected by an Energy dispersive X-ray detector (EDX) which can be used to generate maps, line-scans or point compositional data for elemental distribution or point composition [286,287].

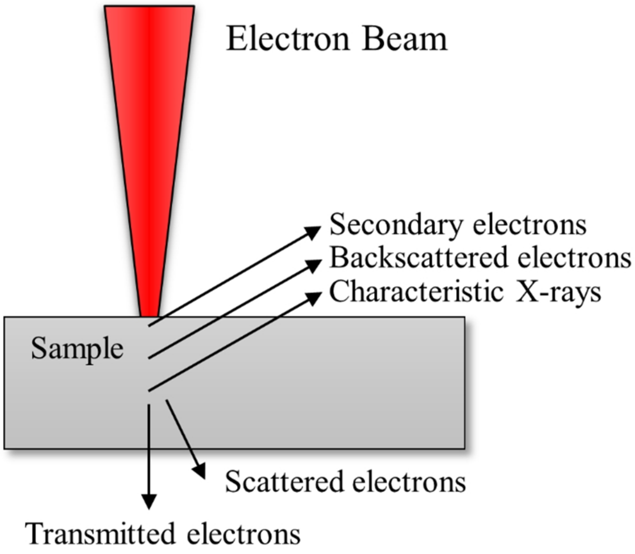

Figure 4.7: *Interaction of surfaces with an electron beam, showing the interactions which result in SEM, TEM and EDX detectable phenomena.*

4.1.1.1.1 Sample preparation

Samples were either deposited onto Pt coated glass disks or onto copper substrates. Glass coated samples were scored with a diamond pen and mounted vertically to view a cross section. Copper coated samples were mounted perpendicularly in conductive resin (Metprep Conducto-mount) then ground and polished as for the copper disks (*4.1*) with sequentially higher grit silicon carbide paper and colloidal silica. Following polishing samples were sonicated in distilled water (to remove any remaining colloidal silica) and ethanol to remove any organic residue.

Coating of samples containing alumina was carried out using a Q150R Plus coater with C, Pt or Ir depending on the microscope and whether EDX analysis of the sample was required.

Microscopes

A Philips XL 30 ESEM-FEG, was used with the following parameters: working distance of 10 mm, an accelerating voltage of 15 kV and a spot size of 4. This microscope was used for thickness measurements of Al_2O_3 RF deposited films.

A JEOL 7100F FEG SEM was used for high resolution imaging of thin films and their interlayers where thicker than 100 nm. An accelerating voltage of 15 kV and aperture 4 were used along with a working distance of 10 mm. Samples were plasma cleaned before coating. An 8 nm iridium coating was generally used for samples analysed using this instrument.

A Quanta 650ESEM equipped with an oxford instruments silicon drift detector was used for EDX mapping of the surfaces and pull off sites a working distance of 10 mm, with an accelerating voltage of 15 kV and a spot size of 4 was used in order to generate maps of sufficient quality. This microscope was also utilised for tensile testing of coated wire samples.

4.2.4.2 TEM

Transition electron microscopy (TEM) is used for higher resolution imaging than SEM and relies on the detection of electrons which are transmitted through a suitably thin sample (see ***Figure 4.8***). Samples can be thinned by methods such as using a microtome or focused ion beam (FIB) milling using a suitable SEM equipped with an ion-milling gun, as utilised in this work [288].

TEM works from the same principals as SEM where a focused electron beam is used to image a surface however the detection methods are different. There are two common scanning TEM (STEM) modes, bright field and dark field. Bright field mode is the standard imaging mode where electrons are transmitted through the sample with little deflection. Dark field mode however, images only using scattered electrons by tilting the electron beam, and thus is more sensitive to high molecular weight materials which result in a bright image. A third imaging mode known as high angle annular dark field, utilises an annular detector to detect only highly scattered electrons and is used to generate high contrast images with regard to mass [289].

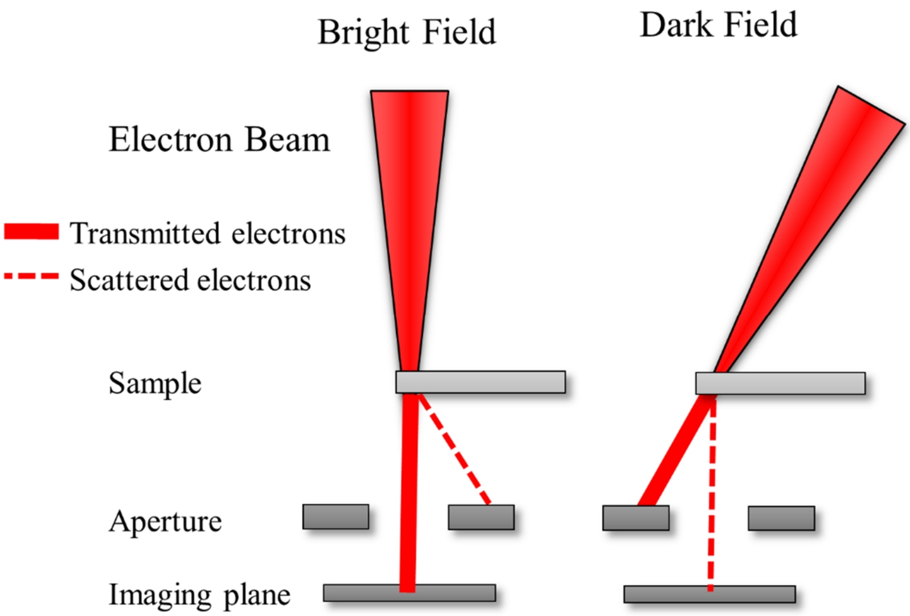

Figure 4.8: *Simplified beam diagrams for bright (left) and dark field (right) TEM imaging modes.*

4.2.4.3 Procedure

Sample cross sectioning was carried out on the samples using FIB lift out techniques at the University of Nottingham NMRC facility. A FEI quanta 200 3D dual beam FIB/SEM equipped with a Ga ion beam (Magnum^{TM} Column). A 5 μm Pt top layer to protect the sample was applied prior to milling around the desired site. Lift outs were performed on BDC and PDC samples, with an average size of 15x5 μm.

Cross sectional STEM was carried out on the lift out sample in order to obtain high resolution images of the film structure. In particular looking for any short range order which would could avoid detection in XRD. A JEOL JEM 2100+ was used for imaging with an accelerating voltage of 200 kV. The microscope was equipped with a Gatan US1000XP detector and a JEOL STEM detector for conventional imaging and bright field and annular dark field scanning TEM respectively. An Oxford instruments X-MAX 150 was used for EDX analysis.

4.2.5 Atomic force microscopy

Atomic force microscopy (AFM) utilises a cantilever which scans over a surface to give information about surface topography [290]. A laser focused on the back of the cantilever tip feeds back to a detector and allows the contours of the surface to be mapped. A range of scanning modes can be used, commonly tapping mode, where the tip is oscillated and changes in amplitude are used to map the surface and is used if sample preservation is desired, opposed to contact mode where the tip is moved whilst in contact with the sample surface. AFM is also capable of performing electrical measurements including conductive mapping and breakdown measurements as well as mechanical testing, such as nano indentation and tensile testing [109].

4.2.5.1 Procedure

Atomic force microscopy (AFM) was carried out using a Bruker Fast Scan Bio Dimension ICON instrument in peak force mode using 01-0.025 Ohm-cm antinomy (n) doped Si tips (model TAP525A). Gwyddion software was used to generate roughness values, assess surface artefacts and generate 3D images. Roughness values taken as an average from n=5 surface locations.

4.3 Electrical measurements

Dielectric breakdown of thin films as deposited onto disks was assessed using two methods a standard probe method (***Figure 4.9***) and an AFM based method. Electrical characterisation of coated wires was carried out using a crossed pair method.

4.3.1 Electrical breakdown probe methods

Direct voltage stress evaluation of the dielectric breakdown for each coating was carried out according to ASTM D3755-14 "Standard Test Method for Dielectric Breakdown Voltage and Dielectric Strength of Solid Electrical Insulating Materials Under Direct-Voltage Stress" with modification in the electrodes that were used to accommodate the coated disk geometry. A schematic of the circuit used for measuring dielectric strength can be found in (***Figure 4.9** and **Equation 4.4***). A brass spring loaded electrode (RS pro 2.54 mm pitch spring test probe with flat head tip 3 A) was used as the top electrode whilst the copper substrate was used as the bottom electrode. An EA PSI 8720-15 power supply (max 750 V, 15 A) was ramped stepwise with steps of 10 V for 20 s (500 mVs^{-1}) until film breakdown occurred. Breakdown was defined as the point at which an abrupt increase in current density was observed and the film completely failed to resist the flow of current. Voltage across a resistor in parallel (470 kΩ metal film) was measured to allow leakage current density to be calculated by dividing the current flow across the sample by the probe area which was 2.8 mm^2. Voltages were measured using Kiethley 2700 and 2010 series multi meters. For each film 5 sample sites were measured.

***Equation 4.4:** current calculation for in house probe testing*

$$A = \frac{Vr}{Rr}$$

***Equation 4.5:** equation to calculate current density*

$$Acm^{-2} = \frac{A}{electrode\ area\ mm^2}$$

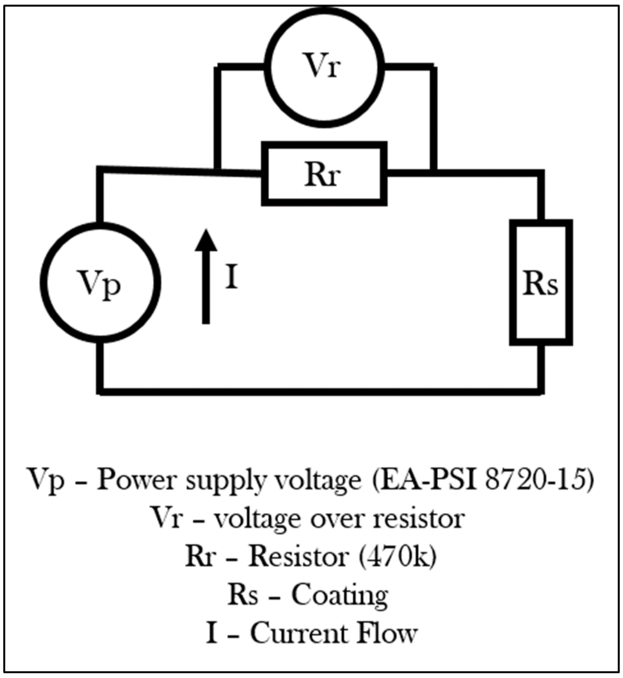

Figure 4.9: *Schematic for in house electrical probe breakdown testing apparatus.*

4.3.2 AFM dielectric breakdown measurement

Conductive AFM is a powerful tool for assessing the electrical properties of thin films because of its high spatial resolution, granted by the small tip radius [109]. AFM dielectric breakdown measurement (DB) is a process which is used to measure local electrical properties of materials, and given a sufficiently large power supply with respect to the film thickness material breakdown can be characterised. ***Equation 4.5*** was used along with the voltage data generated by the probe to calculate the leakage current density prior to breakdown.

4.3.2.1 Procedure

AFM dielectric breakdown (AFM DB) measurements were carried out using AFM using an Oxford instruments Cypher equipped with a high voltage module and an asylum research ASYELEC.02 Ti/Ir coated tip was used to apply a voltage ramp (top electrode) of 0 - 150 V over 40 s or until a sharp increase in current was seen above 20 nA. Thinned DC and BDC samples were produced for these measurements with an alumina deposition time of 12.5 min hence aluminium interlayer was acting as the bottom electrode.

4.3.3 Crossed pair method

The crossed pair method used for measuring the electrical properties of the coated magnet wire is often used to determine the dielectric strength of the isolative coatings, measurements following mechanical and thermal strain could also be made (with heat treated samples for instance). In this method current is passed through one wire and the current in the second wire is monitored, giving an idea of leakage current and values for breakdown strength once there is no resistance. As with the AFM DB measurements, IV data can be used to generate information about conduction methods and film resistance.

4.3.3.1 Procedure

Measurement of AC breakdown was carried out by measuring the breakdown in a crossed pair of wires which were taped with polyimide to ensure continuity between the wires. The coating was removed from the ends of each wire using 1200 grit silicon carbide paper. Using a Megger DELTA400 series 12 kV insulation diagnostic system, a voltage ramp of 10 $\mathrm{Vmin^{-1}}$ was applied to the sample until breakdown occurred. Breakdown measurements were recorded using the same Megger instrument. Measurements were carried out according to ASTM D1676 “Standard Test Methods for Film-Insulated Magnet Wire” [26].

4.4 Mechanical Properties

Mechanical properties were analysed in order to assess the adhesion for the ceramic insulators to copper substrates. This was carried out with the wider goal of depositing these materials onto copper substrates including onto wires.

4.4.1 Disk

The following tests were used to assess the adhesion of alumina thin films as deposited onto copper substrates, with varying interlayer and film deposition parameters: DC, BDC, PDC and all multilayer variants. Annealing of PDC and PDC multilayer films was carried out in order to assess the mechanical properties following thermal treatments and determine whether any decrease in adhesion was observed.

4.4.1.1 Stub adhesion

Stub adhesion is a technique which is commonly used to measure adhesive strength of films and gives additional information about the films mechanical properties through the determination of failure mode and the failure strength (MPa) [160,161].

4.4.1.2 Procedure

Pull off testing was carried out using a P.A.T. handy (DFD instruments) pull off adhesion testing unit. Dollies of 2.8 mm diameter were glued to the film surface using DFD E1100S epoxy and cured at 140 ^{o}C for 60 min on a heat plate in direct contact with the base of the coated disk. Prior to curing stubs were cleaned with compressed air to remove any particulate, stubs were pressed down once the epoxy was applied to remove any air bubbles. Excess glue was removed with the supplied DFD cylindrical cutting tool following curing. Stubs were then removed from the surface using the P.A.T Handy instrument. Removal sites were analysed using light microscopy using a Nikon LV100ND, to determine the failure mechanisms because it was possible to differentiate between the different materials using this method. Failure mechanisms and procedure are outlined in ***Figure 4.10***.

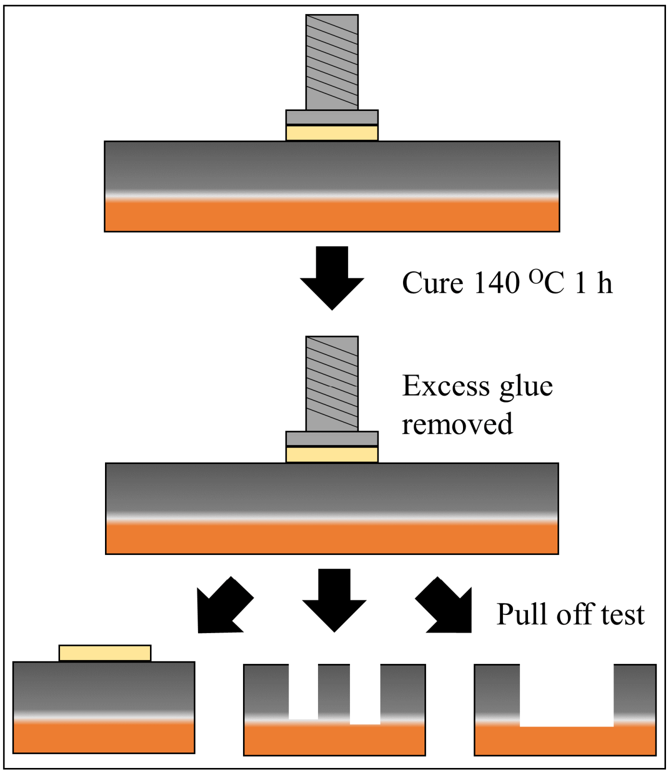

Figure 4.10: *Pull off adhesion schematic, showing the procedure as well as representations of adhesive and partial and complete interfacial failures.*

4.4.1.3 Scratch testing

Scratch testing is a commonly applied technique for assessing the adhesion of thin films to substrate materials, which is dependent on the characteristics of both substrate and surface materials as indicated in ***Figure 4.11***. In this technique an indenter is drawn across a sample surface with either a constant or increasing load for a predetermined time and distance. Cohesive failure is caused by tensile stress within the coating and results in cracking and chipping. Adhesive failure occurs between the substrate and coating and results in coating de-adhesion a result of compressive stress in front of the indenter [157].

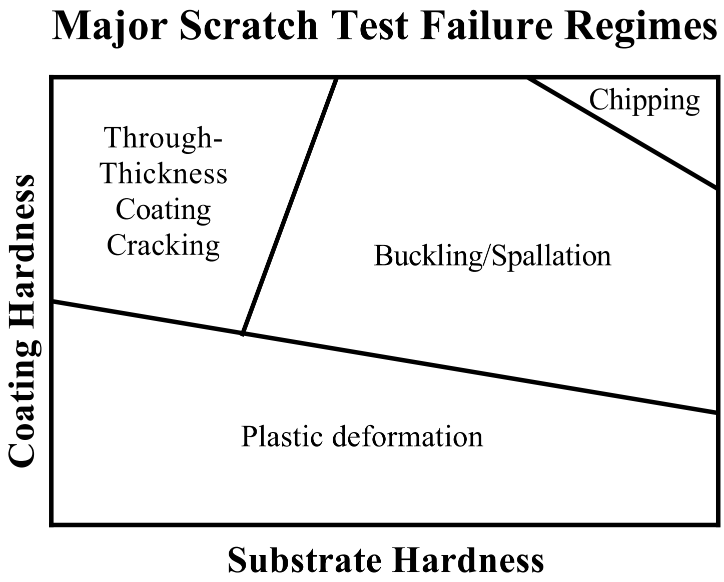

Figure 4.11: *Major scratch test failure mechanisms with respect to substrate and coating hardness, re-processed from* [157].

4.4.1.4 Procedure

Scratches were made using a CETR UMI multiple specimen test system equipped with a Rockwell C indenter. The indenter was cleaned using isopropyl alcohol and dried after each scratch. A force ramp of 0.75 Ns^{-1} was used to apply a 3 mm scratch over a period of 20 s with a max load of 15 N. Large image capture was carried out using a Nikon LV100ND to map whole length of the scratches. Image J software was subsequently used to analyse scratches with cohesive, adhesive and complete interfacial failures being identified. Failures in this case were defined as the first appearance of specific failure. Testing was carried out in accordance to BS EN ISO 20502:2016. A schematic of scratch testing and failure has been included in ***Figure 4.12***.

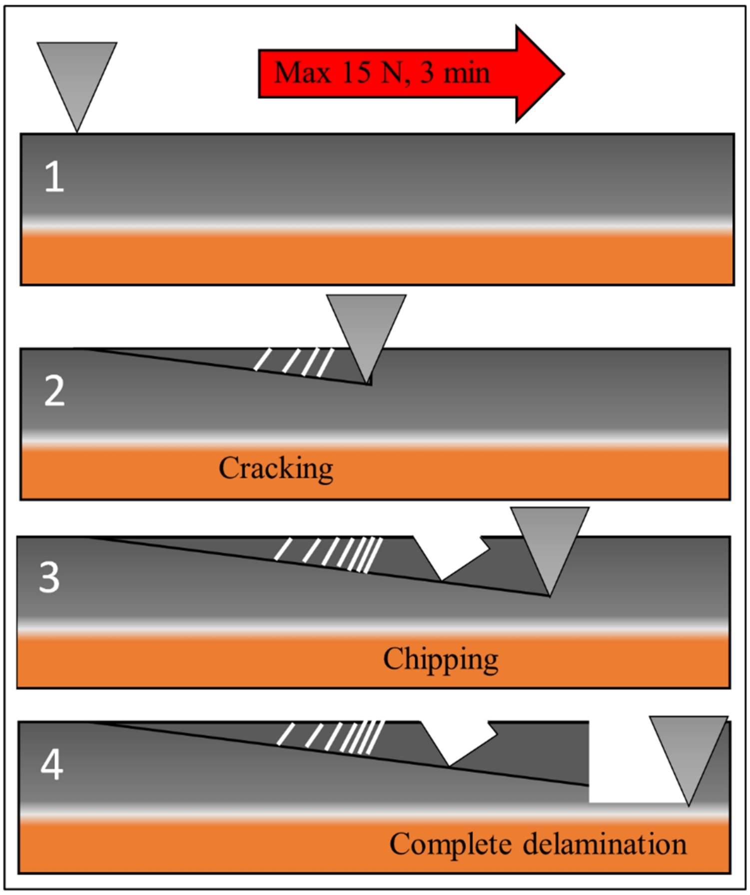

Figure 4.12: *Scratch testing depicting 1) test parameters 2) cohesive film failure (cracking) 3) further cohesive failure with partial film removal and 4) adhesive failure and complete film delamination.*

4.4.2 Wire

The following tests were carried out on coated wire to determine the adhesive properties. Much like large scale macro testing the testing will yield a stress strain relationship from which critical failure strains can be determined.

4.4.2.1 Tensile testing

Tensile testing was used to assess the onset of cracking and delamination in the coatings. Failure in the coating occurs as a result of plastic deformation in the substrate, as with scratch testing cohesive and adhesive failures loads can be determined by finding the onset of cracking and delamination as well as give information about the critical bending radius [168]. The crack density can also be generated from surface micrographs [150,167].

Equation 4.6: *Calculation for the determination of the critical bending radius in thin film coatings* [168].

$$\varepsilon_{top} = \left(\frac{d_f + d_s}{2R}\right)\frac{(1 + 2\eta + \chi\eta^2)}{(1 + \eta)(1 + \chi n)}$$

Where the strain (ε_{top}) on the top of the sample can be calculate using ***Equation 4.6*** where d_f is the film thickness d_s is the substrate thickness, R is the bending radius and $\eta = d_f/d_s$ and $\chi = Y_f/Y_s$ (where Y is the Young's modulus).

4.1.1.1.2 Procedure

Wire sections were cut to 55 mm in length and a 5 mm section of wire was bent into right angles at each end in opposite directions to produce the tensile specimen see ***Figure 4.13***. Samples were loaded into a Deben© Microtest 200N with a maximum load of 200 N. A motor speed of 1.5 mm min^{-1} was applied with a sample time of 500 µs. The tensile stage was then loaded into a quanta 650 electron microscope. An accelerating voltage of 15 kV and a spot size of 4.5 were used with a sample separation of 30 mm, to prevent crashing and charging on the samples. Secondary electron Images were then taken to determine critical failure sites at tensile loads of 40, 80, 120, 160, 180, 190 and 200 N. Critical failure modes were determined by observation of cracking and delamination in the coatings. Image J was also used to determine the average crack density.

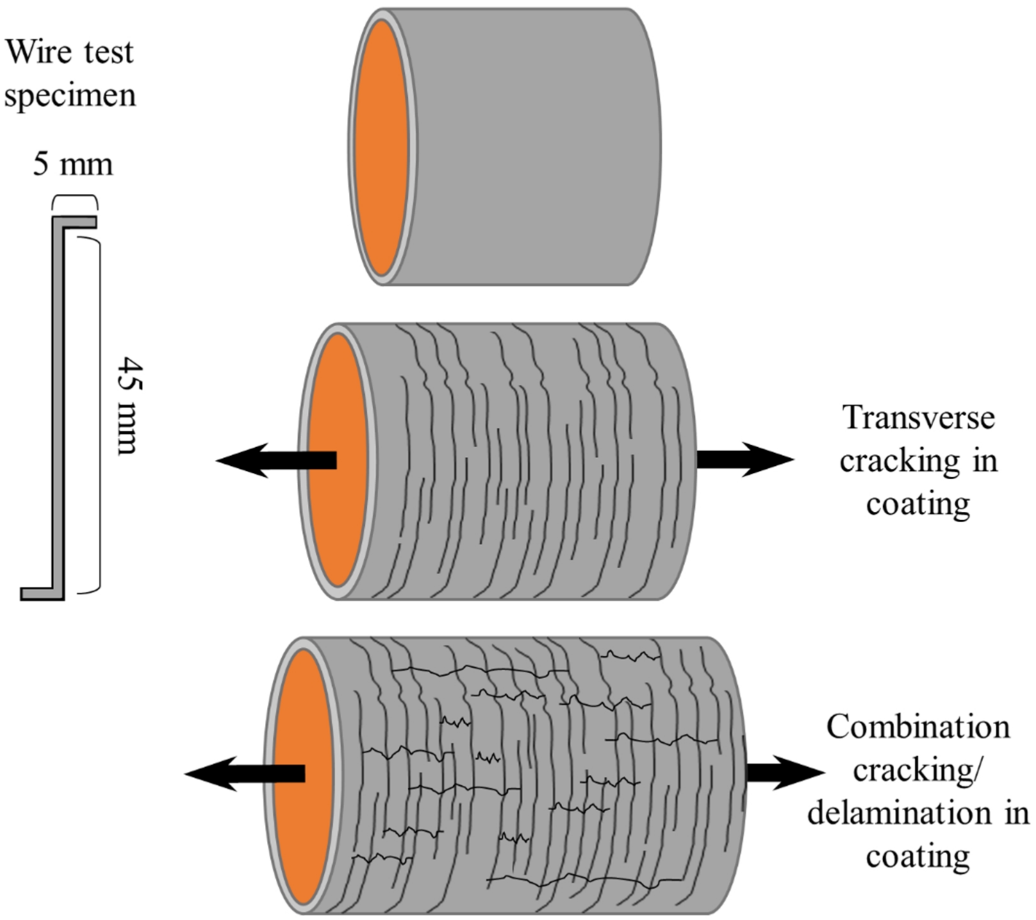

Figure 4.13: *Test specimens and failure motif during micro-tensile testing of wire. Arrows indicate direction of force applied to each end of the specimen.*

5 Results: DC and RF sputtering

This first results chapter is focused on depositing Al_2O_3 with a breakdown strength above 300 Vµm^{-1} onto copper using RF and DC sputtering techniques. Additionally this chapter will explore the effect of using mixed interlayers, increasing substrate bias and increasing layer thickness on the structural, compositional, electrical and adhesive properties of the films.

Primarily this section will display the results obtained for different deposition methods used for alumina layers. Starting with a short appreciation of initial RF deposition with IR and Thickness analysis of these films. Following this a more comprehensive assessment of the DC deposition results including: structural, mechanical and electrical properties. This will lead onto the next results chapter which focuses on the characterisation of films produced using PDC deposition techniques.

5.1 RF materials characterisation

RF samples were deposited according to the procedure outlined in section (*4.1.1*). The sample target separation, gas flow rate and target composition were modified. Bias etching and sample cleaning and sonication were also assessed for their effect on film adhesion.

5.1.1 Al_2O_3

Film composition was assessed using FTIR. Spectra of the films showed LO phonon vibration peak at 904 and 897 cm^{-1} for Al-O respectively as shown in ***Figure 5.1***. This confirmed the presence of alumina.

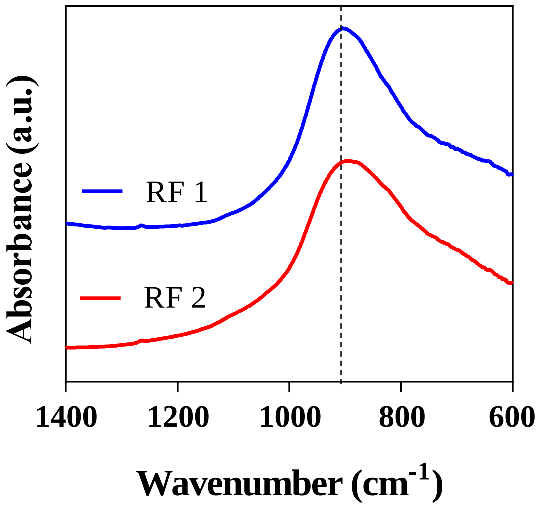

***Figure* 5.1:** *FTIR spectra for 8 hour (RF 1) and 19 hour (RF 2) RF deposited alumina (Cu disk substrates) using a target holder target separation of 55 and 120 mm respectivley.*

SEM cross sections taken from glass cover slips were used to assess deposition rate and film structure. RF deposition rates in this study were found to be much too slow to produce films of a suitable thickness with deposition rates of 16 nmh^{-1} and 11 nmh^{-1} respectively (***Figure*** **5.2**).

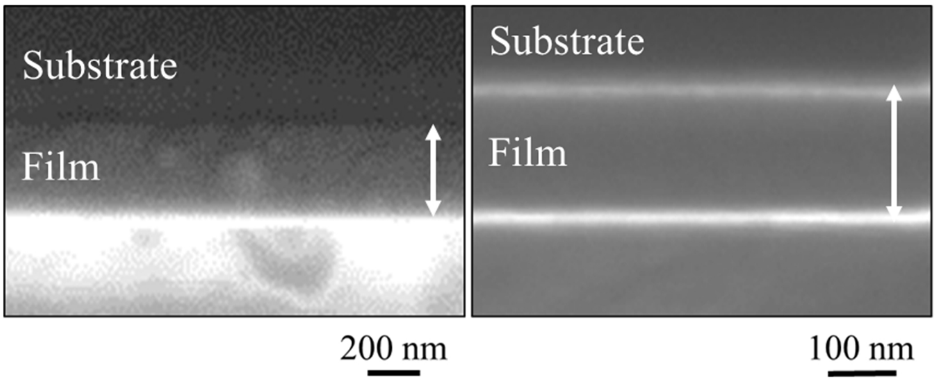

Sample	*Thickness (nm)*
RF1	*117 ± 2*
RF2	*217 ± 4*

Figure 5.2: *Backscattered electron SEM cross sections of RF thin films as deposited onto borosilicate cover slides with thickness of 217 nm (RF 2 deposited for 19 h with a target separation of 100 ± 0.5 mm) and 117 nm (RF 1 deposited for 8 hours with a target separation of 55 ± 0.5 mm).*

XRD of RF samples as deposited onto Cu, confirmed that the RF deposited films were X-ray amorphous in nature. Peaks for the copper substrate were apparent in the diffraction pattern seen in ***Figure 5.3*** with no contribution from a potential crystalline alumina phase. No amorphous hump was seen for the film because of the lack of instrument sensitivity.

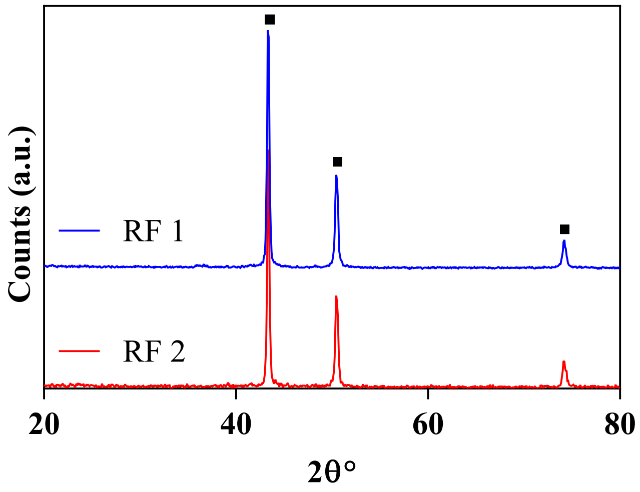

Figure 5.3: *Diffraction pattern for RF deposited alumina on a Cu disk (RF 1 8h and RF 2 19 h). Diffraction peaks result from the copper substrate which were matched to PDF 01-085-1326.*

Material adhesion was assessed on RF deposited films in order to examine the extent of the effect of target substrate separation on the pull off adhesion strength, of the alumina films on copper. RF 1 films deposited onto non-sputter cleaned copper substrates had a failure strength of 6.9 ± 0.2 considerably lower than RF 2 samples deposited onto cleaned substrates having a pull off strength of 45.7 ± 3.8, see ***Table 5.1***.

Table 5.1: *Ahession strength and failure mechanisms for RF deposited alumina films RF 1 and RF 2 as deposited onto Cu disks.*

Sample	***Failure strength (MPa)***	***Main failure mechanism***
RF 1	*6.9 ± 0.2*	*partial interfacial failure*
RF 2	*45.7 ± 3.8*	*Partial interfacial failure*

Failure occurred mainly through partial interfacial delamination for RF 1 and RF 2 samples as seen in ***Figure 5.4***.

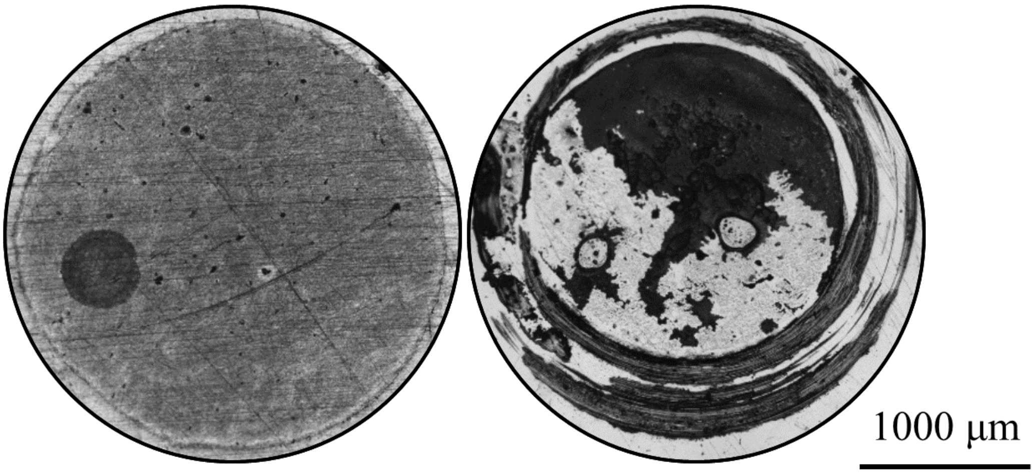

Figure 5.4: *Light microscope images of pull off failure images of RF 1 (complete interfacial delamination) and RF 2 (partial interfacial delamination) as deposited onto Cu disks.*

5.1.2 RF sputtered SiO_2 and Ta_2O_5

5.1.2.1 Characterisation

FTIR analysis of RF sputtered SiO_2 gave spectra with peaks at 1150.5 and 807.2 cm^{-1} resulting from Si-O. The same analysis of Ta_2O_5 films gave a spectra with a broad absorbance peak at 754.1 cm^{-1} with shoulders at 650.0, 806.2 and 890.1 cm^{-1}. See ***Figure 5.5*** for spectra and peak positions.

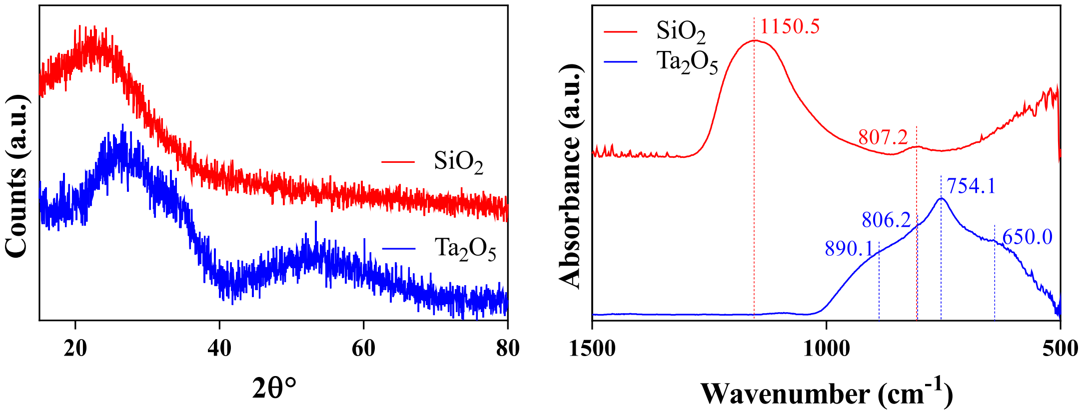

Figure 5.5: *(left) XRD diffraction patterns for RF SiO_2 and Ta_2O_5 films deposited onto silicate glass substrate. (right) FTIR spectra for SiO_2 and Ta_2O_5 RF sputtered films as deposited onto copper foil.*

XRD analysis showed that all of the RF films were X-ray amorphous as expected for RF sputtered films with relatively low substrate bias, see ***Figure 5.5*** for diffraction patterns. Large amorphous humps were seen in the spectra at *ca.* 20 ° for SiO_2 and between 20 and 40 ° and 40 and 70 ° for Ta_2O_5.

SEM analysis showed Featureless films for both of the RF sputtered materials, some detachment from the substrate was seen along with some artefacts from the polishing stage. Films were found to be 154 and 774 nm thick (See ***Figure 5.6***) for SiO_2 and Ta_2O_5 films respectfully. The thicknesses gave deposition rates of 19 and 97 nmh^{-1} for SiO_2 and Ta_2O_5 films respectively.

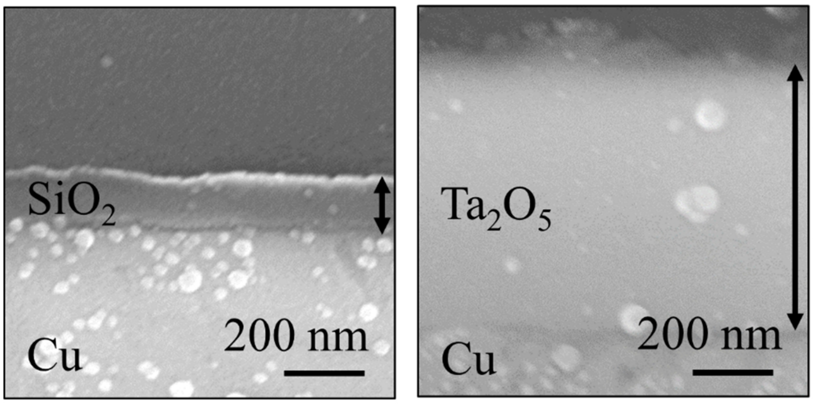

Figure 5.6: *Secondary electron SEM cross sectional micrographs of SiO_2 and Ta_2O_5 films as deposited onto Cu disks at 100 W RF power for 8 h.*

XPS survey scans were used to determine a Si:O ratio of 0.43 and a Ta:O ratio of 0.36 for RF deposited films. The survey spectra was also used to generate high resolution scans of Si_2P and Ta_4f electron emissions. Si_2P showed a single peak at 97.53 eV. Ta_4f showed a doublet consisting of Ta $4f_{5/2}$ at 28.25 eV and Ta_$4f_{7/2}$ at 26.37 eV. See ***Figure* 5.7** for XPS survey and high resolution spectra. Two peaks in the survey spectrum for the RF sputtered SiO_2 likely resulted from Mg surface contaminants as has been indicated in **Figure 5.7**.

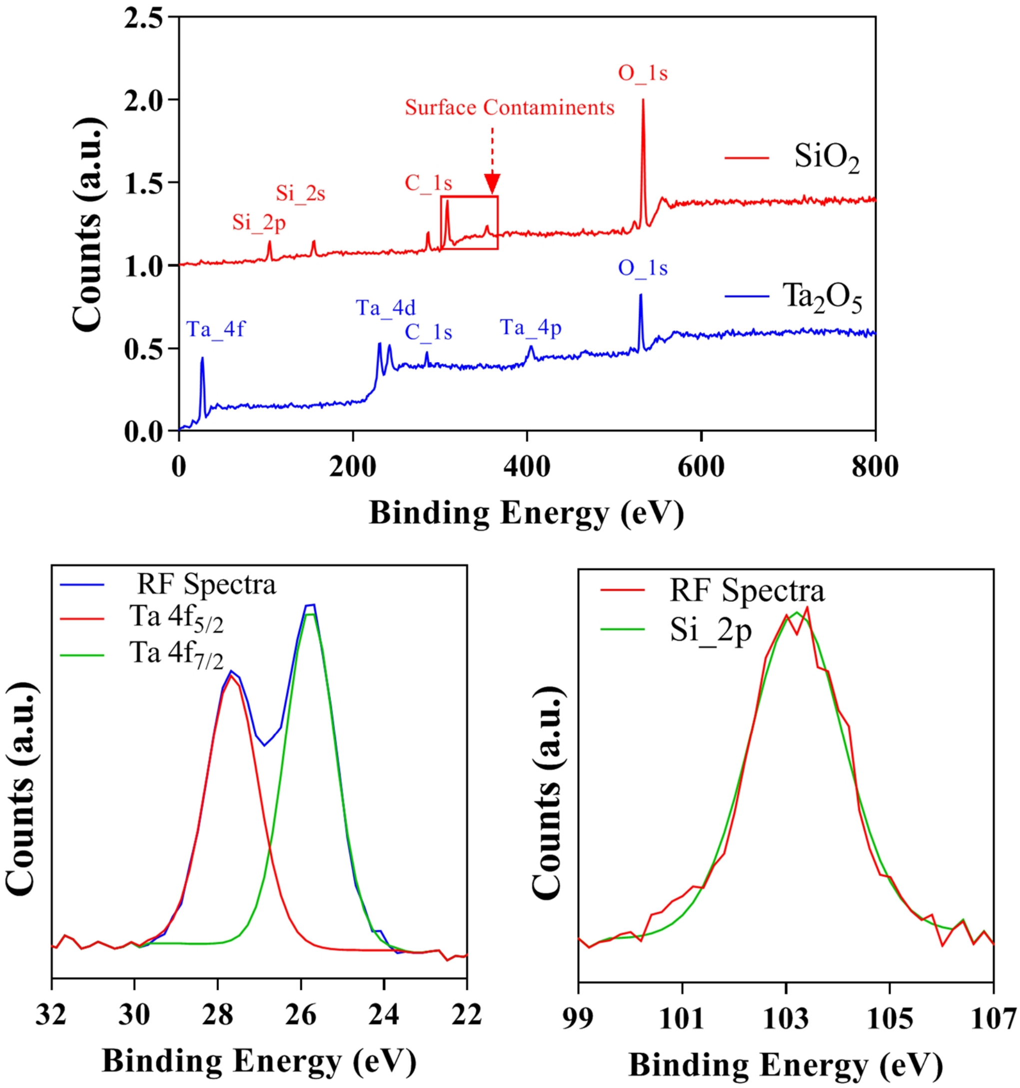

Figure 5.7: *XPS survey spectra for 8 h RF deposited SiO_2 and Ta_2O_5 films as deposited on Cu disk substrates. High resolution spectra for Ta_4f and Si_2p photoelectron emissions are fitted with constituent peaks depending on the spin and charge of the ejected electron.*

5.2 DC Material characterisation

Materials in the following section were deposited using DC deposition according to section (*4.1.2*), see ***Figure 5.8***. However, it is important to reiterate the naming system, where DC refers to films deposited via reactive DC sputtering and BDC refers to films deposited using the same method with an additional mixed RF Cu, DC Al interlayer. The number following the DC/ BDC nomenclature refers to the substrate bias used during deposition.

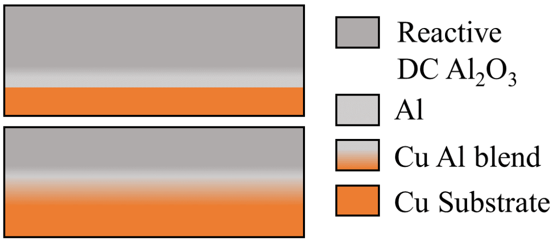

Figure 5.8: *DC (top) and BDC (bottom) layer configuration see experimental section for more details.*

5.2.1 FTIR

DC and BDC films showed Al-O bonding with longitudinal optical phonon vibrations (LO) between 800 and 950 cm^{-1}. Shifts between the peaks were seen and displayed in ***Figure 5.9.*** The Al-O peaks for DC and BDC films were comparable but those for BDC were lower in wavenumber than DC films deposited at the same bias voltage.

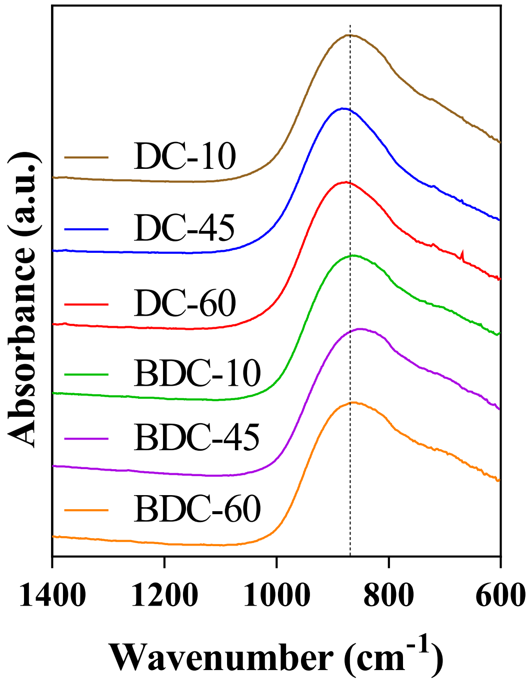

Film	*Al-O LO phonon peak (cm^{-1})*
DC-10	*867.9*
DC-45	*883.4*
DC-60	*875.7*
BDC-10	*865.0*
BDC-45	*849.6*
BDC-60	*862.2*

Figure 5.9: *FTIR spectra and peak positions for Al-O bonding in DC and BDC Al_2O_3 films as deposited onto Cu foil. Samples were deposited onto Copper foil to achieve sufficient ATR crystal contact.*

5.2.2 XRD

DC and BDC films were deposited onto borosilicate glass slides and were assessed by XRD. Diffraction results (***Figure 5.10***) showed no distinguishable peaks relating to crystalline alumina. Amorphous humps were present between 20 and 40 2θ° in the spectra. Four diffraction peaks at 38.3, 44.6, 65.0 and 78.4 2θ° were found to be associated with metallic aluminium ICDD-PDF-00-004-0787.

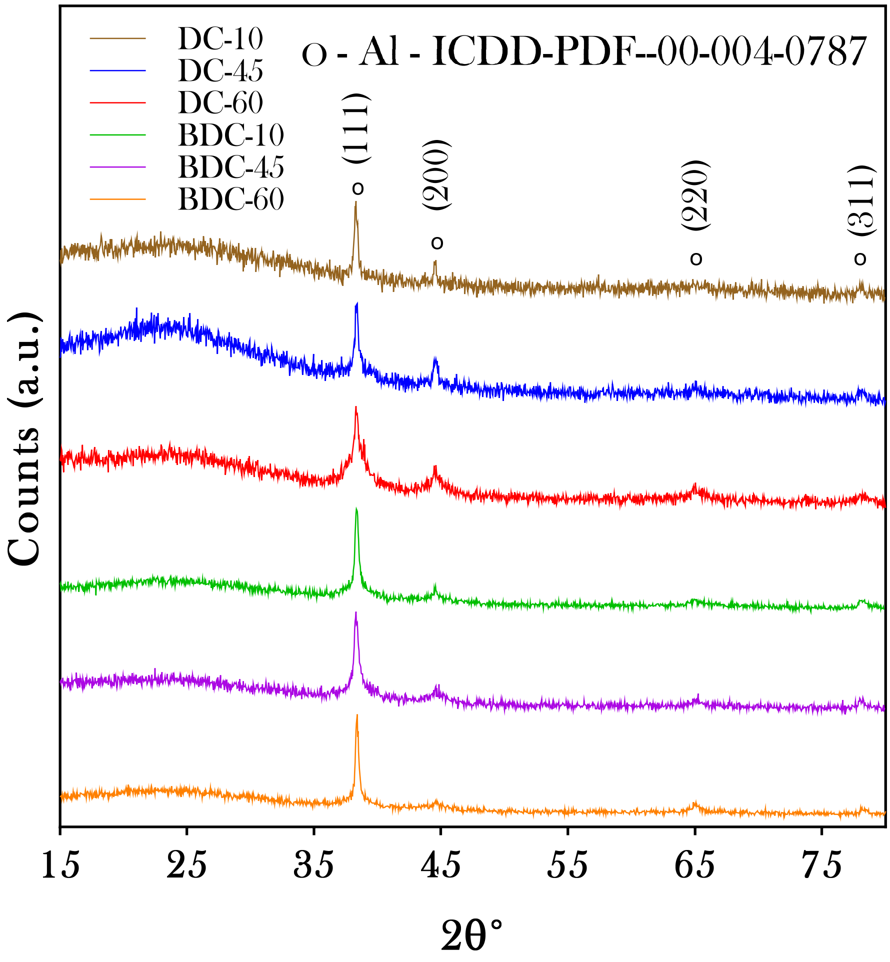

Figure 5.10: *XRD diffraction data for DC and BDC Alumina films. Diffraction peaks were attributed to the metallic Aluminium ICDD-PDF-00-004-0787 whilst the amorphous hump present between 20 and 40 2θ° was attributed to the combined structure of the film and glass substrate.*

5.2.3 XPS

As deposited surface compositions and structures of DC and BDC films on copper substrates were analysed by XPS. The Al_2P photoelectron emission was present in all high resolution spectra located between 74.18 and 74.85 eV and was attributed to Al^{3+} (Al_2O_3) [97]. DC and BDC sputtered films contained a distinct shoulder on the Al^{3+} Al_2P emission peak, at variable locations between 71.77 and 72.20 eV associated with Al^0/metallic aluminium, see ***Figure 5.11***.

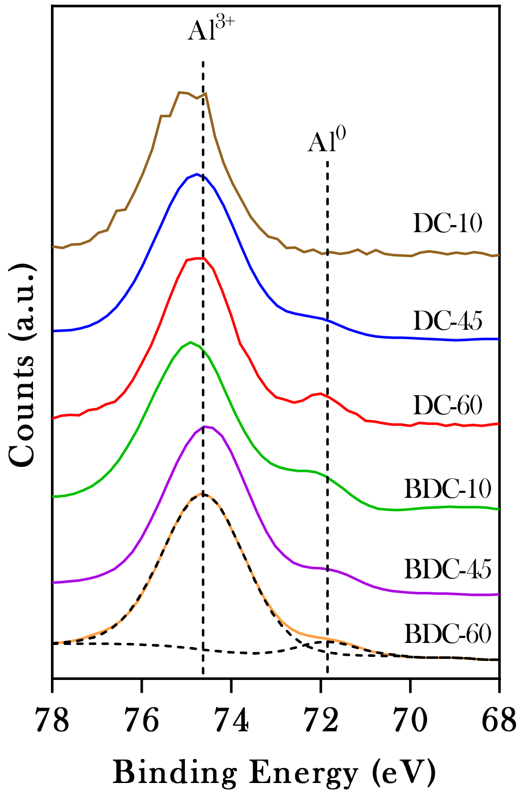

Figure 5.11*: XPS spectra containing DC and BDC alumina films as deposited onto Cu disks. Peak deconvolution for BDC-60 is also included to show the shoulder position, with the dashed black curves representing* Al^{3+} *and* Al^0*components as labelled.*

The percentage of Al^0 in DC and BDC films were found to vary from 0.8 to 16.6% following quantitative peak deconvolution. Additionally Al:O ratios were obtained from the survey spectra for all films and were found to vary from 0.37 and 0.67. An increase in the negative bias from -10 to -60 V for DC and BDC films resulted in improved Al:O ratios closer to the stoichiometric alumina ratio of 0.66 (***Table 5.2***).

Table 5.2: *Component positions and % concentration for the de-convoluted Al_2P photoelectron emmisions. Al:O ratios for deposited films were calculated from the O_1S and Al_2P relative peak areas in CASA XPS software. See* ***Figure 5.11*** *for the peak deconvolutions for Al_2P photo electron emission of DC, BDC and PDC films.*

Film	***Al:O Ratio***	***Al_2p/Al^{3+} Position (eV)***	***Al_2p/Al^{0} Position (eV)***	***Al^{0} (%)***
DC-10	*0.74*	*74.99*	*71.77*	*1.88 ± 0.03*
DC-45	*0.51*	*74.75*	*72.10*	*5.48 ± 0.04*
DC-60	*0.66*	*74.73*	*71.98*	*19.5 ± 0.10*
BDC-10	*0.37*	*74.85*	*72.20*	*13.4 ± 0.28*
BDC-45	*0.56*	*74.53*	*71.77*	*7.81 ± 0.07*
BDC-60	*0.62*	*74.60*	*71.84*	*5.79 ± 0.06*

5.2.4 Film structure and topographical features

5.2.4.1 SEM

The thickness of DC and BDC films varied with bias voltage and interlayer configuration, yielding average deposition rates of 1.1 and 1.2 μmh^{-1} for DC and BDC films respectively. No structure was seen in SEM cross sectional imaging colluding with the XRD data. See ***Figure 5.12*** for cross sections and thickness measurements. Interlayers were seen more clearly in DC samples also indicated in ***Figure 5.12*** and no discrete layers were seen for Cu and Al in BDC films. Analysis of the interlayers shows a preferential growth of the aluminium interlayer in the direction perpendicular to the substrate. The metallic layers also showed some signs of columnar growth motif with a thickness of *ca.* 200 nm.

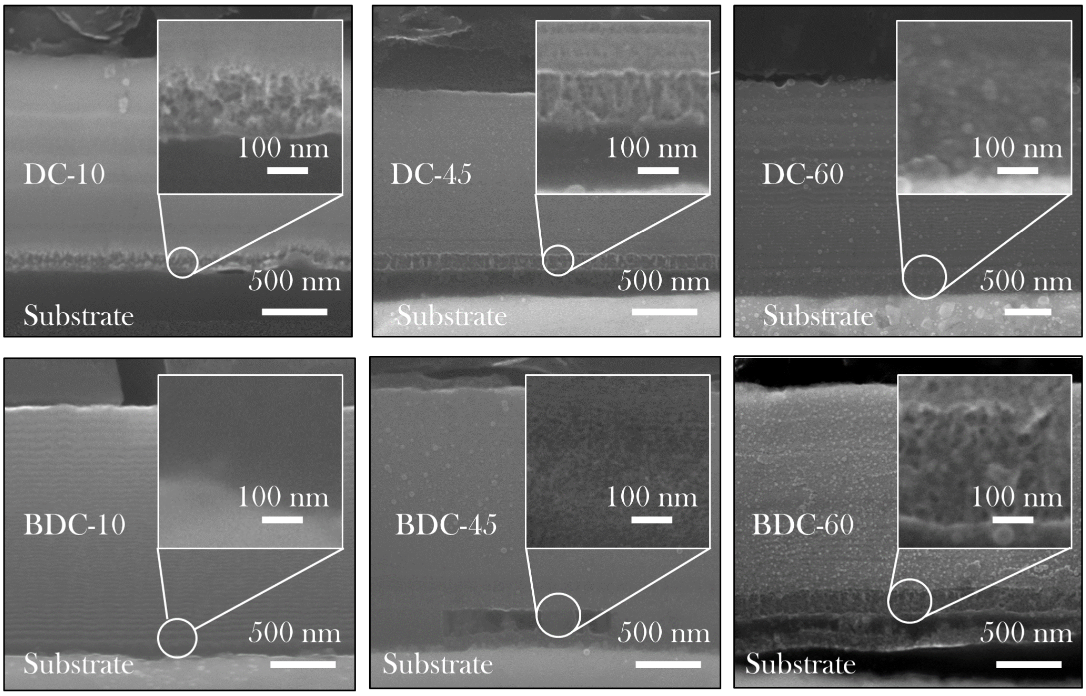

Sample	***Thickness (nm)***
DC-10	*1566 ± 27*
DC-45	*1326 ± 6*
DC-60	*2095 ± 10*
BDC-10	*1755 ± 12*
BDC-45	*1854 ± 13*
BDC-60	*1868 ± 13*

Figure 5.12: *Thickness of Al_2O_3 films determined using SEM micrographs of sputtered alumina films, as deposited onto copper substrates and mounted in conductive resin to obtain a cross section. High resolution images of the interlayer section have been inset in the top right of each image.*

5.2.4.2 TEM

TEM analysis of a BDC-60 sample displayed in ***Figure 5.13*** showed the DC films contained materials with short range order with a diameter in the order of 10 nm. The films also contained striated layers with varying oxygen content as seen in the EDX analysis.

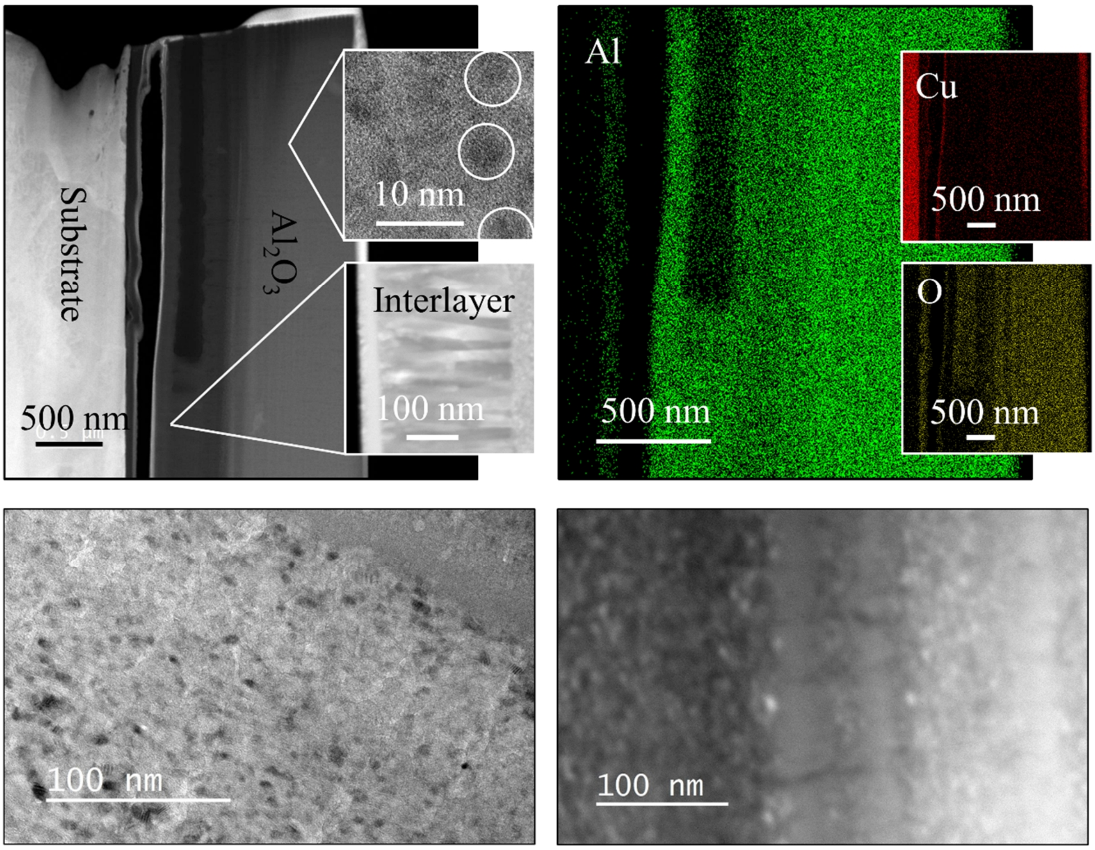

Figure 5.13: *(top row) TEM analysis of BDC films showing layer configuration and short range order (circled) and finally EDX mapping for Al, Cu and O. (bottom row) TEM micrographs displaying short range order and cracking seen in the films respectively. Striations running through the material can be seen in the EDX analysis as well as the micrographs on the bottom row.*

Film deposition led to an increase in surface roughness when compared to the uncoated polished copper substrates which had an average roughness of Ra 5.6 ± 1.1 nm the addition of the PVD film increased roughness each time with the bias and deposition procedure having little effect.

5.2.5 Dielectric strength and leakage current

The following section will display the results of probe based and AFM DB measurements of the dielectric strength of the DC and BDC films.

5.2.5.1 Probe based methods

The breakdown strength of each film was determined to be at the point at which the leakage current abruptly increased. DC and BDC films showed very substantial increases in current leakage density during the voltage ramp from 5 to 10 V. In every case for the DC and BDC films current leakage was above 10 nAcm^{-2} even at an applied voltage of 5 V, which relates to a different field strength depending on film thickness. Dielectric strength values are given in ***Table 5.3***, the standard error associated with the voltage measurements has also been included.

Table 5.3: *Breakdown strength and dielectric strength of DC and BDC films as deposited onto 5 mm Cu disks and measured using the in house probe based methods.*

Sample	***Thickness (nm)***	***Breakdown AVG. (V)***	***Dielectric Strength (Vµm^{-1})***
DC-10	*778 ± 34*	*93.3 ± 44*	*120 ± 57*
DC-45	*557 ± 47*	*212 ± 44*	*366 ± 82*
DC-60	*637 ± 31*	*48.3 ± 9.3*	*23.1 ± 4.6*
BDC-10	*721 ± 16*	*100 ± 19*	*139 ± 27*
BDC-45	*633 ± 40*	*167 ± 25*	*263 ± 43*
BDC60	*835 ± 30*	*88.0 ± 22*	*47.1 ± 12*

It can be seen from the breakdown voltage and the current leakage graphs below that the measurements had a large degree of inconsistency within samples (note the logarithmic scale on the x axis in ***Figure 5.14***) as well as differences in the current leakage profile. Meaning an analysis of the conduction mechanism was unfeasible.

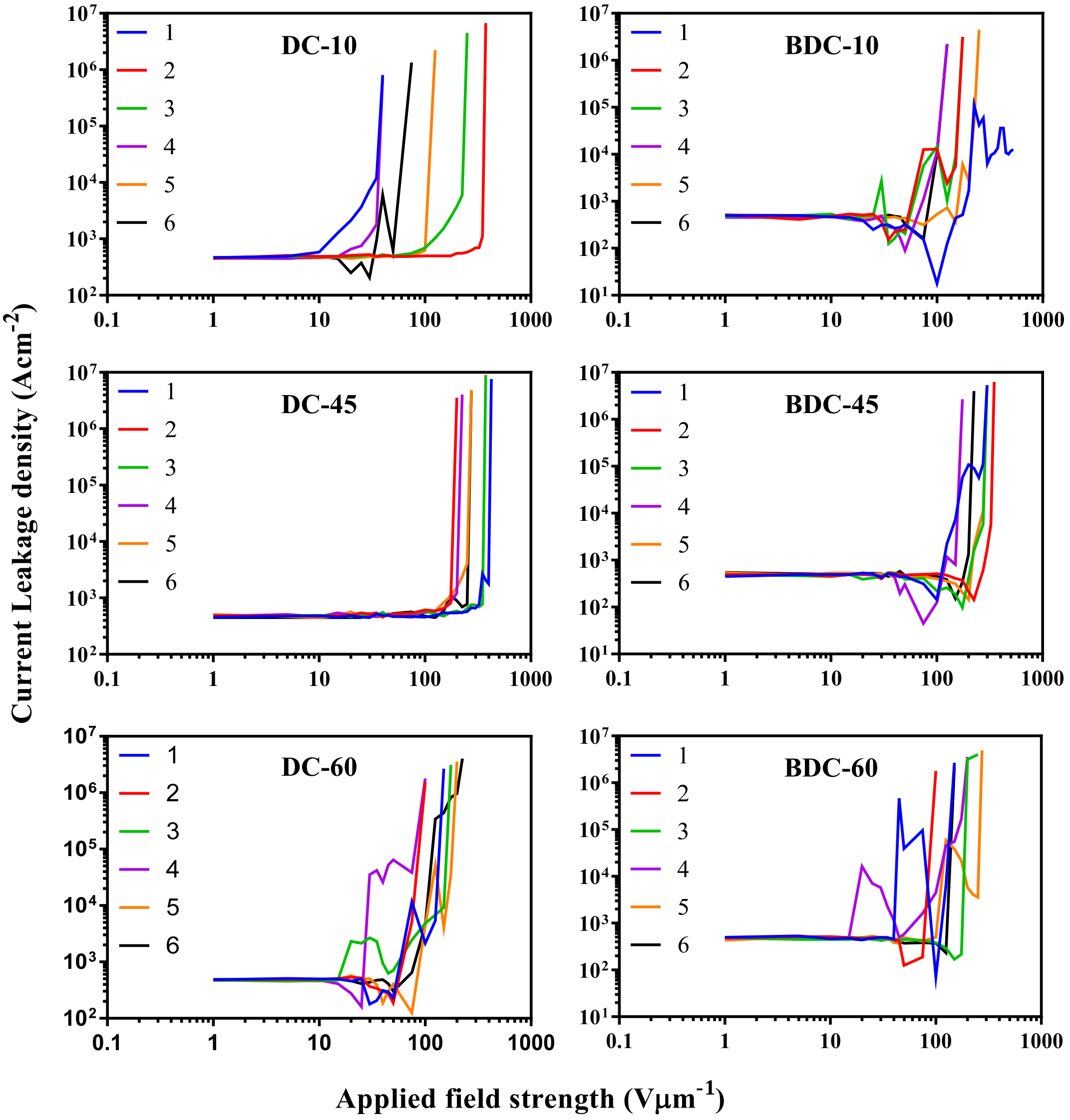

Figure 5.14: *Applied voltage plotted against leakage current density for DC and BDC films as deposited on Cu substrate and tested using the in house breakdown testing equipment.*

5.2.5.2 AFM DB measurements

Films deposited for 12.5 min had breakdown voltages assessed using AFM DB methods, the shorter sputtering time was used in order to produce films which broke down before the end of the 150 V voltage ramp.

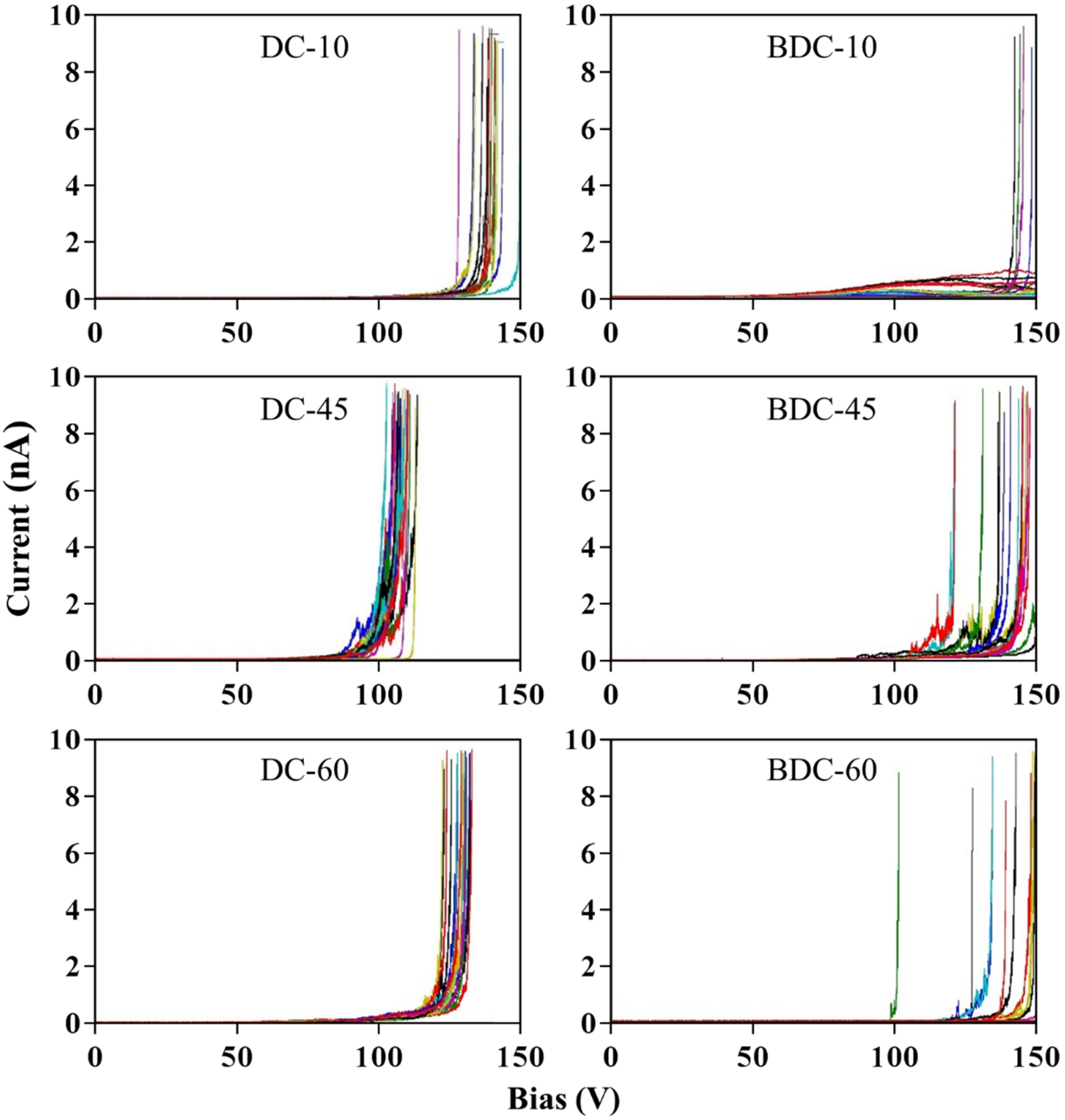

***Figure 5.15** AFM electrical breakdown of films deposited for 12.5 min, DC films deposited with a bias voltage of -10, -45 and -60 V (left) and BDC films deposited with a bias voltage of -10, 45 and -60 V (right). Current voltage measurements for this data were carried out using AFM DB methods on a 30x30 µm array.*

The average breakdown across all applied biases was found to be lower for films deposited without the mixed material interlayer. It was also noted that for DC samples all 16 tests resulted in the breakdown of electrical properties. For the BDC films a varying number of film failures occurred between 4 and 14 further details are displayed in ***Table 5.4 and Figure 5.15***. However whilst the complete breakdown and average breakdown voltage was higher for the BDC films higher initial leakage was seen in these materials, with oscillations prior to breakdown seen in all sets of films. There was no significant difference in breakdown voltage when varying the bias conditions.

Table 5.4: *AFM DB summary where N is the number of tests out of 16 which broke down below the 150 V limit of the power supply. Dielectric strength calculated from breakdown voltage (V) and thickness.*

Sample	***Thickness (nm)***	***Breakdown AVG. (V)***	***N***	***Dielectric Strength (Vμm^{-1})***
DC-10	*778 ± 34*	*128 ± 5*	*16*	*166 ± 9*
DC-45	*557 ± 47*	*108 ± 3*	*16*	*195 ± 17*
DC-60	*637 ± 31*	*128 ± 3*	*16*	*201 ± 11*
BDC-10	*721 ± 16*	*145 ± 3*	*4*	*202 ± 6*
BDC-45	*633 ± 40*	*139 ± 9*	*14*	*221 ± 20*
BDC-60	*835 ± 30*	*137 ± 15*	*10*	*165 ± 19*

The dielectric strength values as calculated were shown to be higher than when measured with the probe based methods as well as having lower standard error and lower variation between samples, see ***Figure 5.16*** for breakdown voltage comparison.

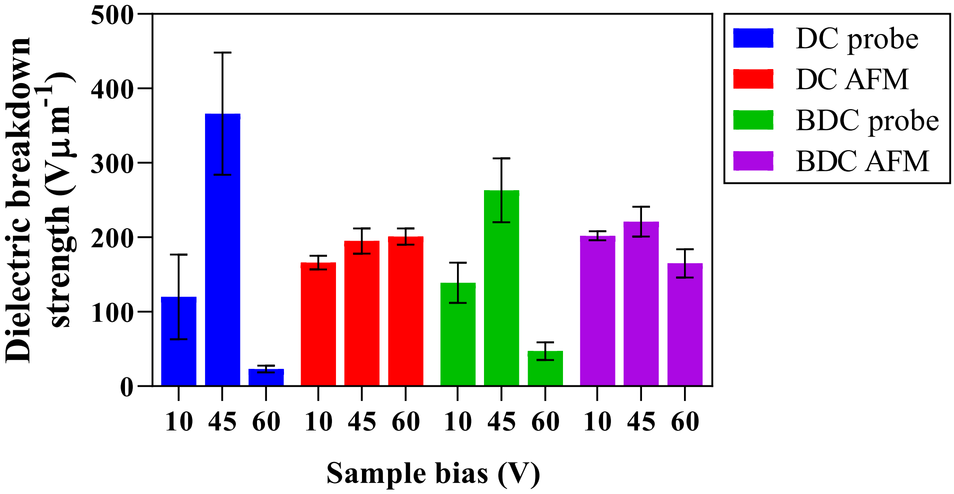

Figure 5.16: *summary of the dielectric breakdown strength values obtained for DC and BDC films measured using in house probe based methods and AFM DB methods with respect to the substrate bias.*

5.2.5.3 Determination of conduction mechanism

The conduction mechanism in these films was determined with further current voltage curve analysis. SE, PF and FN analysis were carried out on the films in order to confirm or rule them out as possible conduction mechanisms. It was determined for DC and BDC-60 films that Fowler-Nordheim tunnelling potentially acted as the conduction mechanism at high fields, containing multiple tunnelling barriers indicated by multiple linear regions see ***Figure 5.17***. At low fields it wasn't possible to determine a mechanism due to high variance in the measured current at low fields.

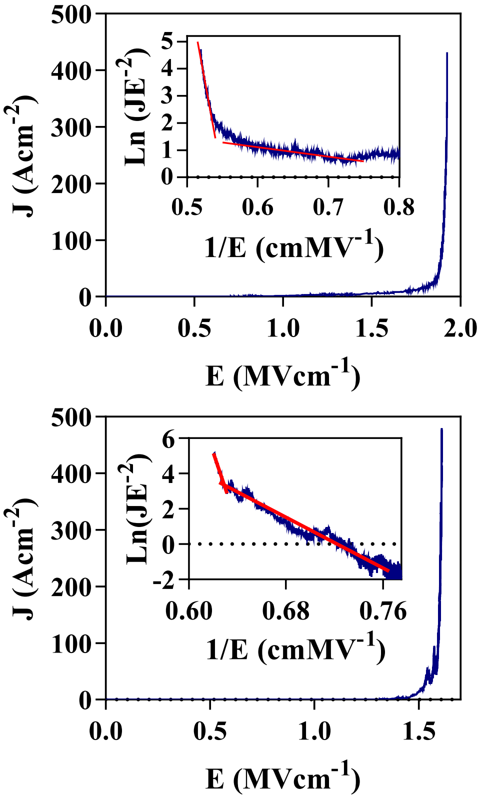

Figure 5.17: *Current leakage plotted against applied field for DC and BDC films as deposited for 12.5 min onto Cu disks. Inset are Fowler-Nordheim plots with multiple linear regions highlighted in each case (indicating multiple tunnelling barriers).*

5.2.6 Mechanical properties

Coating substrate adhesion was assessed for all coatings deposited onto copper for 90 min using pull off testing and scratch testing, the loads at which complete adhesive failure occurred in these films was found to vary substantially with the inclusion of a mixed material interlayer and the use of a pulsed power option, as shown in section (6.5).

5.2.6.1 AFM

Topographical analysis using AFM showed surface artefacts in all films, with the largest seen to be in the magnitude of 1000 nm. AFM also showed the presence of pores in the structure with some penetrating deeply into the coatings (***Figure 5.18***). Pores were not common, only being found in BDC-60 and BDC-45 samples and were typically > 1000 nm wide. It is also important to note that the defects on the surface could also be introduced during measurement.

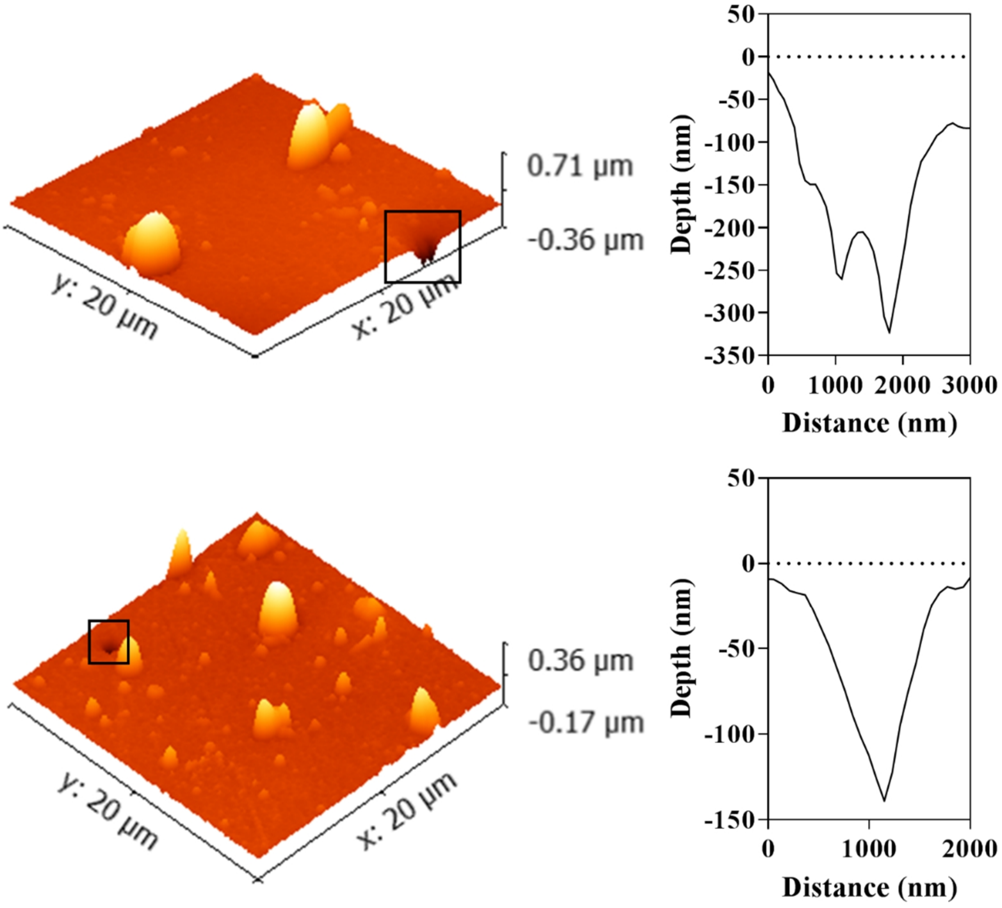

Figure 5.18: *Pores found in BDC-45 and BDC-60 films with 3D view and graphical pore profile. Pore profiles were generated for the area within the black squares using the Gwyddion AFM analysis package.*

Surface roughness (Ra) values varied between 5.6 and 38.2 nm for DC-60 and DC-45 respectively. Generally higher roughness was seen for BDC films as seen in ***Table 5.5***.

Table 5.5: *Average AFM surface roughness Ra (nm) for DC and BDC alumina films as deposited onto CU disk, as averaged from five 400 μm^2 scans with standard error values included (nm).*

Sample	***Average Ra (nm)***	***Error (nm)***	***Sample***	***Average Ra (nm)***	***Error (nm)***
DC-10	*20.8*	*± 2.9*	***BDC-10***	*17.7*	*± 4.2*
DC-45	*38.2*	*± 7.0*	***BDC-45***	*30.7*	*± 7.9*
DC-60	*5.6*	*± 5.7*	***BDC-60***	*30.6*	*± 11.2*

5.2.6.2 Pull off adhesion testing

Pull off failures consisted of a mixture between complete and partial interfacial delamination and failures within the adhesive layer. With adhesive failures occurring between the adhesive and film surface and within the epoxy layer see ***Figure 5.19***

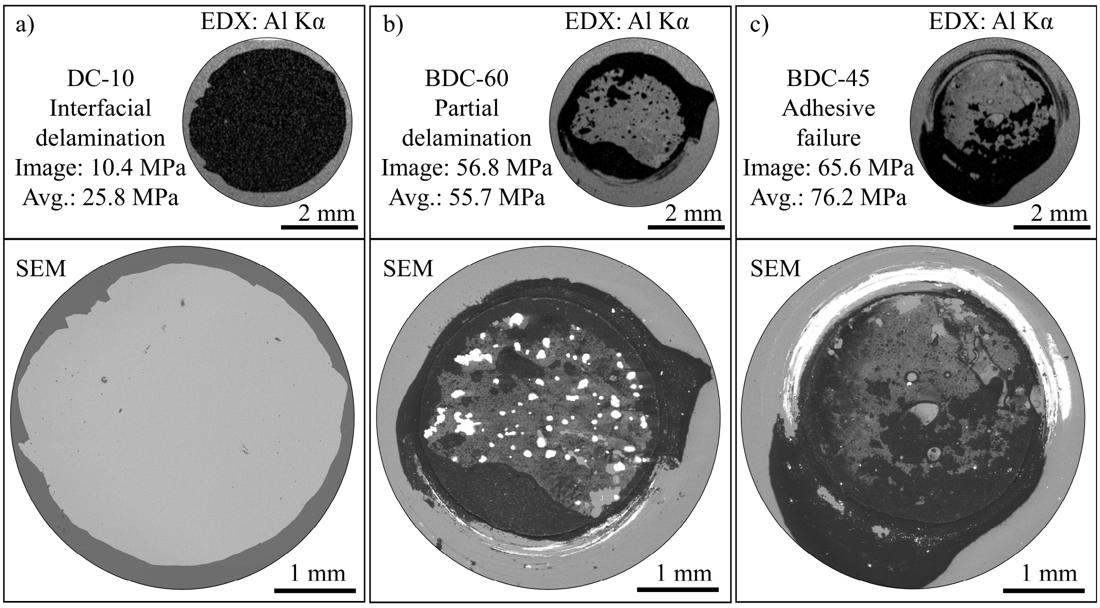

Sample	***Average failure strength (MPa)***	***Complete interfacial failure***	***Partial interfacial failure***	***Failure in adhesive***
DC-10	*25.8 ± 9.8*	*3*	*5*	*0*
DC-45	*64.3 ± 6.4*	*0*	*8*	*0*
DC-60	*63.0 ± 6.4*	*0*	*8*	*0*
BDC-10	*73.0 ± 3.6*	*0*	*6*	*2*
BDC-45	*76.2 ± 3.3*	*0*	*6*	*2*
BDC-60	*72.3 ± 5.6*	*5*	*2*	*1*

Figure 5.19: *Failure modes in pull off adhesion tests a) DC-10 interfacial delamination b) BDC-60 partial film delamination c) BDC-45 failure in adhesive. The remaining Al appears light in the EDX maps. Average adhesive failure values are given in the table below with standard error as well as a summary of failure modes from each sample.*

Pull off adhesion testing showed that the range of film/substrate adhesive failure for alumina films deposited onto copper via reactive DC magnetron sputtering was above 25.8 MPa, the upper limit was not determined due to cohesive failure within the epoxy before film failure occurring at *ca.* 75 MPa. The mechanisms behind this failure included complete adhesive failure and complete cohesive failure. BDC films showed failure strengths between 72.3 and 76.2 MPa showing an improvement with respect to DC samples produced at -10 V bias. Failure of BDC films was a mixture between partial interfacial delamination and failure in the adhesive, with samples produced at -60 V bias also showing complete interfacial delamination.

5.2.6.3 Scratch testing

In the cases of DC films the decrease in substrate bias to -60 V increased the force required to initiate cohesive and adhesive failure compared to films deposited with - 10 and -45 V substrate biases. Cohesive failure occurred in the form of a combination of arc tensile and chevron cracking between 0.58 and 1.6 N critical loads. Adhesive failures of the same films generally consisted of buckling spallation occurring between 1.21 and 2.14 N, with maximum observed at -60 V bias (***Figure 5.20***).

Cohesive failures in the form of chevron and arc tensile combination cracking, were noted to occur at lower critical load in BDC samples between 0.35 and 0.52 N increasing with applied bias. The onset of adhesive failure was higher in BDC samples occurring between 2.25 and 4.38 N. Both maximum values were achieved at -60 V substrate bias. The critical load for adhesive failure in BDC films was higher than for DC films deposited at comparative substrate bias, however, the critical loads for cohesive failure were higher in DC films.

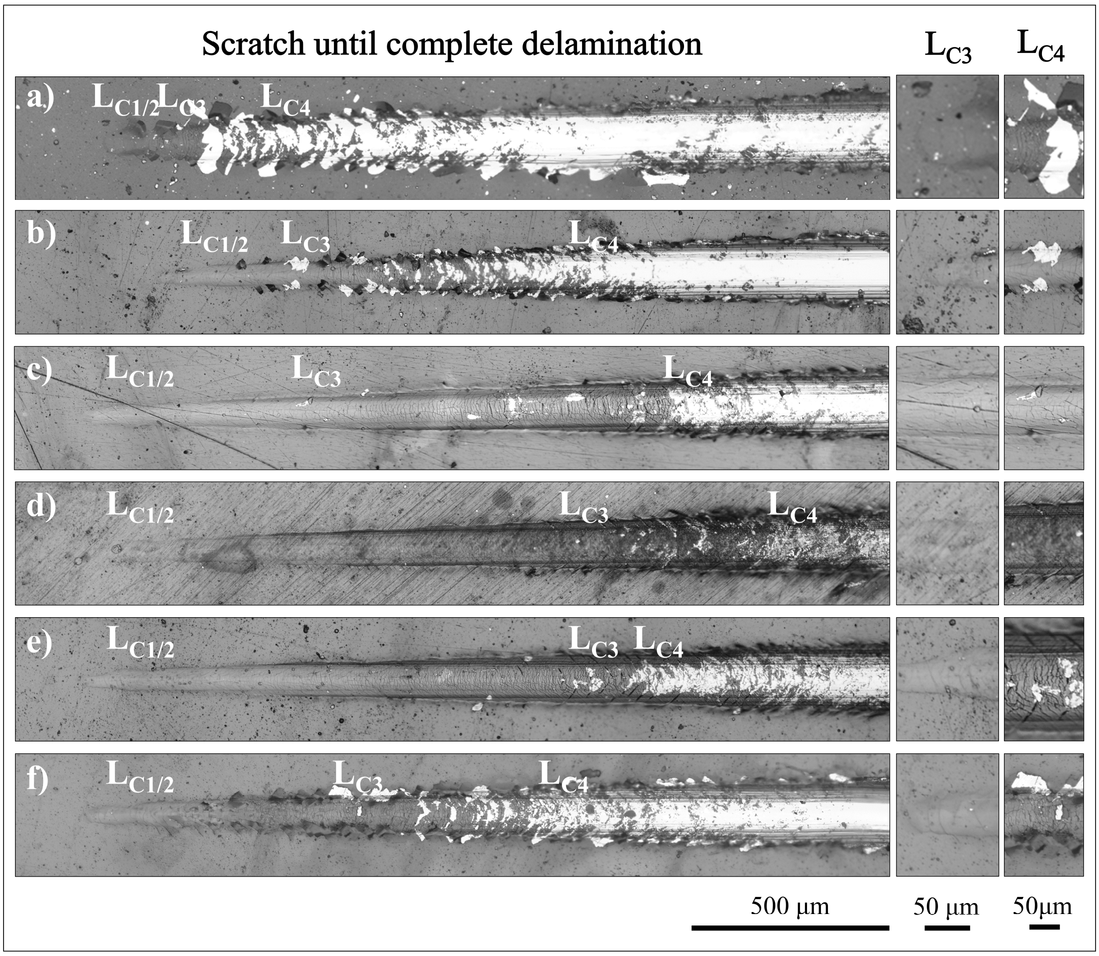

Sample	*Cohesive scratch failure*		*Adhesive scratch failure*	
	(N)	***Mechanism***	***(N)***	***Mechanism***
a) DC-10	*0.80 ± 0.04*	*Combination*	*1.74 ± 0.25*	*Buckling*
b) DC-45	*0.58 ± 0.53*	*Combination*	*1.21 ± 0.08*	*Buckling*
c) DC-60	*1.60 ± 0.10*	*Combination*	*2.14 ± 0.18*	*Buckling*
d) BDC-10	*0.40 ± 0.08*	*Combination*	*2.59 ± 0.24*	*Buckling*
e) BDC-45	*0.35 ± 0.03*	*Combination*	*2.25 ± 0.24*	*Buckling*
f) BDC-60	*0.52 ± 0.03*	*Combination*	*4.38 ± 0.07*	*Buckling*

Figure 5.20 *Scratch test failure modes and adhesion for DC films produced at a)-10 b)-45 and c) -60 V substrate bias and BDC films produced at d) -10, e)-45 and f) -60 V substrate bias.* L_{c1+2} *indicates chevron, arc tensile and combination cracking,* L_{c3} *indicates the onset of adhesive failure through buckling and* L_{c4} *onset of complete film delamination.*

Graphical representation of the adhesion results presented for DC and BDC films has been included in ***Figure 5.21***

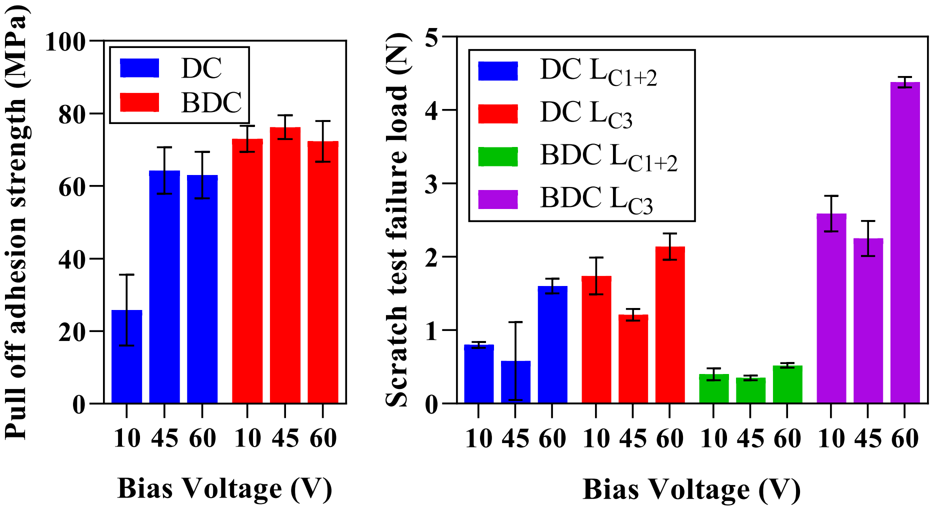

Figure 5.21: *Summary bar charts of pull off adhesion and scratch test failure loads for DC and BDC films deposited under varying sample bias conditions as indicated.*

5.3 Time dependant study on DC deposited films

DC films deposited onto Cu disks with differing deposition times (30, 60 and 120min, DC3, DC6 and DC12 respectively) were all produced with a substrate bias of -60 V. The main reason for the analysis of films deposited at different thicknesses was to assess the effect on the mechanical properties of the film.

5.3.1 Structural characterisation

5.3.1.1 FTIR

FTIR studies of these films showed the characteristic LO phonon vibration peak allocated to Al-O. Shifting in the peaks was seen between the samples. The sample deposited for 30 min had the highest wavenumber with 914 cm^{-1} and samples deposited for 120 min had the lowest at 843 cm^{-1} as seen in ***Figure 5.22***.

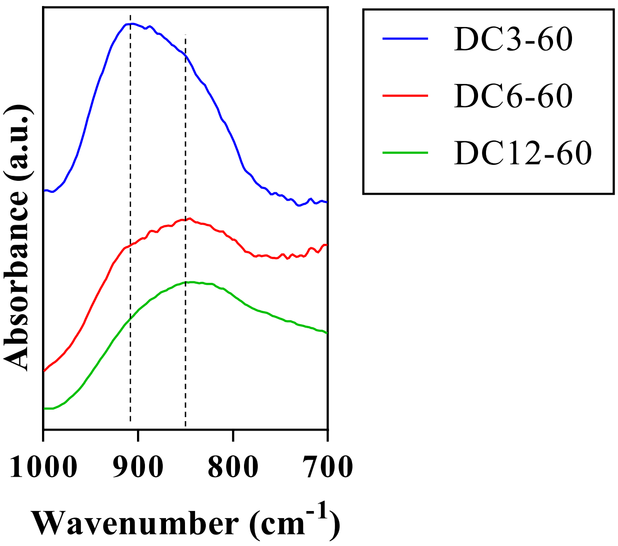

Figure 5.22: *FTIR spectra for Al_2O_3 films deposited onto Cu disks for sequentially longer periods of time all with -60 V bias, the peak positions have been indicated with dashed lines..*

5.3.1.2 XRD

XRD analysis showed that deposition time didn't affect the crystallinity of the deposited films, with all exhibiting X-ray amorphous diffraction patterns as seen in ***Figure 5.23***. With peaks relating to the deposited Al interlayer.

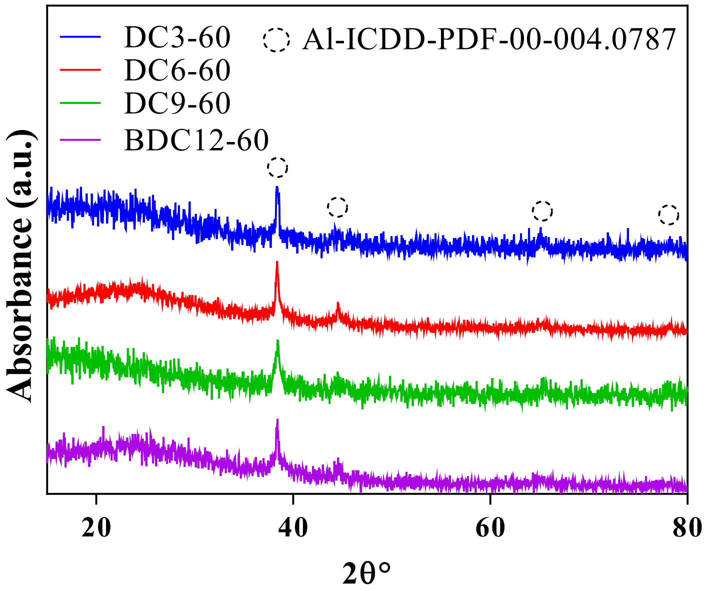

Figure 5.23: *XRD diffraction patterns for films deposited with varying time to produce films of different thickness. Diffraction peaks were attributed to metallic Aluminium (ICDD-PDF-00-004-0787) whilst the amorphous hump present between 20 and 40 2θ° was attributed to the combined structure of the film and glass substrate.*

5.3.1.3 SEM

Films thickness was determined by SEM analysis which also showed the amorphous nature of the films. In DC12-60, however, some through thickness defects were found in the forms of pits. As seen in ***Figure 5.24 d)*** the through thickness defects could be detrimental to mechanical and electrical properties. The micrographs also show a decrease in deposition rate with an increase in sputtering time (from 1520 to 1000 nm h^{-1}) as in ***Figure 5.24***.

Sample	***Thickness (nm)***	***Dep. Rate (nmh^{-1})***
DC3-60	*760 ± 10*	*1520*
DC6-60	*1150 ± 45*	*1150*
DC12-60	*2030 ± 25*	*1000*

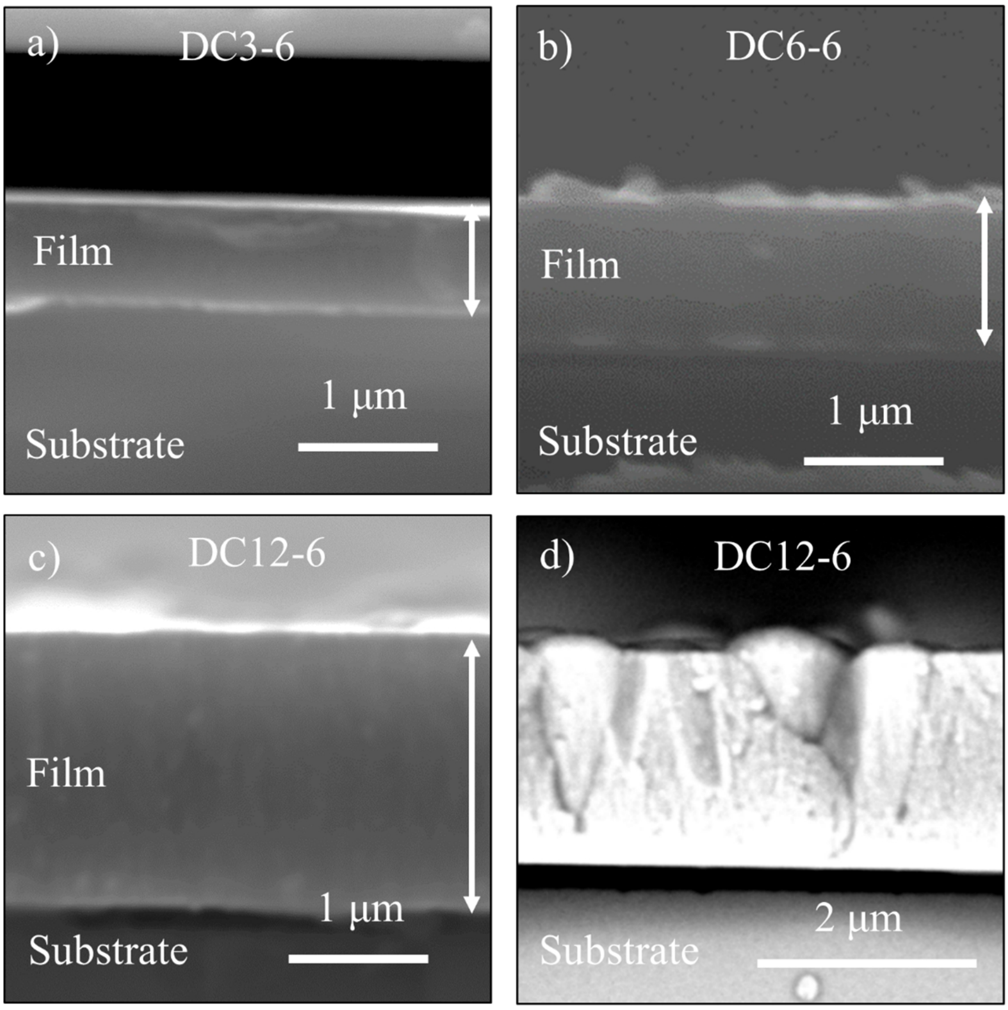

Figure 5.24: *Table of average thickness values for DC films as deposited onto borosilicate glass slides (above). Cross sectional SEM (Backscattered electron) micrographs of DC films deposited onto borosilicate cover slips for different time scales below (Below). d) Shows secondary electron image included to show pinholes which were located in DC12-6 samples (bottom right).*

5.3.1.4 XPS

XPS showed Al_2P peaks confirming the presence of Al^{3+}. Peaks also confirmed the presence of elemental aluminium, with the shoulder at a lower binding energy correlating to the binding energy of Al see ***Figure 5.25 and Table 5.6***.

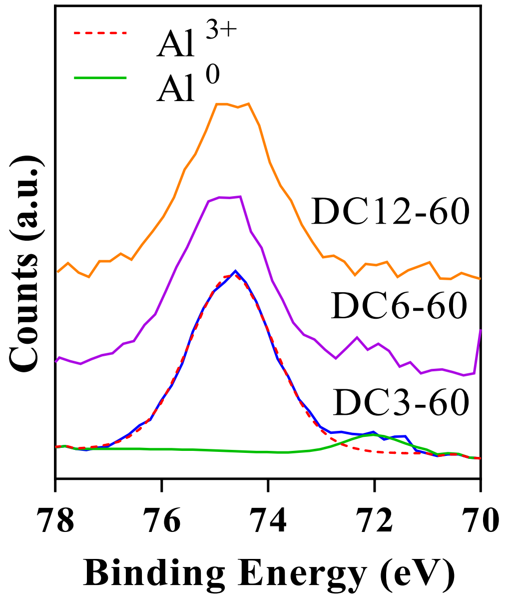

Figure 5.25: *XPS Spectra for Al_2P electrons in DC deposited alumina films on Cu disks. Deconvolution is used to indicate the position of the* Al^0 *shoulder at ca. 72 eV. Note that for the deconvolution shown for DC3-60 the dotted line represents* Al^{3+} *and the solid green line represents* Al^0*.*

The Al_2P peaks were found at 74.72 ± 0.04 eV with elemental aluminium shoulder at 71.92 eV shifting an average of 2.36 eV. The material compositions were shown to be relatively consistent between 0.48 and 0.52, with elemental Al ratios between 3.6 and 7.0 % concentration.

Table 5.6: *XPS peak positions and Al:O ratios for reactively sputtered DC alumina films deposited for different lengths of time (as indicated in the sample name) onto Cu disks.*

Film	***Al:O Ratio***	***Al 2p/*** Al^{3+} ***Position (eV)***	***Al 2p/*** Al^0 ***Position (eV)***	Al^0 ***(%)***
DC3-60	*0.48*	*74.67*	*72.02*	*7.67 ± 0.08*
DC6-60	*0.52*	*74.83*	*72.12*	*5.21 ± 0.07*
DC12-60	*0.50*	*74.67*	*71.61*	*1.01 ± 0.02*

5.3.1.5 Mechanical properties

The mechanical properties of the films were then assessed to facilitate discussion about the effect of thickness on the adhesive properties. Which could be used as an aid for the selection of a coating to use on other geometries.

5.3.1.5.1 AFM

AFM surface measurements were used to determine roughness as well as identify any pores and defects in the films. No pores were found in these films, however this may just be a result of the areas picked for roughness measurements. Roughness (Ra) values were found to be between 10 and 25.6 nm, as seen in ***Table 5.7***.

Table 5.7: *Average AFM surface roughness summary for time dependant DC films as deposited onto Cu disks.*

Sample	***Average roughness (Ra) (nm)***	***Error (nm)***
A3-6	*10.0*	*0.9*
A6-6	*25.6*	*8.7*
A12-6	*10.4*	*2.2*

5.3.1.5.2 Direct pull off method

Pull off studies reviled that the adhesion strength was lowest with 120 min deposited samples. Samples deposited for 60 and 120 min failed with almost exclusively complete interfacial delamination.

Table 5.8: *Direct pull off stub adhesion failure strength (MPa) and failure modes for time dependant DC films.*

Sample	***Average failure strength (MPa)***	***Complete interfacial failure***	***Partial interfacial failure***	***Failure in adhesive***
DC3-6	*51.4 ± 5.4*	*0*	*8*	*0*
DC6-6	*32.4 ± 4.8*	*5*	*1*	*0*
DC12-6	*26.5 ± 2.5*	*6*	*2*	*0*

None of the DC samples in this section failed through adhesive failure in the glue layer see ***Table 5.8***. The average failure strength decreased with increasing film deposition time and therefore thickness (see ***Figure 5.24***) from a maximum of 51.4 to 26.5 MPa. As well as this the failure mode changed from predominantly partial interfacial failure to complete interfacial failure with longer deposition time, seen in ***Figure 5.26***.

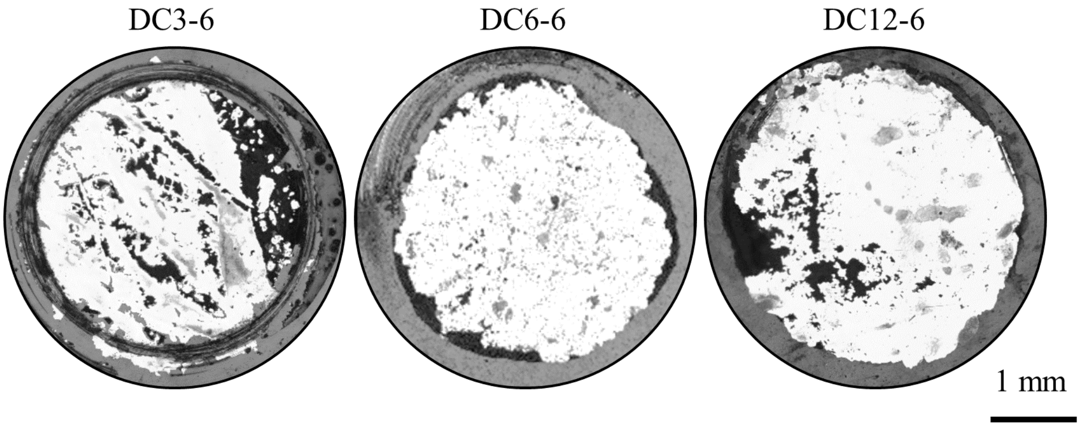

Figure 5.26: *Light microscope images of pull off adhesion failure sites for time dependant alumina films. The most common failure modes were partial interfacial delamination as seen for DC3-60 and complete interfacial failure for DC6-60 and DC12-60.*

5.3.1.5.3 Scratch testing

Scratch testing showed a decrease in both L_{C1+2} and L_{C3} with an increase in deposition time as seen in ***Figure 5.27***. It is shown through DC12-60 that there is a critical thickness value for films deposited at -60 V bias which results in a significant decrease in mechanical properties which is accompanied by a change in adhesive failure mechanism to trackside spallation, with a greater area of delaminated coating.

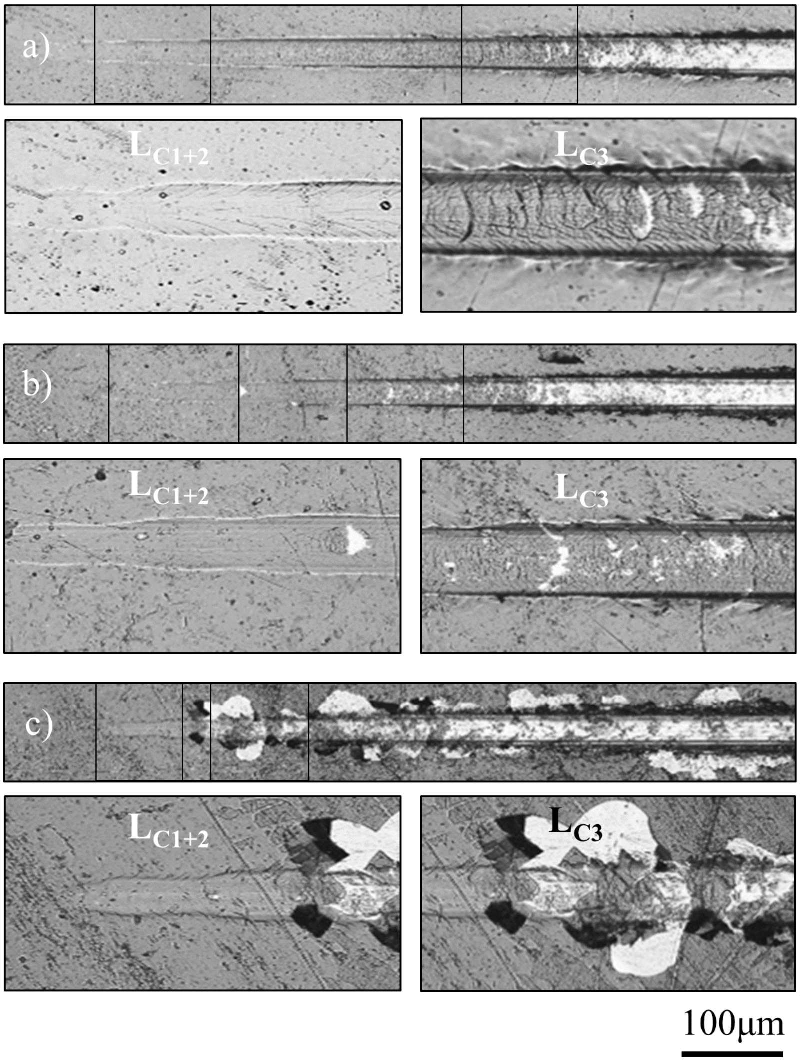

Sample	Cohesive scratch failure		Adhesive scratch failure	
	(N)	Mechanism	(N)	Mechanism
DC3-6	1.45 ± 0.6	Combination	5.04 ± 0.4	Buckling
DC6-6	0.78 ± 0.1	Combination	2.20 ± 0.2	Buckling
DC12-6	0.66 ± 0.1	Combination	1.33 ± 0.1	Trackside spallation

Figure 5.27: *scratch testing carried out on time dependent coatings as deposited onto Cu disks (descending 30 min, 60 min and 120 min) note extensive buckling delamination on D12-60 sample.* L_{C1+2} *and* L_{C3} *failures have been indicated in each case with the attributed mechanism given in the subsequent table.*

5.4 Summary

RF films were generally featureless but were deposited extremely slowly with deposition rates as low as 16 nmh^{-1}. It is exclusively this low deposition rate which limits the application of RF sputtered films on their own. However, the high quality of the RF films could be utilised in a composite structure, with reports in literature showing their high dielectric strength up to 600 $V\mu m^{-1}$ [121].

The most important link between the deposition technique and results observed in this section is the detrimental effect of arcing on the composition and structure of the reactively sputtered DC films. TEM (***Figure 5.13***) was crucial for imaging defects in the films which were reasoned to result in the premature dielectric breakdown and charge trapping and de trapping in the alumina films. This conclusion is key in progressing to depositing materials with increased breakdown strength above 250 $V\mu m^{-1}$ by removing defects capable of creating conductive pathways.

The mechanical properties of the DC films were also studied and showed the potential for mixed material interlayers to increase pull off adhesion up to 76.2 ± 3.3 MPa and adhesive scratch failure up to 4.38 ± 0.07, through improved material mixing at the interfaces. It is also important to note at this point that increasing the deposition time to 120 min was found to decrease the mechanical properties which is likely a result of increased internal stress due to increased film thickness.

6 Results: PDC deposited films

As eluded to at the start of the previous section PDC deposition needs to be explored as a route to producing insulating coatings with a breakdown strength above that of the DC and BDC films. In order to achieve this PDC has a number of key parameters which need to be optimised such as the duty cycle and pulse frequency. Thus this chapter will look at the development of PDC alumina as a low cost, easily produced base material to be incorporated into composite materials in order to improve dielectric properties through structural and compositional improvement, whilst also relating these improvements to the applied pulse parameters.

6.1 Duty cycle and frequency optimisation

The following section will focus primarily on the modification of pulsing frequency and duty cycle of the pulsed power supply, in order to determine the most suitable deposition parameters. The frequency of the pulse determines how often the voltage will be reversed and the duty cycle determines how long the reverse pulse lasts, so these are key parameters to consider for film quality. The characterisation of these films is presented below.

6.1.1 Structural analysis

6.1.1.1 FTIR

FTIR analysis confirmed Al-O binding with LO phonon peaks at an average of 856.4 and 803.4 cm^{-1} for samples deposited at 20-22.5% and 40% duty cycle respectively. This is indicative of a shift between samples deposited with a duty cycle of 20-24 or 40%, with higher wave numbers mainly seen for films deposited at the higher duty cycle of 40%, films deposited at 50 and 201 kHz with a 40 % duty cycle also having a noticeably less broad peak. See ***Table 6.1 and Figure 6.1*** for FTIR peak position and spectra.

***Table 6.1:** FTIR peak positions for pulsed DC alumina films as deposited onto Cu foil with varying pulse frequency and duty cycle (as designated in the film column).*

Film	*Al-O LO phonon peak (cm^{-1})*
50 kHz 24.0%	*846.7*
50 kHz 40.0%	*908.4*
150 kHz 22.5%	*858.3*
150 kHz 40.0%	*804.3*
201 kHz 24.0%	*864.1*
201 kHz 40.0%	*898.8*

Shifting between samples deposited at different frequencies (with the same duty cycles) was not as noticeable, there was, however, a slight decrease in wavelength seen for samples deposited a 40 % duty cycle compared to the samples deposited at 24 and 22.5 %.

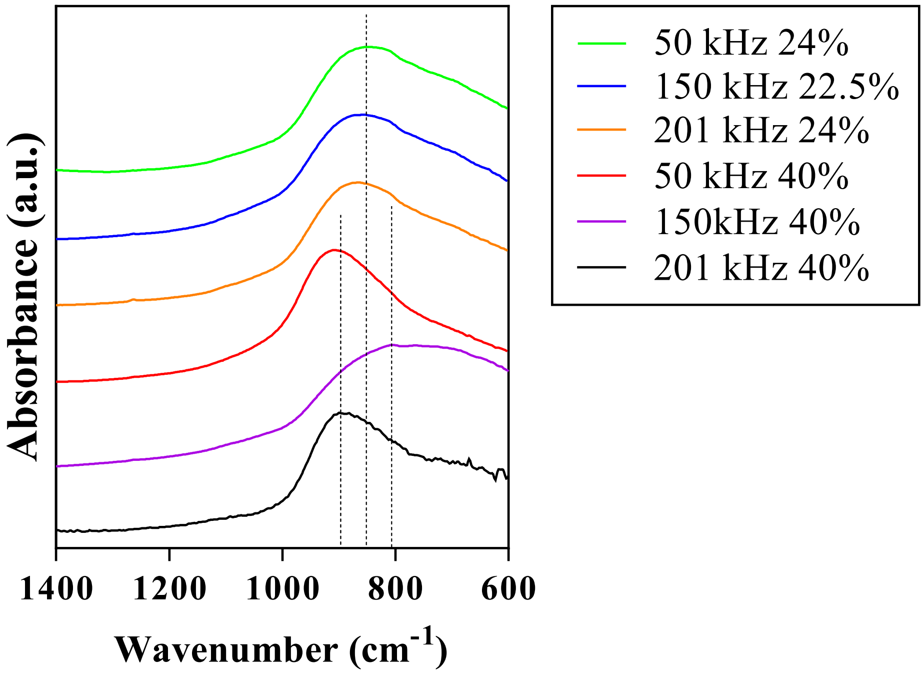

***Figure 6.1:** FTIR spectra for films deposited onto Cu foil using pulsed DC deposition with varying frequency and duty cycle (as indicated in the legend).*

6.1.1.2 SEM

Structural analysis carried out showed that the films were generally featureless as imaged in secondary electron micrographs in ***Figure 6.2***.

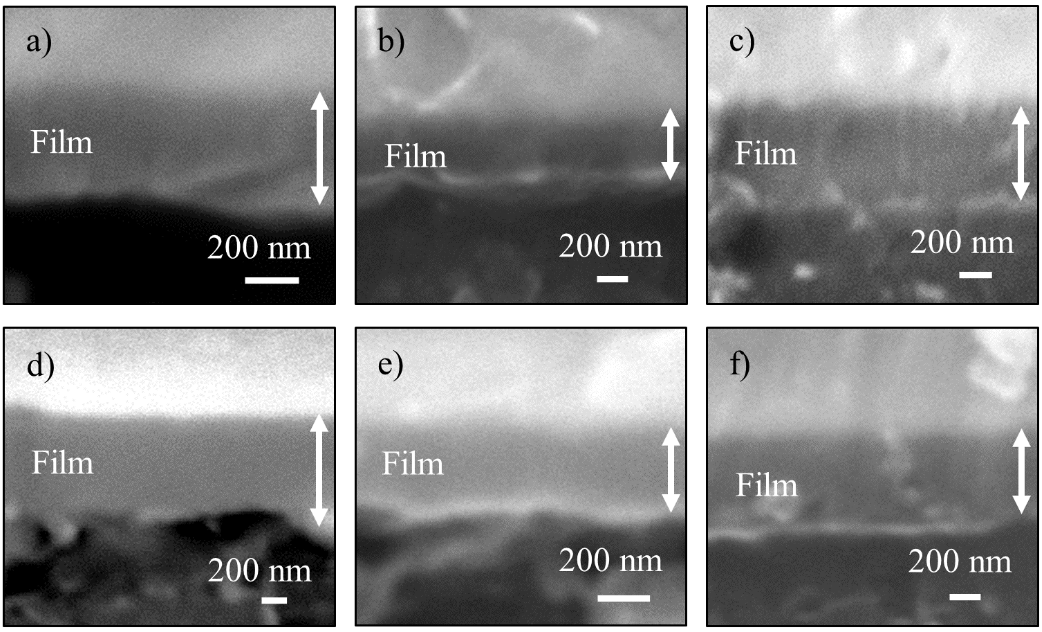

Sample	*Thickness (nm)*	*Rate (nmh^{-1})*
50 kHz 24.0%	*468 ± 24*	*117*
50 kHz 40.0%	*450 ± 23*	*113*
150 kHz 22.5%	*370 ± 4*	*93*
150 kHz 40.0%	*585 ± 12*	*146*
201 kHz 24.0%	*353 ± 9*	*88*
201 kHz 40.0%	*439 ± 11*	*110*

Figure 6.2: *SEM (secondary electron) cross section images of pulsed DC films deposited for 240 min with a -60 V substrate bias onto Cu substrates. The pulse frequency and duty cycle were as follows: a) 50 kHz 24%, b) 50 kHz 40%, c) 150 kHz 22.5%, d) 150 kHz 40%, e) 201 kHz 24% and f) 201 kHz 40%. Additionally to this a table including the thickness and deposition rate of each coating is seen below*

Film deposition rates remained relatively constant in most cases with between 88 and 117 nmh^{-1}, excluding the sample produced at 150 kHz with a 40 % duty cycle which had a deposition rate of 146 nmh^{-1}, see **Figure 6.2** for film thickness and deposition rates.

6.1.1.3 XPS

XPS analysis showed that the surface layer of each film was fully oxidised, as the peak resulting from Al^{3+} lacked any kind of shoulder, which would have indicated metallic impurities. The peak was seen at an average binding energy of 74.22 ± 0.04 eV. Stoichiometry varied between an Al:O ratio of 0.53 and 0.68 with no discernible trend with respect to the applied frequency or pulse width. See ***Figure 6.3** and **Table 6.2*** for XPS summary data.

***Table 6.2:** XPS Al_2P binding energy and Al:O ratio assessed using casa XPS for pulsed DC films as deposited onto Cu disks.*

Sample	***Al_2P binding energy (eV)***	***Al:O***
50 kHz 24.0%	*74.08*	*0.53*
50 kHz 40.0%	*74.26*	*0.61*
150 kHz 22.5%	*74.08*	*0.60*
150 kHz 40.0%	*74.24*	*0.68*
201 kHz 24.0%	*74.36*	*0.60*
201 kHz 40.0%	*74.31*	*0.58*

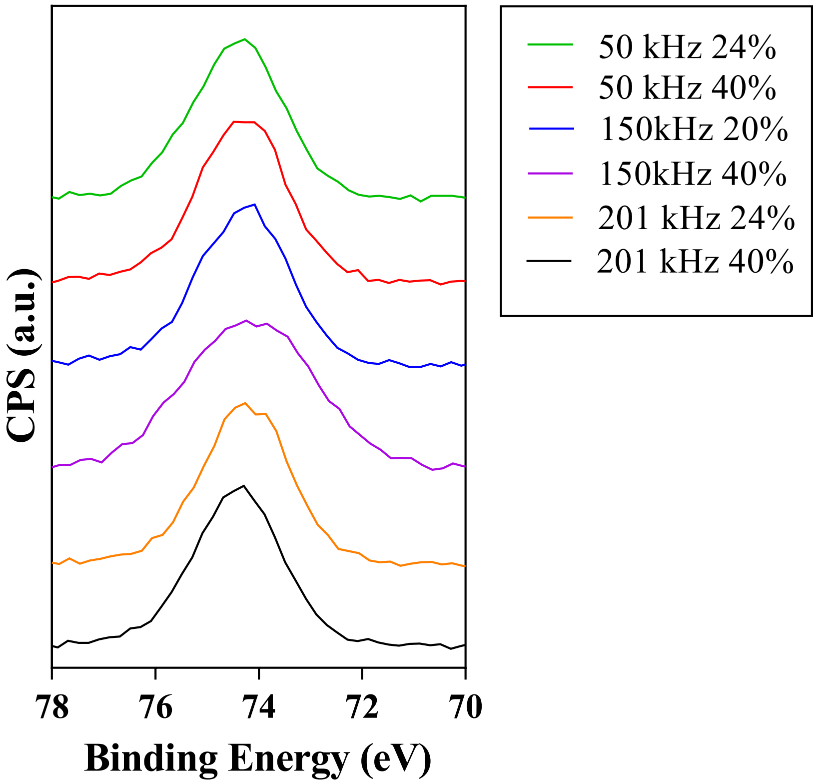

***Figure 6.3*:** XPS Al_2P peaks for films as deposited onto Cu substrate with varying pulse frequncy (kHz) and duty cycle as indicated in the legend.

6.2 PDC-60 characterisation

The PDC deposition parameters of 240 min, with a substrate bias of -60 V, a pulse frequency of 150 kHz and duty cycle of 40% were carried forward and hence called PDC-60. This was reasoned because the produced films had good stoichiometry as shown by XPS (closest to the desired 0.66 Al:O ratio), coupled with the lack of Al^0 in the film which should result in improved electrical properties compared to DC and BDC films. This following section focuses on the production of these films and further characterisation, such as electrical testing, TEM and mechanical analysis.

6.3 PDC-60 structural characterisation

Further characterisation on these films was continued from the previous section with films produced at 150 kHz and with a 40 % duty cycle.

6.3.1 XPS

XPS analysis further confirmed the lack of elemental aluminium at least in the top layer of the films shown by the lack of a shoulder on the Al^{3+} peak, see ***Figure 6.4***. The Al_2P peak position was at 74.37 eV indicative of Al^{3+}.

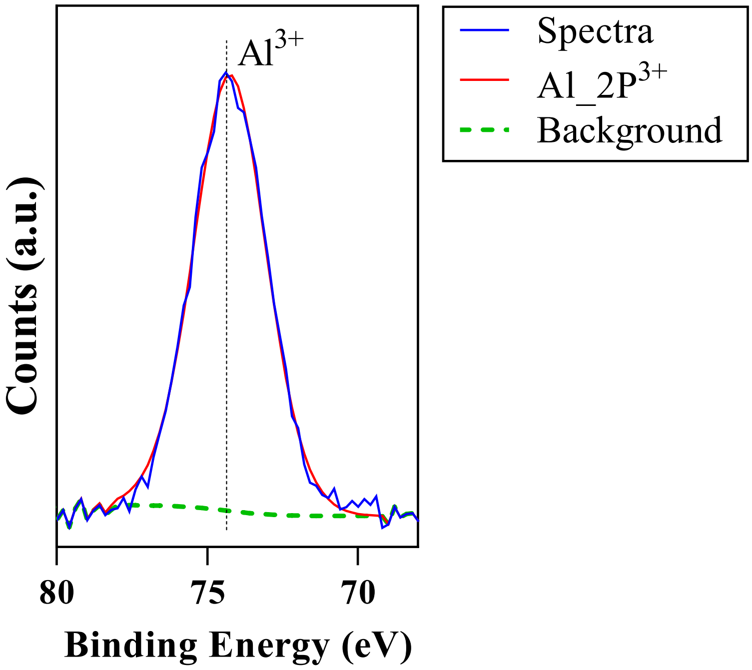

Figure 6.4: *XPS of PDC-60 thin film as deposited onto copper indicating no Al^0 in the surface layer of the film, due to the absence of a shoulder at 70 eV which was seen in DC and BDC films.*

XPS analysis of the sample showed that the films had an Al:O ratio of 0.68, close to that of stoichiometric alumina (0.66).

6.3.2 SEM and TEM

SEM showed that films produced under these conditions had a thickness of 285 ± 3.4 nm with no visible striations or defects (see inset in ***Figure 6.5***). TEM analysis of PDC thin films showed that opposed to DC and BDC films the material contained no visible cracking or striations. The films had a deposition rate of 64 nmh^{-1}. EDX analysis also confirmed consistency across the film with no striations or large crystallite apparent.

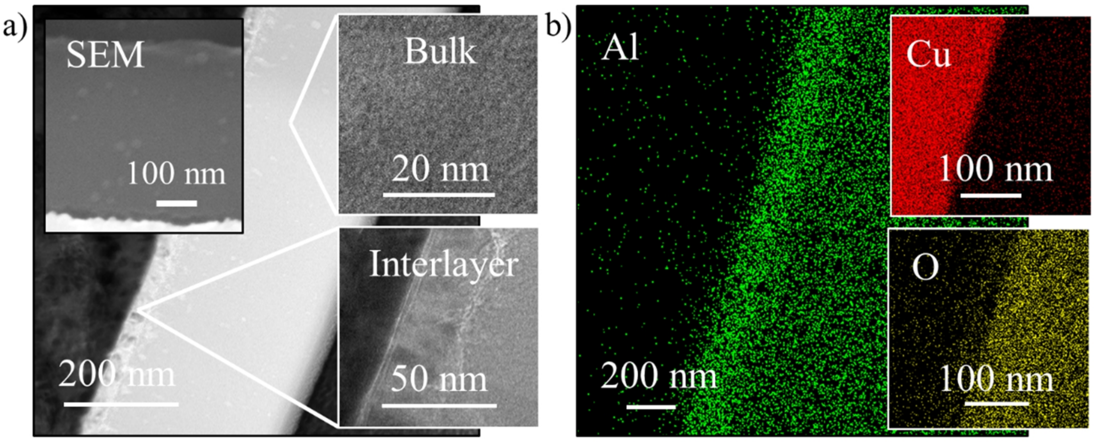

Figure 6.5: *a) TEM (SEM inset) micrographs of PDC-60 as deposited onto Cu, with cross sections showing film thickness, interlayer and structure. b) TEM EDX analysis is included to show the consistency of the oxygen distribution and lack of striations in the films.*

6.4 PDC-60 electrical characterisation

Initial electrical testing showed that the breakdown strength of the materials was superior to that of the DC and BDC alumina films, with breakdown field as high as 275 Vμm^{-1}. However, as measured by probe based methods the average breakdown voltage was 155 ± 37 V yielding a dielectric strength of 265 ± 65 Vμm^{-1}. The maximum leakage current in the PDC film prior to breakdown was $< 10^5$ Acm^{-2} (***Figure 6.6***).

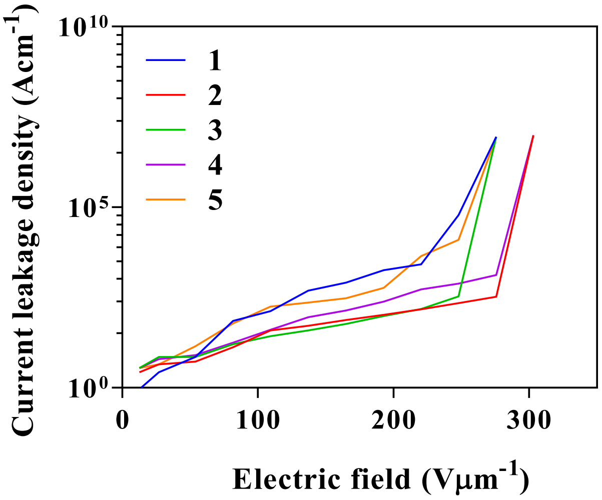

Figure 6.6: *Current leakage density graph for PDC-60 as deposited onto 5mm Cu disks, with measurements made using the in house probe based method based upon ASTM D3755-14.*

Testing using AFM methods showed that the closer the test sites were to each other the lower the breakdown strength, ***Figure 6.7*** shows the results of measurements taken using different sized arrays on PDC-60. The sample measured using a 5x5 µm array showed breakdown voltages between 15 and 150 V. Samples measured using the bigger array lacked any breakdown at all, and showed no significant leakage.

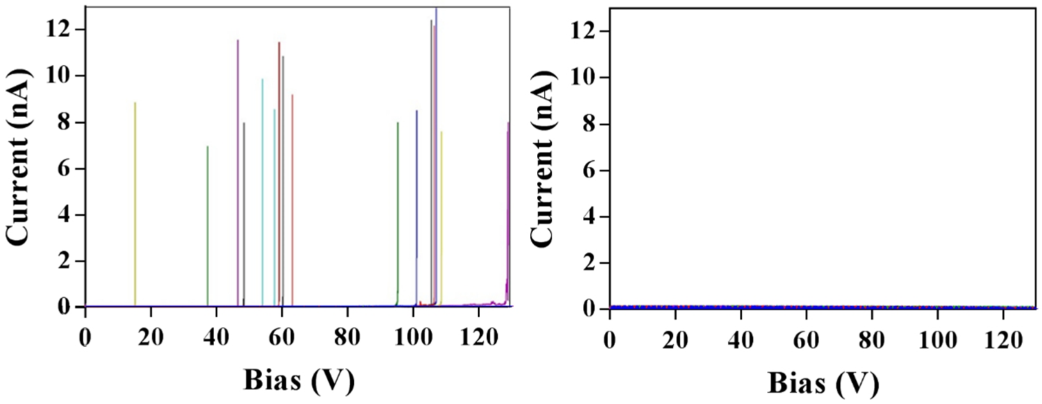

Figure 6.7*: Elctrical testing for PDC-60 as deposited onto 10 mm Cu disks, measured using AFM DB with 5x5 µm (left) and 30x30 µm (right) arrays.*

The testing on PDC-60 films also showed a much more erratic breakdown voltage when the measurements were carried out closer to each other, thus only an array size of 30x30 μm was carried forward.

Testing on PDC-60 samples showed that for 270 nm films no breakdown occurred. Films of 107 ± 3 and 215 ± 10 nm were produced by decreasing the deposition time and testing showed dielectric breakdowns at averages of 31 ± 2 and 67 ± 5 V relating to dielectric strength of 301 ± 22 and 310 ± 26 Vμm^{-1}, which are not significantly different, for the thinner and thicker films respectively. Breakdown occurred relatively quickly after the onset leakage and the maximum leakage current seen was smaller with the thinner films. Current oscillations were seen only in 5 measurements for the 215 nm sample at high applied fields (> 327 Vμm^{-1}), see ***Figure 6.8***.

Sample thickness (nm)	***Dielectric strength (Vμm^{-1})***
107 ± 3	*301 ± 22*
215 ± 10	*310 ± 26*

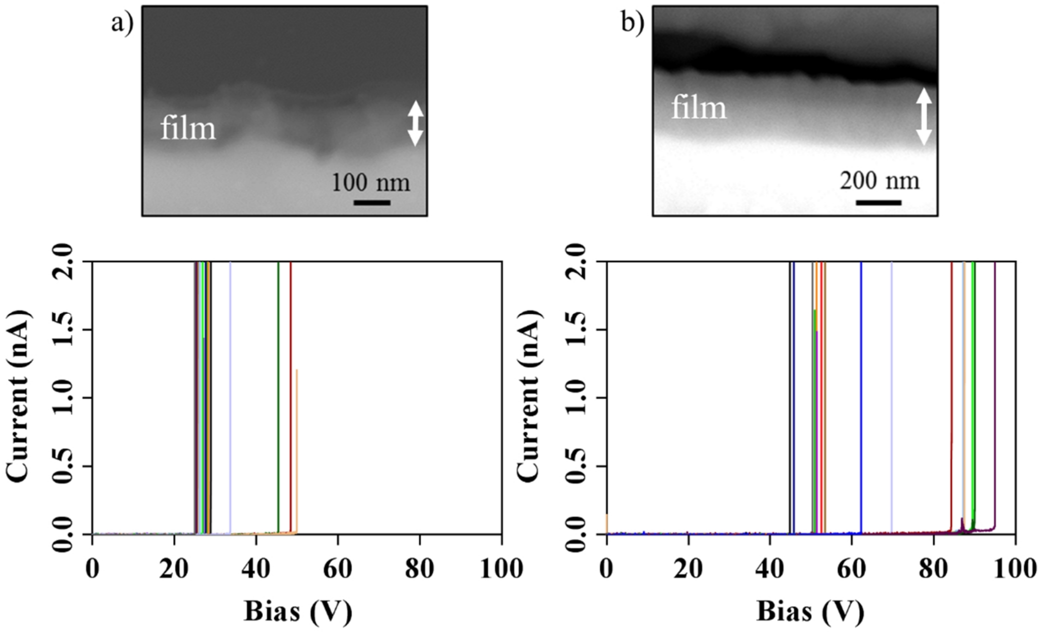

Figure 6.8: *Table displaying dielectric strength with respect to film thickness. Cross sectional backscattered electron SEM micrographs used to determine film thickness and breakdown voltage for PDC-60 as deposited onto 10 mm Cu disks to thicknesses of a) 107 nm and b) 215 nm respectively. Also included below each micrograph is the current voltage data for each sample.*

The conduction mechanism in the PDC films was determined through analysis of the AFM DB current voltage curves for the PDC 200 nm sample. It was determined that a possible mode for conduction was Fowler-Nordheim tunnelling. The single linear region shown indicates a single tunnelling barrier at high applied fields, as seen in ***Figure 6.9***. Analysis of other conduction mechanisms (such as Schottkey or Poole-Frenkel) yielded graphs containing a large spread of data, due to relatively large current distribution meaning no mechanism could be determined at low applied field.

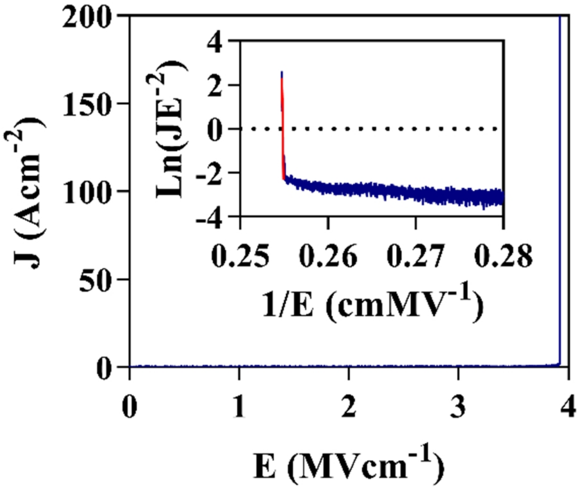

Figure 6.9: *Leakage current density plot for PDC-60, 200 nm samples as deposited onto Cu disk with inset Fowler-Nordheim plot with red highlighted linear region.*

6.5 PDC-60 mechanical characterisation

AFM measurements showed the films had a (Ra) roughness of 11.9 ± 0.4 nm with a minimum of -60.7 nm and a maximum of 380 nm. Films were generally featureless when mapped using AFM.

6.5.1 Direct pull adhesion testing

Mechanical properties of the film was assessed in the same manner as the DC and BDC films. Pull off testing indicated that the average failure for these films occurred at 55.7 ± 2.9 MPa, six samples failed through partial interfacial delamination and two samples failed in the adhesive (***Figure 6.10***).

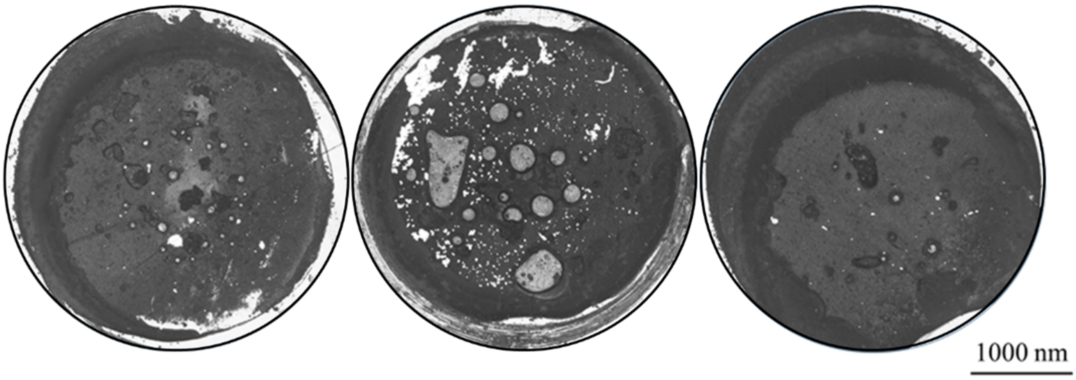

Figure 6.10: *Light micrographs of the prevalent pull off failure mechanisms in PDC* Al_2O_3 *(all indicate some degree of partial interfacial failure).*

6.5.2 Scratch Testing

Scratch testing indicated that the film had the same failure mechanisms that were seen for DC and BDC films. Combinational cracking (L_{C1+2}) was seen at 0.87 ± 0.05 N resulting from cohesive failure and buckling (L_{C3}) at 1.96 ± 0.16 N resulting from adhesive failure. See ***Figure 6.11*** for failure onset and appearance.

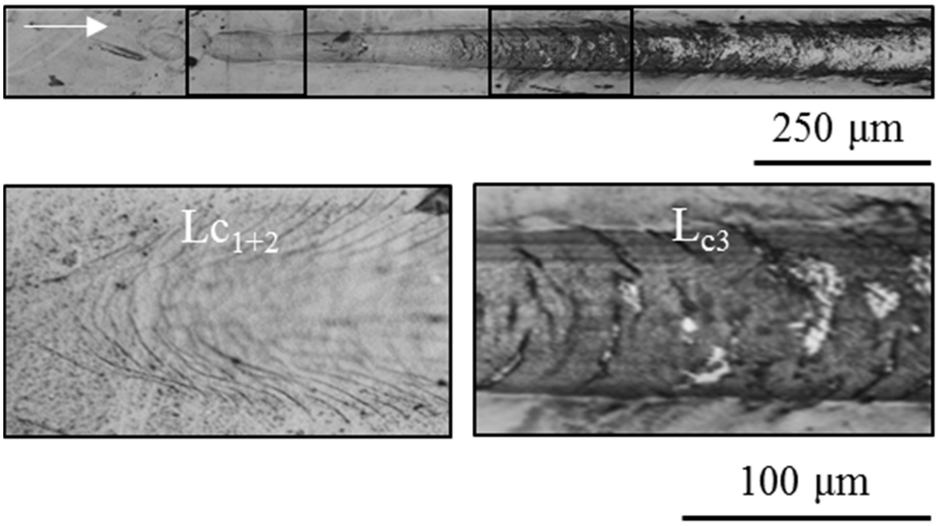

Figure 6.11: *Scratch failure for PDC-60 Films as deposited onto Cu Disk, displaying cohesive and adhesive failures with combination cracking (*L_{C1+2}*) and buckling (*L_{C3}*) respectivley. The maximum scratch load was 15 N, with scratch length of 3 mm.*

6.6 Reproducibility of PDC-60 films

PDC-60 films were remade and analysed accordingly to observe reproducibility in the films. The following data resulted from the reproducibility study.

6.6.1 Structural characterisation

PDC FTIR Al-O LO phonon peaks were shifted from the initial measurement seen in ***Figure 6.12***. XRD and XPS results, however, were the same as previously with XRD confirming the amorphous nature of the film (amorphous hump at low 2θ°) and XPS giving Al_2P binding peak at 73.9 eV with the absence of any shoulder. The Al:O ratio was higher in the second batch of produced films at 0.70 compared to 0.68 for the previous set of films.

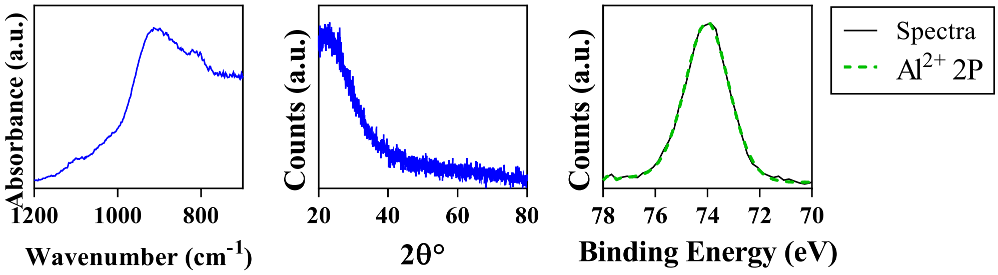

Figure 6.12: *FTIR, XRD and XPS spectra of PDC alumina as deposited onto Cu foil, borosilicate glass slide and Cu disk respectively.*

6.6.2 Mechanical Testing

Pull off adhesion testing showed a maximum adhesive strength of 41.9 ± 2.0 MPa. All failures occurred through partial cohesive failure in the film, showed by the Al seen on the pull off stubs and the lack of copper seen in the micrographs of the failure sites (***Figure 6.13***).

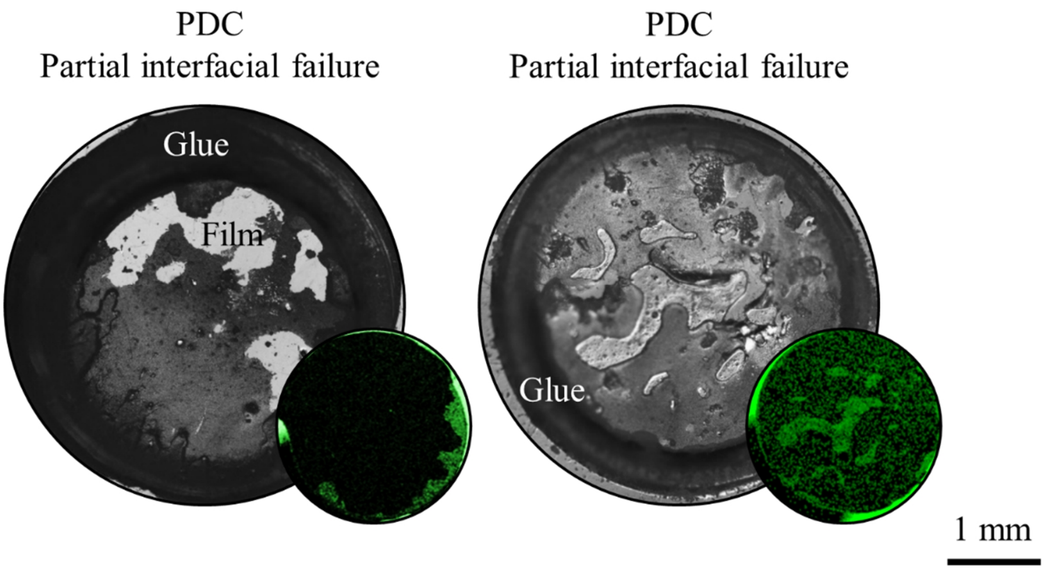

Figure 6.13: *Light microscope images of pull off adhesion failure sites for PDC films. Al EDX of the pull off site is included to show the presence of Al on the pull off stub.*

Scratch testing showed conformal cracking (cohesive failures) at 1.22 ± 0.03 N and buckling (adhesive failure) at 1.29 ± 0.03 N as seen in ***Figure 6.14***.

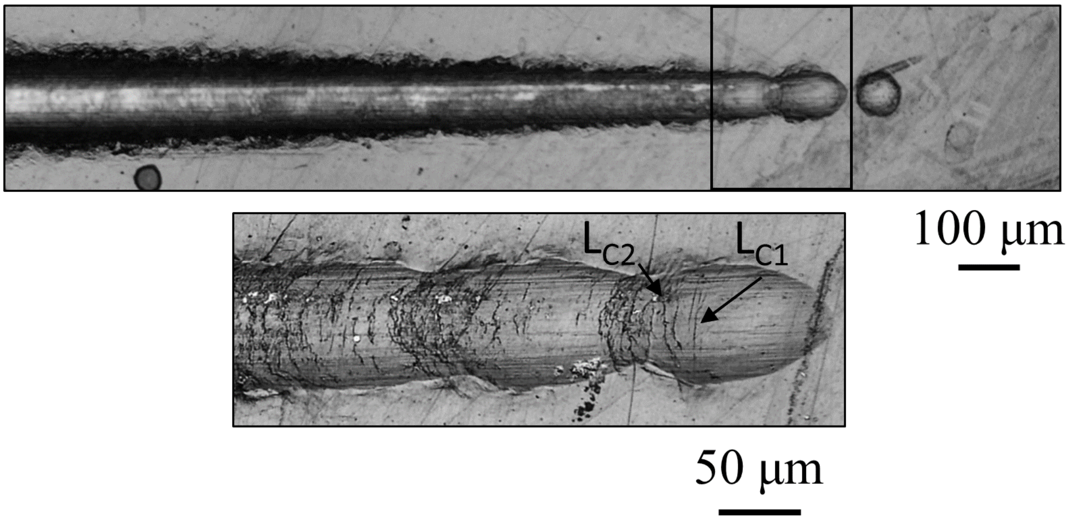

Figure 6.14*: Light microscope images of scratch tests for PDC films deposited to Ca. 200 nm onto Cu disks showing L_{C1} and L_{C2} failure in the high magnification image.*

6.7 Summary

The most crucial result from this section is evident in the TEM analysis of the PDC films (***Figure 6.5***), which show that there are no defects in the form of ordered regions in the structure, which were seen in DC films. This improvement in structure can be used to explain the improvement in dielectric strength up to 310 ± 26 Vμm^{-1} for these films. This is also the reason for the scarce current oscillations seen in the PDC films. It can, however, be seen that the mechanical properties of the films suffered likely as a result of poorer interfacial mixing caused by the slower PDC deposition rate. The pulse parameters studied were shown generally to have an effect on the FTIR results indicating a variation in internal stress when applying different duty cycles because of the varying energy of the sputtered species. This section has shown that PDC Al_2O_3 films are superior to DC films with respect to electrical properties and will be carried forward for use in composite films.

7 Results: Multilayer composite materials

The aim of the work in this results section was to improve upon the electrical and mechanical properties of the materials deposited in results sections 1 and 2, hence, this section concentrates on the production PDC and RF multilayer composites, deposited as outlined in the experimental procedure in section (*4.1.4*) and shown in ***Figure 7.1***. Key considerations for these composites will be the layer frequency and number of layers as well as the interlayer configuration.

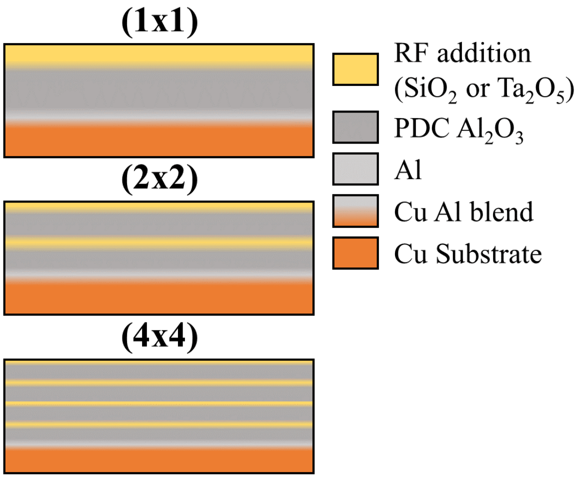

Figure 7.1: *Multilayer film layer configuration for additional information see methodology section.*

Initially results are presented for the first batch of films deposited using PDC (Al_2O_3) and RF (SiO_2). This is followed by the results of films deposited using PDC (Al_2O_3) and RF (SiO_2) or RF (Ta_2O_5) and more refined deposition parameters. Both procedures are outlined in section (*4.1.4*) with the major distinction between the two procedures being the initial method did not utilise the shield to cover the Al target during deposition of the SiO_2.

7.1 Initial Al_2O_3 SiO_2 multilayer materials

An initial study of SiO_2 as a suitable material for composites was carried out, forming 1x1 and 2x2 layered samples. Notably this set of films were produced with no shield movement during deposition, meaning that the Al target was uncovered during SiO_2 sputtering.

FTIR spectrum identified the presence of two main peaks at 830.3 and 825.8 cm^{-1} for Al-O bonding and 1228.6 and 1223.8 cm^{-1} for Si-O bonding. Each of these peaks had a shoulder shifted to a lower wavenumber, see ***Table 7.1*** and ***Figure 7.2*** for peak and shoulder positions.

Table 7.1: *FTIR peak positions for alumina silica composite films (with 2 to 4 layers) as deposited onto Cu foil for maximum ATR crystal contact.*

	Al-O (cm^{-1})		Si-O (cm^{-1})	
Sample	***Peak***	***shoulder***	***Peak***	***Shoulder***
1x1	*919.0*	*830.3*	*1221.9*	*1146.6*
2x2	*915.2*	*825.8*	*1216.6*	*1148.6*

XRD indicated that samples were still amorphous, evidenced by the lack of crystalline peaks. The amorphous hump < 40 ° is a result of the amorphous film structure and amorphous glass substrate, see ***Figure 7.2***.

	Si_2P (eV)	***Si:O***
1x1	*103.41*	*0.3947*
2x2	*103.21*	*0.4164*

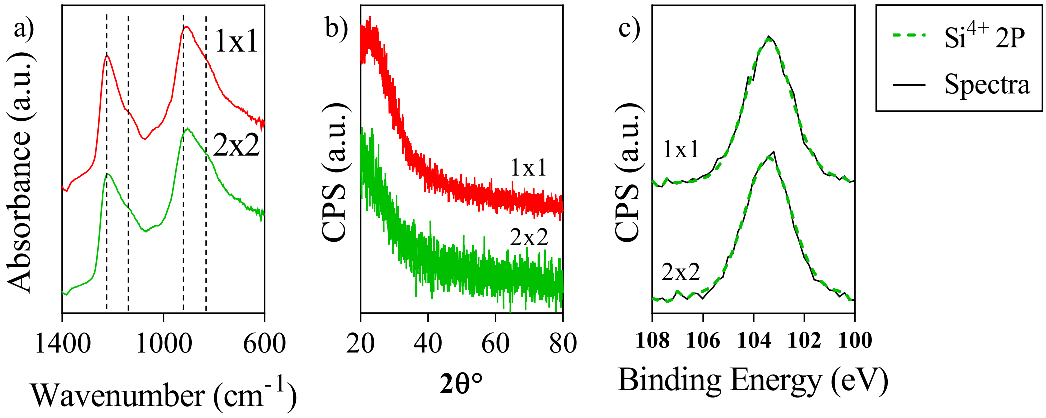

Figure 7.2: *(top) Table showing xps Si_2P peak positions and Si:O ratios. (bottom) a) FTIR, b) XRD and c) XPS data for silica alumina multicomponent films as deposited onto Cu foil (FTIR), borosilicate glass slides (XRD) and Cu disks (XPS) using initial multilayer deposition techniques.*

Si_2P peaks were present in XPS spectra at 103.31 eV corresponding to Si^{4+} and the lack of photo electrons bound at 100 eV indicated the lack of elemental Si. A Si:O ratio of *ca.* 0.4 were determined using the XPS survey spectra where an ideal ratio would be 0.5 see ***Figure 7.2***.

SEM of 1x1 films showed a film of *ca.* 500 nm thick with no clear layer structure at the magnifications used. See ***Figure 7.3*** for film thickness and structure.

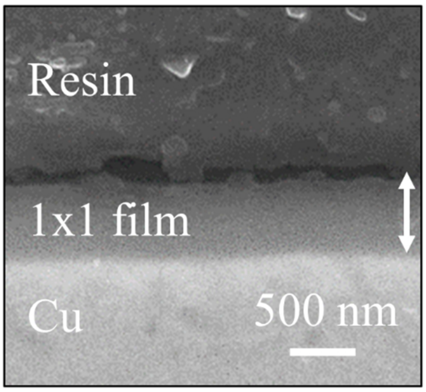

Figure 7.3: *Cross sectional secondary electron SEM of Al_2O_3, SiO_2 multilayer as deposited onto Cu Disk.*

Electrical characterisation of these films revealed that through thickness conduction could be measured using a multi meter indicating the films had very low resistance. As a result of this further electrical testing wasn't carried out and indicated modifications to the deposition procedure were needed.

7.2 Al_2O_3, SiO_2 and Ta_2O_5 multilayer films

As a result of through thickness conduction in the initial multilayer films a number of changes were made. The following section shows the characterisation results for the refined multilayer systems consisting of PDC alumina combined with either RF Ta_2O_5 or RF SiO_2.

7.2.1 Structural characterisation

Similarly to the RF films discussed at the start of this section, FTIR gave information on the bonding in the films. Combination of peaks resulting from the alumina and the RF additions were seen for the films. Analysis of Ta_2O_5 multilayer composites resulted in a broad absorbance band with modes at lower wave number < 900 cm^{-1} attributed to Ta_2O_5 modes, whereas the peak at 901.7 cm^{-1} was attributed to Al-O bonding. For SiO_2 multilayer composites peak shoulders at 825.5 (bending) and 1140.0 cm^{-1} (stretching) were contributed by Si-O bonding, with the peak at 910.4 cm^{-1} again attributed to Al-O bonding. A peak at 1228.6 cm^{-1} was also identified in the SiO_2 multilayer films and attributed to Si-O-Al or Si-O-Si bonding [291]. All peaks as seen in ***Figure 7.4***.

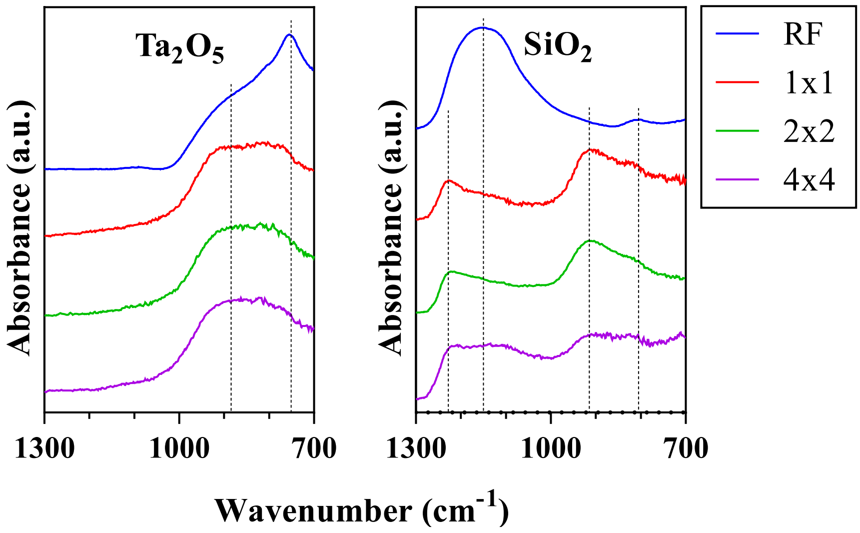

Figure 7.4: *FTIR spectra for Ta_2O_5 (left) and SiO_2 (right) multilayer materials as deposited onto copper foil. Spectra for the RF single Absorbance bands have been marked.*

XRD indicated the amorphous nature of all composite films. Resulting in only amorphous humps and no peaks were seen for the deposited Cu/Al interlayer, see ***Figure 7.5***.

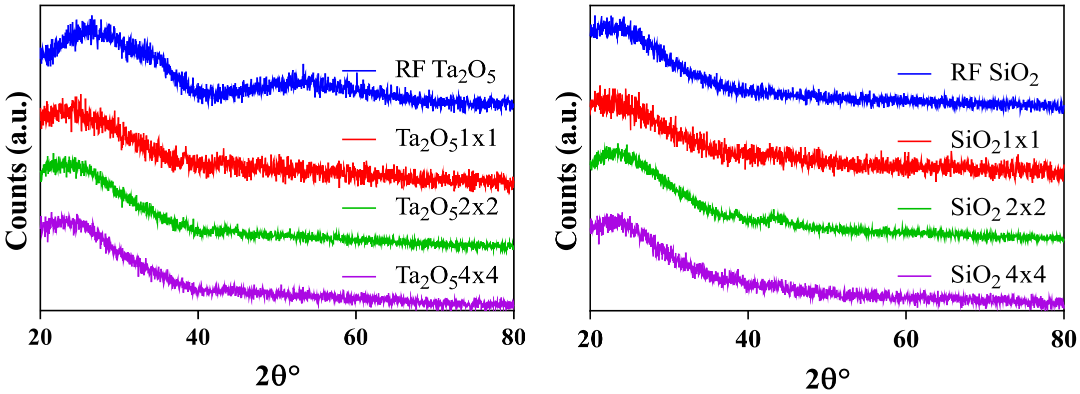

Figure 7.5: *XRD diffraction patterns for multilayer films of ca. 200 nm thick deposited onto glass substrates and 8 hour deposited RF films, with Ta_2O_5 Al_2O_3 composites (left) and SiO_2 Al_2O_3 composites (right).*

XPS analysis of the films confirmed the presence of Si^{4+} and Ta^{5+} with photo electron peaks at 103.23 ± 0.01 eV and 26.30 ± 0.05 eV respectively. The XPS spectra showed a lack of peaks resulting from Ta metal but did, however, reveal the presence of sub stoichiometric silicon, with peaks appearing at 100.45 ± 0.13 eV accounting for up to 15 % of the Si content in the analysis of SiO_2 multilayer composites. See ***Figure 7.6*** for peak positions, Si:O and Ta:O ratios and peak deconvolution results. Ta_2O_5

multilayer films were sub stoichiometric with Ta:O ratios below 0.4 and SiO_2 multilayer films were found to contain excessive Si with ratios generally above 0.5.

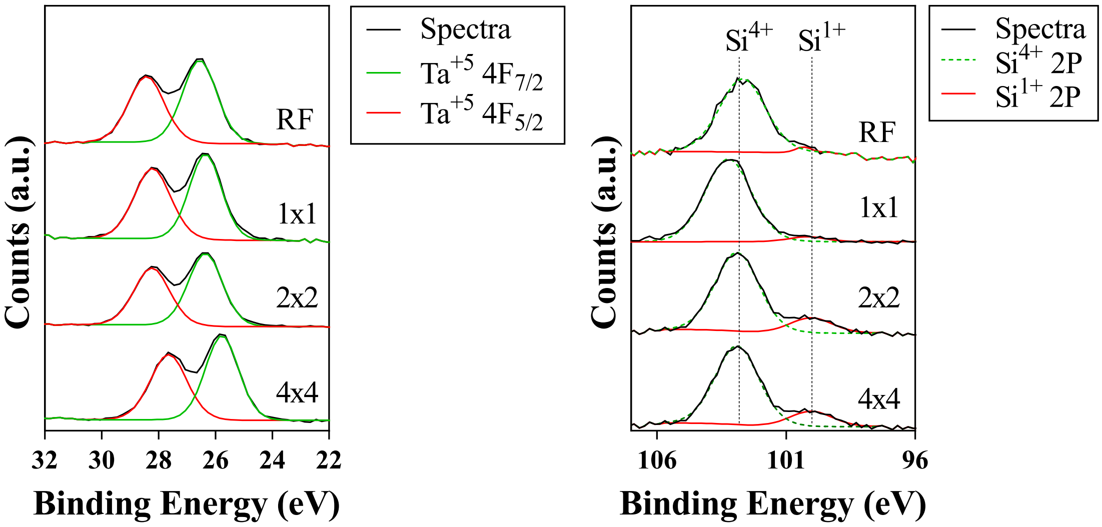

Sample	*Ta^{5+}_4F (eV)*	*Ta^{0}_4F (eV)*	*Ta^{0} %*	*Ta:O ratio*
RF	*26.31*	*N/A*	*N/A*	*0.36*
1x1	*26.45*	*N/A*	*N/A*	*0.35*
2x2	*26.25*	*N/A*	*N/A*	*0.36*
4x4	*26.19*	*N/A*	*N/A*	*0.40*

Sample	*Si^{4+}_2P (eV)*	*Si^{0}_2P (eV)*	*Si^{1+} %*	*Si:O ratio*
RF	*103.20*	*100.80*	*3.46 ± 0.06*	*0.43*
1x1	*103.17*	*100.20*	*1.90 ± 0.01*	*0.62*
2x2	*103.24*	*100.19*	*4.39 ± 0.04*	*0.57*
4x4	*103.25*	*100.37*	*15.76 ± 0.21*	*0.56*

Figure 7.6: *High resolution XPS spectra for multilayer composite films as deposited onto Cu disks, for Ta_4F (left) and Si_2P (right) photoelectrons. Fitting is indicated in the key next to each set of spectra. The subsequent table includes binding energies and atomic ratios.*

Deconvolution of the O_1S peak for the SiO_2 composites gave information as to the binding energy and composition of the Si species, see ***Figure 7.7*** for deconvoluted spectra.

	Si^{4+}		***Shoulder 1***		***Shoulder 2***	
Sample	***(eV)***	***%***	***(eV)***	***%***	***(eV)***	***%***
RF	*532.64*	*68.8*	*534.58*	*29.1*	*531.61*	*2.1*
1x1	*532.53*	*93.9*	*534.51*	*3.4*	*530.22*	*2.6*
2x2	*532.59*	*91.2*	*534.52*	*5.1*	*530.83*	*3.7*
4x4	*532.59*	*93.6*	*534.54*	*4.4*	*530.69*	*2.2*

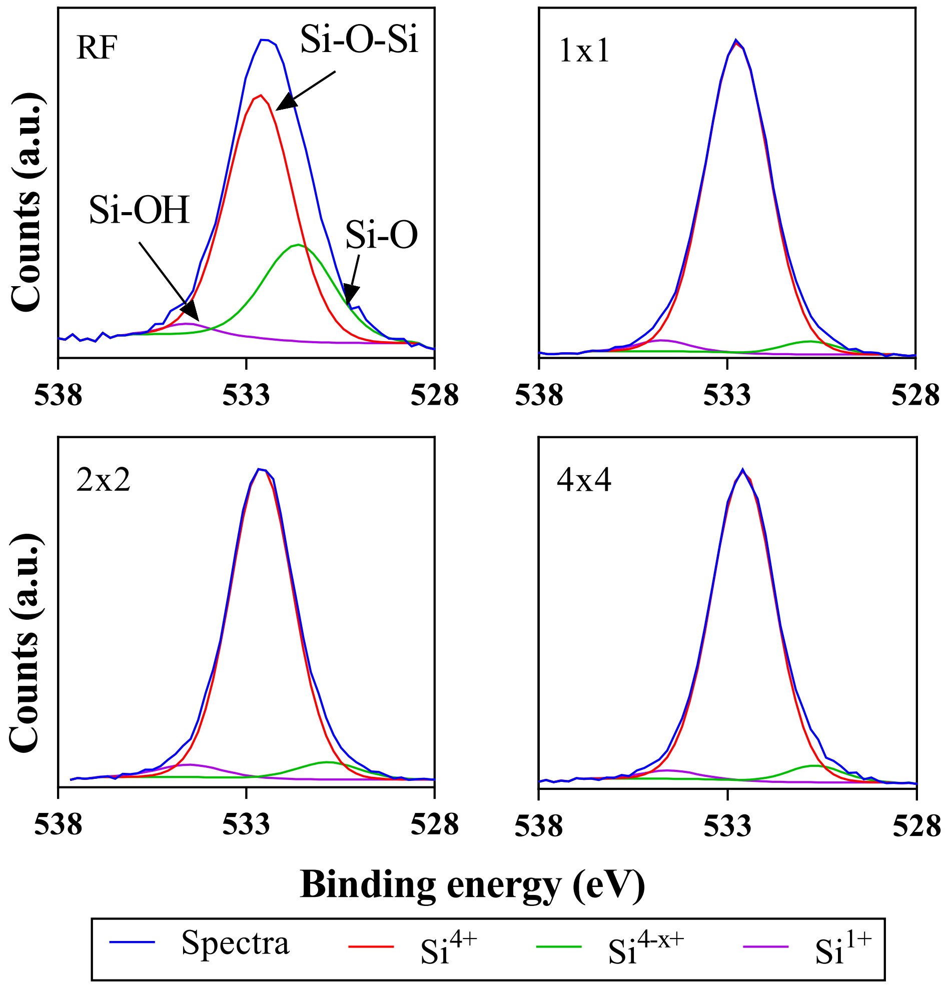

Figure 7.7: *Deconvolution results of XPS O_1S peaks for SiO_2 composites as deposited onto Cu disks. Included below is the deconvolution spectra showing the Si^{4+} peak shoulders.*

SEM micrographs of the film cross sections are given in ***Figure 7.8***. All films were generally featureless and layers were indistinguishable using EDX or secondary electron imaging. However, for Ta_2O_5 composites backscattered electron imaging showed bright sections indicating layer formation. See ***Figure 7.8*** for micrographs and average sample thickness (nm). Thickness varied between 150 and 236 nm with SiO_2 composite films seen to be thicker for 2x2 and 4x4 layered structures.

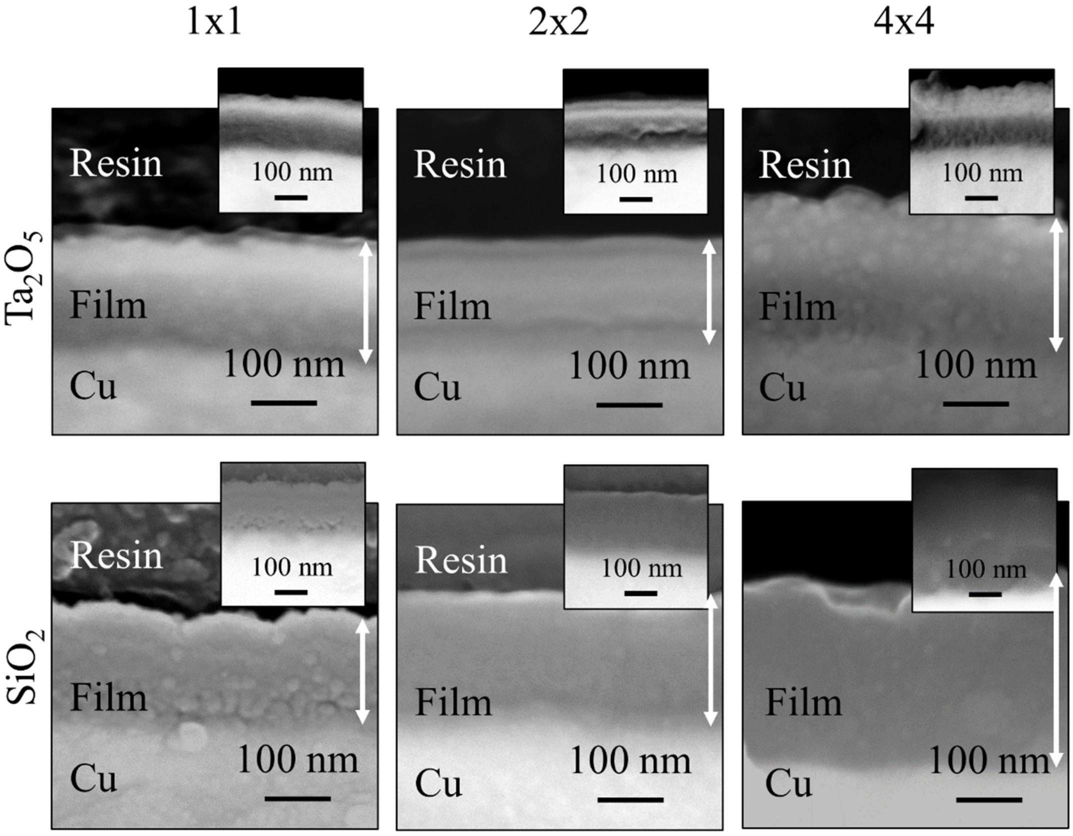

Layers	*Film Thickness (nm)*	
	Ta_2O_5 Composites	*SiO_2 Composites*
1x1	*203 ± 6*	*191 ± 4*
2x2	*152 ± 4*	*182 ± 4*
4x4	*210 ± 9*	*236 ± 11*

Figure 7.8: *Cross sectional secondary and backscattered (inset) SEM micrographs of Ta_2O_5 (top row) and SiO_2 (bottom row) multilayer materials as deposited onto Cu disks. Average thickness values are given in the table below.*

7.2.2 Mechanical Properties

AFM surface roughness values (Ra) varied between 4.7 ± 0.1 nm and 18.1 ± 8.2 nm for the composite films as shown in ***Table 7.2***. No clear trend between the roughness and the number of layers or the composition of the films was observed.

Table 7.2: *Average surface roughness values (Ra) for multilayer composite films as deposited onto Cu disks. Average taken from 3 2x2 μm areas as analysed by Gwyddion AFM analysis software*

Sample	***Ra (nm)***	
	Ta_2O_5	*SiO_2*
1x1	*6.6 ± 1.9*	*11.4 ± 4.4*
2x2	*18.1 ± 8.2*	*4.7 ± 0.1*
4x4	*16.5 ± 3.3*	*17.0 ± 8.3*

7.2.2.1.1 Scratch adhesion testing

Scratches (procedure as outlined in section (*4.4.1.3*)) on the multilayer composites resulted in a maximum cohesive failure loads of 1.22 and 1.25 N for Ta_2O_5 and SiO_2 composites respectively and adhesive failures of 1.40 and 1.34 N for Ta_2O_5 and SiO_2 composites respectively. See ***Table 7.3*** for failure modes and average critical loads.

Table 7.3: *Critical failure loads (N) and failure modes for multilayers deposited onto Cu disks as identified using light micrographs. Whereby conformal cracking has been abbreviated.*

	Sample	***L_{C1} (N)***	***Mode***	***L_{C2} (N)***	***Mode***
Ta_2O_5	*1x1*	*0.98 ± 0.15*	*Conformal C.*	*1.18 ± 0.15*	*Buckling*
	2x2	*1.15 ± 0.04*	*Conformal C.*	*1.40 ± 0.08*	*Buckling*
	4x4	*1.22 ± 0.06*	*Conformal C.*	*1.28 ± 0.06*	*Buckling*
SiO_2	*1x1*	*0.99 ± 0.10*	*Conformal C.*	*0.95 ± 0.11*	*Buckling*
	2x2	*0.84 ± 0.06*	*Conformal C.*	*0.97 ± 0.04*	*Buckling*
	4x4	*1.25 ± 0.20*	*Conformal C.*	*1.34 ± 0.11*	*Buckling*

Cohesive failures occurred generally through conformal cracking and adhesive failure occurred through buckling for all samples as shown in ***Figure 7.9***.

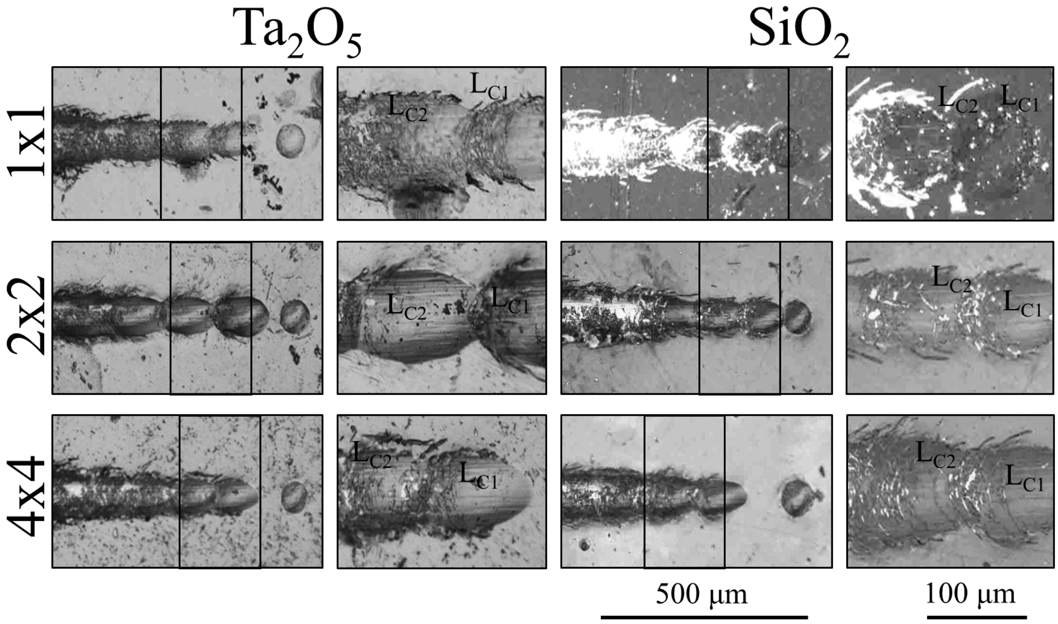

Figure 7.9: *Scratch test images depicting the archetypal failure modes in Ta_2O_5 (left) and SiO_2 (right) multilayer films as deposited onto Cu disks.*

7.2.2.1.2 Pull off adhesion testing

Pull off testing carried out on the multilayer composite films showed that the adhesive strength varied between 11.4 and 34.3 MPa with failure occurring through complete interfacial delamination and partial interfacial delamination mechanisms for all of the films. Average pull off values (MPa) and failure mechanisms for each film are given in ***Table 7.4***.

Table 7.4: *Average adhesive pull off strength (MPa) and failure mechanism for Ta_2O_5 and SiO_2 multilayer films as deposited onto Cu disks.*

	Sample	***Average failure strength (MPa)***	***Complete interfacial failure***	***Partial interfacial failure***	***Failure in Adhesive***
	1x1	*24.6 ± 3.1*	*4*	*3*	*0*
Ta_2O_5	*2x2*	*16.0 ± 2.2*	*8*	*0*	*0*
	4x4	*15.3 ± 2.8*	*8*	*0*	*0*
	1x1	*22.0 ± 3.4*	*6*	*2*	*0*
SiO_2	*2x2*	*11.4 ± 1.8*	*8*	*0*	*0*
	4x4	*34.3 ± 4.4*	*1*	*7*	*0*

It can be seen that the 1x1 Ta_2O_5 films composites had a larger adhesion strength than 2x2 or 4x4 (ca. 1.5 times larger). The 4x4 composite had the highest adhesion strength for SiO_2 composites at least *ca.* 1.6 times larger. EDX mapping of the pull off stubs revealed a layer of copper indicating that failure occurred at the initial Cu-Cu interface, see ***Figure 7.10***.

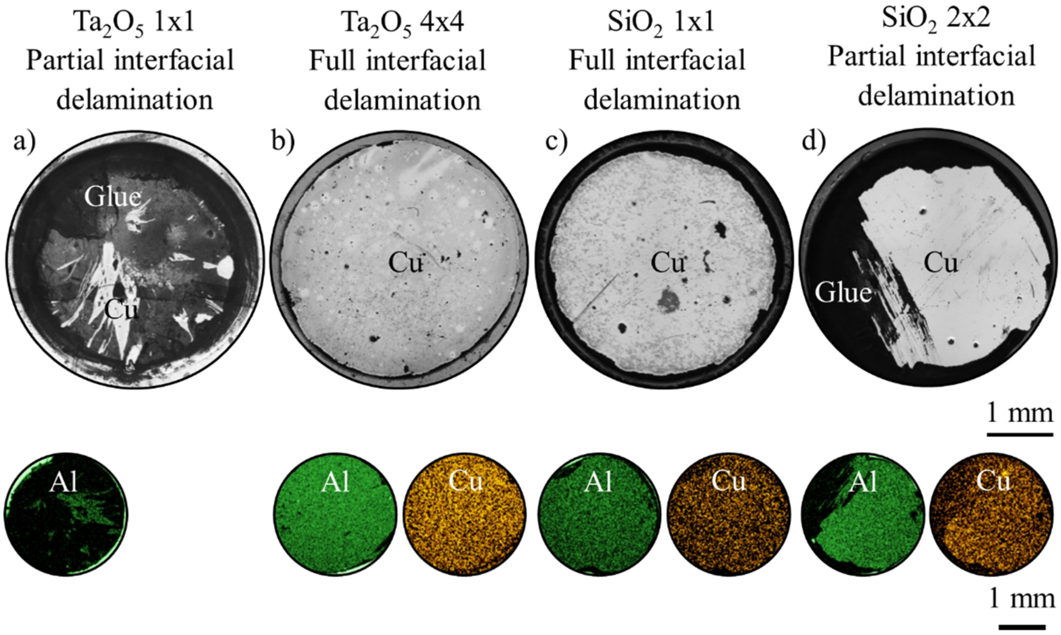

Ta_2O_5 1x1
Partial interfacial delamination

Ta_2O_5 4x4
Full interfacial delamination

SiO_2 1x1
Full interfacial delamination

SiO_2 2x2
Partial interfacial delamination

Figure 7.10: *Pull off adhesion sites showing a) and d) partial interfacial delamination in Ta_2O_5 1x1 and SiO_2 2x2 composites respectively and complete interfacial delamination for Ta_2O_5 4x4 and SiO_2 1x1 composites in b) and c) respectively. Where available EDX maps showing Al and Cu apparent on the stubs following testing are included below the pull off site.*

A summary of the pull off and scratch test failure with respect to the composition and layer configuration of the PDC composite films is given in ***Figure 7.11***.

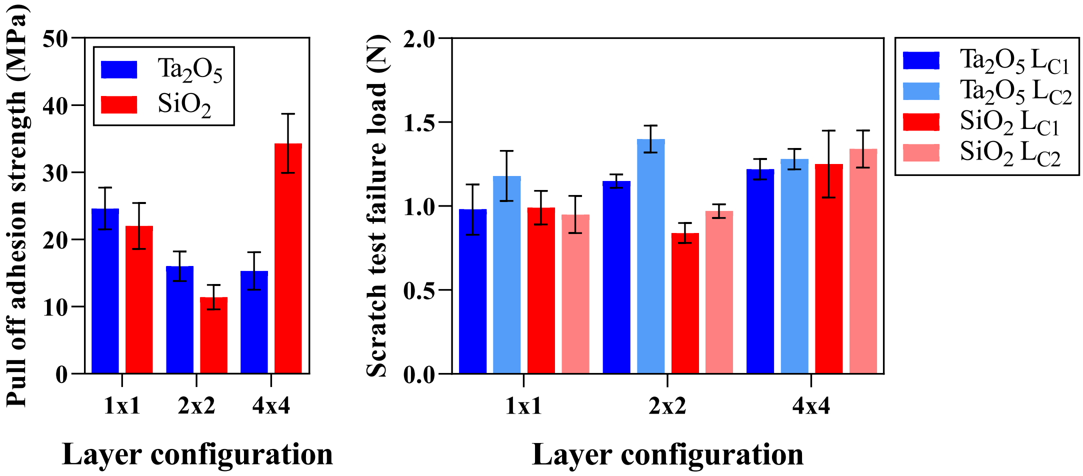

Figure 7.11: *Summary of the mechanical adhesion testing data for PDC composite materials, with pull off adhesion displayed on the left and scratch test critical failures on the right.*

7.2.3 Electrical characterisation

DB measurements were carried out as for the DC, BDC and PDC films. This testing showed a range of breakdowns for the multilayer materials. The highest dielectric strength was provided in both the case of Ta_2O_5 and SiO_2 films by the films with the 2x2 motif, at 513 ± 18 and 466 ± 86 $V\mu m^{-1}$ respectively. The lowest dielectric strength was seen in 1x1 composites at 332 ± 159 and 350 ± 38 $V\mu m^{-1}$ for SiO_2 and Ta_2O_5 respectively.

The standard error in the voltage measurements was much lower for Ta_2O_5 films as seen in ***Figure 7.12***, the error in 1x1 films was also highest for each set of materials. It can be seen in ***Figure 7.13*** *and* ***Figure 7.14*** that leakage current prior to breakdown was larger in the Ta_2O_5 composites with a maximum leakages of *ca.* 6.48, 3.13 and 2.35 nA (1x1, 2x2, 4x4) whilst leakage prior to breakdown was < 1 nA in all SiO_2 composite films. Oscillations in the current leakage prior to breakdown were also seen in Ta_2O_5 composites but not in SiO_2 composites see ***Figure*** **7.13** *and* ***Figure 7.14***.

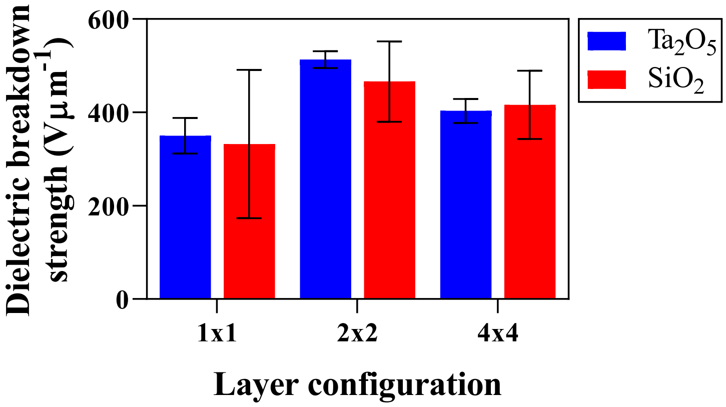

	Sample	*Thickness (nm)*	*Breakdown AVG. (V)*	*N*	*Dielectric Strength ($V\mu m^{-1}$)*
SiO_2	***1x1***	*190.7 ± 3.6*	*63.4 ± 30.4*	*16*	*332 ± 159*
	2x2	*181.9 ± 3.8*	*84.9 ± 15.6*	*16*	*466 ± 86*
	4x4	*235.7 ± 11*	*98.3 ± 16.5*	*16*	*416 ± 73*
Ta_2O_5	***1x1***	*203.0 ± 6.0*	*71.0 ± 7.5*	*16*	*350 ± 38*
	2x2	*152.0 ± 3.5*	*78.0 ± 2.1*	*16*	*513 ± 18*
	4x4	*209.6 ± 9.3*	*84.6 ± 4.1*	*16*	*403 ± 26*

Figure 7.12: *Plot and table of AFM breakdown voltage and dielectric breakdown for Ta_2O_5 and SiO_2 multilayer composites deposited onto Cu disks. Layer structure and film thickness are included (and was used to calculate the dielectric strength). N represents the total measurements that resulted in breakdown (out of 16).*

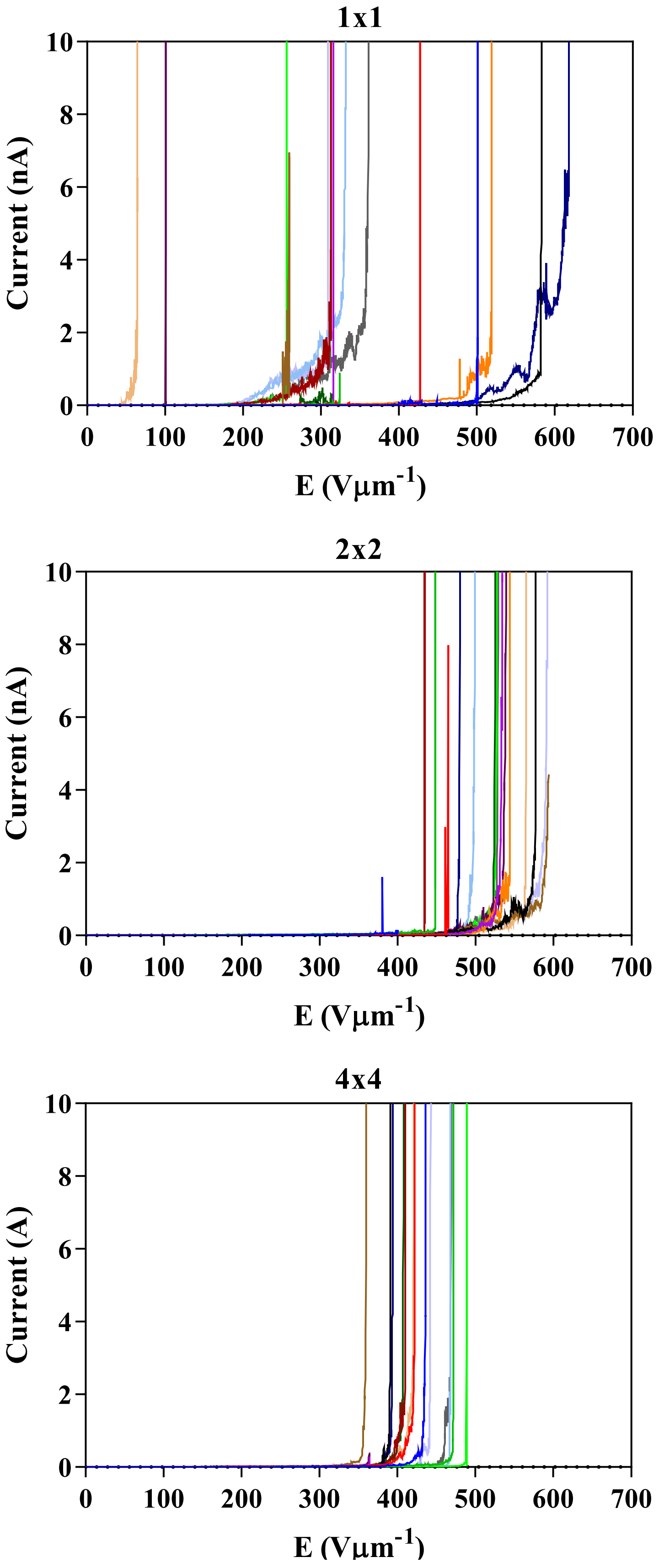

Figure 7.13: *AFM* DB *current, applied field plots, for* Ta_2O_5 *composites deposited onto Cu disks. Layer configuration is indicated on the top of each graph.*

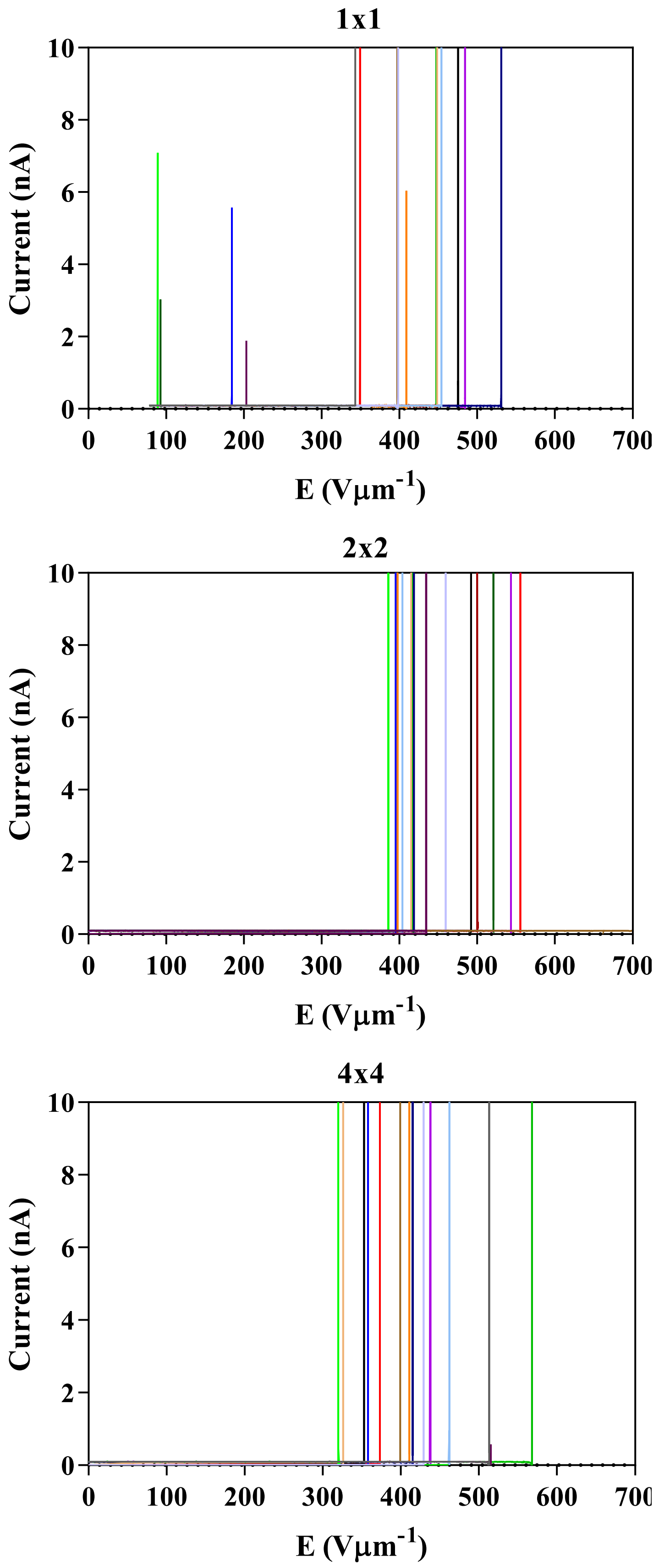

Figure 7.14: *AFM* DB *current, applied field plots, for* SiO_2 *composites deposited onto Cu disks. Multilayer configuration is as indicated on the top of each graph.*

FN, schottky and PF analysis of the current voltage data (AFM DB) gave no clear indication as to the dominant conduction mechanism in the SiO_2 or Ta_2O_5 composites. There was high current variation at low fields and at high applied fields current leakage and oscillations (especially in the Ta_2O_5 composites) made assignment in the high filed region problematic.

7.3 Reproducibility of Ta_2O_5 composites

Ta_2O_5 composite films were produced for a second time and analysed to check the consistency of the deposition procedure. Characterisation in the form of FTIR, XRD and XPS was carried out to confirm structure and stoichiometry, for comparison to previously produced films. All data discussed here is shown in ***Figure 7.15***.

FTIR of multilayer films showed peaks consistent with the measurements made previously in this study, with peaks at 910.4 and 799.1 cm^{-1}. Also exhibiting a slight depression in the peak resulting from Ta-O bonding with an increase in the number of layers. XRD also showed a broad amorphous diffraction peal at ca. 20°. XPS analysis also confirmed the presence of Ta_4F peaks with a binding energy of 26.23 ± 0.09 eV and an absence of peaks resulting from Ta metal. The Ta:O ratio was also generally similar with the exception of 1x1 films which appeared to have a lower Ta:O ratio of 0.29 whereas 2x2 and 4x4 films had Ta:O ratios of 0.35 and 0.33 respectively.

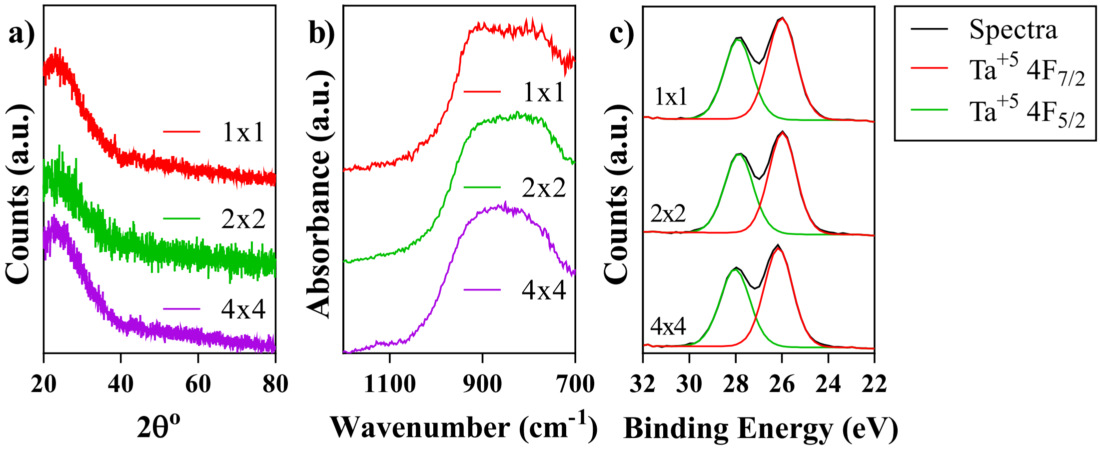

Figure 7.15: *FTIR spectra for Ta-O and Al-O bonding, XRD and XPS Ta_4F results for reproduced* Ta_2O_5 *multilayer films deposited onto Cu foil, borosilicate glass slides and Cu substrates respectively.*

7.1 Summary

Multilayer films have been shown in this results chapter to improve upon the dielectric strength set by the PDC Al_2O_3 films deposited in the previous chapter. The increase in breakdown strength to a maximum of 513 ± 18 $V\mu m^{-1}$ was the result of the inserted RF layers acting as a barrier to charge flow through capping structural or compositional defects. The properties varied with the number and distribution of layers, which was a result of the varying effectiveness of the RF layers to block current flow. The mechanical properties of the composites were shown to be at least 2.4 times lower than the PDC films, this was theorised to be a result of an increased internal stress, because the total thickness and surface pre-treatments were the same for PDC films.

8 Results: Reel to reel coating of wires

Following the production of coatings with breakdown strength > 300 Vμm^{-1} in results chapters 2 and 3, it was considered a priority to apply coatings to wires in order to assess the mechanical and electrical properties when considering the coatings actual application. For the success of such isolating systems it was considered critical to assess the relationship between the thickness and mechanical and electrical properties to maintain coating continuity.

In light of this the following chapter will display the development of the wire coating apparatus, paying close attention to substrate biasing, which was carried out in order to produce coatings which adhere to the wires and provide sufficient electrical isolation. Characterisation of three thicknesses of PDC Al_2O_3 coatings deposited with varying Al interlayer thickness will be included to assess how successful the coatings were. The results in this chapter will be displayed in the following order: the results of an initial deposition of Al utilising a system with plain bushings, results of films that were produced using a coating system which utilised bearings and then coatings made with the assistance of a drive chain. When displaying the results for films deposited on the final coating apparatus, the use of different thickness Al interlayers will progress onto the deposition and characterisation of different thickness Al_2O_3 layers, deposited on top of the aforementioned interlayers.

8.1 Trial deposition

Wires were initially coated with aluminium (15 min, 4A, 140 sccm Ar) for proof of concept, using a prototype coating rig (similar to the resulting rig but made using Al and plain Ag bushings). SEM and EDX analysis confirmed the presence of aluminium on the surface of the wire as indicated in ***Figure 8.1***.

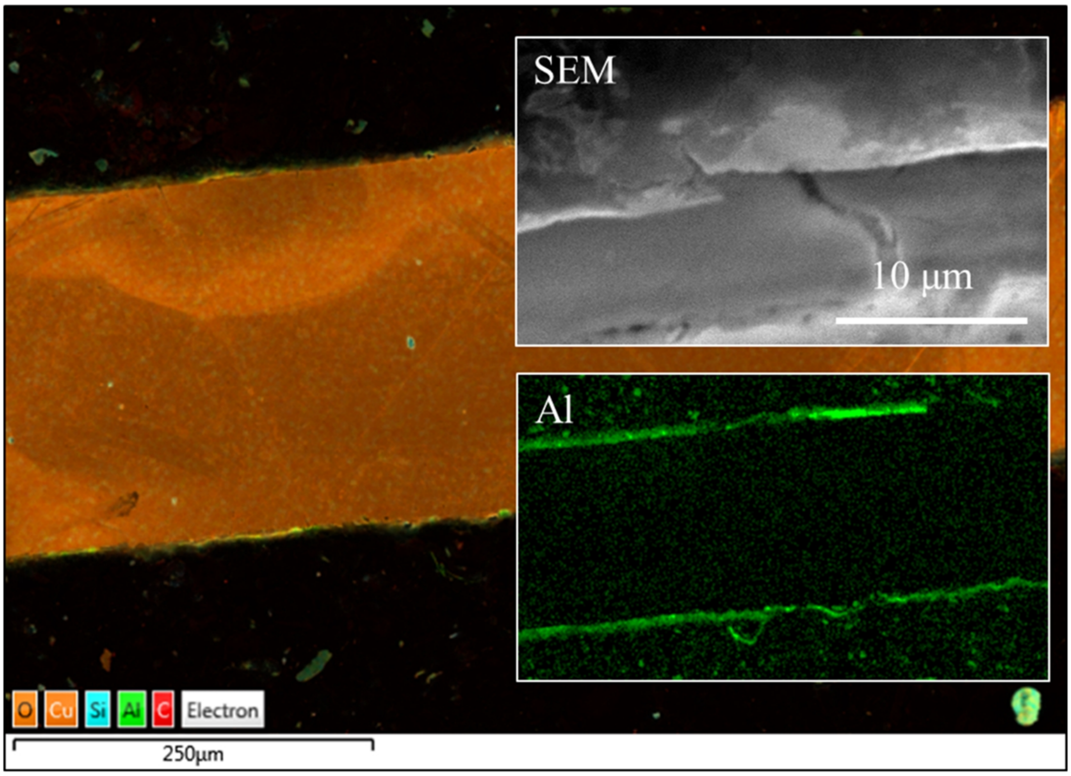

Figure 8.1: *Secondary electron SEM micrographs and EDX mapping of the cross section of an Al coated Cu wire, coated using the trial deposition apparatus.*

The coating was up to 6.7 µm thick, and contained cracking and sites of delamination. This could be a result of the processing methodology and the large thickness of the film. The trial tests showed that the coating rig would apply a coating to the wires.

8.2 Coating without chain drive

Al coatings were deposited as in the methods section using the final coating rig. The Al coatings applied at different rotational speeds, were then implemented as interlayers for subsequent alumina coatings. In these initial coatings polyimide tape was used in the bearing grooves to reduce abrasion as the wire was pulled around the system.

8.2.1 Bias Application

Application of sample bias during the cleaning stage resulted in the etching of surface contaminants from the wires. However, the application of a substrate bias during the deposition period led to arcing along the length of the wire, limiting its use in the deposition of Al and Al_2O_3. Bias voltages during etching was maintained at -40 V because above this there was a risk of the wire arcing and breaking (which occurred for bias etching at -150 and -100 V).

8.2.2 Tensile testing

Tensile testing was used to determine the load required to initiate coating failure. Delamination/ cracking of the coatings as deposited onto 1 mm ø Cu wire was not seen in the force extension graph. However, sample slipping in the jaws resulted in some differences from the response of bare copper see test 1 in ***Figure 8.2***.

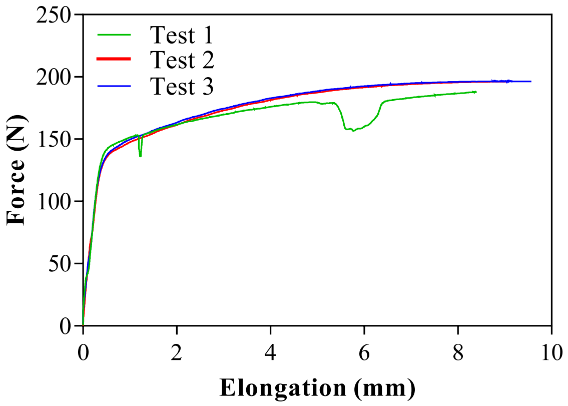

Figure 8.2: *Force extension plots for 2 A 0.5 RPM Al with thickness of ca. 300 nm. Note slipping in test 1 resulted in dips in the plot.*

Light microscopy was used to assess the delamination that was visible in samples following tensile testing. This showed patches of bare copper varying in size along the length of the wire, which were not visible in the coating prior to the testing see ***Figure* 8.3**. This indicated that intermittent tensile testing could be used to determine the extent of coating damage during testing.

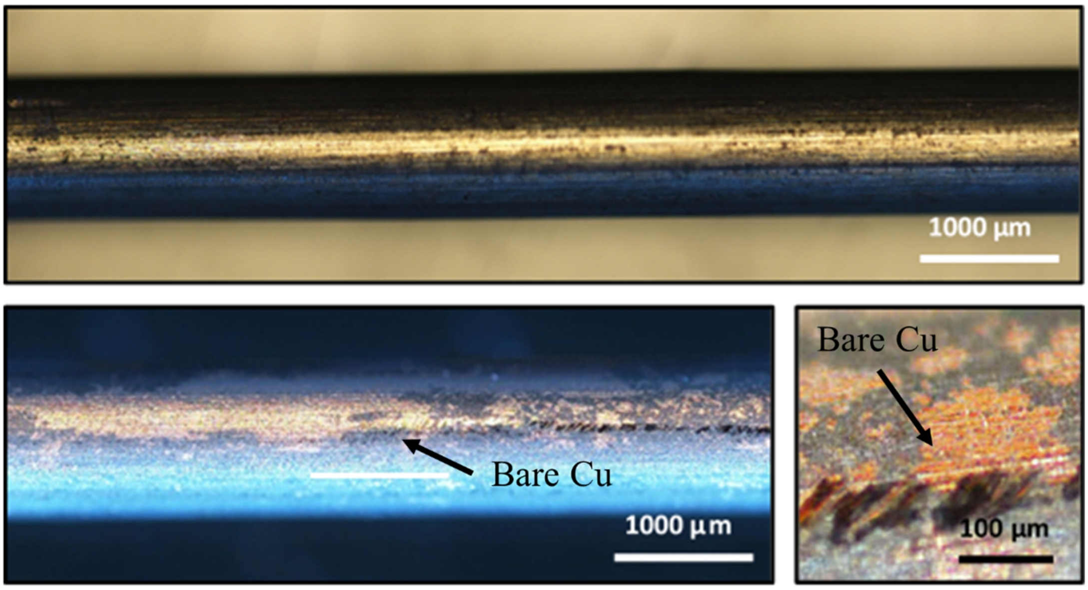

Figure 8.3: *Light micrographs of untested (top) and tensile tested (bottom) Al coated copper wire. Bare copper is seen in the bottom images following testing, as a result of delamination of the wire coating.*

8.2.3 Initial alumina coatings

PDC alumina coatings as developed earlier in this work (section (*4.1.3*)) were applied to the wire following the deposition of an Al interlayer as deposited at 0.5 rpm. FTIR peaks correlating to Al-O bonding were identified in the FTIR taken around a samples of coated wires as in ***Figure 8.4***.

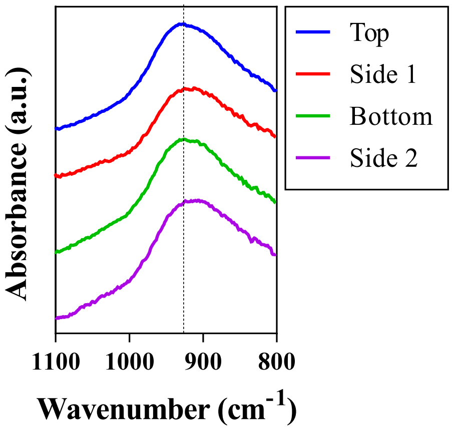

Figure 8.4: *FTIR spectra for wires coated with 1 layer of alumina using the methodology stated in section (4.1.5) with one* Al_2O_3 *coating run. An Al interlayer was deposited on the wire at 1.5 rpm. The legend indicates the measured sites across the wire.*

8.3 Coating with chain drive

Results from this point onward relate to films deposited once the reel to reel drive chain had been implemented along with bias etching of the wire at 0.5 rpm and - 40 V (for two complete reel to reel cycles) with a view to improving adhesion and decreasing wait time for deposition.

8.3.1 Initial deposition at sputtering distance of 55 mm

This section will show the results of wires coated with no substrate bias at a distance of 55 mm. Due to arcing along the wire when depositing using a substrate bias, the bias was turned off when the shield was not in front of the target.

Interlayer deposition was carried out resulting in a colour change as the Cu was coated with Al. Micrographs of the wire didn’t show any significant delamination. However, the adhesion of this film was poor and once bent the films could easily be rubbed off. This made further mechanical testing impractical because the wire would need to be straightened and the ends bent for testing.

The Al_2O_3 films when deposited at this distance showed significant delamination and cracking along the sample as shown in ***Figure 8.5***. Delamination meant that carrying out further mechanical or electrical testing was not beneficial for these coatings, because of short circuiting and the presence of cracking before tensile testing.

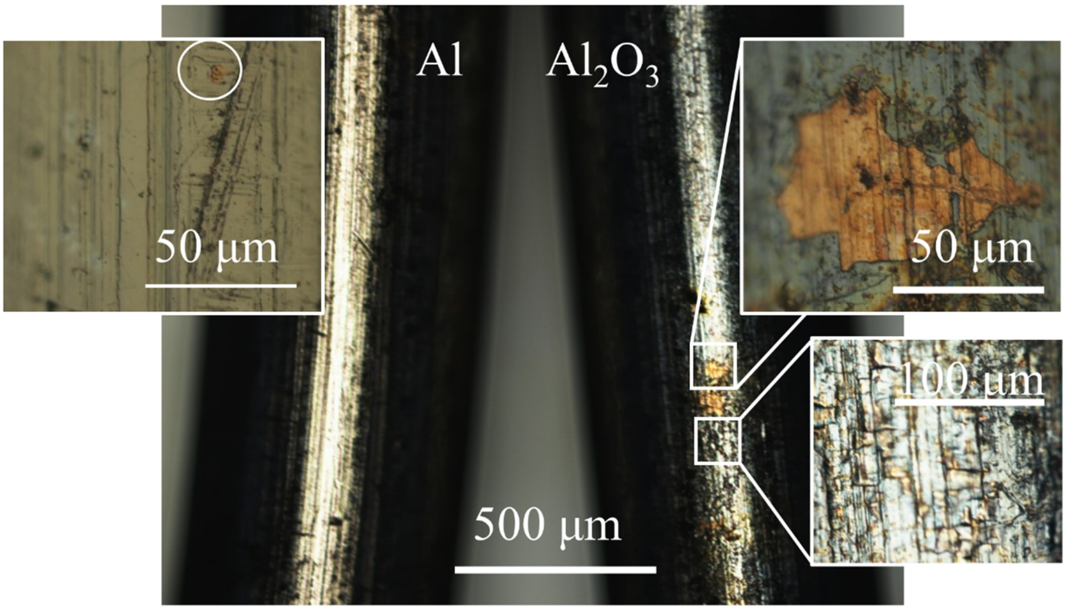

Figure 8.5: *Micrographs of Al (left) and Al_2O_3 (right with Al interlayer) coated Cu wire with inset high magnification micrographs displaying delamination with visible Cu in both cases.*

SEM showed the Al_2O_3 film had a thickness of 349 ± 15 nm and 345 ± 10 nm on the opposite side. The films appeared to be featureless, see ***Figure 8.6***.

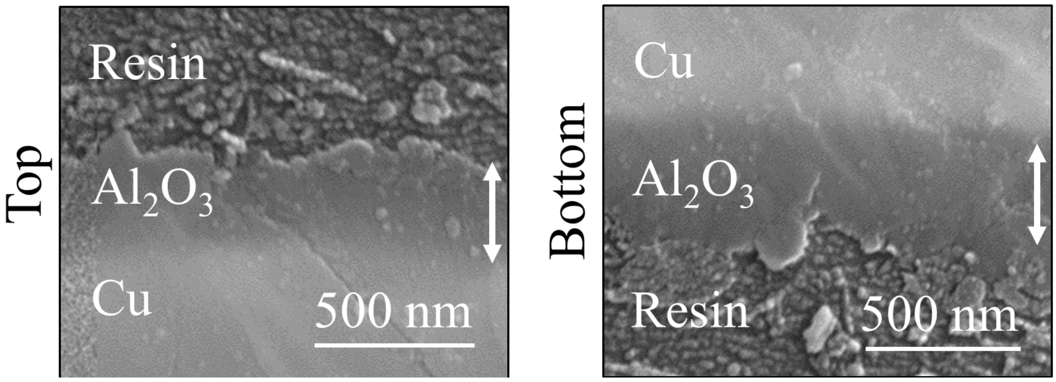

Figure 8.6: *Cross sectional secondary electron SEM micrographs of Al_2O_3 coated wire with an Al interlayer deposited at 1.5 rpm followed by 0.5 rpm reactive PDC Al_2O_3 coating from two opposite sides of the wire.*

FTIR was used to confirm the presence of Al_2O_3 on all sides of the wire and showed a peak with an average position of 917.6 cm^{-1} resulting from Al-O bonding, as shown in ***Figure 8.7***. *A* shoulder in the peak was seen at the higher wavelength of 1107.6 cm^{-1}.

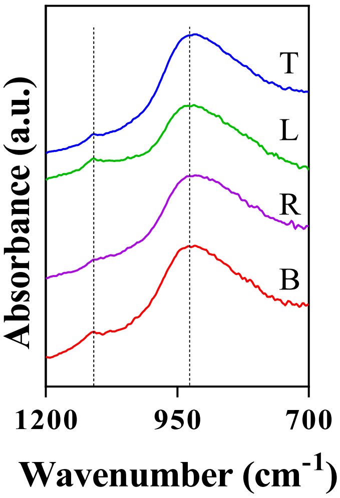

Figure 8.7: *FTIR spectra taken from around the circumference of the Al_2O_3 film as deposited onto Cu wire (T=top, L=left, R=right and B=bottom sides) at a distance of 55 mm with no substrate bias at 0.5 rpm.*

8.3.2 Methods for resolving arcing during deposition with a substrate bias

Whilst the above work has shown it possible to deposit Al and Al_2O_3 films consistently around a wire, the arcing events prevented the use of biasing, leading to poor adhesion and delamination in the Al_2O_3 films. As a possible solution the distance between the substrate and the target was increased from 55 to 100 mm with a view to reducing the charge build up on the wire. However, arcing still occurred upon application of a -40 V bias, which was the lowest which could be consistently applied using the TEER-UDP650.

Removal of bearing insulation (in the form of Kapton® tape) which was initially implemented as a way to remove wire abrasion, was shown at 100 mm wire target distance to resolve arcing issues along the length of the wire. Thus a target separation of 100 mm was maintained without Kapton® with a view to depositing the most adherent films.

8.4 Optimised wire coatings

Using the chain drive, increased substrate distance (100 mm) and longer bias cleaning period (two complete reel to reel cycles at -150 V) and application of bias during deposition Al_2O_3 (- 40 V) coated wire was produced. Al_2O_3 was applied on top of Al interlayers, which were deposited to different thickness by varying the reel to reel rotational speed. Note that in the final films the bearings were machined to remove a step in the wire groove, upon the discovery that the Al_2O_3 coating was being removed following deposition as seen in **Figure 8.9**.

8.4.1.1 Interlayer Characterisation

Light microscope images showed that PDC Al coated the wire regardless of coating speed, however, in each case some small delamination sites could be seen as highlighted in ***Figure 8.8***.

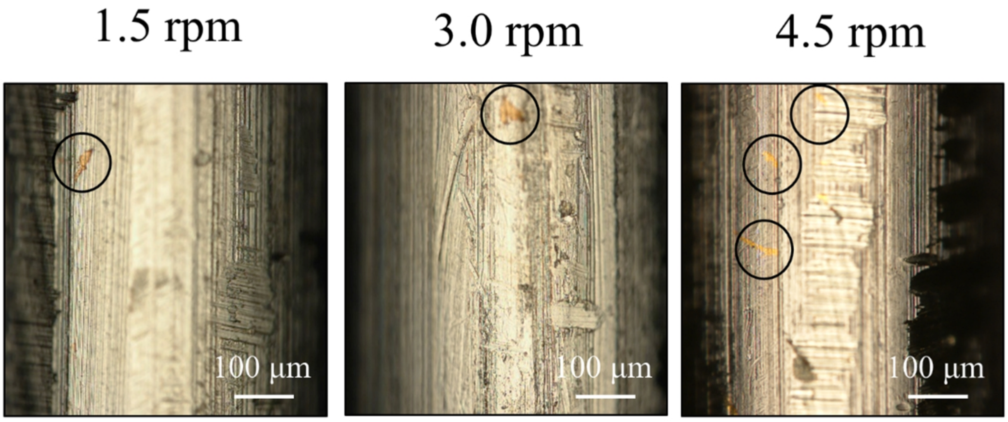

Figure 8.8: *Light microscope images of Cu wires coated in PDC Al, deposited at increasing reel to reel speed to modify the coating thickness as indicated above the micrographs. Defects in the wires have been circled in each instance.*

8.4.2 Al_2O_3 coated wire characterisation

Wires were coated with an Al interlayer as previously shown at 1.5, 3.0 and 4.5 rpm (see ***Figure* 8.8**) and then coated with a single layer of Al_2O_3 applied at 0.5 rpm, using the same PDC parameters as used in section (*4.1.3*). Light microscopy showed bare copper throughout for all of the Al_2O_3 coatings. The delamination was systematic on both sides of the wire which weren't directly exposed to the plasma. Every wire experienced this delamination to a similar extent. Following the machining of the bearing grooves to remove a step it was clear that the wear of the films was considerably reduced. ***Figure 8.9*** shows practically no wear on the samples made with a 1.5 rpm interlayer and smoothed bearings, the bias cleaning stage also implemented a higher bias voltage the smoothed bearing samples.

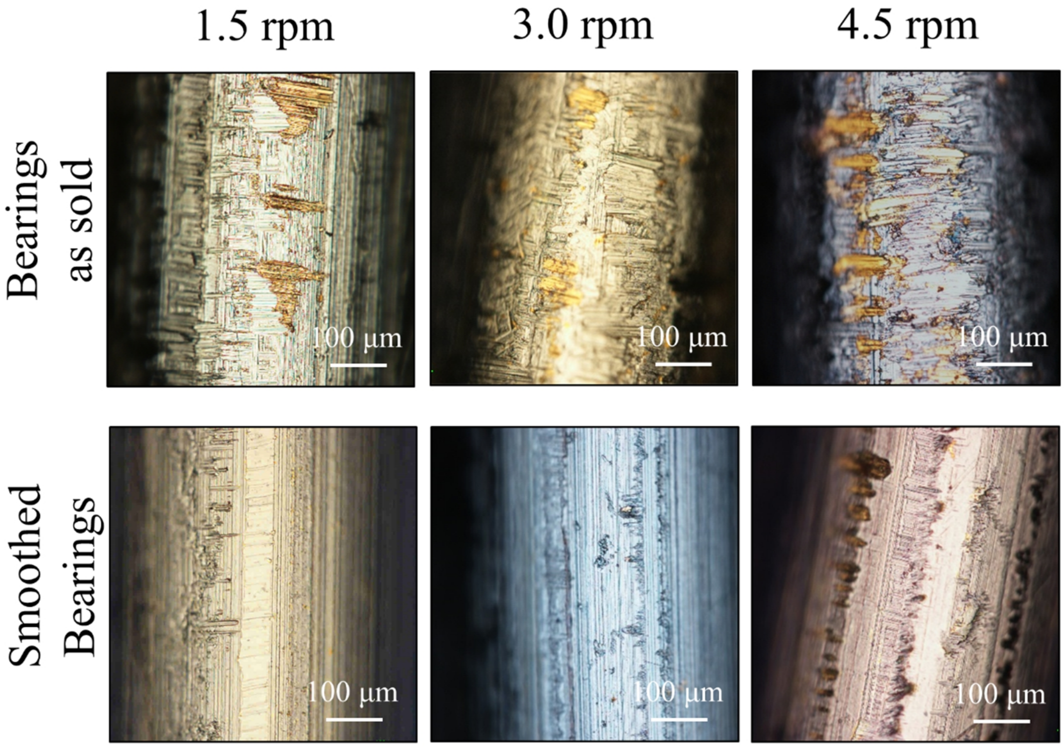

Figure 8.9: *Light microscope images of the surface of Al_2O_3 coated Cu wires with varying rotation speed during interlayer deposition (indicated above the image). (top) With as received bearings, (bottom) with step machined away from the bearing grooves.*

It was shown that the average film thickness for single layer Al_2O_3 films with 1.5, 3.0 and 4.5 rpm interlayers were 312 ± 40 nm, 208 ± 15 nm and 202 ± 16 nm respectively. It can also be seen from ***Figure 8.10*** that the films were generally featureless.

Interlayer speed (rpm)	*Average total film thickness (nm)*
1.5	*312 ± 40*
3.0	*208 ± 15*
4.5	*202 ± 16*

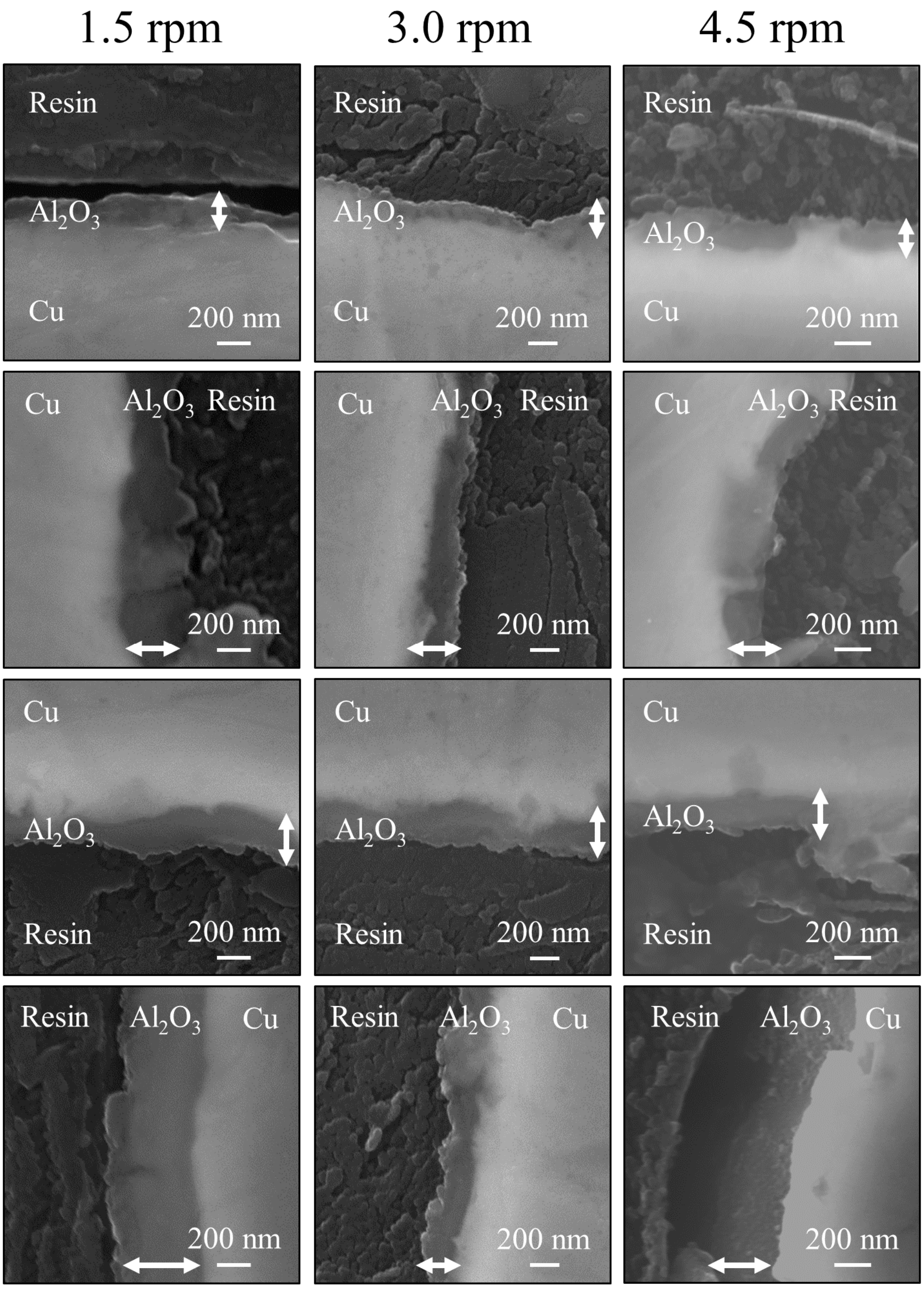

Figure 8.10: *A table of thicknesses followed by secondary electron SEM micrographs from the cross section of Cu wires coated with a single Al interlayer with a deposition speed as indicated above each column and one layer of Al_2O_3, deposited at 0.5 rpm. Images are taken clockwise around the samples going down the columns.*

Tensile testing of the wires showed that coatings produced using a 1.5 rpm Al interlayer and a - 40 V bias cleaning stage had failures at > 180 MPa and > 206 MPa resulting from transverse and combination cracking/ delamination respectively (***Figure 8.11***). Samples produced using the same conditions except with smoothed bearings and a bias clean at -150 V produced coatings with transverse and longitudinal cracking failures stress of > 177 and > 216 MPa respectively; minimum possible failure strain and stress are shown in ***Figure 8.11***.

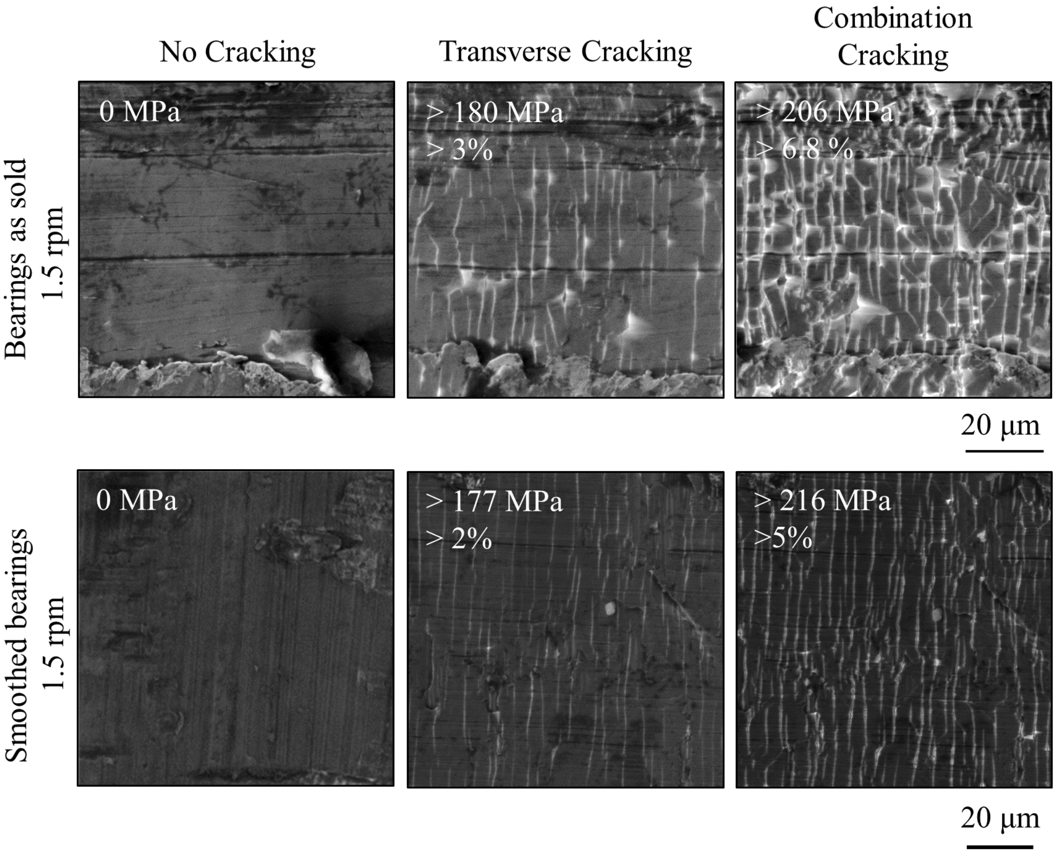

Figure 8.11: *Cracking in Cu wires coated with an Al interlayer deposited at 1.5 rpm and 1 layer of PDC Al_2O_3 deposited at 0.5 rpm. It can be seen that transverse cracking is followed by combination cracking during tensile testing at loads above 125 MPa. Note tensile stress was applied in the direction horizontal to the page.*

As a result of the decreased wear (see optical images ***Figure 8.9***) in the films produced using the smoothed bearings the following characterisation was carried out on wire cleaned at - 150 V bias using the new bearings. FTIR analysis showed the presence of Al-O bonding on all sides of the wire in all cases despite different interlayers (see ***Figure 8.12***). There was also no shift in the FTIR peak position regardless of the side of the wire the spectra was taken, or the thickness of the interlayer.

Interlayer (rpm)	***Wavenumber (cm^{-1})***			
	Top	*Bottom*	*Left*	*Right*
1.5	*924*	*922*	*922*	*920*
3.0	*910*	*916*	*889*	*899*
4.5	*899*	*920*	*897*	*921*

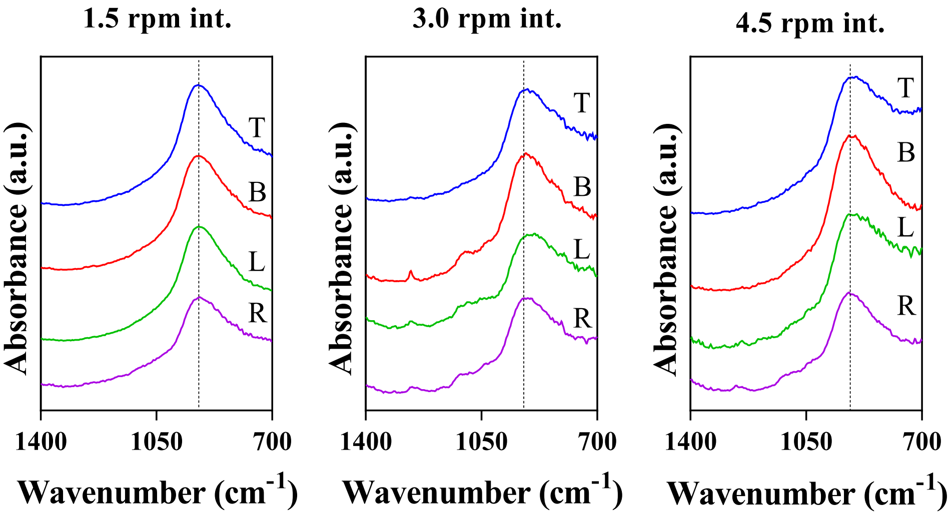

Figure 8.12: *FTIR Al-O peak positions for coated wire, measured around the circumference of same samples, coated with an Al interlayer with speed as indicated and a single layer of Al_2O_3. Associated spectra from around the wire are included below.*

Electrical testing of the wire was not possible in this case because the layer of Al_2O_3 was not thick enough to prevent wire to wire conduction in wound pairs, as identified using a multi meter.

8.4.3 Multi-pass Al_2O_3 films

8.4.3.1 3 layer Al_2O_3 coatings

Multiple passes of the PDC Al_2O_3 coating were applied in order to give a thicker Al_2O_3 layer. This was carried out in order to facilitate electrical measurements of the film. FTIR again showed the presence of Al-O peaks in all of the coatings regardless of the number of coating passes. Using interlayers deposited at speeds higher than 1.5 rpm resulted in broader peaks with a lower wavenumber, see ***Figure 8.13***.

Interlayer (rpm)	***Wavenumber (cm^{-1})***			
	Top	*Bottom*	*Left*	*Right*
1.5	*921*	*914*	*916*	*923*
3.0	*842*	*860*	*833*	*842*
4.5	*866*	*831*	*854*	*826*

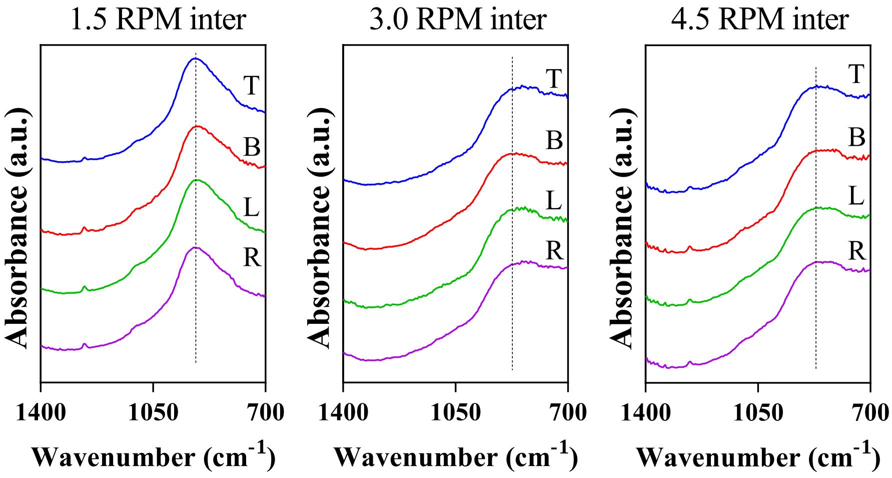

Figure 8.13: *FTIR Al-O peak positions for coated wire, measured around the circumference of same samples, coated with an Al interlayer as indicated and 3 layers of Al_2O_3. Associated spectra are included below.*

SEM thickness analysis showed average thickness as laid out in ***Table 8.1*** respective to interlayer deposition speeds of 1.5, 3.0 and 4.5 rpm. The thicknesses were relatively consistent around the cross section of the wire and the largest variation of 300 nm was seen in 1.5 rpm films. The greatest variation within the measurements was seen between samples which were perpendicular to each other, see ***Table 8.1*** for thickness variations. SEM also showed the films to be generally featureless with no crystal structure apparent as seen in ***Figure 8.14***.

Table 8.1: *Average, minimum and maximum coating thickness and in sample variation for Cu wires coated with 1 layer of Al (speed indicated in the left column) and 3 layers of* Al_2O_3 *deposited at 0.5 rpm.*

Sample interlayer speed (rpm)	***Average coating thickness (nm)***	***Error (nm)***	***Min (nm)***	***Max (nm)***
1.5	*470*	*25*	*355*	*650*
3.0	*395*	*10*	*315*	*442*
4.5	*375*	*20*	*262*	*432*

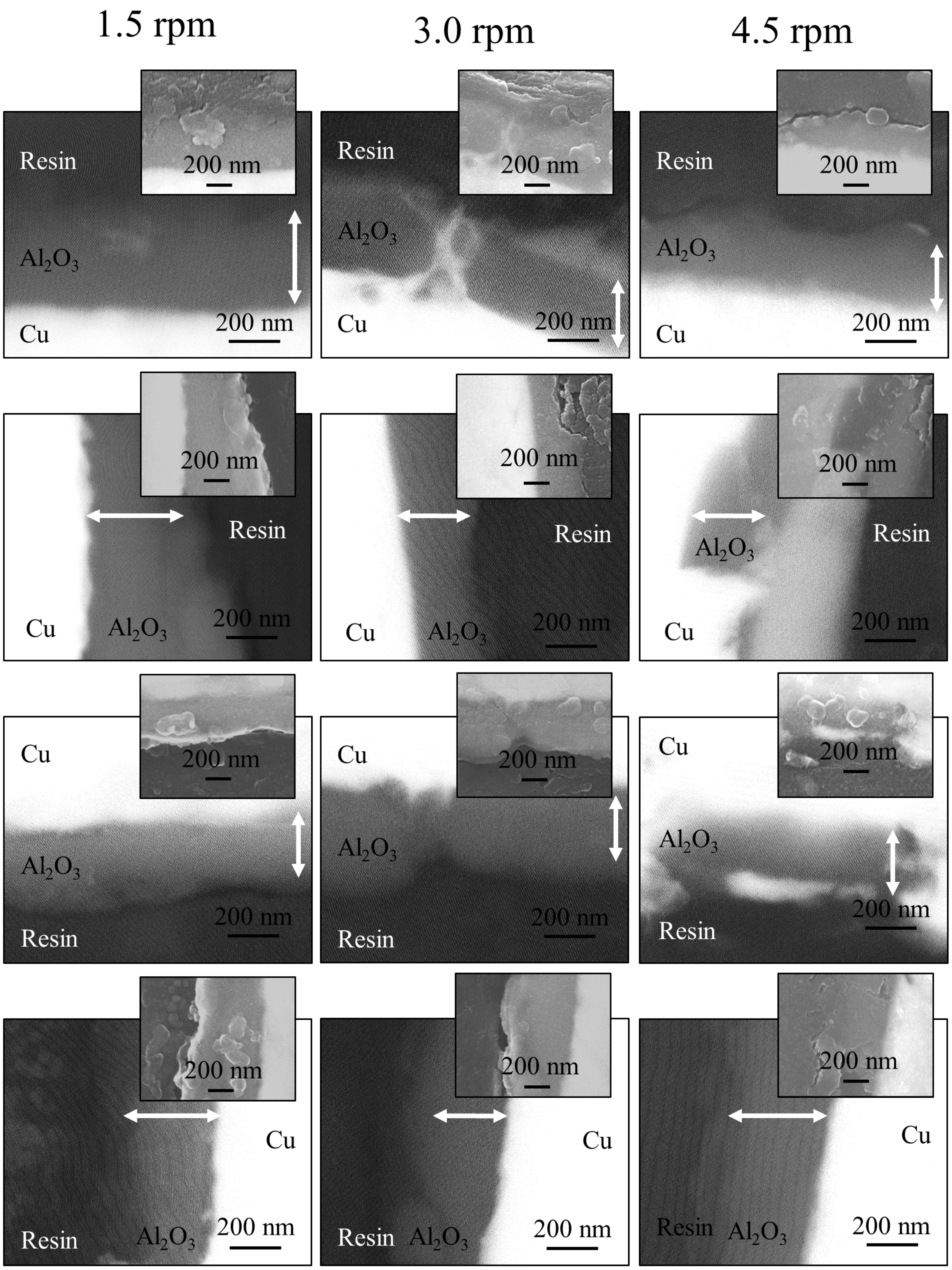

Figure 8.14: *Cross sectional back scattered SEM (with secondary electron inset) images of wire coated with 3 passes of* Al_2O_3 *on top of an Al interlayer deposited at the speed indicated. Images are taken from around a cross section of the corresponding wire moving around in a clock wise fashion down the columns.*

Light microscopy showed some wear on the wires much less, however, than when the as received bearing were used and when the lower substrate bias was applied. Wear was most obvious in the wire coated with thinner interlayers as seen in ***Figure 8.15***. It appears that the Cu which is seen has come from wear caused by the processing, opposed to delamination caused by poor adhesion or high internal stress, as seen in ***Figure 8.5***.

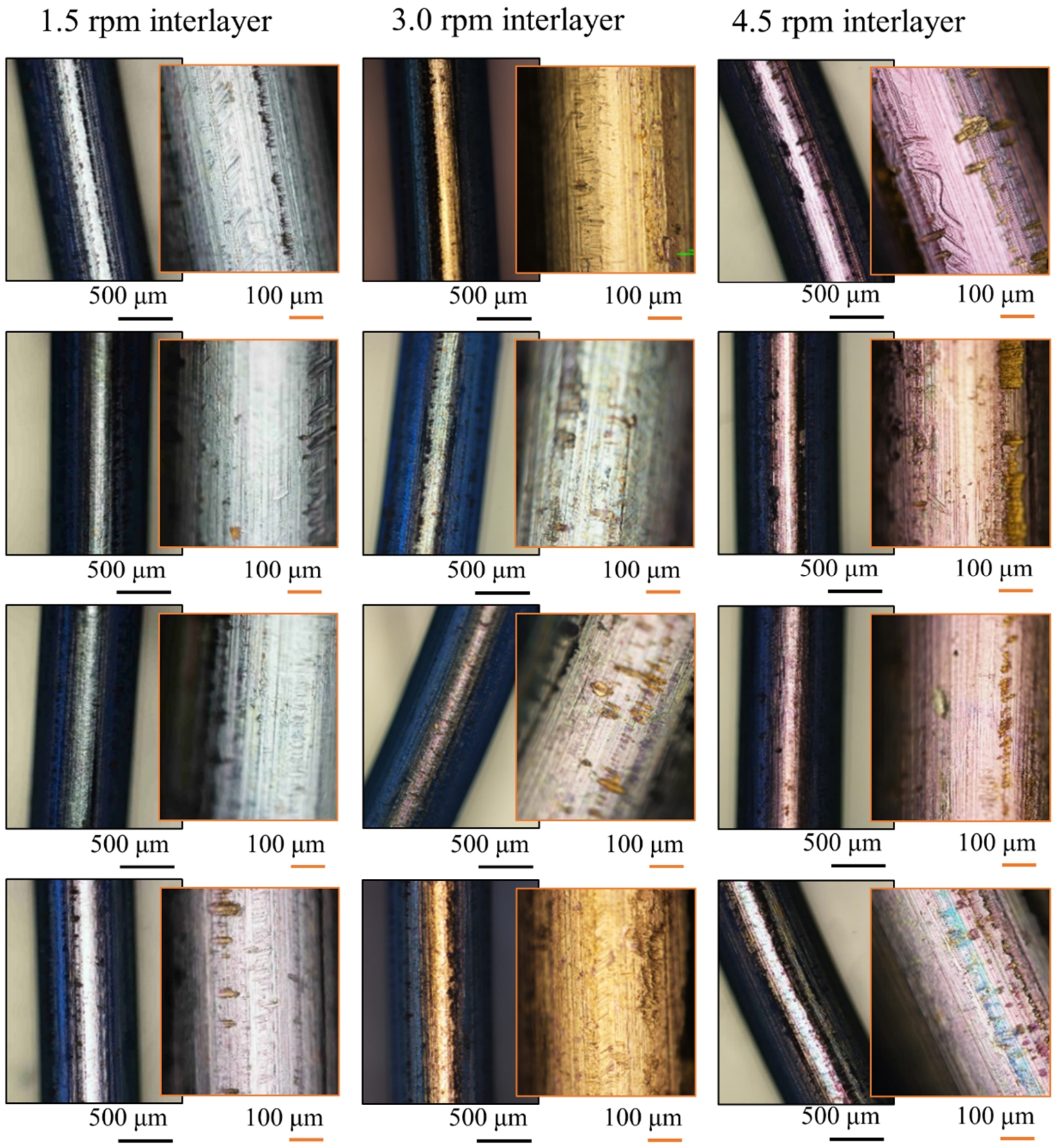

Figure 8.15: *Light microscope images of Cu wire bias cleaned at -150 V for two winds and coated with an Al interlayer at 1.5, 3.0 or 4.5 rpm and then coated with 3 Al_2O_3 layers deposited at 0.5 rpm. Cu which is visible through the coating is more prevalent in the 3.0 and 4.5 rpm interlayer coatings. Top row taken from the top side, 2nd row images from the inside of the wire as wound onto the on reel, 3rd row from the outside and the 4th row taken from the bottom of the wire.*

8.4.3.1.1 Mechanical Testing

Tensile testing showed the lowest possible onset of cracking failure in the Al_2O_3 coating was above a strain of 1.5 % and a stress of 177 MPa. Cracking initially appeared perpendicular to the direction of the wire, with longitudinal cracking occurring at a minimum strain of 4 % and a stress of 204 MPa. ***Figure 8.16*** shows crack formation and gives the minimum possible stress and strain at formation for each sample.

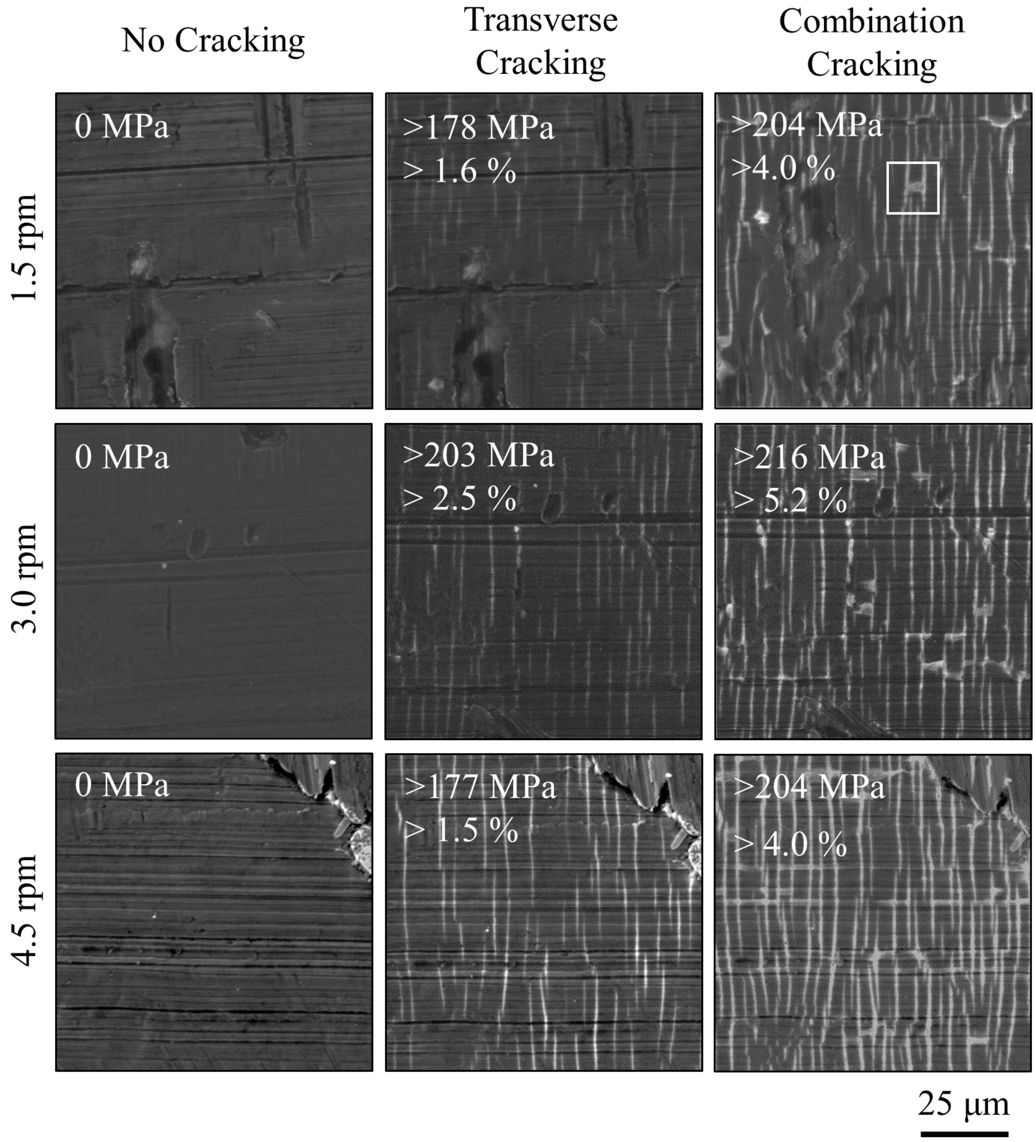

Figure 8.16: *Coating crack formation (secondary electron SEM images) on Cu wires. The coatings consist of an Al interlayer deposited at 1.5, 3.0 or 4.5 rpm followed by 3 layers of* Al_2O_3 *deposited at 0.5 rpm. Inset are the minimum failure stress and strain for each test group. Note tensile stress was applied in the direction horizontal to the page. A longitudinal crack has been highlighted in the top right tile.*

The minimum and maximum possible failure values were determined from the SEM micrographs and the stress strain data that was obtained. This data shows no specific relationship between the tensile properties and interlayer thickness (***Table 8.2***).

Table 8.2: *Minimum and maximum cracking failures perpendicular and parallel to the direction of tensile stress for Cu wire samples coated with 3 layers of* Al_2O_3 *at 0.5 rpm on top of an Al interlayer as outlined in the table.*

	Cracking, (Strain (%) (Stress (MPa))		***Longitudinal / Delamination, (Strain (%) (Stress (MPa))***	
Al int. (rpm)	***Min***	***Max***	***Min***	***Max***
1.5	*1.6 (178)*	*1.7 (204)*	*4.0 (204)*	*12.9 (229)*
3.0	*2.5 (203)*	*6.3 (216)*	*5.2 (216)*	*32 (229)*
4.5	*1.5 (177)*	*1.6 (178)*	*4.0 (204)*	*8.0 (216)*

Crack density for the tested samples was determined and showed that samples produced with a 3 rpm interlayer had the lowest crack density up to 15% strain as seen in ***Figure 8.17.***

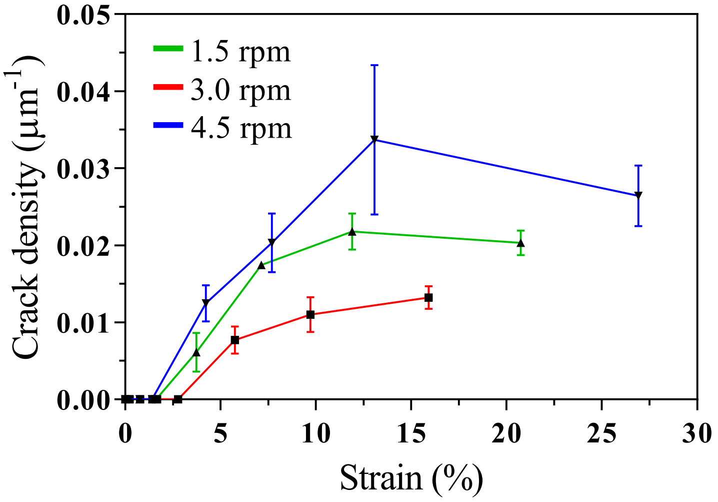

Figure 8.17: *Crack density - resulting from tensile testing - for Cu Wire coated with 3 layers of* Al_2O_3 *at 0.5 and an Al interlayer deposited at 1.5, 3.0 or 4.5 rpm.*

8.4.3.2 5 layer Al_2O_3 coatings

Coatings with a 1.5 rpm Al interlayer and 5 layers of Al_2O_3 were produced as previously. FTIR identified a broad absorbance band < 1000 cm^{-1} with a peak at an average wavenumber of 802 cm^{-1} indicating Al-O bonding, as seen in ***Figure 8.18***.

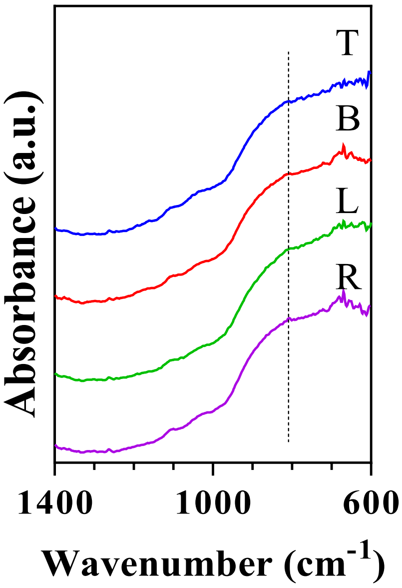

Figure 8.18: *FTIR spectra for Cu wire coated with 1 layer of Al at a speed of 1.5 rpm and 5 layers of Al_2O_3 deposited at 0.5 rpm. Where measurements were taken around a sample T (top), B (bottom), L (left) and R (right).*

Light microscopy of the wires showed that there were areas of bare copper wire exposed, these appeared to be the result of external wear, as opposed to a delamination caused by the deposition process. However, the extent of the wear was not as detrimental as in samples deposited using the original unaltered bearings see ***Figure 8.19***.

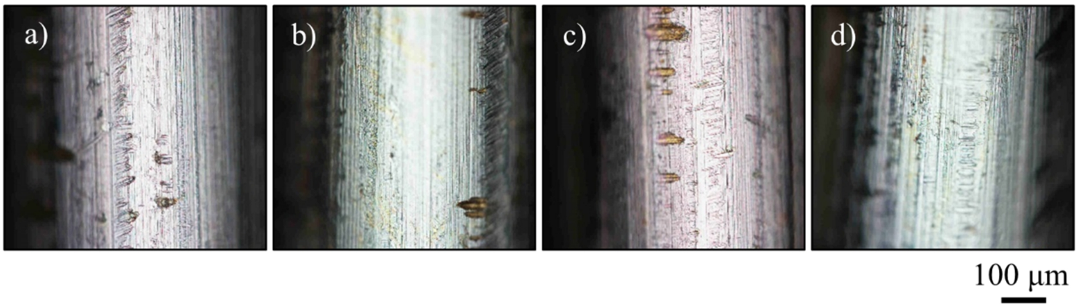

Figure 8.19: *Light micrographs of Cu wire coated with 1 Al layer deposited at 1.5 rpm and 5 layers of Al_2O_3 each deposited at 0.5 rpm. Where a) is the top b) is the inside, c) is the bottom and d) is the outside of the wire respective to the off reel of the coating apparatus.*

SEM analysis showed these films had an average thickness of 1160 ± 74 nm, see ***Figure 8.20*** for cross sectional SEM images of the wire, which also show no morphology which would indicate a crystalline structure.

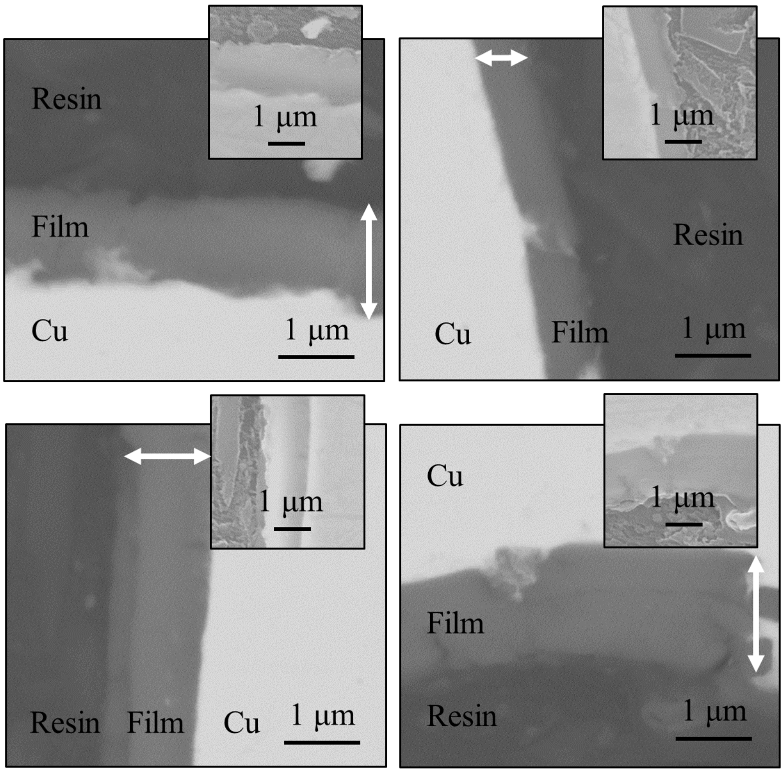

Figure 8.20: *Cross sectional SEM of Cu wire coated with one layer of Al at 1.5 rpm and 5 layers of Al_2O_3 at 0.5 rpm showing the thickness around the wire. Backscattered electron micrographs are displayed with secondary electron images inset.*

Tensile testing revealed that the coatings initially failed above a strain of 1.6 % and a stress of 179 MPa. Further failure in the form of longitudinal cracking occurred above a strain of 4.4 % and a stress of 216 MPa. Longitudinal and transverse cracking occurred as seen in ***Figure 8.21***.

	Transverse cracking (Strain (Stress (MPa)))		*Longitudinal cracking (Strain (Stress (MPa)))*	
Al_2O_3 layers	***Min***	***Max***	***Min***	***Max***
1	*2.3 (177)*	*7.5 (216)*	*4.9 (216)*	*20.2 (242)*
3	*1.6 (178)*	*4.1 (204)*	*4.0 (204)*	*12.9 (229)*
5	*1.6 (179)*	*4.8 (216)*	*4.4 (216)*	*9.4 (229)*

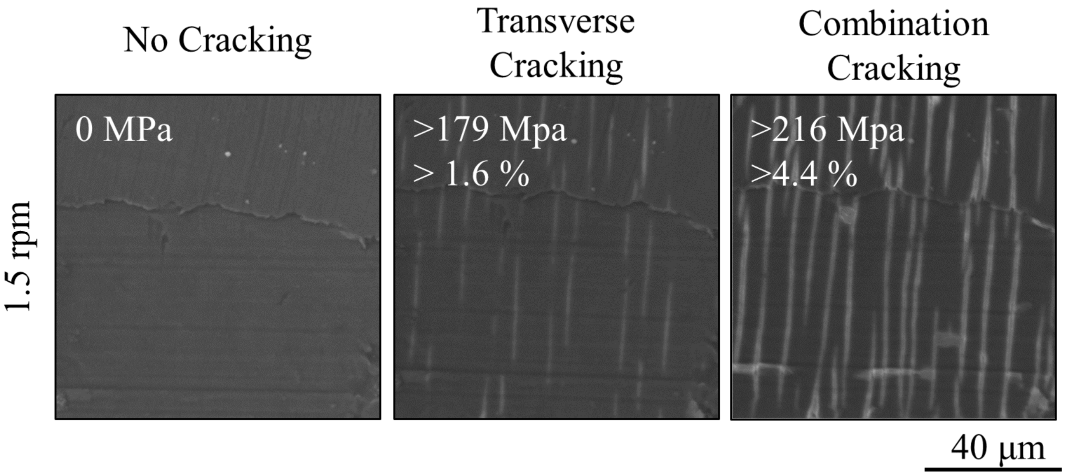

Figure 8.21: *Maximum and minimum range for cracking failure seen in multilayer Al_2O_3 (deposited at 0.5 rpm) coated wire with an Al interlayer (Deposited at 1.5 rpm). Data was generated by finding the maximum and minimum possible onset of failure from SEM micrographs. (Below)Tensile test failure sites for Cu wire coated with an Al interlayer deposited at 1.5 rpm and 5 layers of PDC Al_2O_3 deposited at 0.5 rpm. Note tensile stress was applied in the direction horizontal to the page*

Crack density was determined to increase with decreasing film thickness as seen in ***Figure 8.22***, where the minimum crack density was seen for samples produced with 5 layers of Al_2O_3.

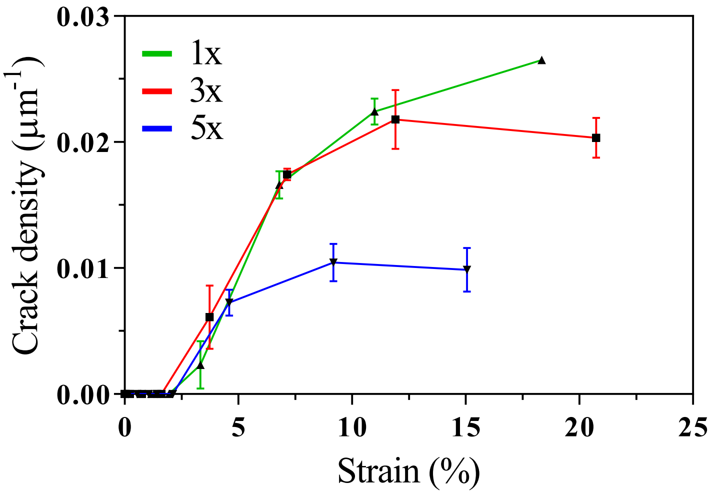

Figure 8.22: *Crack density in Al_2O_3 coated wires with an Al interlayer deposited at 1.5 rpm with varying layers of Al_2O_3 applied at 0.5 rpm (1x, 3x and 5x).*

The critical bending radius was calculated using the equations outlined in the experimental procedure (see section (*4.4.2*)). These calculations resulted in the values given in ***Table 8.3***. Calculated critical bending radii were found to be relatively consistent within the range between 200 and 333 µm.

Table 8.3: *Critical bending radii as calculated for Al_2O_3 coated copper wires with various interlayer and coating thickness.*

Interlayer	***Al_2O_3 layers***	***Calculated Critical Bending radius (µm)***
1.5	*1*	*217*
	3	*313*
	5	*313*
3.0	*3*	*200*
4.5	*3*	*333*

8.4.4 Electrical testing

Because of the apparent reduction in the amount of delamination seen in ***Figure 8.9*** 1.5 rpm interlayer wires produced with the - 150 V bias cleaning stage were used for electrical measurements. The tested samples had 3 or 5 Al_2O_3 layers on top. However, breakdown testing was not possible as the testing resulted in short circuiting of the system. This suggested discontinuity in the coating. This was shown to be the case for both 3 and 5 layer coatings in crossed pair, wound and single wire measurement configurations.

8.4.5 Cost summary

A cost analysis taking into account raw materials and power required to run the rig was carried out to show a standing cost to load the rig which also takes into account the cost of cleaning and the dead length of wire in the rig and would need to be added to the cost of every run and a cost per additional meter of coated wire. This was purely looking at the cost on a research scale, and costs could be reduced by scaling the experiment. The following costs took into account system elements including the PSU, pumps and the water chiller as well as consumables such as solvents, substrates, targets and gases.

- Standing cost including a pump down time of 5 h: £13.05
- Cost to coat each additional m of wire: £1.60

Further note on cost analysis: these costings take into account stated power ratings of equipment and that the equipment is running at full capacity and has not factored in any deterioration in running specifications. The initial equipment coat has also not been taken into account.

8.5 Summary

The alumina coatings deposited in this chapter have shown that the deposition process needs to be carefully tailored to avoid defects in the films. Coatings were shown to conform around the circumference of the wire and FTIR confirmed the composition of the films. The thickness was shown to shift in Al-O binding peak suggesting a change in internal stress, which could be a limiting factor in future coating design. Additionally transverse cracking at strains below 1.6 % was followed by longitudinal cracking below 4.0 % as a result of plastic deformation in the coatings during tensile testing. Defects in the wire did, however, cause problems with electrical continuity.

9 Results: Heat treatment of sputtered films

It was hypothesised that heat treatment could be a route to improving the electrical and mechanical properties of the as deposited PDC films and PDC + RF composites; through removal of defects and intrinsic stress. This treatment would also have the potential to increase interfacial blending in the composites which could improve adhesion. Thus an initial investigation into heat treatment of PDC samples revealed that 300 and 500 °C hour long treatments resulted in no observable delamination and FTIR analysis showed that there was no shift in the peak position for the Al-O phonon vibrations see ***Figure 9.1***. Thus 500 °C was chosen because it was higher than the polymeric insulation and would demonstrate the coatings high temperature potential. Further to this results outlining the effect of heat treatment on the composites is included with the goal of assessing whether heat treatment improved these properties.

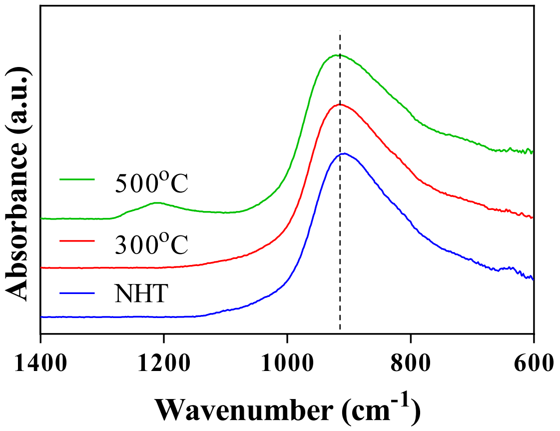

Figure 9.1: *FTIR spectra for thermally treated PDC thin films as deposited onto copper foil.*

There were varying degree of colour change between the samples, those treated at 500 °C became transparent showing only a copper surface where those treated at 300 °C showed the same change to a lesser extent. As there was no observable delamination upon a 500 °C heat treatment, it was chosen as the treatment temperature for subsequent films.

9.1 Heat treatment of PDC films

The following section concerns the structural, mechanical and electrical characteristics of PDC films, as produced for section (*4.1.3*) and heat treated at 500 °C in air for one hour as in section (*4.1.6*).

9.1.1 Characterisation

FTIR showed two main peaks, one resulting from Al-O LO phonon vibrations at 921.94 cm^{-1} and one at 1219.93 cm^{-1}. XRD analysis showed the deposited material was X-ray amorphous with an amorphous hump seen > 20 °. XPS analysis showed an electron binding energy of 74.2 eV for Al_2P electrons and a Al:O ratio of 0.73. No additional hump for Al^0 was seen in the Al_2P high resolution spectra. See ***Figure 9.2*** for FTIR, XPS and XRS spectra.

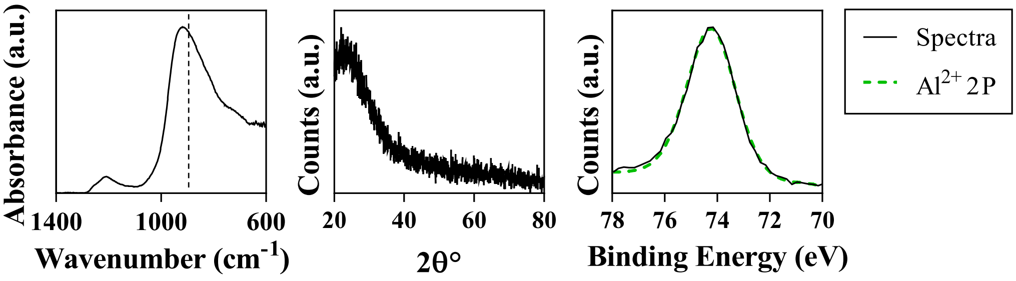

Figure 9.2: *FTIR, XRD and Al_2P high resolution XPS spectra for PDC thin films deposited onto Cu foil, borosilicate glass coverslips and Cu disk respectively, all having a post deposition heat treatment at 500 °C.*

The pull off adhesion strength for heat treated PDC films was 21.8 ± 3.4 MPa *ca.* two times lower than that of non-heat treated films. All tested samples failed through partial adhesive failure between the substrate and Al_2O_3 films, shown by Al on the pull off stubs analysed by EDX and the lack of substrate seen in the light micrographs, see ***Figure 9.3*** for stub EDX and typical failure images profiles.

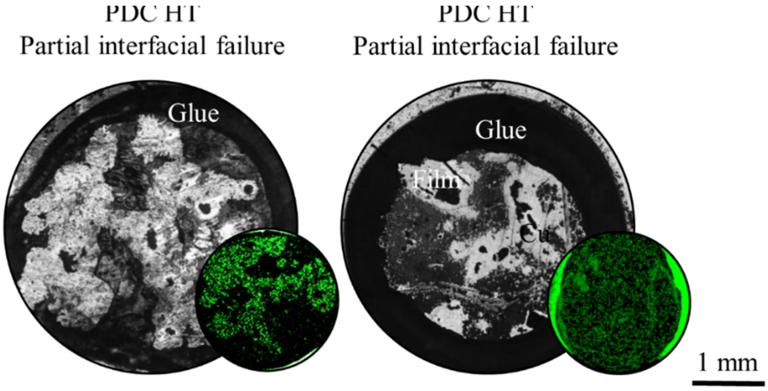

Figure 9.3: *Pull off test light micrographs showing typical pull off partial interfacial delamination for heat treated PDC films as deposited onto Cu disks. Al EDX of the pull off stub has been included to the bottom right of each sample, note that high amounts of Al seen around the side of the sample result from the Al stub holder.*

Surface roughness of the heat treated samples was determined by AFM to be 59 ± 36 nm. Analysis of scratch tests revealed that cohesive failure occurred at 1.55 ± 0.35 N through arc tensile cracking with adhesive failure occurring through buckling at 1.79 ± 0.43 N see ***Figure 9.4***. Note that the combination cracking seen in thicker PDC films was not present in the thinner PDC or as in this case heat treated PDC films.

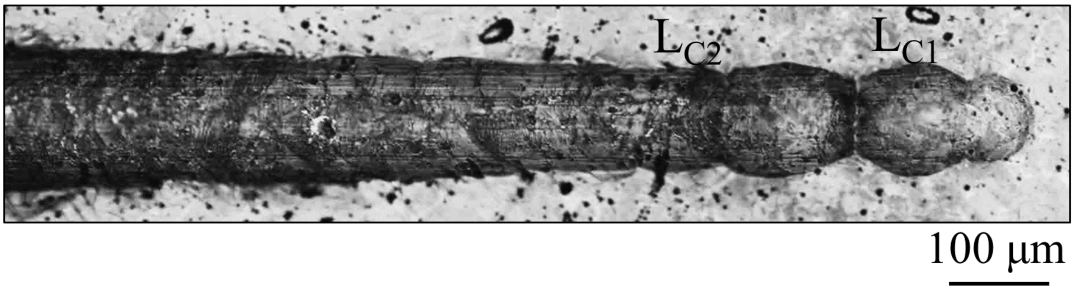

Figure 9.4: *Scratch test failure mechanisms for heat treated PDC films as deposited onto Cu disks. L_{C1} indicates the onset of tensile cracking and L_{C2} indicates the onset of buckling.*

PDC films had a breakdown voltage of 67.6 ± 5.8 V corresponding to a dielectric strength of 330 ± 30 $V\mu m^{-1}$ given an average thickness of 205 ± 6 nm as determined from the cross sectional SEM micrographs. The maximum leakage current prior to breakdown varied considerably with the maximum being *ca.* 10 nA as seen in ***Figure 9.5***.

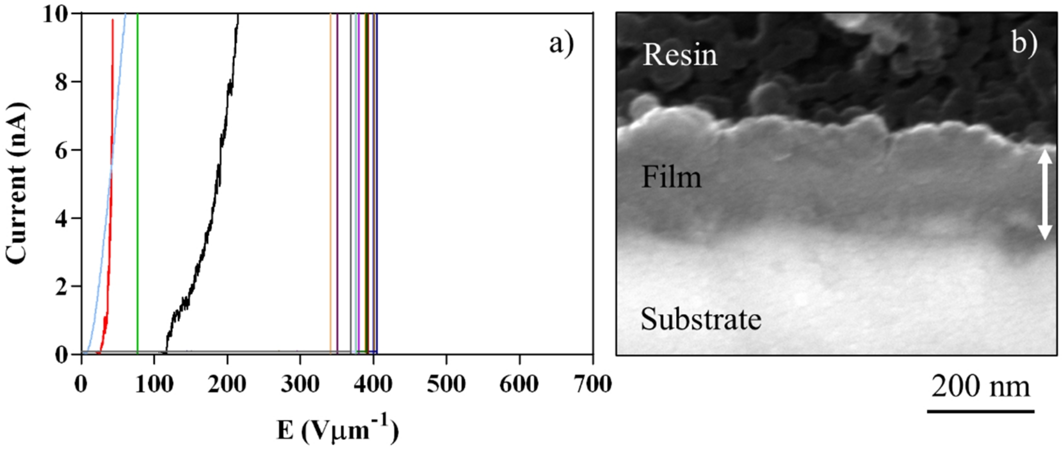

Figure 9.5: *a) AFM DB dielectric breakdown measurements of heat treated PDC alumina films deposited onto Cu disks as carried out using AFM DB. b) Cross sectional secondary electron SEM of heat treated PDC films as mounted in resin.*

9.2 Heat treatment of multilayer films

The Al_2O_3 composites containing either SiO_2 or Ta_2O_5 with 1x1, 2x2 or 4x4 layer configurations (as discussed in section (*4.1.4*)) were heat treated using the same procedure as the PDC films, see section (*4.1.6*).

9.2.1 Characterisation

A colour change was seen upon heat treatment of the samples, Ta_2O_5 multilayer films were generally a metallic blue colour and evolved into a more silver purple colour, SiO_2 multilayers were generally deep blue and became more copper coloured following heat treatment see ***Figure 9.6***.

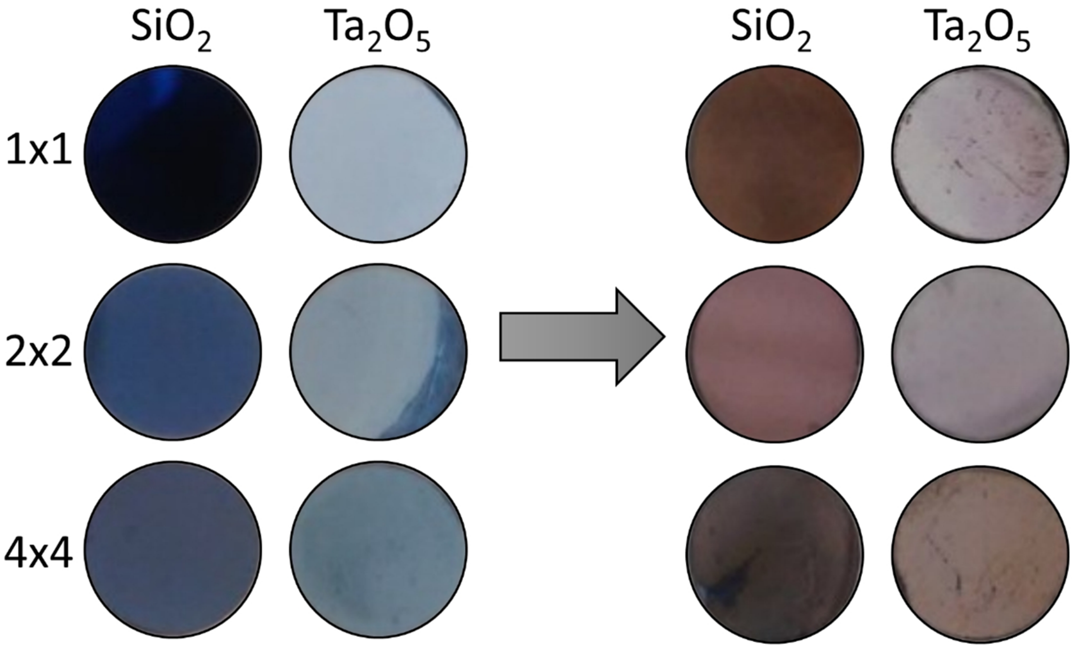

Figure 9.6: *Images of SiO_2 and Ta_2O_5 multilayer films as deposited onto Cu disks before (left) and after heat treatment (right) at 500 °C. Layer configuration is as indicated on the left of the images.*

However, in some samples the colour change wasn't complete, showing patches of original colour dispersed in the second colour. Signs of delamination appeared in a number of the films, on one disk of each of the 1x1 and 4x4 SiO_2 composites and on two disks for the 2x2 Ta_2O_5 multilayer composites. This was only partial and at the extremities of the disks such that it didn't prevent mechanical or electrical testing from being carried out on any of the samples.

FTIR spectra showed that heat treated SiO_2 films had two peaks, at 922.6 and 1240.8 cm^{-1}. In both cases the peaks had shoulders at lower wavenumbers (839.0 and 1172.0 cm^{-1} respectively). Ta_2O_5 films also showed two peaks with average positions of 1259.5 and 911.0 cm^{-1}, the peaks at 911.0 cm^{-1} all had a shoulder at *ca.* 804 cm^{-1}, which slightly decreased in intensity with respect to the main peak, as the RF layer thickness decreased, as in ***Figure 9.7***.

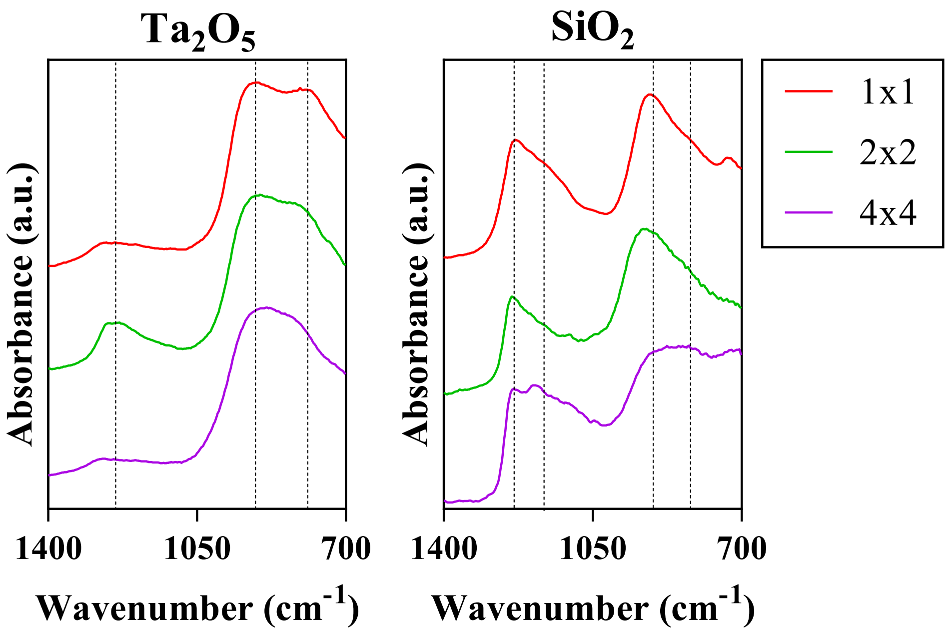

Figure 9.7: *FTIR spectra for* Ta_2O_5 *(left) and* SiO_2 *(right) multilayer composites as deposited onto copper foil. Peak positions have been indicated using the dashed lines.*

XRD showed a lack of peaks in any film, showing that the 500 °C treatment was insufficient to induce crystallinity in the ceramic materials, with no crystalline diffraction peaks. Amorphous regions in the diffraction patterns were found resulting from the films and substrate. Potential peaks were the result of elemental Al sputtered during the longer Al-Al_2O_3 transition see ***Figure 9.8***. Note that the possible peaks were assigned to Cu/Al materials at the substrate interface.

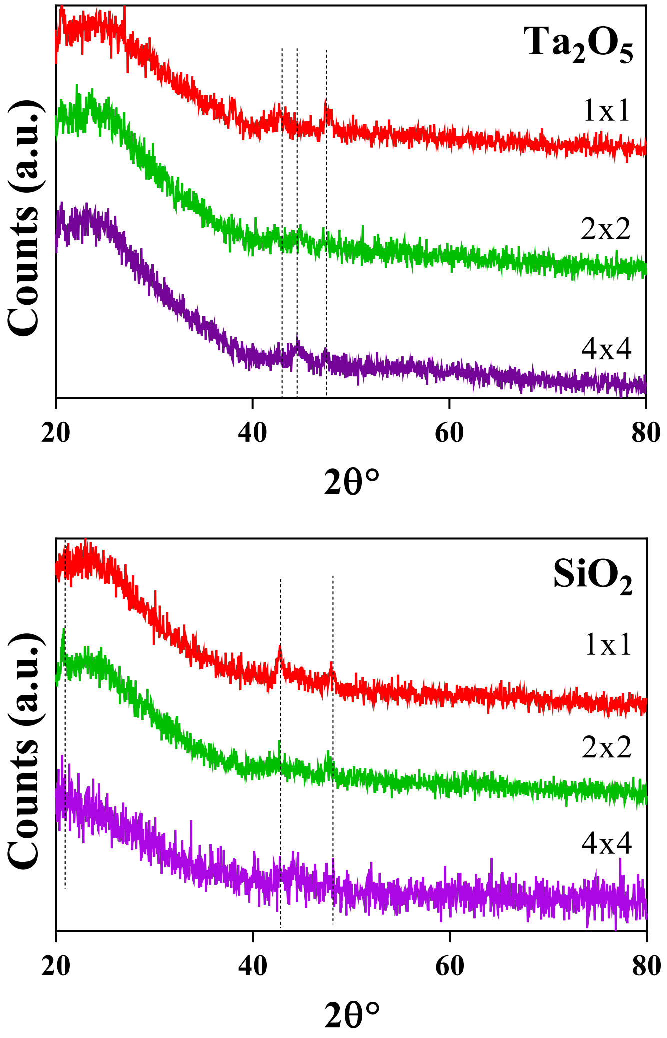

Figure 9.8: *XRD diffraction patterns for Ta_2O_5 composite (top) and SiO_2 composite (bottom) materials with varying layer configuration as deposited onto borosilicate glass slides. Dashed lines are used to indicate potential peaks resulting from the interlayer.*

The photo electron binding energy of Si_2P and Ta_4F electrons in the multilayer films was determined by XPS, which was also used to confirm stoichiometry and the oxidation state of the Si and Ta. Ta_4F and Si_2P electrons had average binding energies of 26.25 ± 0.04 eV and 103.33 ± 0.04 eV respectively corresponding to Ta^{5+} and Si^{4+}.

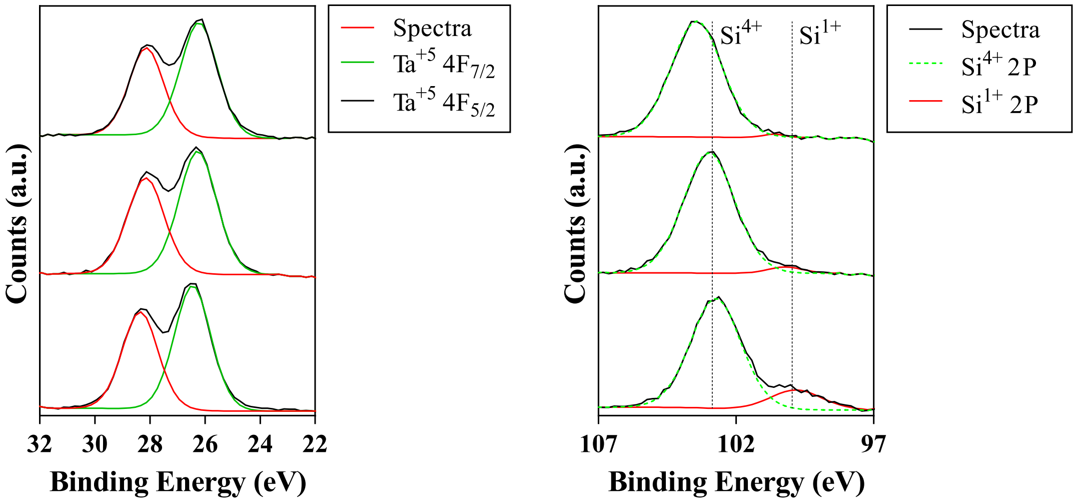

Sample	*Ta^{5+}_4F (eV)*	*Ta^{0}_4F (eV)*	*Ta^{0} %*	*Ta:O ratio*
1x1	*26.17*	*N/A*	*N/A*	*0.29*
2x2	*26.32*	*N/A*	*N/A*	*0.30*
4x4	*26.33*	*N/A*	*N/A*	*0.27*

Sample	*Si^{4+}_2P (eV)*	*Si^{0}_2P (eV)*	*Si^{1+} %*	*Si:O ratio*
1x1	*103.43*	*100.63*	*1.1 ± 0.1*	*0.55*
2x2	*103.32*	*100.55*	*3.4 ± 0.1*	*0.58*
4x4	*103.24*	*100.33*	*15.8 ± 0.2*	*0.61*

Figure 9.9: *XPS high resolution spectra for Ta_4F and Si_2P in Ta_2O_5 and SiO_2 319multilayer composites deposited onto Cu disks, followed by heat treatment at 500 °C. The table contains peak position data as well as Si_2P deconvolution data and Ta:O and Si:O ratios.*

However, as with non-heat treated films, the levels of Si^{1+} increased with an increasing number of layers to a maximum of 15.76 % for 4x4 films determined using the shoulder positioned at 100.5 ± 0.1 eV. The Si:O ratios of the films were all much higher than 0.5 reflecting the excess Si in the composites which increased with an increasing number of layers. Deconvolution of the O_1S peak also revealed that the contribution from the shoulder at 534.4 ± 0.1 eV remained consistent to the % concentration seen prior to heat treatment, whereas the contribution from the shoulder at 530.8 ± 0.1 eV increased. Binding energies and contributions can be found in ***Figure 9.10***. It is important to note that contributions to the component of the O_1S peak at lower binding energy may be made by other metal oxides including for copper as discussed later.

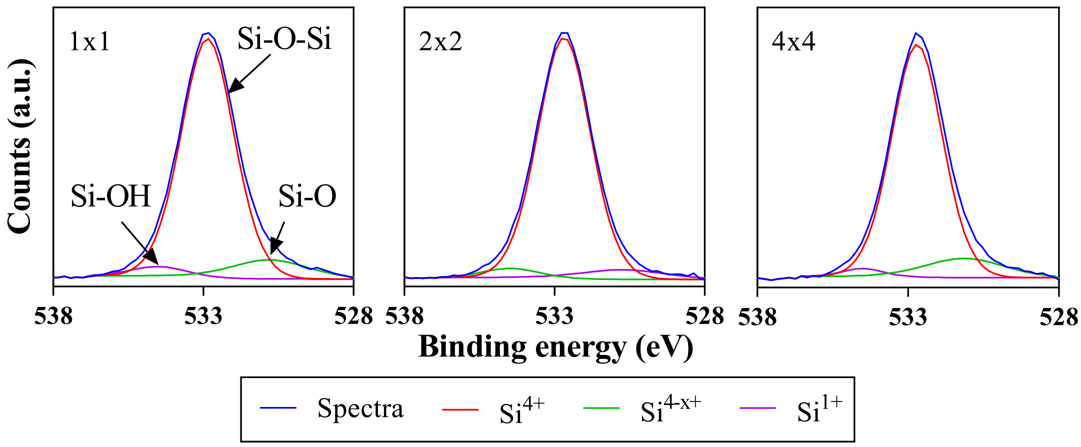

	Si^{4+}		***Shoulder 1***		***Shoulder 2***	
	(eV)	***%***	***(eV)***	***%***	***(eV)***	***%***
1x1	*532.65*	*86.50*	*534.30*	*3.51*	*530.60*	*9.90*
2x2	*532.68*	*90.73*	*534.47*	*3.60*	*530.74*	*5.68*
4x4	*532.70*	*86.63*	*534.51*	*2.34*	*531.14*	*11.04*

Figure 9.10: *Deconvoluted O_1S spectra, peak positions and % contribution, for heat treated SiO_2 composite films as deposited onto Cu disks. Layer configurations are indicated in the top left and peak assignments are indicated in the first spectra.*

No peaks resulting from Ta metal were seen in the films, however, in the survey spectra of both SiO_2 and Ta_2O_5 films, peaks resulting from Cu_2P photoelectrons were seen. The Cu_2P$^{3/2}$ peaks had positions of at 933.3 ± 0.1 eV and 933.2 ± 0.2 eV for Ta_2O_5 and SiO_2 composites respectively. The at.% of copper decreased to a minimum of 0.9 ± 0.01 at.% for the SiO_2 2x2 composites. The at.% of Cu was at least 4 times higher in the Ta_2O_5 composites. The amount of CuO was taken into account when calculating the Ta:O and Si:O ratios; Cu peaks were attributed to CuO (Cu^{2+}) because of the large satellite peaks characteristic of this oxidation state, see ***Figure 9.11*** . This CuO could also contribute to the sub stoichiometric SiO_2 shoulder seen in the O_1S peak in ***Figure 9.10***.

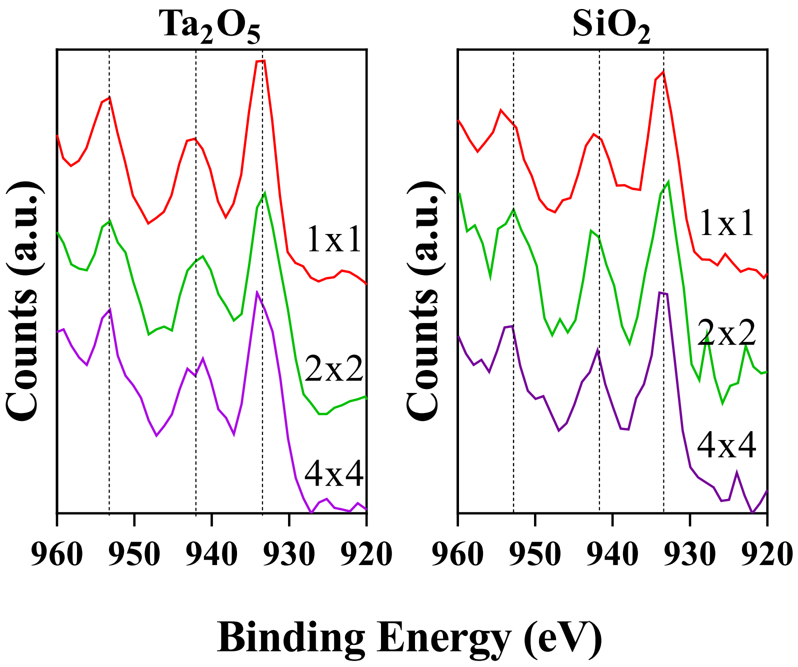

	Cu (% concentration)	
Sample	***HT Ta_2O_5***	***HT SiO_2***
1x1	*12.4 ± 0.1*	*2.7 ± 0.1*
2x2	*7.3 ± 0.1*	*0.9 ± 0.1*
4x4	*5.2 ± 0.1*	*2.0 ± 0.1*

Figure 9.11: *XPS spectra for Cu_2P$^{3/2}$ and Cu_2P$^{1/2}$photoelectrons from Ta_2O_5 (left) and SiO_2 (right) multilayer composites as deposited onto Cu disks and heat treated at 500 °C for 1 h. Peaks have been identified, including satellites at a higher binding energy and are indicated using a dashed line. The table below displays the Cu at.% in the composites.*

There was a large prevalence of delamination in resin mounted heat treated films imaged using SEM. Cracking and delamination was apparent in some of the films especially in the Ta_2O_5 composites. Heat treated films were generally featureless and showed thickness similar to that of non-heat treated films. Thickness and cross sectional imaging of films is provided in ***Figure 9.12***.

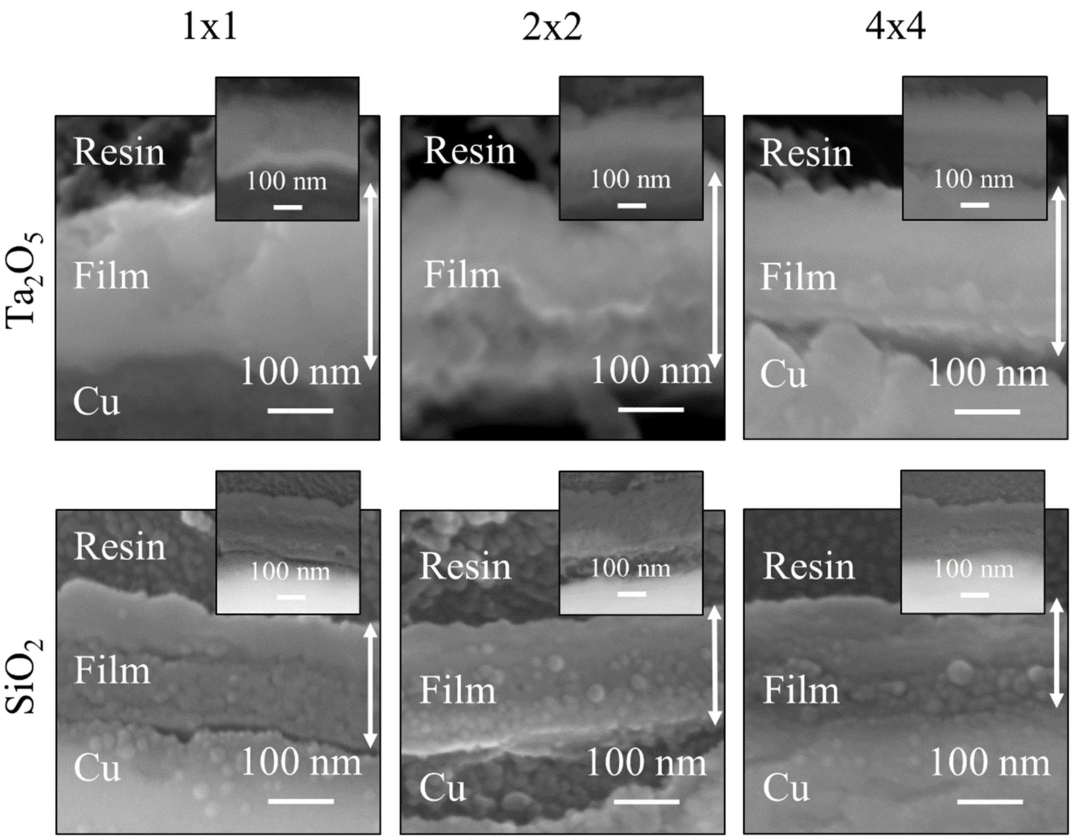

Sample	***Film thickness (nm)***	
	Ta_2O_5	***SiO_2***
1x1	*221 ± 21*	*185 ± 6.3*
2x2	*210 ± 8.5*	*187 ± 6.0*
4x4	*226 ± 8.0*	*171 ± 5.0*

Figure 9.12: *Cross sectional secondary electron SEM images of heat treated Ta_2O_5 composites (top row) and SiO_2 composites (bottom row) with inset backscattered electron images.*

9.2.2 Electrical properties

AFM DB measurements made on heat treated samples showed the highest breakdown values for heat treated composite films, with the 2x2 layer configuration. With dielectric breakdown occurring at 358 ± 31 and 517 ± 24 Vµm^{-1} for Ta_2O_5 and SiO_2 composites respectively. The 1x1 composites had the lowest dielectric strength in the case of both sets of composites, as seen in ***Figure 9.14** and **Figure 9.15*** .

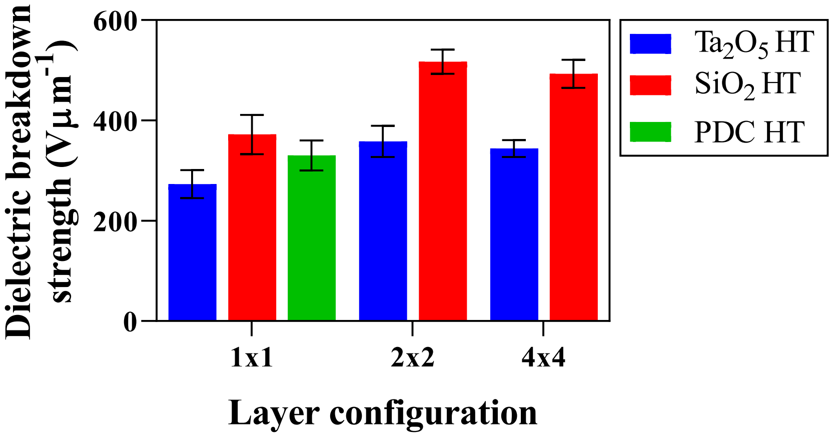

Sample		*Thickness (nm)*	*Breakdown AVG. (V)*	*N*	*Dielectric Strength (Vµm^{-1})*
SiO_2	***1x1***	*185 ± 6.3*	*68.8 ± 6.8*	*16*	*372 ± 39*
	2x2	*187 ± 6.0*	*96.8 ± 3.2*	*16*	*517 ± 24*
	4x4	*171 ± 5.0*	*84.4 ± 4.0*	*16*	*493 ± 28*
Ta_2O_5	***1x1***	*221 ± 21*	*60.3 ± 2.1*	*16*	*273 ± 28*
	2x2	*210 ± 8.5*	*75.2 ± 5.8*	*16*	*358 ± 31*
	4x4	*226 ± 8.0*	*77.7 ± 2.6*	*16*	*344 ± 17*

Figure 9.13: *Graphical and tabulated AFM breakdown voltage and dielectric strength values for heat treated Ta_2O_5 and SiO_2 multilayer composites as deposited onto Cu disks. Composite thickness and the number of test sites achieving breakdown (N) are also shown.*

As can be seen in these results, the SiO_2 composites had higher dielectric strength than the Ta_2O_5 composites (a minimum increase of 36 % as seen in 1x1 composites) when comparing samples with the same layer configuration. The maximum current leakages prior to breakdown were *ca.* 9 and *ca.* 7 nA for Ta_2O_5 and SiO_2 composites respectively, as seen in ***Figure 9.14*** and ***Figure 9.15***.

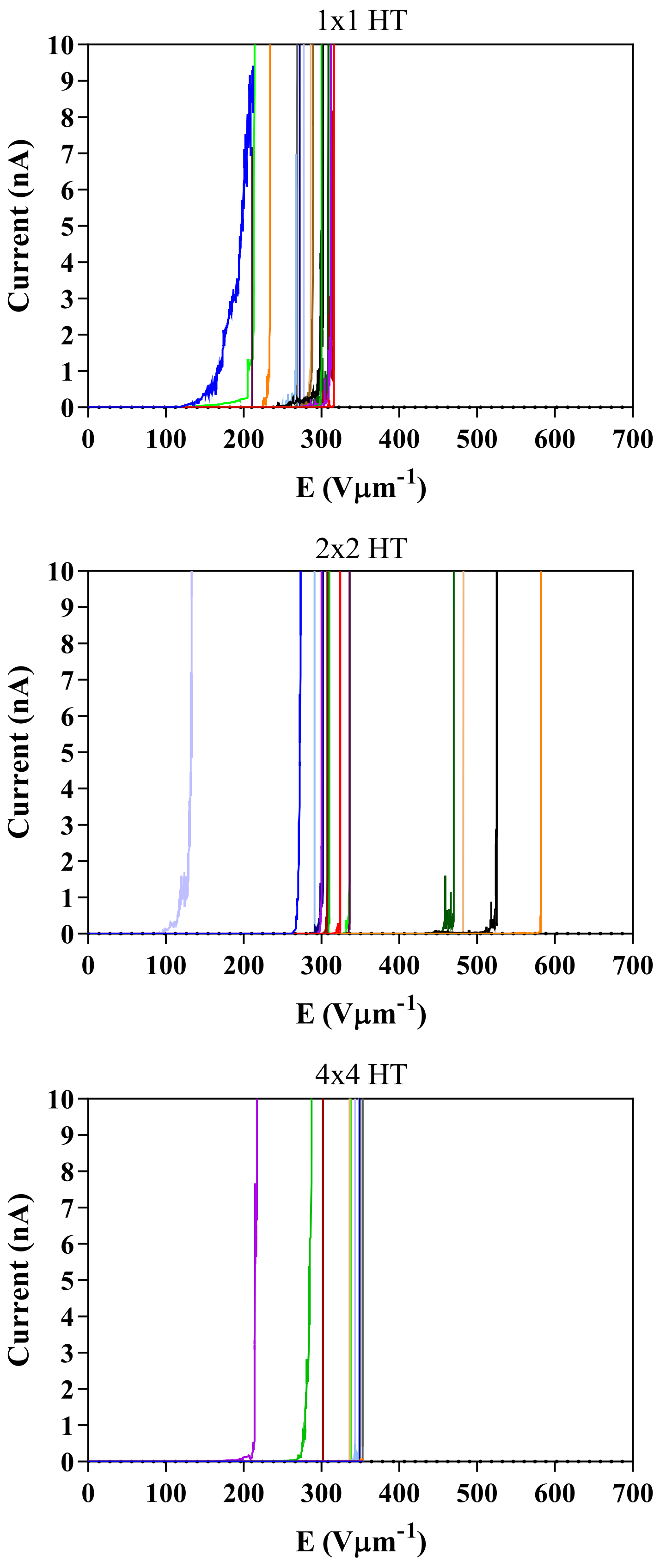

Figure 9.14: *AFM* DB *current plotted against applied field for heat treated* Ta_2O_5 *composite films as deposited onto Cu disks. The layer configuration is as indicated at the top of each graph.*

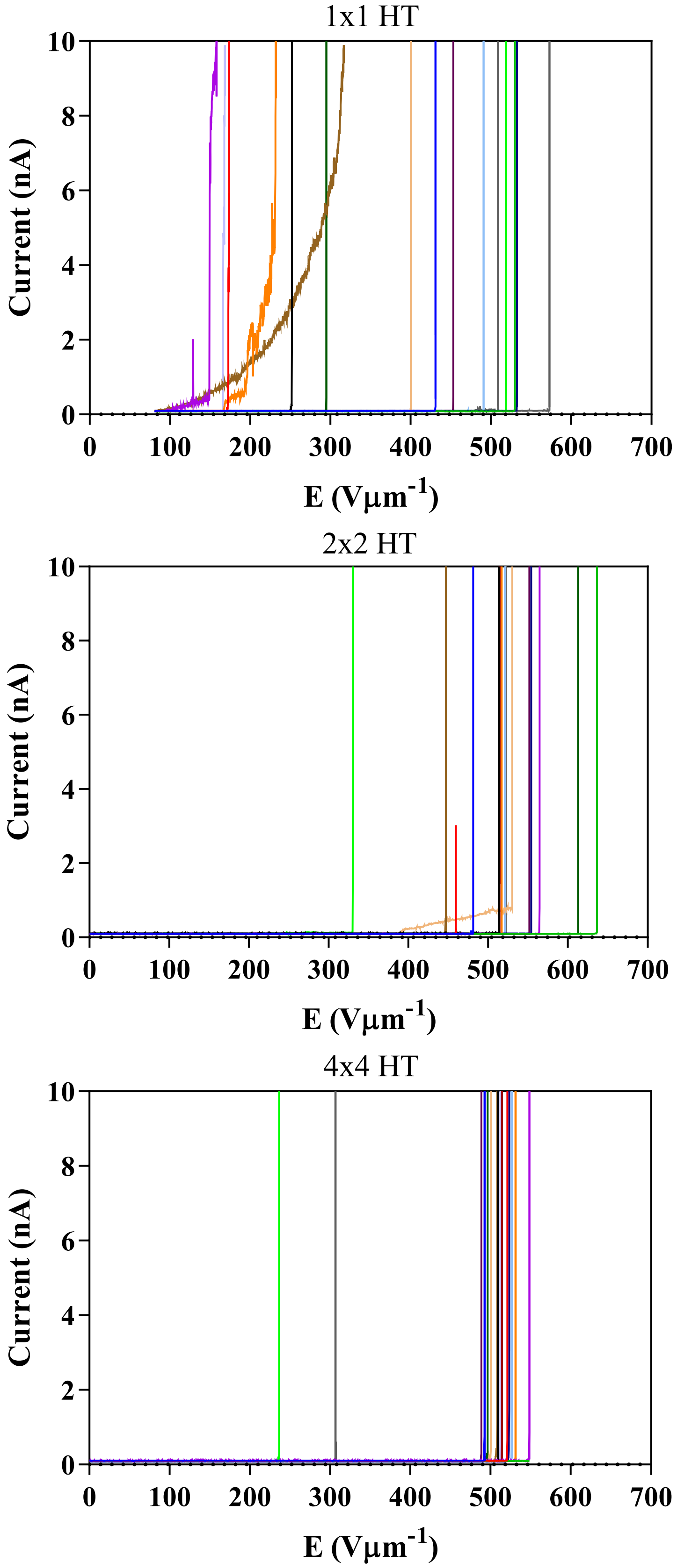

Figure 9.15: *AFM DB current plotted against applied field for heat treated SiO_2 composite films as deposited onto Cu disks. The layer configuration is as indicated at the top of each graph.*

Graphical analysis of the data was used as an indicator to conduction mechanism in the films. Schottky, Poole-Frenkle and Fowler-Nordheim analysis were all tested for their applicability, but due to high current variation and leakage a mechanism could not be reliably assigned.

9.3 Mechanical properties

AFM surface roughness values are included in ***Table 9.1*** and ranged between a Ra of 35 and 9 nm with the roughest films seen for the 2x2 films.

Table 9.1: *AFM average surface roughness (Ra) for heat treated multilayer films as deposited onto Cu disks.*

Sample	***Ra (nm)***	
	Ta_2O_5	***SiO_2***
1x1	*9 ± 2*	*10 ± 1*
2x2	*22 ± 5*	*35 ± 24*
4x4	*12 ± 2*	*10 ± 3*

Roughness of heat treated films was generally consistent regardless of treatment or layer configuration as seen in ***Figure 9.16***.

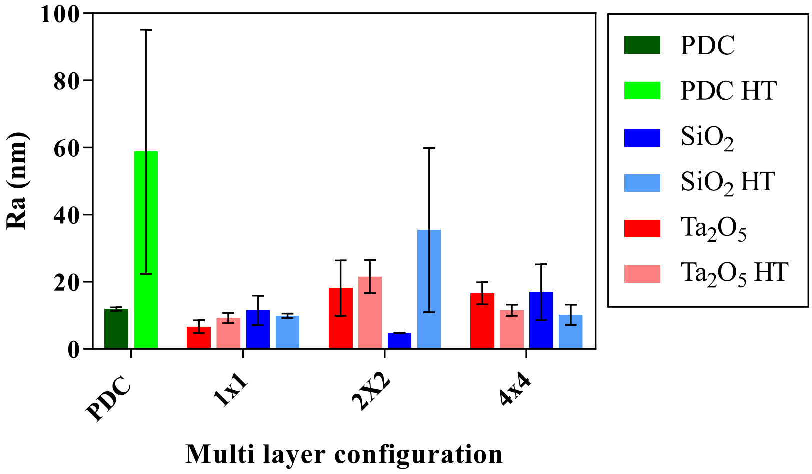

Figure 9.16: *Surface roughness (Ra, taken from 4 μm^2 surface maps) values given for multilayer and heat treated multilayer films as deposited onto Cu disks.*

9.3.1 Scratch testing

Scratch test failures for heat treated composite films showed critical failures at a maximum of 1.38 ± 0.35 and 1.19 ± 0.09 N for L_{C1+2} (combination cracking) in Ta_2O_5 and SiO_2 composites respectively, both maximums occurring for 1x1 films. 1.99 ± 0.13 and 1.52 ± 0.37 N were the maximum L_{C3} (buckling failure) loads for Ta_2O_5 and SiO_2 composites respectively. All critical loads and micrographs of failure can be found in ***Figure 9.17***.

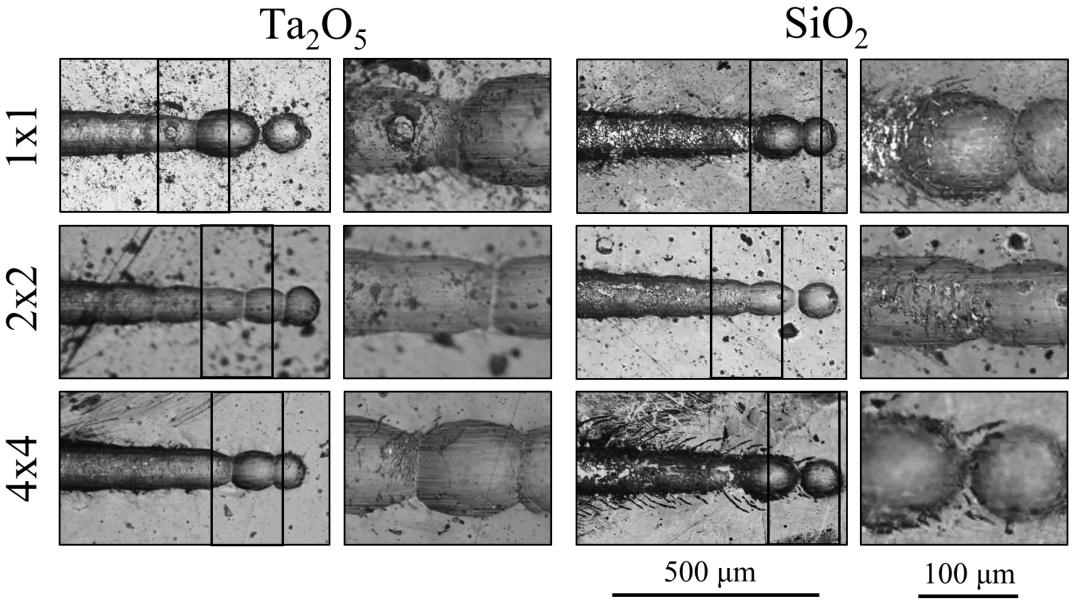

	Sample	*L_{C1+2} (N)*	*L_{C3} (N)*	*Complete interfacial delamination (N)*
Ta_2O_5	*1x1*	*1.38 ± 0.35*	*1.99 ± 0.42*	*6.40 ± 2.34*
	2x2	*1.35 ± 0.11*	*1.95 ± 0.18*	*10.8 ± 0.68*
	4x4	*0.97 ± 0.10*	*1.48 ± 0.16*	*9.90 ± 0.68*
SiO_2	*1x1*	*1.19 ± 0.09*	*1.02 ± 0.13*	*4.00 ± 0.32*
	2x2	*1.14 ± 0.07*	*1.52 ± 0.37*	*6.18 ± 0.37*
	4x4	*0.77 ± 0.05*	*1.01 ± 0.08*	*6.68 ± 0.25*

Figure 9.17: *Scratch test failure for heat treated composite materials as determined by light microscopy, high magnification images for the identification of failure mechanisms have been included.*

9.3.2 Pull off testing

Pull off testing on heat treated multilayer materials yielded an average adhesive strength which varied between 9.7 and 20.1 MPa. Average pull off values and failure mechanisms for each film are given in ***Table 9.2***. Films failed through complete interfacial delamination or partial interfacial delamination at the coating substrate interface, and no cohesive failure within the films was seen. EDX analysis revealed Cu on the surface of the film removed on the stub indicating failure at the Cu-Cu interface opposed to the Al-Cu interface.

Table 9.2: *Average failure strength for heat treated (500 °C) multilayer films as deposited onto copper disks, with corresponding failure mechanisms for each sample.*

	Sample	***Average failure strength (MPa)***	***Complete interfacial failure***	***Partial interfacial failure***	***Failure in Adhesive***
	1x1	*14.6 ± 2.6*	*4*	*4*	*0*
Ta_2O_5	*2x2*	*13.2 ± 3.5*	*6*	*2*	*0*
	4x4	*19.7 ± 3.4*	*8*	*0*	*0*
	1x1	*9.70 ± 0.8*	*6*	*2*	*0*
SiO_2	*2x2*	*20.1 ± 0.9*	*0*	*8*	*0*
	4x4	*17.5 ± 2.1*	*3*	*5*	*0*

There was no significant difference in pull off adhesion for Ta_2O_5 composites when compared to the as deposited samples. A larger scatter was seen within the SiO_2 composites, as seen in ***Table 9.2***. Generally a significant trend in adhesion strength upon heat-treatment was not seen except for those films produced in a 1x1 layer fashion where a decrease in adhesion strength was seen compared to the other SiO_2 composites (***Figure* 9.18**).

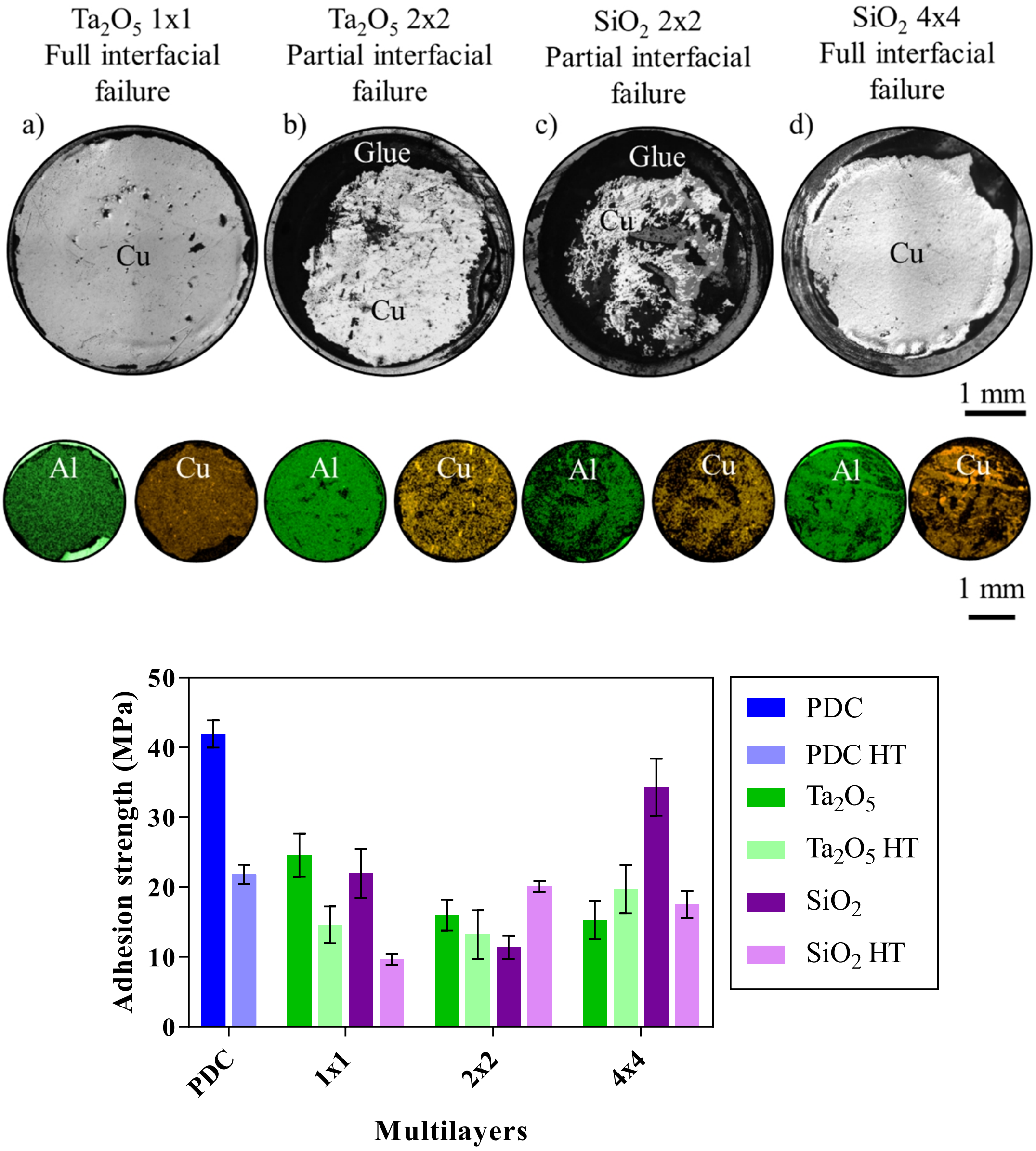

Figure 9.18: *Illustrative adhesive light microscope failure sites for heat treated Ta_2O_5 and SiO_2 multilayer composites as deposited on Cu disks, with Al and Cu EDX maps of the associated pull off stub below. Included below is a plot of average failure strength (MPa) for as deposited and heat-treated multi-layer composite samples.*

Failure mechanisms were confirmed using a light microscope and SEM/EDX analysis (confirming the failure interface). This confirmed complete interfacial delamination occurred generally at the substrate film interface, through the presence of Cu on both the stub and pull off site see ***Figure 9.18***.

9.4 Heat treated Al_2O_3 coated wire

Cu wires as coated with varying thicknesses of Al_2O_3 (using an increasing number of coating passes) with an Al interlayer deposited at 1.5 rpm were heat treated in order to study the effect of temperature on their mechanical properties.

FTIR of the samples showed the Al-O phonon peak as seen in all previous wires confirming the presence of Al_2O_3. There was also a shift to a lower wavenumber accompanied by an increase peak broadness as the number of Al_2O_3 layers increased, see ***Figure 9.19***.

Al_2O_3 Layers	***Average Wavenumber (cm^{-1})***
1	*907*
3	*818*
5	*705*

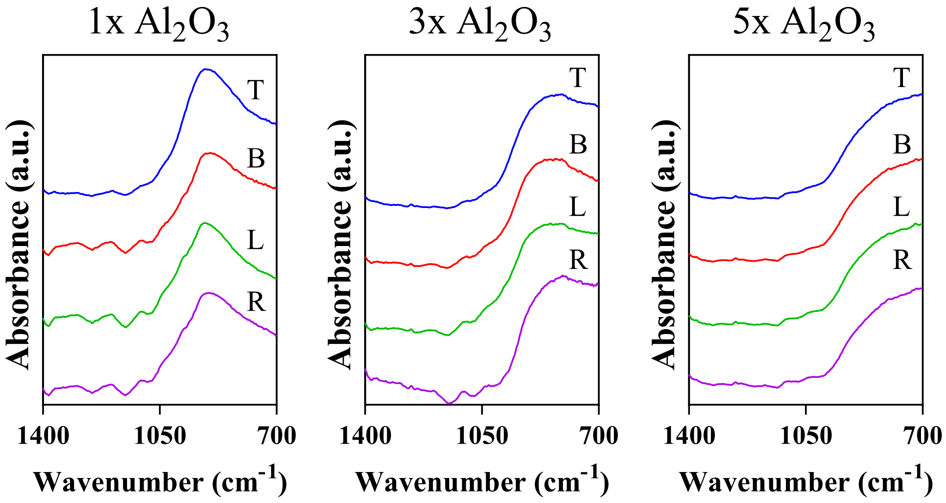

Figure 9.19: *FTIR average peak position and spectra for heat treated films as deposited onto Cu wire cleaned at -150 V bias and with a 1.5 rpm Al interlayer with 1, 3 or 5 layers of Al_2O_3 deposited at 0.5 rpm.*

Light microscopy of the heat treated samples showed that there were some delamination sites within the wire upon heat treatment. Cracking was also seen in certain samples as indicated in ***Figure 9.20***.

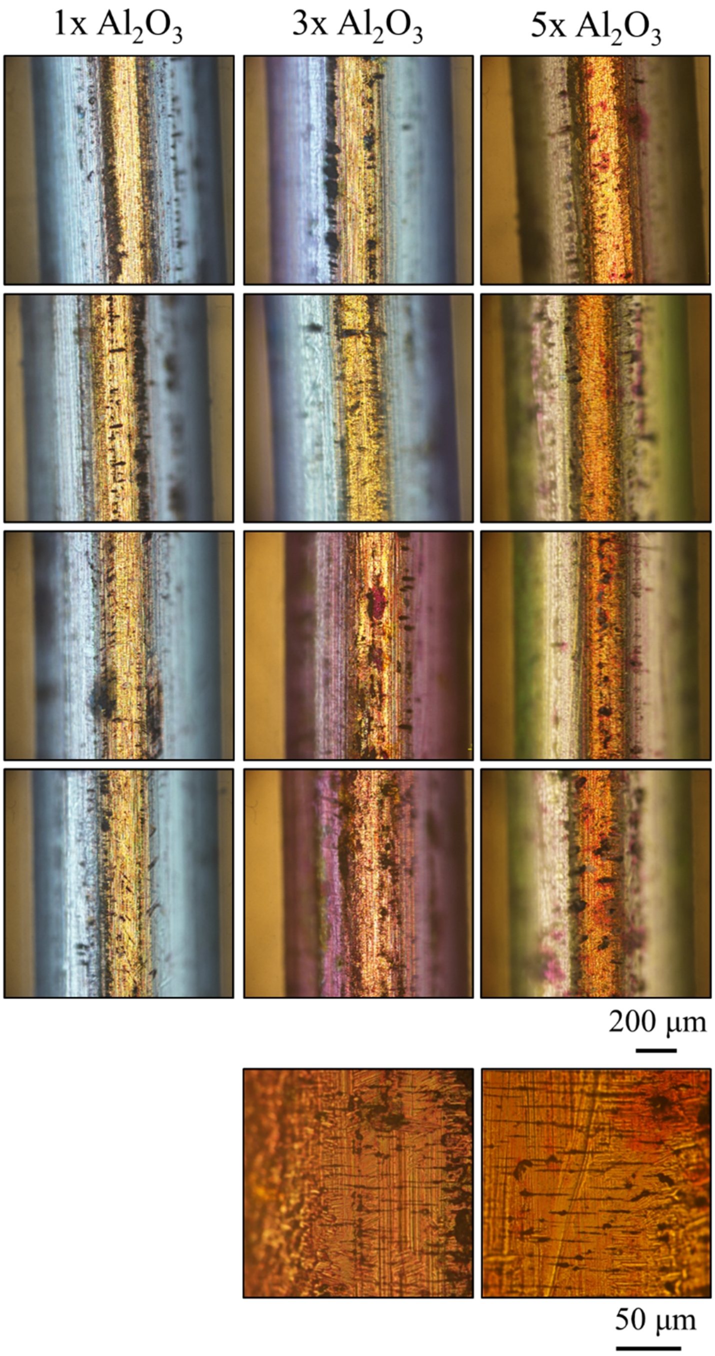

Figure 9.20: *Optical microscope images taken from sites around the circumference of the Cu wires as bias cleaned at - 150 V and coated with a 1.5 rpm Al interlayer with 1, 3 or 5 layers of* Al_2O_3 *deposited at 0.5 rpm. Below the corresponding columns are high magnification images of transverse cracking found on the inside of the 3 layer* Al_2O_3 *coating and on the outside of the 5 layer* Al_2O_3 *coating.*

SEM cross sectional imaging showed that films were unchanged in terms of structure, showing no features relating to defects. However, the film thickness decreased following the heat treatment for 5 layer films see ***Table 9.3*** and ***Figure 9.21*** for thickness and cross sectional SEM images.

Table 9.3: *Average coating thickness for heat treated* Al_2O_3 *coated wires with a 1.5 rpm Al interlayer. Also included is the lowest and highest average thickness.*

	Thickness (nm)		
Al_2O_3 layers	***Average***	***Min***	***Max***
1	*220*	*185*	*283*
3	*423*	*373*	*469*
5	*708*	*613*	*783*

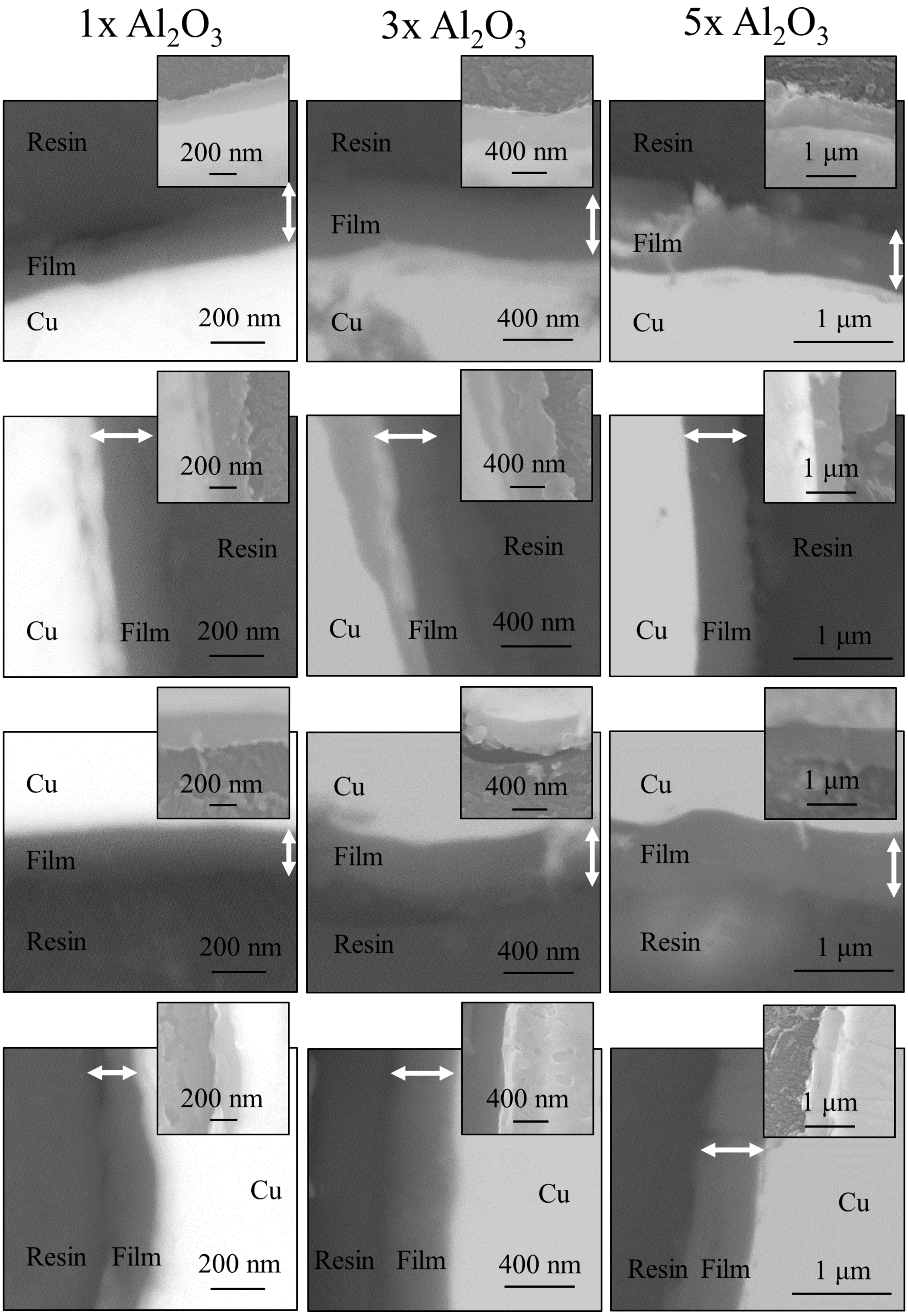

Figure 9.21: *Back scattered electron (secondary electron inset) SEM micrographs for heat treated coated wires with 1, 3 and 5 layers of* Al_2O_3 *deposited on top of an Al interlayer deposited at 1.5 rpm. Images are taken from sites around a cross section of wire mounted in conducting resin.*

9.4.1 Mechanical testing

9.4.1.1 Tensile testing

The heat treatment softened the Cu wire substrate, which resulting in cracking and delamination failure occurring at a minimum of 0.4 and 3.7 % strain with applied stress of 49 and 102 MPa respectively, see ***Figure 9.22*** and ***Table 9.4***.

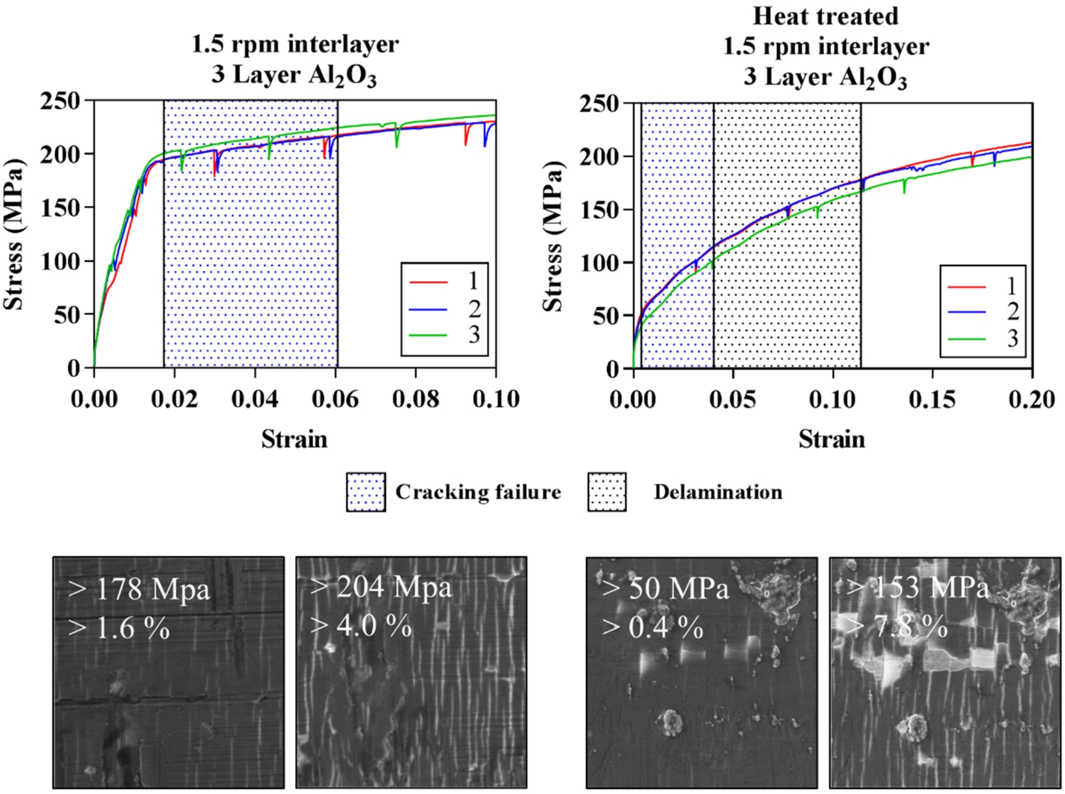

Figure 9.22: *Stress strain curves for the tensile testing of non-heat treated and heat treated Cu Wires coated with 3 layers of Al_2O_3 and an Al interlayer deposited at 1.5 rpm. With imaging of cracking and delamination failure modes and the average stress and strain at which they were observed. Note that depressions in the data relate to losses during imaging and tensile stress was applied in the direction horizontal to the page*

See ***Figure 9.22*** for a comparison of heat treated and non-heat treated failures in three layer Al_2O_3 coatings and ***Table 9.4*** for the failure ranges for heat treated coated wire. From this data it can be seen that increasing the film thicknesses with multiple passes has little effect on onset of cracking but decreased the minimum strain at the onset of delamination.

Table 9.4: *Maximum and minimum failure stress and strain for tensile failure in heat treated Al_2O_3 coated wires with an Al interlayer deposited at 1.5 rpm.*

	Cracking, (Strain (%) (Stress (MPa))		***Delamination, (Strain (%) (Stress (MPa))***	
Al_2O_3 layers	***Min***	***Max***	***Min***	***Max***
1	*0.5 (51)*	*7.5 (152)*	*11.3 (178)*	*12.4 (179)*
3	*0.4 (50)*	*4.0 (103)*	*7.8 (153)*	*11.4 (178)*
5	*0.6 (49)*	*4.0 (102)*	*3.7 (102)*	*9.4 (152)*

Cracks such as those seen in the light microscopy (***Figure 9.20***) were not seen during the micro tensile testing of the wires. The crack density of the heat-treated samples was similar to that seen in non-heat treated samples. The highest average crack densities were seen for samples with a single layer Al_2O_3, however, when taking into account the error there was no significant difference between the samples. For measured crack densities see ***Figure 9.23***.

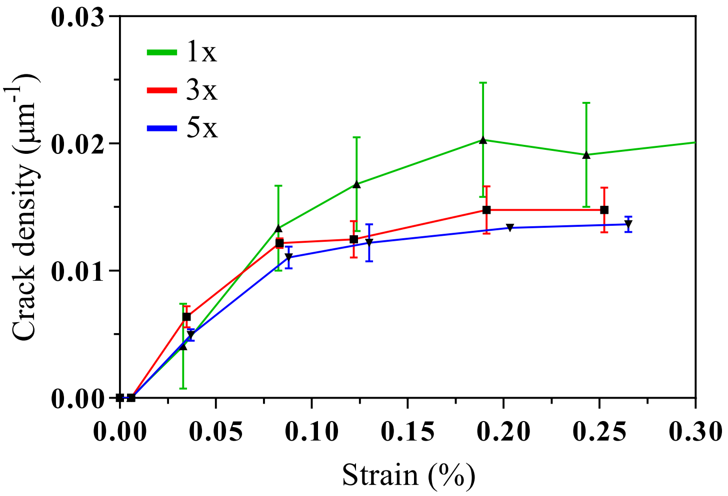

Figure 9.23*: Crack density in heat treated Cu wires coated with an Al interlayer at 1.5 rpm and 1,3 or 5 layers of Al_2O_3 deposited at 0.5 rpm.*

The critical bending radius was calculated using equations as given in the experimental procedure, see section (*4.4.2*). Results of these calculations resulted in the values given in ***Table 9.5***.

Table 9.5: *Critical bending radii calculated using critical stress from tensile testing on wires deposited with a 1.5 rpm interlayer and varying layers of Al_2O_3.*

Interlayer	***Al_2O_3 layers***	***Calculated critical bending radius (mm)***
1.5	*1*	*1.00*
	3	*1.25*
	5	*0.83*

9.4.2 Electrical testing

As with non-heat treated wires continuity was found to be lacking because of problems with delamination/ micro cracking in the coatings, which were either a result of the coating apparatus or of the post deposition manipulation. The continuity issues were preventative to electrical testing and cross pair, wound pair and single samples on a Cu electrode all displayed continuity issues which prevented measurement.

9.5 Summary

Heat treatment of the PDC Al_2O_3 coatings on disks showed no significant change in electrical properties but did show a decrease in mechanical properties which was a result of thermal expansion mismatches. PDC Al_2O_3 coated wires also suffered mechanically, a result of the softening copper substrate which decreased the minimum failure strain for transverse and longitudinal cracking to 0.4 and 3.7 % respectively.

Heat treatment of the PDC composites revealed that the Ta_2O_5 composites were insufficient for isolative purposes at higher temperatures. Increased leakage current and premature breakdown strength in these films was potentially a result of copper migration and partial crystallisation of the Ta_2O_5 layers resulting in defect sites capable of trapping charge. Conversely the SiO_2 composites dielectric strength didn’t decrease and rose on average of 12 %, which is potentially a result of a decrease in defect density caused by annealing. The heat-treatment did not, however, have the desired effect of improving the adhesive properties, which again resulted from the thermal expansion mismatches in the layered structures.

10 Discussion

The initial section of this discussion will examine the selection of reactive DC deposition over RF sputtering and the further refinement to pulsed DC sputtering, for the production of insulating coatings. Contained within is an assessment of the effect of deposition parameters such as: interlayer configuration, bias voltage, deposition length and pulsing parameters on the films mechanical and electrical properties. This data will be used to validate the selection of pulsed DC deposition for further Al_2O_3 coatings.

Following this an account of the electrical and mechanical properties of composites produced using PDC alumina will be discussed in (*10.2*) including a comparison of the effect of the composition, layer thickness and number of dielectric layers applied in such composites.

Finally, in section (*10.3*) the exploration of the mechanical and electrical properties of the as deposited and heat treated PDC Al_2O_3 coatings on Cu wires is discussed. This assessment is critical to the suitability of these coatings for their purpose and will be used to determine future stages of coating development.

10.1 RF, DC, BDC and PDC films

The following section will focus on the characterisation of Al_2O_3 films as deposited using RF, DC and PDC power supply variants, as well as looking at the properties of heat treated PDC films. Characterisation will be organised into sections consisting of: Structure and compositional analysis, electrical properties and mechanical properties. A critical assessment of these results will be used to determine the candidate material most suitable for use as an electrical isolative layer. This material will then be carried through further studies, in the following sections of this discussion.

10.1.1 Structure and composition

FTIR analysis of the bonding in the films as deposited onto Cu foil confirmed the presence of Al_2O_3, showing Al-O LO phonon peaks regardless of the deposition parameters, confirming the formation of Al_2O_3 [292,293]. FTIR analysis of RF SiO_2 and RF Ta_2O_5 films confirmed the main bonding within the films as Si-O and Ta-O respectively, with major peaks for SiO_2 at 1150.5 and 807.2 cm^{-1} resulting from Si-O stretching and bending respectively [193,294]. Major Ta_2O_5 peaks at 890.1, 806.1, 650.0 and 745.1 cm^{-1} were attributed to Ta-O-Ta stretching vibrational modes in Ta_2O_5 and its sub oxides. The FTIR confirmed the bonding in the oxides to be consistent with the literature [52,295]. FTIR, SEM and XPS results presented in the results section are also summarised in ***Table 10.1***.

Shifting in the wavenumber of the Al-O binding peaks between films was also observed, because of its potential to divulge information about the intrinsic stress in the films these relationships were examined further. RF deposited films had a higher wavenumber than all of the DC and BDC films at 901 cm^{-1}, where the LO phonon absorption bands were seen between 862.2 and 875.7 cm^{-1} (see ***Table 5.2*** and ***Figure 5.9***). Within the DC and BDC films the application of different substrate bias did not have a clear effect on the position of the Al-O peak, however, the implementation of the blended Cu-Al interlayer resulted in wavenumbers shifting to lower values by an average of 17 cm^{-1}. FTIR measurements of DC samples deposited for shorter and longer amounts of time revealed an increase in wavenumber for thinner films and a decrease for thicker films, showing that there was a wavenumber thickness dependence for the films, see results for DC, 30, 60, 90 and 120 in ***Table 10.1***. The position of Al-O bands in pulsed DC films were also found to be heavily reliant on the duty cycle, generally shifting to a lower wavenumber (e.g. 903 to 856 cm^{-1}) was seen when decreasing the duty cycle.

In the results discussed above it is likely that the decreased wavenumber resulted from an increase in internal stress, thus the RF films, thin DC films (deposited for 30 min), PDC films deposited at 40 % duty cycle and the heat treated PDC samples had the lowest internal stress. Part of the reason for the lower internal stress in the films is the result of lower thickness where a maximum thickness of 760 ± 10 nm was observed for RF, PDC and thin DC films. The slight shift in the BDC films was seen as a result of the additional material at the interface and can also be attributed to thickness effects. The PDC sample produced at 150 kHz where a duty cycle of 40 % was used showed a shift in the Al-O FTIR absorption band to 805 cm^{-1}. This could also be an indicator of higher levels of intrinsic stress within this specific PDC film when compared to DC and BDC films and the other pulsed DC films deposited at the same duty cycle. The intrinsic stress of a film system can be in tension or compression and is heavily dependent on the film deposition parameters. Often for increasing thickness a transition from compressive to tensile stress is seen. For instance in Cu films studied by *Liu et al.* a shift from compressive stress to tensile stress was seen between 500 and 1000 nm and a *ca.* 3.5 fold increase in the tensile stress was seen when increasing the film thickness from 1000 to 2000 nm [296]. Thus the shift in wavenumber can be accounted for by considering as the residual stress become more tensile in character for the bond length increases and thus the FTIR frequency decreases.

Studies of PDC deposited amorphous carbon films and ITO (indium tin oxide) glass have shown a 4.5 times increase in internal stress with increasing duty cycle from 30 to 50 %, a result of the increase in the energy of the sputtered particles, and the bond lengths in the resulting material respectively [297,298]. Reinforcing the idea that the shift in the FTIR results in this work was the result of an increase internal stress caused by increasing the duty cycle. Shifting in the wavenumber (920 to 970 cm^{-1}) of Al_2O_3 thin films when increasing deposition temperatures has also been noted by *Haanappel et al.* (for CVD films) [138] . Thus the stress likely increased due to cooling from the deposition temperatures and the mismatch between the substrate and coatings thermal expansion, hence the shifting to a lower wavenumber was the result of an increasing internal stress as discussed above.

All RF and reactively sputtered (DC, BDC and PDC) films were X-ray amorphous in structure as evidenced by the lack of Bragg diffraction peaks associated with crystalline alumina in the XRD scans (***Figure 5.3***, ***Figure 5.5***, ***Figure 5.10*** and ***Figure 6.12***). There were however some peaks in the diffraction patterns, which resulted from the crystalline aluminium interlayer deposited between the substrate and alumina coating. The films analysed by XRD were deposited on borosilicate glass substrates to eliminate copper Bragg diffraction peaks from the spectra- resulting in an amorphous hump. Increase in deposition bias has been shown to aid the formation of crystalline Al_2O_3 films deposited at high temperature [299]. This shows that the substrate biases applied in this study were not high enough to induce crystallinity.

Deposition rates for the RF films in this work were measured using cross sectional SEM ***Figure 5.6***. Ta_2O_5 was deposited at 96 nmh^{-1} whereas Al_2O_3 and SiO_2 had similar deposition rates of *ca.* 18 nmh^{-1}. The much higher deposition rate seen for Ta_2O_5 compared to SiO_2 is unexpected as a number of sources determine the sputtering rate of SiO_2 should be higher; the sputtering yield of SiO_2 was reportedly up to two times faster than Ta_2O_5 [300–302]. This phenomena could be a result of a number of different parameters including: different levels of target erosion, the varying effect of substrate biasing or target thickness in combination with thermal conductivity, whereby a target would produce a different thickness of film depending on how well cooled the target surface was, which can also play a part in film structure [303]. *Takatsuji et al.* studied the effect of target cooling and showed a poor cooling efficiency could cause outgassing from the chamber, which caused the formation of an amorphous top layer in layer in their Al-Cu films caused by reaction with outgassed N_2 and O_2 affecting the thickness of the film [304]. However, in the current study the chamber of the TEER-UDP650 coating rig is cooled with a double skin, reducing the likelihood of outgassing. The melting temperatures of SiO_2 and Ta_2O_5 are also similar at 1710 and 1872 °C respectively, mitigating potential for any hot cathode effects (caused by mismatches in the melting temperature of the target materials), the bond dislocation energies are also relatively similar at 800 and 839 $kJmol^{-1}$ respectively, showing that the bond strength didn’t contribute to the observed increase [305,306]. It is therefore postulated that the difference seen in coating rate, in contrast to the theoretical rates mentioned above, resulted from a combination of reasons including the different levels of erosion in the targets, target thickness and through thickness target cracking which was seen in the targets which gave the lower sputtering rate: Al_2O_3 and SiO_2.

The thickness of DC and BDC films varied with deposition bias, in both the case of DC and BDC applied substrate bias of -10 V yielded the thinnest films (1566 ± 27 and 1755 ± 12 nm respectively for a 90 min run). There was no significant difference in the thickness seen in the BDC samples produced at -45 and -60 V, however, in the case of DC films there was a *ca.* 500 nm increase in thickness for the films deposited at -60 V. Typically, however, a reduction in thickness is expected once a larger bias is used, due to densification and or re-sputtering effects. This could be the result of the substrate bias being too low to influence an increase in the mobility of the condensing species/ re-sputter deposited species but being large enough to increase the number of sputtered ions condensing into the film. Such an effect has been noted in IPVD deposition of Al and Al_2O_3 by *Brown et al.*, who reported an increase in deposition rate at low substrate bias, once the bias was increased above -90 and -300 V for Al and Al_2O_3 respectively the deposition rate decreased [307]. The use of the blended interlayer increased the coating thickness due to the additional copper and 5 additional minutes of OEM set point time, leading to a thicker transition layer. The average deposition rate of the reactively sputtered DC films deposited for 90 min was *ca.* 44 times higher than those deposited by RF using an Al_2O_3 target. As the sputtering time increased a decrease in sputtering rate was observed, from a maximum of 1520 nmh^{-1} at 30 min to a minimum of 1000 nmh^{-1} at 120 min. The deposition rate decrease is a result of the Al target becoming increasingly poisoned throughout deposition. The reduction in deposition rate with increasing reactive gas flow rate has been reported widely and shows that poisoned targets have lower sputtering rates (Ti targets sputtered by *Chen et al.* decreased by over half upon the introduction of a 20 % O_2 flow) and would account for the decrease seen in this work [80,91].

Cross sectional SEM analysis of PDC films showed that the thickest films were produced at higher duty cycles except for 50 kHz films where there was no significant change in the thickness. This was expected because of the combined larger target sputtering time when using the higher duty cycle. The highest deposition frequency of 201 kHz, was shown to produce the thinnest films with an average thickness of 792 ± 14 nm, there was no significant difference between the other frequencies.

Following heat treatment of the sample deposited at 150 kHz and 40 % duty cycle there was no significant densification observed.

The effect of deposition frequency has been studied by *Kelly et al.* for sputtered aluminium doped zinc oxide which showed a clear decrease in sputtering rate with an increase in deposition frequency where a six fold decrease accompanied a 250 kHz increase in pulsing frequency. This dependence was attributed to a dead zone in the "on" cycle [308]. The decrease in sample thickness of the 201 kHz samples deposited in this study are attributed to similar reasoning applied by *Kelly et al.*, see ***Table 5.2***. This phenomena has also been seen in other pulsed deposition techniques such as pulsed electrodeposition [309]. The deposition rates for PDC were *ca.* 10 times lower than DC alumina but *ca.* 4 times higher than RF films. The variance in deposition rate between the different power supplies was a direct result of the down time caused by the reverse cycles in RF and PDC methods, these reversals are however key for the stability of the deposition by removing target arcing.

It is important to note that whilst it is possible that intrinsic stress changes in the film caused the observed FTIR shifting, it could also be a result of optical effects which have been shown by *Gunde* to result in thickness dependant peak position of absorbance lines which was noted in this work [310].

10.1.2 Film quality

Cross sectional SEM showed the films were mostly featureless indicative of an amorphous nature, however, striations parallel to the substrate were seen and increased in frequency closer to the surface of the films, were apparent in micrographs of DC-10 and -60 and BDC-10 and -60 films, see ***Figure 5.12.*** TEM analysis of BDC films revealed further defects in the form of cracking as seen in ***Figure 5.13***, which may have been caused by the intrinsic stress incorporated during deposition. Additionally, TEM revealed the presence of short range order, which likely resulted from target arcing, despite XRD analysis indicating the films were amorphous. The sites of short range order were dispersed within the X-ray amorphous films in the sub 10 nm size range as indicated in ***Figure 5.13***. AFM also revealed the presence of pore defects in the BDC45-6 and BDC6-6 samples, see ***Figure 5.18***. These defects would be detrimental to the film's isolative properties as they could promote current leakage and premature breakdown. Such defects were found only in two cases in AFM analysis, however, the sparsity suggests that the pores could be an issue for other films but simply weren't observed. The striations within the films were also apparent (as alluded to in SEM) with TEM EDX identifying layers of oxygen deficient material. These striations became more abundant with increasing sputtering time. Hence this is likely a result of target poisoning cycles resulting in more arc events. This short range order and striations, which were throughout the film, are important when considering the electrical properties of the films and will be discussed in section (*10.1.4*).

Crystallite defects in reactive DC deposited films are not uncommon and have been previously noted in alumina systems, for instance metallic crystallites has also been noted in sputtered aluminium nitride, aluminium oxynitride and tantalum pentoxide [72,84,209]. The number of defects seen by *Koski et al.* in reactively sputtered aluminium oxide decreased 6 fold from 98 to 630 defects mm^{-2} when the target voltage was increased from 405-330 V [311]. This was because the target was in compound mode at low voltages, in the current study because of the large number of defects in the films it can be assumed the target was poisoned during deposition. Meaning that an increase in target voltage could provide a route to improving the quality of DC films.

Conversely TEM analysis of the PDC films (***Figure 6.5***) showed a purely amorphous structure absent of crystallites/ short range order; moreover, the film had no striations, which were commonplace in the BDC films. This is directly a result of the pulsed power and the improved process stability, allowing the formation of an amorphous film with fewer defects and an absence of cracks and striations. The use of pulsed DC power has been summarised by *Kelly and Arnell*, who state that the use of a sputtering frequency between 10 and 200 kHz can reduce the number of arcs, supporting the case for removal of crystalline defects as seen when using pulsed power in the current study [72].

10.1.3 Stoichiometry and composition

XPS analysis found the Al:O ratios at the surface (top 5 nm) of the films to be variable compared to stoichiometric alumina (0.66) with values between 0.37 and 0.67. In addition to the Al^{3+} photo electron peak a shoulder in the Al_2P peaks for DC and BDC films was observed, indicating the presence of metallic aluminium which could become part of conductive pathways (***Figure 5.11***). The Al_2P shoulder was at a lower electron emission energy than the peak for Al^{3+} by an average of 2.78 eV as stated in ***Table 5.2***, confirming the presence of Al^0. XPS of alumina films deposited by Reddy *et al.* showed the presence of peaks with a binding energy for aluminium oxide at 74.0-74.9 eV and metallic aluminium at 73.0-72.3eV, supporting the assignment of Al^{3+} and Al^0 in this study [97]. An increase in sputtering time resulted in a variable Al:O ratio and elemental Al content, however, this was likely due to the poisoning cycles as discussed above. This is potentially the reason why no clear trends were seen when assessing the effect of the bias voltage on the Al:O.

Films produced using pulsed DC deposition with varying pulse parameters yielded Al:O ratios between 0.53 and 0.68. No specific trend in the ratio was seen with respect to duty cycle or pulse frequency. Further to this XPS also revealed that none of the films contained any elemental aluminium as evidenced by the lack of shoulder on the Al_2P photo electron peak which was seen in DC and BDC films.

Metallic Al was introduced into the films during arcing caused by the build-up of the dielectric material on the target surface, resulting in the ejection of metallic target material [100]. Hence the removal of elemental aluminium was a direct result of the use of pulsed power, which considerably reduces arc events resulting it the removal of Al droplets. Pulsed DC power also has the potential to selectively sputter poisoned sites on the target surface during the reverse section of the pulsing cycle as discussed by *Kelly et al.*. XPS analysis of alumina films reported by *Kelly et al.*, showed that stoichiometric alumina could be deposited reactively using an OEM set point of 25% [76]. In this study, film stoichiometry was determined for films produced at 23% of the maximum 100 % OEM response, where the reduced value was selected in order to ensure the films were not rich in Al, which supports the formation of close to stoichiometric alumina by the PDC methods use in this study.

Table 10.1: *FTIR Al-O phonon peak positions, SEM cross sectional thickness and XPS Al:O ratio and Al^0 content for RF, DC and PDC Al_2O_3 thin films.*

				SEM	**FTIR**	**XPS**	
Sputt. method	**Sample**		**Bias (V)**	**Thick. (nm)**	**Al-O peak position (cm^{-1})**	**Al:O**	**Al^0 (%)**
RF	Al_2O_3	480 min	-60	170 ± 10	901	/	/
DC	DC	90 min	-10	1566 ± 27	868	0.74	1.88 ± 0.03
		90 min	-45	1326 ± 6.0	883	0.51	5.48 ± 0.04
		90 min	-60	2095 ± 10	876	0.66	19.58 ± 0.10
	DC	30 min	-60	760 ± 10	914	0.48	7.67 ± 0.08
		60 min	-60	1150 ± 45	844	0.52	5.21 ± 0.07
		120 min	-60	2030 ± 25	843	0.50	1.01 ± 0.02
	BDC	90 min	-10	1755 ± 12	865	0.37	16.56 ± 0.28
		90 min	-45	1854 ± 13	850	0.56	7.39 ± 0.07
		90 min	-60	1868 ± 13	862	0.62	5.79 ± 0.06
	Pulse freq. (kHz)	**Duty cycle (%)**	**Bias (V)**	**Thick. (nm)**	**Al-O peak position (cm^{-1})**	**Al:O**	**Al^0 (%)**
PDC	50	24.0	- 60	468 ± 24	847	0.53	/
	50	40.0	-60	450 ± 23	908	0.61	/
	150	22.5	-60	370 ± 4.0	858	0.60	/
	150	40.0	-60	585 ± 12	805	0.68	/
	201	24.0	-60	353 ± 9.0	864	0.60	/
	201	40.0	-60	439 ± 11	898	0.58	/
HT PDC	150	40	-60	205 ± 6.0	922	0.73	/

10.1.4 Electrical properties

DC and BDC Films deposited for a duration of 12.5 min onto polished copper substrates had varying dielectric strength, as measured by AFM DB methods and the in-house probe. AFM measurements gave considerably lower standard error than those made using the probe (see ***Table 5.3*** and ***Table 5.4***) hence all disk measurements made subsequent to DC and BDC films utilised the AFM DB method. The benefits of the AFM DB method stem from the high spatial resolution of the AFM tip, which also allows measurements to be carried out in a well-defined matrix. Therefore, the following discussion will focus on the AFM DB electrical results.

The DC and BDC films had dielectric strengths of ≥ 220 Vμm^{-1}, however, the breakdown was not instantaneous, a maximum leakage prior to breakdown of *ca.* 2 nA was seen. The pre-breakdown leakage included current oscillations in some cases as displayed in ***Figure 5.15.*** These oscillations were attributed to charge trapping and de-trapping, whereby sites containing short range order and elemental aluminium in the material likely acted as trapping sites within the films, see ***Figure 10.1***. This is reinforced by the TEM analysis which identified short range order and other defects in the films, and further supported by the presence of elemental aluminium in the surface of the film as evidenced in the XPS data, see sections (*10.1.2*) and (*10.1.3*).

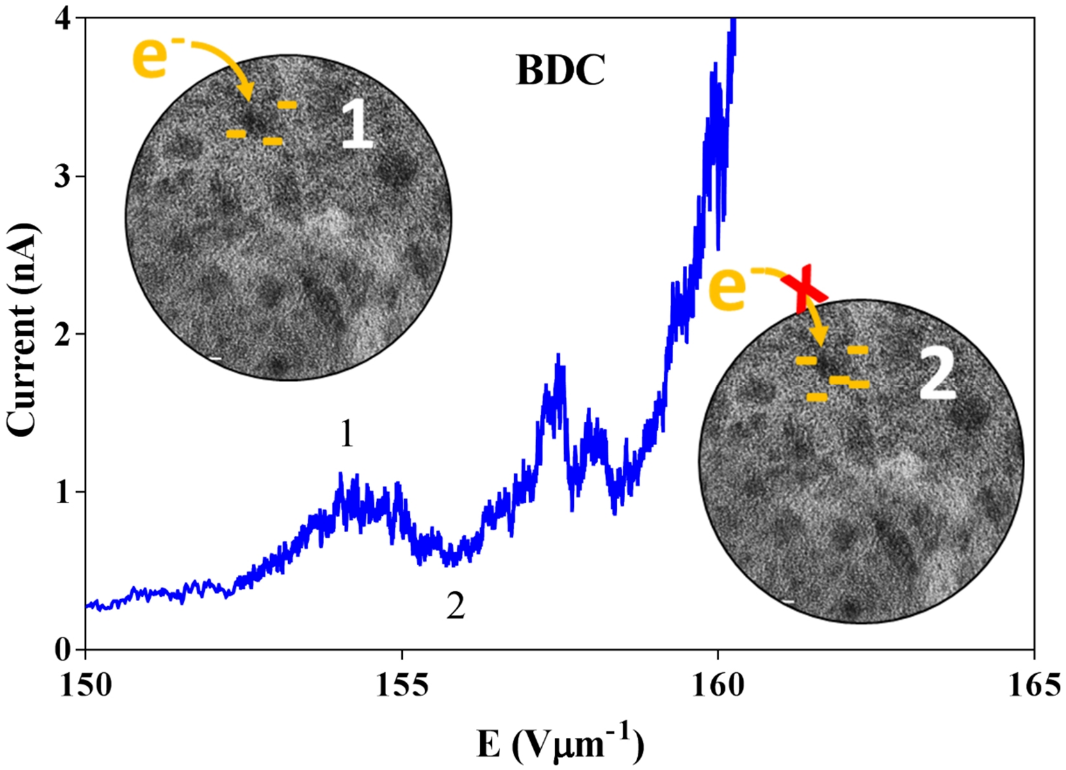

Figure 10.1: *Schematic to describe charge trapping and de-trapping in reactive DC sputtered* Al_2O_3 *films. In stage one electrons can flow from the electrode into defects in the material structure causing an increase in current. Stage two shows the negative charge that has built up in a defect repelling the addition of further charge. It is these actions cycling, which cause the oscillations in the current prior to breakdown.*

No clear effect on the dielectric strength could be seen despite changing the substrate bias voltages between -10 and -60 V. For instance, in the DC films a bias voltage of -45 or -60 V produced films with the highest dielectric strength, however, for BDC films the application of a substrate bias of -60 V was shown to decrease the dielectric strength. The interlayer addition was found to have no significant effect on the electrical properties, with average AFM DB dielectric strength values of 187 ± 23 and 196 ± 28 Vμm^{-1} for DC and BDC films respectively, see ***Table* 10.2** for all AFM DB results. It was expected that an increased bias would improve the dielectric strength, through densification and defect removal. For instance the leakage current in TiO_2 as shown by *Chandra Sekhar et al.* decreased by seven times with the application of a -150 V substrate bias, which was attributed to structural changes in the system [73]. This suggests that application of a bias higher than that applied in this study could potentially be another route to improving the dielectric strength. The lack of trend in the deposition rate as discussed above could also indicate that a higher bias voltage would be required to have a reliable effect on the films.

AFM DB measurements were investigated relative to matrix size for PDC Al_2O_3 films. As seen in ***Figure 6.7,*** the breakdown voltages in films measured using a 5x5 µm AFM matrix were considerably lower (between 15 and 150 V) than measurements made using a 30x30 µm matrix where no breakdown was observed, showing it is likely that the breakdown paths affected further measurements when they were made too closely together. Thus the 30x30 µm matrix was maintained for further measurements. As no breakdown was observed when using a 30x30 µm matrix, films of a *ca.* 200 nm thickness were required in order to measure the breakdown voltage. The implementation of pulsed power gave rise to a stark increase in dielectric strength, with PDC Al_2O_3 films showing a 1.7 times increase in dielectric strength when compared to DC and BDC films, with an average of 310 ± 28 $V\mu m^{-1}$. This is a direct result of their improved structure, as discussed in (*10.1.2*), see ***Figure 10.2***. The leakage current was also considerably lower than the DC and BDC films with an average maximum leakage of 0.13 nA. The electrical properties remained similar following heat treatment having a dielectric strength of 329 ± 33$V\mu m^{-1}$. However, the heat-treated sample had three measurement sites where breakdown occurred with increased leakage current of up to 10 nA, indicating that some defects could have been incorporated into the structure during heat treatment.

Both as deposited and heat-treated PDC films exhibited high breakdown strength, better than that for polyimide films, for instance films deposited using chemical methods by *Diaham et al.*, achieved values ≥ 200 $V\mu m^{-1}$, which is encouraging as polyimide is commonly used in magnet wire insulation [312]. The 310 $V\mu m^{-1}$ achieved for PDC Al_2O_3 is, however, lower than breakdown seen in films produced by *Bartzsch et al.* using pulsed DC sputtering from a double ring magnetron having a breakdown of 620 $V\mu m^{-1}$. Dielectric strength was also four times lower than films produced by *Carreri et al.*. Their higher value was attributed to the use of mid frequency pulsed DC power supplies, equipped with special arc handling equipment, producing films which had a breakdown strength of 1.5 $kV\mu m^{-1}$ [121,186]. These works showed that there was still room for improvement in the dielectric strength of the PDC films, however, the routes mentioned above would require considerable investment to implement thus other routes will be explored in (*10.2*).

Current voltage analysis has been used regularly to generate information about conduction mechanisms in metal insulator metal (MIM) or metal oxide semiconductor (MOS) systems. Conduction in such systems is routinely a result of one of the following mechanisms: Fowler-Nordheim tunnelling, Schottky emission or Poole-Frenkel emission. Charge transport mechanisms and graphical analysis of current leakage have been studied extensively [104,132]. This analysis was used to generate information about the conduction mechanisms in the deposited films.

At lower electric fields conduction mechanisms in DC, BDC and PDC films were not clear due to high variation in current, which carried through in further analysis making fitting the data impractical. Despite this, it is likely that thermionic emission contributes to the conduction at lower fields in the DC and BDC films, as the presence of a crystalline material, as seen in high resolution TEM micrographs in ***Figure 5.13*** and ***Figure 6.5***, could facilitate charge trapping, meaning that Poole-Frenkel emission could be a suitable conduction mechanism. The presence of elemental aluminium, as seen in the XPS results, could form conductive pathways through the material contributing to conduction, whereby the conduction mechanism would be determined by the conduction between such defects/pathways. Tunnelling between metallic channels in sputtered AlN_xO_y films, similar to metal insulator metal (MIM) structures has been documented by *Borges et al.,* lending credit to the theory that the metallic Al in the films produced in the current study, were detrimental to the electrical properties of the films specifically resulting in premature breakdown [84].

Conduction at high applied fields prior to breakdown in the DC and BDC films was observed based upon the analysis of E-J curves as in ***Figure 5.17***. The analysis shows a linear relationship between the reciprocal of the applied field ($cmMV^{-1}$) and ln (JE^{-2}) at high fields relative to breakdown ($< 120\ V\mu m^{-1}$), which is consistent with the Fowler-Nordheim mechanism. In the current study two linear regions were observed for both BDC and DC films, in their Fowler-Nordheim plots. This indicated that there were multiple barriers being tunnelled through. Fowler-Nordheim conduction at high fields has also been seen by *Groner et al.,* in ALD alumina films thinner than 10 nm, at fields of above 380 $V\mu m^{-1}$ [119]. Such multiple linear regions have been observed in Fowler-Nordheim analysis of GaN nanorods by *Evtukh et al.,* where the regions resulted from tunnelling barriers with different barrier heights, see ***Figure 5.17*** [313].

Current leakage in PDC films had an average maximum of 0.13 nA as seen in ***Figure 6.8***. This clear improvement over leakage seen in DC films prior to breakdown is a result of the improved structure as seen in TEM and XPS as discussed previously (*10.1.2*). The removal of elemental aluminium and short range order from the surface and bulk of the materials is a direct result of reduction in arc events, due to the implementation of the pulsed power supply. This reduction in the number of potential charge trapping sites directly contributed to the improved dielectric strength, as well as the reduced leakage current. Current oscillations were seen only for a number of measurements and were again attributed to charge trapping and de-trapping. Fowler-Nordheim tunnelling is again proposed as a candidate for the conduction mechanism at high fields due to the linear response when plotting E^{-1} against ln (JE^{-2}), see ***Figure* 6.9**. Thinner films (107 ± 3 nm) gave breakdown values of 31.3 ± 2.1 V, equating to a dielectric strength of 301 $V\mu m^{-1}$. However, typically dielectric strength is inversely proportional to sample thickness due to an increased number of defects [103]. The lower value obtained for the 107 nm films compared to the *ca.* 200 nm films obtained in this work, could be a result of different conduction mechanisms in the thinner film.

Conductive AFM measurements were carried out by *Ganesan et al.* in order to assess the electrical properties of thin alumina films <1 nm produced by ALD, reiterating that an increase in dielectric strength should accompany decreasing thickness. The work also showed breakdown voltages as high as 13 $kV\mu m^{-1}$. Pre breakdown oscillations such as those seen in DC and BDC films (***Figure 5.15***), were seen in these ultra-thin alumina films and were also attributed to charge trapping and de-trapping [103,120]. Defects created by the applied field contributed to stress induced leakage current within their studies, and is likely to be the origin of the oscillations in PDC films from the current study. Conduction mechanisms in alumina films have been studied widely and often attributed to multiple mechanisms at different applied field strengths as seen by *Zhu et al.* who explored the resistive switching within anodic alumina structures (finding ohmic, Poole-Frenkel and Schottky mechanisms) [131]. Poole-Frenkel conduction has also been determined to be the predominating conduction mechanism in alumina films, as seen by *Kolodzey et al.* [188]. This body of work shows that the conduction mechanism in Al_2O_3 films varies widely as a result of the films intrinsic properties.

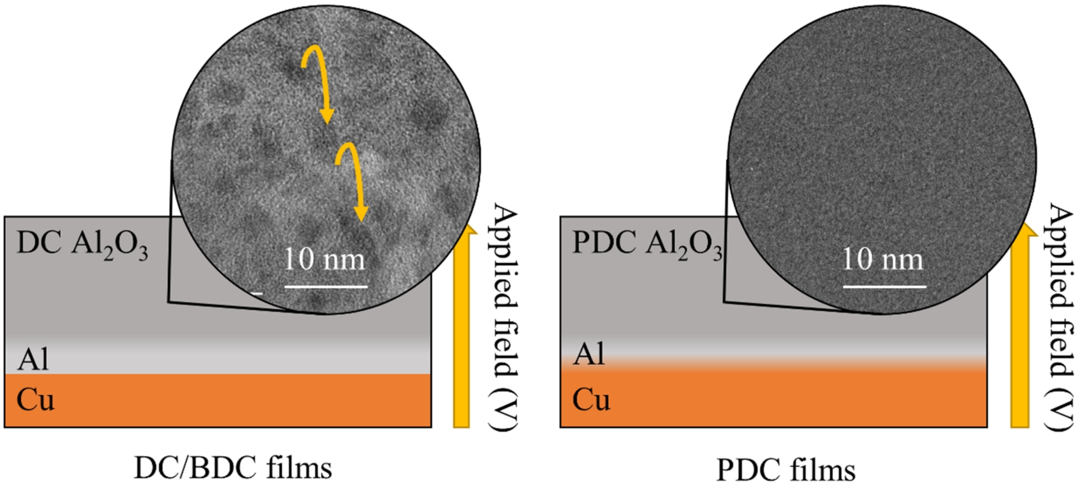

Figure 10.2: *Schematic showing the reasoning behind the improved breakdown characteristics of the PDC films, TEM micrographs showing short range order in the DC/BDC films and the lack of such order in PDC films are inset. Defects shown in DC sputtered films were potentially a route to their premature electrical breakdown.*

For the PDC films a heat treatment was carried out to assess any improvements in electrical properties, which could potentially be the result of removal of compositional or structural defects. It was shown however, that the electrical properties remained similar to those of the non-heat-treated films. The heat-treated sample had three measurement sites where breakdown occurred with increased leakage current of up to 10 nA, otherwise the other test sites had very low leakage < 0.1 nA and all test sites reached breakdown before the 150 V limit of the equipment. The areas of high leakage could be caused by defects generated during heat treatment. However, because the breakdown strength was relatively high at 329 Vμm^{-1}, the material may still be suitable as an insulating layer depending on the allowable leakage current of the specific application.

Table 10.2: *Summary of the AFM DC properties of DC, BDC and PDC Al_2O_3 films as deposited onto Cu disks and heat-treated in the case of PDC films.*

Sputtering method	***Sample***	***Sample Bias (V)***	***Sample thickness (nm)***	***Breakdown voltage (V)***	***Dielectric strength***
DC	*DC*	*-10*	*778 ± 34*	*128.76 ± 4.4*	*166 ± 9*
		-45	*557 ± 47*	*108.59 ± 2.9*	*195 ± 17*
		-60	*637 ± 31*	*128.14 ± 3.3*	*201 ± 11*
	BDC	*-10*	*721 ± 16*	*145.33 ± 2.5*	*202 ± 6*
		-45	*633 ± 40*	*139.54 ± 9.0*	*221 ± 20*
		-60	*835 ± 30*	*137.40 ± 15*	*165 ± 19*
PDC	*PDC*	*- 60*	*215 ± 10*	*66.7 ± 4.6*	*310 ± 26*
	HT PDC	*-60*	*205 ± 6*	*67.6 ± 5.8*	*329 ± 30*

10.1.5 Mechanical properties

The mechanical properties of DC, BDC and PDC films are of importance because of the flexibility and adhesion required in winding wire insulation. Pull off and scratch testing were carried out in order to assess the film suitability for purpose as a thermally stable insulator. The surface roughness (Ra) of all films was below 40 nm, meaning that it was suitable to carry out scratch testing on the films as deposited onto polished copper substrates.

The mechanical adhesion of the DC films presented in this study appeared to improve with the addition of this bi-metallic interlayer, which also included a longer sputtering period, during the transition between aluminium and alumina whereby DC and BDC films had pull off adhesion of 63.0 ± 6.4 and 72.3 ± 5.6 MPa respectively. The improved adhesion strength is a result of higher amounts of material mixing at the Cu-Al interface facilitated by the RF Cu sputtering [314]. The lack of pull off failure at the Al-Al_2O_3 interface for DC films, suggests that the additional time taken to reach the 23% OEM set point was not necessary for promoting adhesion at this interface. The prevalence of partial interfacial delamination in DC films could be a result of non-uniform film stress distribution, arising from the lack of Cu in the interlayer. Pull off testing for PVD deposited alumina is not widely documented but values obtained in this study agree well with results published for electron beam evaporated copper deposited onto sputter cleaned polycrystalline alumina by *Erck et al.*, who achieved a maximum pull off adhesion strength of 88 MPa [160]. Variance in the applied bias had no significant effect on the adhesion strength of the coatings, suggesting there was no appreciable change in internal stress, which was also eluded to by the lack of discernible trend in the Al-O phonon shifting in the FTIR of samples with comparable interlayers (but variable bias voltages), see ***Table 10.1***. However, increasing the sputtering time beyond 90 min for the DC films resulted in an appreciable decrease in the pull off adhesion strength to 26.5 ± 2.3 MPa, also see ***Table 10.3***. This suggested increase in internal stress is also indicated by the FTIR shifting from 876 to 843 cm^{-1} for the films deposited for 90 and 120 min respectively.

The pull off failure strength of 55.7 ± 2.9 MPa for PDC films was 25 % lower than the average for BDC films. Due to the lower sputtering rate of the PDC process it can be assumed that the Al interlayer was smaller and that there was a lower amount of material mixing in the Cu/Al blending stage, which would have resulted in a sharper interface which has been shown to be detrimental to adhesive properties [221]. The heat treatment of PDC films resulted in a further two fold decrease in pull off adhesion strength, caused by the mismatch in thermal expansion of Cu and Al_2O_3 (bulk copper 17.1×10^{-6} and 5.4×10^{-6} $°C^{-1}$ for sputtered Al_2O_3). Such a mismatch would potentially cause micro-cracking at the interface upon heating, weakening the adhesive properties as seen for the PDC films [315]. This suggests that the material mixing stage employed for the heat-treated films was insufficient to promote adhesion.

Alumina adhesion has been explored using various substrates and with a number of interlayer configurations. *Järvinen et al.* showed a delamination in alumina film at 10 % strain (RF deposited) deposited on copper where a Ti or TiN interlayer was not used. The benefit of interlayers in alumina thin film systems has been widely shown and other metal systems have also shown promise [143,181,182]. *Vuoristo et al.* have produced thin Al_2O_3 coatings on copper substrates using magnetron sputtering with varying power supply options focusing on the use of the coatings for electronic applications. Adherence was again found to improve with the application of a suitable bond layer, such as Ti or Cr to protect the coating from delamination during thermal cycling [182].

Scratch testing showed the DC films exhibited average L_{C1+2} and L_{C3} forces of 1.0 ± 0.5 and 1.7 ± 0.3 N and BDC films had average failure loads of 0.4 ± 0.1 and 3.1 ± 0.3 N for L_{C1+2} and L_{C3}, with both sets of films exhibited combination tensile cracking and buckling. Despite the addition of Cu and the longer Al-Al_2O_3 blending in BDC films improving the pull off adhesive strength, no significant change in L_{C1+2} critical loads (cohesive failure) were noted, however, an increase in the average L_{C3} was seen following the implementation of the blended interlayer. For PDC films the failure load at cohesive failure (L_{C1}, conformal cracking) and adhesive failure (L_{C2}, buckling failure) compared favourably to the DC films at 0.87 ± 0.05 N and 1.96 ± 0.16 N. No change in failure mechanism was seen following heat treatment of PDC films, which resulted in cohesive failure at 1.55 ± 0.35 N and adhesive failure at 1.79 ± 0.43 N which compared favourably to the as deposited PDC films. All the scratch test adhesion data is summarised in ***Table 10.3***.

The application of bias voltage had no consistent effect within DC or BDC films. However, the application of a -60 V substrate bias during Al_2O_3 deposition did increase the average adhesive and cohesive failure load in DC and BDC films, see ***Table 10.3***. This is likely a result of film thickness effects or because of the – 60 V bias potential to reduce internal stress in the films, however, no FTIR shift was seen. There was no clear relationship between sputtering time and the critical load for cohesive failure in the DC films, however, the critical load for adhesive failure showed a clear decrease in every instance where the sputtering time was increased from a maximum of 5.04 ± 0.4 to 0.66 ± 0.1 N, for 30 and 120 min deposition times for DC films respectively, see ***Table 10.3***. This relationship is likely a result of an increased stress in the films caused by the increased thickness and processing times.

Scratch failure modes studied by *Bull et al.* in Al_2O_3 scales were similar to those observed in the current study for the alumina films, displaying cohesive failure through conformal cracking and subsequently adhesive failure through buckling, as seen in the scratch test imaging of sample in this study, see ***Figure* 5.20** [144]. Scratch loads identified in the current study were comparable to those of alumina films deposited by CVD onto stainless steel by *Haanappel et al.* which showed critical loads of *ca.* 0.130 N for 1 μm thick films [159]. The work by *Haanappel et al.* also outlined the improvements seen in critical loads with increasing film thickness, which was not the case in this work with respect to the cohesive failure of thicker BDC films produced with a -60 V substrate bias. Elsewhere the lack of trend in scratch test results may be because the difference in thickness was not substantial.

Table 10.3: *Summary of the pull off and scratch adhesion of DC, BDC and PDC Al_2O_3 films as deposited onto Cu disks and heat treated in the case of PDC films.*

Sputtering method	***Sample Bias (V)***	***Sample thickness (nm)***	***Pull off adhesion strength (MPa)***	***Lc1 (N)***	***Lc2 (N)***
DC	*-10*	*1566 ± 27*	*25.8 ± 9.8*	*0.80 ± 0.04*	*1.74 ± 0.25*
	-45	*1326 ± 6*	*64.3 ± 6.4*	*0.58 ± 0.53*	*1.21 ± 0.08*
	-60	*2095 ± 10*	*63.0 ± 6.4*	*1.60 ± 0.10*	*2.14 ± 0.18*
DC	*-60*	*760 ± 10*	*51.4 ± 5.4*	*1.45 ± 0.6*	*5.04 ± 0.4*
	-60	*1150 ± 45*	*32.4 ± 4.8*	*0.78 ± 0.1*	*2.20 ± 0.2*
	-60	*2030 ± 25*	*26.5 ± 2.5*	*0.66 ± 0.1*	*1.33 ± 0.1*
BDC	*-10*	*1755 ± 12*	*73.0 ± 3.6*	*0.40 ± 0.08*	*2.59 ± 0.24*
	-45	*1854 ± 13*	*76.2 ± 3.3*	*0.35 ± 0.03*	*2.25 ± 0.24*
	-60	*1868 ± 13*	*72.3 ± 5.6*	*0.52 ± 0.03*	*4.38 ± 0.07*
PDC	*- 60*	*215 ± 10*	*55.7 ± 2.9*	*0.87 ± 0.05*	*1.96 ± 0.16*
HT PDC	*-60*	*205 ± 6*	*21.8 ± 3.4*	*1.55 ± 0.35*	*1.79 ± 0.43*

10.1.6 Reproducibility

Reproducibility studies of the PDC film deposited at 150 kHz and 40 % duty cycle were carried out. These repeats showed that the films were consistently X-ray amorphous, and free of elemental defects at the surface of the films. The Al:O ratio was slightly larger at 0.70 and the FTIR peak shifted to a higher wavenumber. These discrepancies could be a result of target aging and increased race track erosion, which has been shown by *Madsen et al.* to effect deposition rates during reactive pulsed DC sputtering [303]. The mechanical properties of the films were still lower than those of the DC and BDC films and adhesive and cohesive failure mode remained the same.

10.1.7 Summary

The properties discussed in this section lead to the determination that PDC Al_2O_3 films were the most suitable for isolative coatings. Specifically, the samples produced at 150 kHz with a duty cycle of 40% were selected as the Al:O ratio of 0.68 was closest to ideal for alumina. Thus from this point in the discussion PDC will refer to samples produced with these conditions. Whilst the deposition rate was lower than DC deposited films, the rate was still four times that of RF films and the films had an appreciably higher dielectric strength than the DC films, which was the result of a reduced number of defects caused by the diminished amount of target arcing.

There was no observable trend between applied substrate bias and the properties of these films. An increase in sputtering time for the DC films was shown to have a negative effect on the mechanical properties for both pull off and scratch testing; as a result of an increased internal stress. The effect of sputtering time on structure and stoichiometry was, however, shown to be inconstant.

However, when looking at the dielectric strength of other films such as *Bartzsch et al.* and *Carreri et al.*, it is clear there is room for improvement [121,186]. Thus routes to improve the dielectric strength of the materials further will be focused upon in the next section (*10.2*).

10.2 Multilayer composite films

The objective of this section was to take the optimised single layer PDC Al_2O_3 and improve it further through the use of multilayers. The highest dielectric strength material produced in the previous section (*10.1.4*) was the PDC Al_2O_3 and thus it was chosen to be combined with additional candidate layers to improve dielectric strength further. This study combined it with SiO_2 or Ta_2O_5 RF layers with the goal of achieving a higher dielectric strength. Multilayers have shown promise in improving the electrical properties of Al_2O_3 previously in Al_2O_3-SiO_2 systems. It is also noteworthy that SiO_2 and Ta_2O_5 are utilised widely in electronics and would not be disconcerting or hazardous to an end user.

In addition, the multilayer composites will also be combined with the interlayer used in the BDC films which exhibited increased adhesion as seen in the previous section. Given that the thickness of the coating is one of the main issues for application as insulating coatings because of packing space as well as deposition time and increasing defects in thicker films and ultimately the higher the dielectric strength the thinner that allows the isolative coating to be. The multilayer composites were characterised in order to assess their suitability for insulating coatings.

10.2.1 Initial SiO_2 composites

SiO_2 layers were initially added to PDC Al_2O_3 without moving the shield during deposition however this led to films which suffered from through thickness conduction and thus were not fit for purpose. The films contained no elemental Si as evidenced by the Si_2P binding electron energy being at 103 eV correlating to Si^{4+}. XPS did, however, reveal that the films were Si deficient, with Si:O ratios of 0.39 and 0.41 for 1x1 and 2x2 motifs respectively. FTIR analysis suggested that the films contained Al_2O_3 and SiO_2 with a combination of peaks resulting from Al-O and Si-O bonding, see ***Figure 7.2***.

The XPS results combined with the fact that films conducted through thickness suggested that during ramping of the Al target, elemental Al may have been sputtered into the films causing conduction, a similar effect to the arcing seen in DC and BDC films.

10.2.2 Structural characterisation of PDC RF composites

As shown for the RF films at the start of the discussion section (*10.1.1*), the deposition of amorphous thin SiO_2 and Ta_2O_5 using RF power was possible. These materials were combined with PDC alumina with a view to improving current leakage and breakdown strength, whilst maintaining a reasonable deposition rate. To mitigate the through thickness conduction which was seen for initial deposition of SiO_2 composites, see section (*10.2.1*), layer blending was carried out by ramping only the RF target (turning off the Al target during blending stages). The following section will discuss the characterisation of such films, deposited with 1x1, 2x2 and 4x4 layer configurations with RF sputtered SiO_2 or ta_2O_5. For nomenclature see section (*4.1.4*) and ***Figure 7.1***. As in the last section heat treatment was used with a view to improve the films mechanical and electrical properties further and will be discussed in tandem with the as deposited films.

For the composite films multiple infrared absorption peaks associated with the constituent layers of the composite films were seen, see ***Figure 7.4***. For Ta_2O_5 composites a broad absorbance peak resulted from Al-O phonon vibrations combined with Ta_2O_5 peaks at *ca.* 785 cm^{-1} which decreased in intensity from 0.97 to 0.92 with an increasing number of layers as less of the Ta_2O_5 was at the surface. The FTIR spectra of SiO_2 composites as shown in ***Figure 7.4***, consisted of overlapping Al-O and Si-O peaks. There was also a peak at 1229 cm^{-1} assigned to Al-O-Si bonding at the Al_2O_3-SiO_2 interfaces, which may lead to improved adhesion [291]. However, because of the mismatch in thermal expansion coefficients between SiO_2 and Al_2O_3 the adhesion was only better for the SiO_2 composites (when compared to Ta_2O_5 composites) where the 8 layer structure was used, see (*10.2.4*).

Upon annealing in air, the composite multilayer structures underwent colour changes. SiO_2 composites went from a deep blue to a copper like colour. The Ta_2O_5 films transitioned from a light metallic blue towards a copper colour, see ***Figure* 9.6**. Transitions in the colour of heat-treated films suggest that they become transparent as a result of oxidation of the underlying Al interlayer. This suggests that upon heat treatment, oxygen from the film is being used to oxidise the film and is supported by the colour and oxidation of the Ta_2O_5 composites discussed below. Another explanation could be oxidation through pinholes; however, no pinholes were found in

AFM or SEM analysis of the films. The XPS results which show an increase in the amount of oxygen at the surface of the heat treated Ta_2O_5 composites but not for the heat treated SiO_2 composites suggests that the oxidation of the interlayer occurs through different methods in each set of composites. Thus it is likely that oxygen migrates through the film in Ta_2O_5 composites and that in SiO_2 composites oxygen migrates only from the area close to the interlayer. The activation energies for oxygen diffusion in the amorphous ceramics are all in the order of 1 eV, suggesting that the mechanism variation must be a result of structural/ compositional defects in the Ta_2O_5 composites [316,317].

In the heat-treated Ta_2O_5 composites a decreasing layer thickness resulted in a diminished absorption peak for Ta-O-Ta bonding, as seen in the as deposited composites. Peaks positioned at 781 cm^{-1} with a shoulder at 817 cm^{-1} observed by *Mannequin et al.* in electron beam evaporated and sputtered Ta_2O_5 films, again agreed well with the peaks observed in the heat-treated films [205]. The same combination of peaks seen for as deposited SiO_2 composites - resulting from Al_2O_3 and SiO_2 vibrations and Al-O-Si linkages was maintained following heat-treatment. Aerogels consisting of Al_2O_3 and SiO_2 produced by *Wu et al.* showed the same peak combinations and suggested the existence of Si-O-Al bonding with the evolution of a peak at 1181 cm^{-1} [318]. Hence assignment of the peak at 1229 cm^{-1} was to either Al-O-Al bonding or Al-O-Si bonding in the current study.

The XRD pattern for RF Ta_2O_5 was not replicated in multi-layer Ta_2O_5 films, which was because of their much thinner nature of up to ca. 50 nm compared to 774 nm and a lack of sensitivity from the XRD instrument. All as deposited and heat-treated film samples were X-ray amorphous as evidenced by the lack of diffraction peaks for the constituent materials in the XRD diffraction patterns. Possible peaks in the diffraction patterns of heat-treated composites resulted from Al/Cu mixing at the interlayer. Discrete layers were too thin to be imaged in any of the as deposited or heat-treated composite films using SEM techniques, with all films appearing relatively featureless as seen in ***Figure 7.8***. The heat-treated composites showed an average thickness of 219 ± 8 and 181 ± 4 nm for Ta_2O_5 and SiO_2 composites respectively. These values were not far removed from the thickness of non-heat-treated films at 188 ± 6 and 203 ± 6 nm. This lack of significant thickness change suggests no significant densification, possibly prevented by the layered structure.

XPS of both sets of composites indicated the presence of oxide material as seen for the films reviewed at the start of the discussion chapter (*10.1.1*). For the SiO_2 composites XPS showed that the level of Si^{1+} increased in every instance where the number of layers was increased (1.9 to 15.8 for 2 and 8 layers respectively), see ***Figure 7.6***. The lack of Al in the survey spectra rules out the influence of compound material at the boundaries such as Al-O-Si as suggested by FTIR, this is therefore likely a result of the increase in total sputtering time resulting in preferential sputtering effects when considering the multiple blending stages required in the 4x4 films, which increased the amount of compositional defects. Deconvolution of the O_1S peaks was used to determine the identity of the Si^{1+} species (***Figure 7.7***). This analysis showed that the Si^{1+} shoulder was made up of contributions from surface hydroxides with a peak at 534.52 ± 0.01 eV accounting for between 2.13 - 3.73 % of the Si in the film, and a SiO_{2-X} peak at 530.58 ± 0.15eV accounting for between 3.4 - 5.1 % of the Si in the film. The amount attributed to SiO_{2-X} species was much lower than the 29.1 % seen for RF films [319]. This improvement with respect to the level of SiO_{2-X} in RF films, is attributed to target conditioning during reactive PDC Al_2O_3 sputtering as well as the decreased sputtering time [96]. Upon heat treatment the Si:O remained consistent suggesting that no further oxidation took place at the surface see ***Table 10.4***. An unintended consequence of the heat treatment was through thickness copper migration from the substrate, which is discussed below.

Conversely to this Ta_2O_5 films contained only Ta^{5+} and all experimental Ta:O ratios were close to stoichiometric (between 0.35 and 0.4, see ***Figure 7.6***). The variance in the stoichiometry is likely the result of preferential sputtering from the RF target and the number of conditioning stages (where the RF target was off during PDC Al_2O_3 sputtering), which could influence the level of oxide on the target surface. The 4x4 layer material which had the shortest conditioning stages had the best Ta:O ratio of 0.4 and were not oxygen rich, suggesting that the extended conditioning stages in the other configurations could be causing the offset in the Ta:O ratio. Deconvolution of the O1_S peak in the XPS results for the Ta_2O_5 composites yielded two peaks, similarly to work by *Mannequin et al.* who showed the possibility of the peaks resulting from O-H, oxygen vacancies or O-C from contaminants or surface species [205,320]. Following heat treatment, the materials became increasingly oxygen rich with Ta:O ratios falling from an average of 0.38 to 0.31. As with the SiO_2 composites an undesired consequence of the heat treatment was the migration of copper from the substrate.

Copper migration was identified through analysis of the survey spectra for both sets of heat-treated composites, which revealed the presence of Cu_2P photoelectrons at an average binding energy of 933.4 ± 0.2 eV suggesting either Cu or Cu^{2+} (see ***Figure 9.11***). The scan contained strong satellite peaks ultimately leading to the CuO (Cu^{2+}) designation and as only the top surface of the film is analysed by XPS the copper had to have migrated through the whole film thickness [321]. This effect was not seen in the heat treated PDC films, suggesting that Al_2O_3 acted as a sufficient barrier to copper migration. The 2x2 layer configuration displayed the lowest amount of Cu migration in both cases with 7.3 and 0.9 at.% at the Ta_2O_5 and SiO_2 composites surface respectively, showing the importance of multiple barrier layers of suitable thickness in the structure [322]. The amount of copper in the SiO_2 composites was *ca.* six times lower than in the Ta_2O_5 ***Figure 9.11*** suggesting that the SiO_2 layers were more suitable for insulation at higher temperatures. Whilst XRD showed the material was X-ray amorphous, the migration issues are likely the result of small amounts of crystallisation related defects in the films or defect channels such as pores, whereby copper diffusion would be facilitated at these sites. This is supported by the fact that crystallisation to some degree has been seen in Ta_2O_5 films sputtered with a high substrate bias and at 400 °C by *Huang et al.* [322,323].

Migration behaviour of Cu has been studied due to its use in microelectronics and many materials including sputtered metal nitrides have been suggested as barriers because of their high thermal stability and conductivity [322,324]. Ta prevents diffusion of Cu because it doesn't form a compound with it and Cu and Ta are also immiscible, with no stable Ta-Cu compounds being known [325]. The addition of N or O to Ta barrier films was shown to improve the barrier properties, and this was reasoned to be a result of obstruction of Cu diffusion at the grain boundaries. Such additional materials could be implemented to mitigate problems seen here in Ta_2O_5 composites. Oxidation of Cu nanorods has been seen by *Qin et al*. through a porous Al_2O_3 nano structure, causing an outward diffusion of Cu ions, resulting in a build-up of CuO/CuO_2 on the surface [326]. However, once a non-porous coating was applied no migration/oxidation was seen. In the case of the films produced in this study, PDC Al_2O_3 and the RF SiO_2 composites showed little to no copper migration to the surface layer, XPS analysis showed no Cu^{2+} photo electron peaks for heat treated PDC and Cu^{2+} accounted for up to 2.7 at.% to in the case of heat treated SiO_2 composites, as shown in ***Figure 9.11***. This suggests that the films were mainly non-porous and thus suitable for high temperature isolative applications.

Migration of Si through Ta_2O_5 films was seen upon annealing of films Ta_2O_5 films at 350-430 °C produced by *Chaneliere et al.* using CVD methods [133]. It is likely therefore that the Ta_2O_5 layers in this study changed the composite structure sufficiently to allow Cu^{2+} diffusion, as noted by *Wang et al*. for Ta and TaN diffusion barriers above 650 °C, who concluded that diffusion could occur through localised defects in their diffusion barriers [322]. Whilst no crystallinity was noted in XRD analysis, it is possible the migration of the copper coincided with the beginning of crystallisation of the Ta_2O_5 layers in the films. Such an effect was seen above 600 °C in ALD and electrostatic spray deposition deposited Ta_2O_5 deposited onto Si by *Lintanf Salaün et al.* [327] This could be the reason for the much higher levels of copper migration in the Ta_2O_5 composites.

10.2.3 Electrical properties of multilayer PDC films

AFM DB measurements of the as deposited composite films showed that using SiO_2 or Ta_2O_5 as an additive layer had the potential to improve the dielectric strength by a maximum of 203 ± 28 $V\mu m^{-1}$ for 2x2 Ta_2O_5 composites compared to PDC Al_2O_3 alone. The dielectric strength was shown to be dependent on the layer configuration. In the heat-treated samples which will be discussed later in this section, the breakdown was again shown to be dependent on layer structure but the composition was shown to play a much larger role in the dielectric strength. Heat treated samples displayed a maximum increase of 188 ± 49 $V\mu m^{-1}$ for SiO_2 2x2, compared to heat treated PDC Al_2O_3 alone.

The maximum increase in the as deposited films resulted from the 2x2 samples increasing by an average of 156 ± 48 $V\mu m^{-1}$, whereby 2 layers each of PDC and RF addition were used. These improvements are likely to be a result of the barrier properties of the inserted layers, whereby they inhibit the flow of current through the films. However the 4x4 composites had lower average dielectric strength than the 2x2 films but still significantly higher than the as deposited PDC Al_2O_3 with an average increase of 100 ± 38 $V\mu m^{-1}$. The reduction in dielectric strength of the 4x4 composites with respect to the 2x2 films, may be due to the decreased layer thickness of the added RF layers, which act as poorer defect capping layers as a result. Further justification for this decrease in dielectric strength can be taken from the 4x4 SiO_2 composites increased number of compositional defects, coming in the form of Si^{1+} as shown in in ***Figure 7.6***. The 1x1 composites exhibited the lowest average dielectric strength, which were not significantly increased when compared to the PDC films. This likely results from an insufficient number of barrier layers. Thus the superior electrical properties observed for 2x2 composites, showed that for a fixed film thickness, a compromise between the number of defects produced and the number of layers incorporated was made.

In contrast to the as deposited samples the dielectric strength of the heat-treated Ta_2O_5 composites decreased by an average of 22 %, whilst the dielectric strength of the heat-treated SiO_2 composites increased by an average of 12 %. The trend in dielectric strength where 2x2 composites gave the highest values, followed by 4x4 and then 1x1 composites was preserved following heat treatment although an increase in error of measurement meant that the difference 2x2 and 4x4 composites was not significant.

Layer dependence as observed in the as deposited and heat-treated composites, has been previously documented, such as in HfO_2 Al_2O_3 composites produced by *Park et al.* whereby composites with 7 and 5 layers had enhanced breakdown characteristics compared to three layer materials. This phenomena was attributed to the blocking of current through grain boundary channels [328]. Further support for the benefits of barrier effects come in the form of studies on solid polymer dielectrics by *Gefle et al.* who discussed a mechanism by which material interfaces prevent charge propagation across films improving the dielectric strength such as by increasing the time needed for tree growth and an increase in the failure-initiation time [329]. *Mattox* also noted that the use of multi-layered composites can be useful for decreasing the number of pinholes resulting from abnormalities during growth [330]. In ceramic multi-layered composites a two times improvement of up to 92 ± 7.0 $V\mu m^{-1}$ in the dielectric strength of sputtered SiO_2, Al_2O_3 composite coatings was noted by *Martinez-Perdiguero et al.;* this condition was met when 2,4 and 8 layer materials were used instead of the single layer alumina. The efficacy of the layer configurations also mirrored those seen in the current study whereby composites with two layers of both Al_2O_3 and SiO_2 showed the greatest improvement, the composites with one or four layers of each material were not significantly different from each other [116]. Improvements of this kind could be the result of added layers masking structural or compositional defects, such as in the Al_2O_3-SiO_2 gas diffusion barrier films, produced using ALD by *Dameron et al.* [279].

Taking this research into account it can be seen that incorporating barrier layers with a higher dielectric strength relative to the base material has the potential to increase breakdown strength and lower leakage current. It is therefore suggested that the mechanisms for the improvement in SiO_2 and Ta_2O_5 composites include: defect capping (structural and compositional), prevention of charge injection and disrupting the growth of breakdown channels, see ***Figure 10.3***. *Ren et al.* have shown an improvement in dielectric strength by up to 17.2 % with the clay modification of polymers [331,332]. The improvement was attributed to the suppression of charge injection and migration, whereby this resulted in the inhibition of an electron cascade. The biaxially orientated poly propylene only had marginal improvements of 1.1 % because of its intrinsic dielectric strength, showing in that case that materials with sufficient intrinsic breakdown strength weren’t affected by layering. It is because of this that the RF deposition method is seen as key to producing films with high enough breakdown voltage to act as sufficient barrier layers in the PDC Al_2O_3.

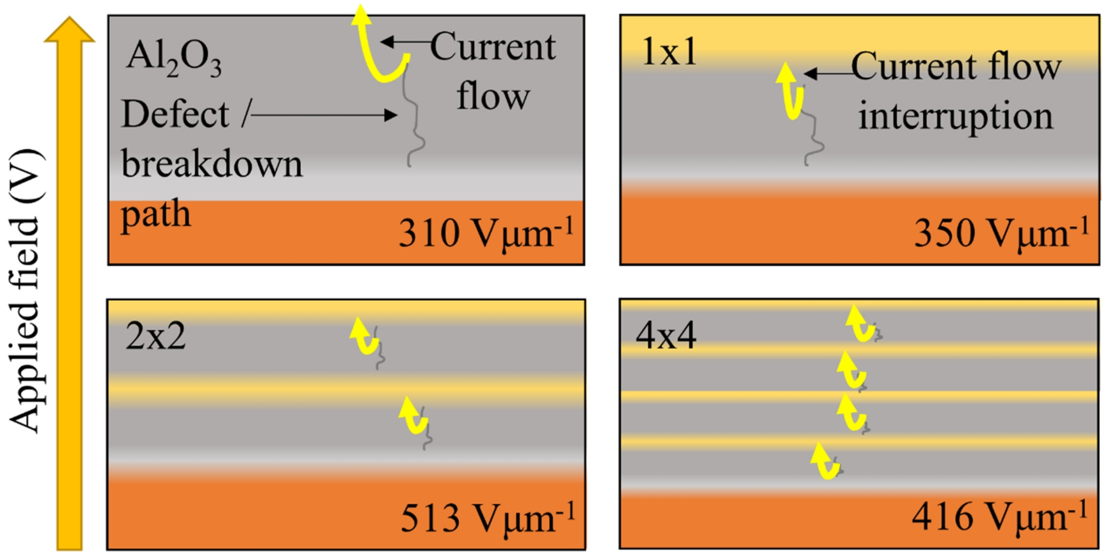

Figure 10.3: *Effect of multilayers for capping and barrier properties in resisting current flow and disrupting breakdown paths in thin ceramic composites. Defects are shown to be passivated in the films having a multilayer configuration. The dielectric strength is highest for the 2x2 films and the maximum dielectric strength for each layer configuration given in the bottom right of each illustration.*

SiO_2 and Ta_2O_5 were chosen because they are commonly sputtered materials and can be produced using RF power. Further to this films sputtered especially by RF sputtering have been shown to have high dielectric strengths up to 570 and 600 Vμm^{-1} for RF sputtered SiO_2 and Ta_2O_5 respectively and potential as film insulators in capacitors, especially Ta_2O_5 with a high dielectric constant of 23 [121,206].

Whilst as deposited Ta_2O_5 composites had a higher maximum dielectric strength than the SiO_2 composites, they suffered from higher leakage and large current oscillations which were noticeably more severe in 1x1 composites see ***Figure 7.13***. As mentioned for the DC and BDC samples (*10.1.4*) this was attributed to charge trapping and de-trapping. However, as evidenced by TEM, the PDC films should be relatively defect free, suggesting that either stress induced leakage current becomes an issue or the presence of defects in the Ta_2O_5 films supported the current oscillations. It is possible that there is a larger number of defects in the Ta_2O_5, this theory is supported by the fact that the maximum current flow prior to breakdown was *ca.* 6 and < 1 nA for Ta_2O_5 and SiO_2 composites respectively. This shows that the RF SiO_2 acted as a superior barrier layer to Ta_2O_5, which must have been a result of better intrinsic properties in the RF sputtered layers. It is therefore likely that the SiO_2 layers contained fewer defects capable of trapping charge.

Heat treatment of SiO_2 composites resulted in a minimum breakdown strength 36 % higher than comparable heat treated Ta_2O_5 composites. The dielectric strength in the SiO_2 composites increased by an average of 12 % following heat treatment and the Ta_2O_5 composites decreased by an average of 22 %. The dielectric strength of SiO_2 heat treated composites were 132 ± 63 Vμm^{-1} higher than heat treated PDC Al_2O_3 respectively, whereas there was no significant difference between the dielectric strengths for heat treated Ta_2O_5 composites and the heat treated PDC films.

This decrease in the electrical properties of Ta_2O_5 films can be accounted for by considering that at 500 °C it is possible that nano crystallisation in the Ta_2O_5 films, which may have been initiated but was not observable by XRD. Any crystallites or impurities from the substrate could well act as charge trapping sites and potentially act as a route to premature breakdown. Another effector for the deterioration in dielectric strength in the Ta_2O_5 films compared to the SiO_2 ones could be the *ca.* six times higher levels of Cu defects in the film as evidenced by the XPS, see (*10.2.2*).

With respect to the improvement seen in SiO_2 composites, rapid thermal annealing of RF SiO_2 films investigated by *Choi et al.* was shown to improve the breakdown field from a minimum of 12 to a maximum of >400 $V\mu m^{-1}$ [265]. This improvement was a result of a reduction in the fixed charge density and the density of charge trapped at the interfaces. A similar effect was seen in Y_2O_3 films sputtered by *Quah and Cheong*, whereby annealing reduced the amount of defects and created an interfacial layer, resulting in an *ca.* 1.5 times higher dielectric strength and lower leakage current in films when annealed at 1000 °C for 15 and 45 min, caused by an increase in Fowler-Nordheim barrier height from 3.6 to 4.4 eV [333]. Multilayer composites deposited by *Martinez-Perdiguero et al.* also showed a decrease in leakage current by at least one order of magnitude for PVD multi-layer Al_2O_3 SiO_2 films when a 2 µm sample deposited on stainless steel was annealed for 60 min at 500 °C [116]. In the current study heat treatment was shown to increase the dielectric strength of the SiO_2 composites in accordance with the previously mentioned research, suggesting that the number of defects in the SiO_2 layers decreased.

High current variability in low field regions of the AFM DB measurements, combined with large current oscillations and variance between measurements made for the same samples and very little leakage for SiO_2 composites, meant that a conduction mechanism prior to breakdown could not reliably be assigned for either as deposited or heat-treated samples. Conduction mechanisms in the constituent RF SiO_2 and Ta_2O_5 have been attributed to Fowler-Nordheim tunnelling, as well as Schottky or Poole-Frenkel mechanisms [134,207]. So it could be the case that these mechanisms play a role in the conduction through the multilayer composites.

AFM was used to measure the dielectric strength of thin films by *Ganesan et al.* and even to perform layer by layer breakdown testing on BN by *Hattori et al.* [103,224]. However, AFM DB measurements have not been widely used for multilayer ceramic composites. It was hoped that the technique could help divulge information about the conduction mechanisms through the films, however, due to the high current variation at low fields and charge trapping and de-trapping at high fields in these specific films it was unfeasible.

10.2.4 Mechanical characterisation of PDC RF composites

The pull off adhesion strengths of all of the as deposited composites was shown to be on average 2.4 times lower than that of the solely PDC alumina films [334]. Additionally pull off adhesion of the heat treated SiO_2 and Ta_2O_5 composites resulted in an average adhesion strength which was 35.1 ± 8.1 MPa lower than the as deposited PDC films, see ***Table 10.4***. Upon heat treatment there was no significant trend in the adhesion when comparing as deposited and heat-treated composites, the average adhesion strength was also not significantly different and it was 39.9 ± 6.7 MPa lower than the as deposited PDC Al_2O_3 films.

The failure mechanisms in the as deposited and heat-treated samples also shifted from predominantly partial interfacial failure to complete interfacial failure, see ***Table 7.4***. This failure mechanism was preserved following heat treatment. The substrates in both cases were treated using the same methods, thus the decrease seen between PDC and the composites must be ascribed to the use of multilayers. It is likely that implementation of the layered structure resulted in a higher level of intrinsic stress. Intrinsic stress in PVD thin films originate from either variation in thermal expansion between the substrate and the film or from growth induced stresses formed during condensation. Therefore, the decrease following heat treatment is likely a result of the mismatches in thermal expansion, which will be expanded upon later in this section. The prevalence of complete interfacial failure at the Cu-Cu interface in the current study indicates that the blending stages were sufficient to mitigate cohesive failure between the sputtered layers.

Knotek et al. have explored the effect of PVD deposition techniques on intrinsic stress, showing the dramatic effect of processing parameters, showing a 1 GPa reduction of growth induced compressive stress when applying substrate heating increasing from 200 to 500 °C [335]. This reduction was measured for TiN using bending gauge and X-ray methods. For instance a *ca.* two times increase in film adhesion was the result of a decrease in intrinsic stress from 4.84×10^{-9} to 0.21×10^{-9} Nm^{-2}, caused by chopping of CeO_2 films as deposited by *Patil et al.*, who also showed the same effect in ZnS films [336,337]. The use of multilayers also increased intrinsic stress in $BaTiO_3$/ Ni composite ceramic capacitors, analysed by Park *et al.* [338,339]. An increase in the $BaTiO_3$/ Ni layer frequency increased the compressive in plane stress, which reached a maximum at < -135 MPa. Blending stages have been used extensively for improving the adhesion of diamond like carbon films. For instance, a number of graded layers such as Ti or TiN can be used to avoid de-adhesion and avoid high interfacial stresses [100]. Thus, the use of blending combined with the low adhesive strength at the Cu-Cu interface resulted in the lack of cohesive failure between layers in the films presented here.

The 1x1 and 2x2 Ta_2O_5 composites had superior combined average pull off adhesion compared to the equivalent SiO_2 composites, yielding values of 22.6 ± 2.7 and 15.8 ± 1.2 MPa respectively. For both sets of films the adhesion decreased when moving from 1x1 to 2x2 films, which could be a result of an increased internal stress at the Cu-Cu interface caused by the increased number of interfaces. There was no clear trend carried through to the pull off adhesion results of the heat treated samples with respect to either the number of layers or their composition. The pull off adhesion was generally lower for the heat treated samples. This decrease is likely the result of the mismatch in coefficients of thermal expansion, where literature reports expansion coefficients for Al_2O_3, SiO_2 and Ta_2O_5 of $5.4x10^{-6}$, $5.1x10^{-7}$ and $3.6x10^{-6}$ °C^{-1} respectively [242]. Thus the coefficient of thermal expansion mismatch led to an increase in internal stress within the composites, decreasing their adhesion strength. See ***Figure 9.18*** for a summary of the pull off adhesion strength values.

Scratch testing of as deposited composite materials showed similar cohesive failure to PDC Al_2O_3 films, failing by conformal cracking at 1.07 ± 0.29 N, but exhibited a much decreased adhesive failure load manifesting as buckling at 1.18 ± 0.24 N (***Figure 7.9*** and ***Table 7.3***). The failures in PDC materialised as combination cracking failures at 0.87 ± 0.05 N and buckling failures at 1.96 ± 0.16 N. The slight increase in film thickness for the 4x4 samples can also be used to explain the trend for 4x4 films to generally have the greatest scratch failure loads, because of the higher load required to deform the substrate. Following heat treatment there was no significant difference in the average onset of cohesive conformal cracking failure at 1.13 ± 0.40 N or adhesive buckling failure at 1.50 ± 0.63 N compared to the as deposited films. The layer configuration similarly had no consistent effect on the scratch adhesion see ***Table 10.4***.

Scratch testing of sputtered Ti/TiB_2 multilayer composites has been reported by *Chu and Shen* [340]. Their work found strong links between hardness and critical scratch test failures: as the bi layer thickness increased from *ca.* 1.9 to 9.8 nm the hardness decreased by 50 %, the cohesive failure remained the same at 10 N and the adhesive failure decreased by 79 %. These changes were attributed to higher levels of intermixing between the Ti and TiB_2 layers as the bi layer thickness decreased. Therefore, the critical load increases (see ***Figure 7.5***) seen in the 4x4 films could be attributed to increased hardness because of the smaller bi layer thickness.

10.2.5 Multilayer composites summary

The use of RF Ta_2O_5 or SiO_2 layers improved the dielectric strength of the PDC Al_2O_3 films by a maximum of 203 ± 28 $V\mu m^{-1}$. This was a result of defect capping and the disruption of breakdown paths forming through the dielectric. The mechanical properties suffered resulting in a pull off strength 2.4 times lower than PDC Al_2O_3 and was the result of increased intrinsic stress introduced through the implementation of multilayers.

Because of the increased stress and implementation of interfaces seen in the multilayer composite materials, which resulted in poorer mechanical properties compared to DC and BDC films (***Table 10.3***) a heat treatment was applied to the samples. This was done with a view to improving both electrical and mechanical properties. This was shown to improve the electrical properties of the SiO_2 films increasing the dielectric strength by a maximum of 188 ± 49 $V\mu m^{-1}$, but was detrimental to the Ta_2O_5 films resulting from an increase in oxygen content, potential for crystallisation and heat treatment induced defects such as copper migration. The adhesion properties of the films were greatly reduced following heat treatment a result of the thermal mismatches at the substrate surface.

Table 10.4: *Compositional, electrical and mechanical properties of as deposited and heat treated SiO_2 and Ta_2O_5 composite films.*

Layer config.		**Thick. (nm)**	**Si:O or Ta:O**	**Dielectric strength ($V\mu m^{-1}$)**	**Pull off adhesion (MPa)**	**Lc1 (N)**	**Lc2 (N)**
SiO_2	1x1	191 ± 4	0.62	332 ± 159	24.6 ± 3.1	0.99 ± 0.10	0.95 ± 0.11
	2x2	182 ± 4	0.57	466 ± 86	16.0 ± 2.2	0.84 ± 0.06	0.97 ± 0.04
	4x4	236 ± 11	0.56	416 ± 73	15.3 ± 2.8	1.25 ± 0.20	1.34 ± 0.11
Ta_2O_5	1x1	203. ± 6	0.35	350 ± 38	22.0 ± 3.4	0.98 ± 0.15	1.18 ± 0.15
	2x2	152 ± 4	0.36	513 ± 18	11.4 ± 1.8	1.15 ± 0.04	1.40 ± 0.08
	4x4	210 ± 9	0.40	403 ± 26	34.3 ± 4.4	1.22 ± 0.06	1.28 ± 0.06
HT SiO_2	1x1	185 ± 6.3	0.55	372 ± 39	9.70 ± 0.8	1.38 ± 0.35	1.99 ± 0.42
	2x2	187 ± 6.0	0.58	517 ± 25	20.1 ± 0.9	1.35 ± 0.11	1.95 ± 0.18
	4x4	171 ± 5.0	0.61	493 ± 29	17.5 ± 2.1	0.97 ± 0.10	1.48 ± 0.16
HT Ta_2O_5	1x1	221 ± 21	0.29	273 ± 28	14.6 ± 2.6	1.19 ± 0.09	1.02 ± 0.13
	2x2	210 ± 8.5	0.30	358 ± 31	13.2 ± 3.5	1.14 ± 0.07	1.52 ± 0.37
	4x4	226 ± 8.0	0.33	344 ± 17	19.7 ± 3.4	0.77 ± 0.05	1.01 ± 0.08

10.3 Wire coating

As the PDC Al_2O_3 was the most promising of the single component films with respect to dielectric strength it was decided to carry this material forward into wire coating trials. Heat treatments were also carried out on the wires in order to assess the effect of potential high temperature working environments on the coatings. Cu wires coated with an Al interlayer deposited at 1.5, 3.0 or 4.5 rpm and 1, 3 or 5 layers of Al_2O_3 were assessed for their electrical properties as well as the mechanical adhesion and thus suitability as a coating for wire material. An initial deposition using an experimental rig and the coating rig without a drive chain showed that the coating of wires was possible and that a coating could be applied to the full circumference of the wire.

10.3.1 Initial deposition at 55 mm and drive chain

The following section concerns the deposition of an Al interlayer, with a 55 mm substrate to target distance, with a drive chain which allowed reel to reel coating in the reverse direction. The Al interlayer was applied at 1.5 rpm in order to maintain a similarity in Al thickness *ca.* 170 nm to DC and BDC interlayers, in the interest of keeping adhesive properties. Al_2O_3 was then deposited at the lowest speed of 0.5 rpm, in order to deposit the maximum amount of Al_2O_3 per cycle. Total film thicknesses of 349 ± 15 nm and 345 ± 10 nm on the opposite side were seen, showing that both sides of the wire were coating evenly. During this stage a substrate bias could not be applied during the sputtering because it caused large arcing events along the wire, causing delamination, material inconsistencies and wire breakages. These events were attributed to the build-up of charge at a faster rate than it could migrate. As a result adhesive properties of the Al interlayer at this point were poor, as seen by delamination in Al_2O_3 coated wire seen in ***Figure 8.5***. Application of a substrate bias has often been shown to improve adhesion in sputtered films, resulting from the aspects discussed in section (*3.1.1.2*) [341]. Once bent the coating would detach from the substrate. The poor adhesion meant that further mechanical and electrical testing could not be carried out on the wires, because delamination in the Al_2O_3 also meant that twisted pairs of wire could not be prepared.

10.3.2 Deposition at 100 mm with drive chain

Increasing the sample target separation was viewed as a way to decrease the rate of charging. Thus the front bearing of the coating rig was moved away from the Al target to 100 mm from the initial 55 mm, with a view to eliminating arcing when a substrate bias was applied. However, arcing was still prevalent during deposition. The removal of polyimide tape used to prevent coating wear from the bearings alongside the increase in separation to 100 mm, eliminated arcing during deposition.

Al_2O_3 films deposited onto the 1.5 rpm Al interlayer with a substrate bias of -40 V and a target separation of 100 mm showed transverse cracking at strains above 3 % strain (>180 MPa) and combination cracking/ delamination above 6 % strain (>206 MPa). FTIR analysis of each side of the wire confirmed the presence of Al-O bonding and no peak shifting was seen in any of the films suggesting that there was no change in internal stress. However, since the Kapton® tape which had been used to diminish wear on the coating was removed from the bearings, regions where the coating had been worn back to the Cu were present. This wear was visible in all coated wires which had been drawn back through the system see ***Figure 8.9***.

10.3.3 Effect of Al and Al_2O_3 coating thickness

The coatings which will be discussed in the following section were produced using bearings which were machined to remove the step, which had been used to hold the wire in place but was detrimental to coating continuity. Bias cleaning prior to coating at -150 V and use of the smoothed bearings has a clear effect of reducing the wear and delamination in films deposited onto wire as shown in the surface light micrographs as seen in ***Figure 8.9***.

Each additional layer of Al_2O_3 added an average of 82 ± 4 nm with average interlayer thickness of 233, 115 and 125 nm for 1.5, 3.0 and 4.5 rpm interlayers respectively. Samples deposited with a single Al_2O_3 layer had a consistent Al-O FTIR peak position, at an average position of *ca.* 912 cm^{-1}. Samples deposited with 3 layers of Al_2O_3 had a clear red shift for the sample deposited with the thickest interlayer with an average of 919 cm^{-1} for 1.5 rpm interlayer compared to an average of 844.25 cm^{-1} for 3.0 and 4.5 rpm interlayers. As discussed earlier for RF, DC and PDC films (*10.1.1*), the shift in wavenumber could be a result of increased intrinsic stress in the films [342]. Further to this it could be reasoned that the thicker interlayer helped to reduce the internal stress in the samples deposited with three layers of Al_2O_3. Despite this there was a decrease in average wavenumber to 802 cm^{-1} for the coating deposited with the thickest interlayer and 5 layers of Al_2O_3 compared to the other thinner Al_2O_3 coatings. This could be an indicator that the level of internal stress in the thickest Al_2O_3 coatings was much higher than in the other cases. Following heat treatment, a decrease in wavenumber of the Al-O peak was seen in three and five layer samples 904-907, 918-818 and 802-705 cm^{-1} for as deposited/heat treated one, three and five layer Al_2O_3 coatings). *Ali et al.* noted an increase in the residual stress from -1.2 to -1.5 GPa in AlN films with an Al bond layer, which was caused by stress build up in the interlayer during cooling [343]. This supports the idea that heat treatments applied in this study were detrimental to the adhesion of the film and expansion effects nullified any improvement in material mixing at the interfaces.

10.3.3.1 Mechanical properties

The tensile failure of the as deposited coatings was found to be relatively similar for all samples (see ***Table 8.2*** and ***Figure 8.21***) regardless of the interlayer implemented. With respect to the coating thickness the highest minimum onset of longitudinal and transverse cracking were seen for samples deposited with a single layer of Al_2O_3 (see ***figure 8.21***). A decrease in crack density was also seen, where fewer cracks were propagated in the thickest coating with five layers of Al_2O_3 resulting in the lowest crack density at 0.01 μm^{-1}.

Post heat treatment a decrease in the minimum possible value for transverse cracking failure strain was 0.5% (49 MPa), which *ca.* three times lower than the minimum seen for as deposited samples. Delamination events were also much more common within the testing range for heat treated samples, as seen in ***Figure 9.22***, whereas it was common place for longitudinal cracking to be seen in as deposited samples. These delamination events occurred above 3.7 % strain (102 MPa) for the 5 layered alumina increasing to 11.3 % (178 MPa) for wire coated with one layer of Al_2O_3. This echoed the tendency for an increase in failure strain with decreasing film thickness, which was seen in as deposited films and resulted from a higher internal stress suggested by the FTIR results, see ***Figure 9.19***. Post heat treatment the ductility of the Cu wire increased, due to dislocation untangling and annihilation and this increase had a large effect on the: failure mechanism moving towards delamination, failure strain and crack density of the tensile tested films. The thermal expansion mismatch, between the wire and coating is another contributor to the decrease in mechanical properties seen for the heat treated samples and as discussed for the heat treated disks (*10.1.5*). The crack density maintained an inversely proportional relationship to the coating thickness following heat treatment, where a significant decrease was seen between 1 and 5 layer coatings, see ***Figure 9.23*** [150]. Critical bending radii calculated for each of the films (***Table 7.3***) using the critical loads, was very small between 0.20 – 1.25 mm, meaning that the coating should not be removed by winding even around relatively small stators/ rotors.

Cracking in thin film alumina under tensile deformation has previously been reported on Teflon substrates by *Jen et. al.* and showed a critical tensile strain of between 0.52 and 2.41 %, similar to the values seen for the coated Cu wire in this work [150]. A similar crack density dependence on layer thickness was observed by *Jen et al.*, who showed, a threefold increase in crack density when the film thickness was decreased from 40 to 12.5 nm [150]. However, the crack density was reported for much thinner films and thus produced much higher crack densities. The thickness crack/density relationship is a result of the increasing fracture energy required in thicker films as simulated by *Jansson et al.*, who also stated that the crack initiation strain generally decreased with increasing thickness, supporting the decrease in crack initiation strain seen in this work [344,345]. Crack combination could account for some of the lower than expected crack densities seen for thinner films, see ***Figure 8.17***.

10.3.3.2 Electrical properties

Short circuiting was an issue for testing the electrical properties of the insulation, preventing breakdown measurement amongst other testing. Continuity issues were not widely detected using simple voltmeter tests. High pot (AC) and High voltage DC testing resulted in short circuiting instantaneously, regardless of the configuration of the tested wire. This suggests that the issues with the wire were there before manipulation (winding/ straightening). Because issues of this nature were not seen in disk samples, they must be attributed to the winding process during sputtering. This could be remedied by winding directly onto the desired item or through further modifications to the bearings and on/off reels. Heat treatment of the wires had no effect with respect to the electrical properties, as the flaws still existed in the films meaning that continuity was still problematic.

10.3.4 Coated wire summary

The use of PVD coating for wires has the potential for producing coatings of varying thickness by changing the number of deposition cycles. FTIR and SEM studies showed coating around the full circumference of the wires. However, it is likely that discontinuities in the films was caused by abrasion or the winding process itself, resulting in electrical inconsistencies. Great improvements in the coating system were made which resulted in considerably fewer delamination events. Further solutions to this could include further modification of the deposition equipment but also could include the use of a multilayer system which has the potential to passivate such defects by combining the superior dielectric strength of the multilayer composites developed in this study with the reel to reel wire coating apparatus. Heat treatment was seen not to improve the mechanical properties due to Cu annealing. The complete circumference coating combined with the possibilities of multilayer coatings provided by the developed coating rig result in a powerful tool for producing insulating wire coatings.

11 Conclusions

The aim of this thesis was to develop a magnetron sputtered ceramic film with high breakdown strength combined with good adhesive properties to copper. Ideally developing a coating which could be used as electrical insulation for magnet wire and ultimately in motor windings.

Initial development on DC sputtered films showed that the use of a mixed material interlayer improved the film systems mechanical properties from an average pull off adhesion strength of 63.0 ± 6.4 to 72 ± 5.6 MPa. However, instability during the DC deposition process was shown to lead to defects within the films, such as short range order as identified by TEM and elemental aluminium as evidenced by XPS, which lead to premature breakdown with maximum dielectric strengths of 201 and 221 $V\mu m^{-1}$ for DC and BDC films respectively. Conduction at high field was ascribed to Fowler-Nordheim tunnelling.

Thus the use of pulsed DC deposition was implemented to help with deposition stability. Pulsed DC deposition led to improved electrical properties with a dielectric strength of 310 $V\mu m^{-1}$, because of the removal of arcing and the resultant Al defects. Despite these improvements a slight decrease in the adhesion properties was seen, owing to poorer interlayer mixing. Pulsing and duty cycle parameters of 150 kHz and 40 % were chosen because they were shown to produce films with good stoichiometry where the Al:O was 0.68, at a reasonable deposition rate of 64 nmh^{-1} as determined by TEM, see ***Figure 5.13*** and ***Figure 6.5***.

Multilayer composite materials deposited to *ca.* 200 nm with varying layer configurations were shown to be consistent with the materials sputtered, however, the stoichiometry and composition of the SiO_2 and Ta_2O_5 RF layers were thought to be affected by preferential sputtering. This was due to the Si^{1+} content of SiO_2 composites. The dielectric strength of these composite coatings were shown to be superior to those of non-layered materials and this improvement was thought to be a result of a combination of barrier effects and structural defect passivation. The maximum dielectric strengths were 466 and 513 $V\mu m^{-1}$ for SiO_2 and Ta_2O_5 composites with a 2x2 layer configuration respectively. The 2x2 layer was shown to give the best compromise between frequency of layers and layer thickness. The mechanical properties of the composites suffered from a perceived increase in intrinsic stress because of the application of multilayers. This increase resulted in decreased adhesive properties when compared to those PDC films alone. A change within the samples was also seen whereby pull off adhesion was generally lowest for films with more layers.

Heat treatment of Ta_2O_5 composites resulted in a decrease in the dielectric strength. This decrease was likely a result of crystallisation of the Ta_2O_5 layers despite being X-ray amorphous and or copper migration through the films. The copper migration was most severe in the 1x1 composites. Conversely, in SiO_2 composites the copper migration was much slighter and there was even an increase in dielectric strength upon heat treatment. This improvement was potentially the result of a reduced number of defects such as charge trapping sites following annealing.

The coating of wires was shown to be possible within the magnetron sputtering apparatus. Coating quality was found to be highly dependent on the quality of the finish on the bearings, with smoothed bearing producing much improved coatings. The tensile properties of the coatings was shown to be relatively independent of the Al interlayer thickness, where the only effects seen were in the crack density. Coating continuity was, however, found to be lacking resulting in problems measuring the electrical properties of the coated wires. Tensile testing showed a trend for the crack density to decrease with increasing coating thickness. Heat treatment of the coated wires resulted in softening of the copper wire, hence tensile testing resulted in greater incidences of delamination failure and indicated a lower applied strain required to initiate cracks in the coatings.

The use of magnetron sputtering as a method for depositing thin multilayer isolative coatings onto copper wire has been demonstrated. However, further refinement of the deposition system and parameters is required to produce wires of improved quality and continuity for use in motor windings.

12 Future work

Further work on this project would centre on the continual development of highly adhesive isolative systems mainly focusing on improvement of the wire coating system:

- Development of highly isolative sputtered films with suitable interlayer configurations, so as to make them highly adhering to copper, further to the work presented in this thesis. This could include the use of materials such as DLC with specifically designed non-conductive interlayers to aid adhesion to other ceramic layers.

- Fine tuning of the layering system used for the composites to yield films with higher breakdown strength and better thermal stability.

    - Tuning of the oxygen flow during multilayer deposition to make sure that all the materials are fully stoichiometric, this could include additional target conditioning phases or leaking O_2 during RF sputtering. In the case of SiO_2 a small amount of O_2 could be added during deposition to remove Si^{1+} defects.
    - Tuning of the layer thickness and ratio to PDC alumina to make the most effective barriers whilst also considering deposition time and ultimate film properties.
    - Tuning of the interlayer to prevent the decrease in adhesion seen upon heat treatment. This could be achieved through using a graded interlayer motif as seen in some DLC films to mitigate abrupt changes in thermal expansion coefficient.

- Fine tuning of the wire coating rig to facilitate deposition of **high continuity** coatings on Cu wire, in much greater quantities than demonstrated in this work. This could include the use of bearings designed as to have as low effect on the wire and coating as possible as well as the use of more bearings to utilise the whole height of the target. The use of a spring loaded tension arm could be used to keep wire tense for longer thus the sputtering time wouldn't be so limited.

    - Further to this scale up procedures could be implemented to produce larger sections of coated wire. Such improvements could include utilising larger on and off reels and increasing the number of bearings utilised in front of the targets which would also decrease deposition time.
    - Studies on the effect of coating wires which have been annealed to remove work hardening.

- Development of testing to characterise the **aging characteristics** in an operating environment. Use of the wires in applications such as actuators and motors in high stress environments and monitoring of their electrical and mechanical performance over time, could be used as a metric to decide how well suited coatings are for their actual application.

- Deposition and process development of **multilayer composite coating systems** onto wire, for improved electrical properties. This will include using additional magnetrons with the current setup within the rig to deposit composite multilayer coatings with high isolative potential to be applied to wire. The deposition procedure will need to be carefully considered in order to produce continuous films.

13 References

[1] G.J. Reynolds, M. Kratzer, M. Dubs, H. Felzer, R. Mamazza, Electrical Properties of Thin-Film Capacitors Fabricated Using High Temperature Sputtered Modified Barium Titanate., Materials (Basel). 5 (2012) 644–660.

[2] W. Cai, X. Ma, J. Zhang, A. Song, Transparent Thin-Film Transistors Based on Sputtered Electric Double Layer., Materials (Basel). 10 (2017) 1–8.

[3] F. Larmat, J.R. Reynolds, Y.-J. Qiu, Polypyrrole as a solid electrolyte for tantalum capacitors, Synth. Met. 79 (1996) 229–233.

[4] High Temperature Insulation Materials Market Worth $5.1 Billion by 2019, Mark. Mark. (2014) 1.

[5] A. Pamu, L. Dokos, D. Kannan, Analysis of the North America Wire and Cable Materials Market- Executive Sumamry, 2012.

[6] O. Gutfleisch, M.A. Willard, E. Brück, C.H. Chen, S.G. Sankar, J.P. Liu, Magnetic Materials and Devices for the 21st Century: Stronger, Lighter, and More Energy Efficient, Adv. Mater. 23 (2011) 821–842.

[7] P. Stenzel, P. Dollinger, J. Richnow, J. Franke, Innovative needle winding method using curved wire guide in order to significantly increase the copper fill factor, in: 2014 17th Int. Conf. Electr. Mach. Syst., IEEE, 2014: pp. 3047–3053.

[8] L. Fang, I. Cotton, Z.J. Wang, R. Freer, Insulation performance evaluation of high temperature wire candidates for aerospace electrical machine winding application, in: 2013 IEEE Electr. Insul. Conf. EIC, 2013: pp. 253–256.

[9] R.J. Kerkman, D. Leggate, G.L. Skibinski, Interaction of drive modulation and cable parameters on AC motor transients, IEEE Trans. Ind. Appl. 33 (1997) 722–731.

[10] International Energy Agency, Global EV Outlook 2017 Together Secure Sustainable Global EV outlook 2017, 2017.

[11] Y.T. Chen, C.L. Chiu, Y.R. Jhang, Z.H. Tang, R.H. Liang, A driver for the single-phase brushless DC fan motor with hybrid winding structure, IEEE Trans. Ind. Electron. 60 (2013) 4369–4375.

[12] N. Hashemnia, B. Asaei, Comparative study of using different electric motors in the electric vehicles, in: 2008 18th Int. Conf. Electr. Mach., IEEE, 2008: pp. 1–5.

[13] M. Torrent, E. Martinez, P. Andrada, Assessing the environmental impact of induction motors using manufacturer’s data and life cycle analysis, IET Electr. Power Appl. 6 (2012) 473–483.

[14] R.A. Matula, Electrical resistivity of copper, gold, palladium, and silver, J. Phys. Chem. Ref. Data. 8 (1979) 1147–1298.

[15] H.C. de Groh III, Consideration of Conductive Motor Winding Materials at Room and Elevated Temperatures, Ohio, 2015.

[16] P.D. Desai, H.M. James, C.Y. Ho, Electrical Resistivity of Aluminium and Manganese, J. Phys. Chem. Ref. Data. 13 (1983) 1131–1172.

[17] A.A. Mills, The early history of insulated copper wire, Ann. Sci. 61 (2004) 453–467.

[18] K.N. Mathes, A Brief History of Development in Electrical Insulation, Electr. Electron. Insul. Conf. 1991. Boston’91 EEIC/ICWA Expo. Proc. 20th. (1991) 147–150.

[19] C. Zuidema, W. Kegerise, R. Fleming, M. Welker, S. Boggs, A short history of rubber cables, IEEE Electr. Insul. Mag. 27 (2011) 45–50.

[20] R. Liao, C. Lv, L. Yang, Y. Zhang, W. Wu, C. Tang, The Insulation Properties of Oil-Impregnated Insulation Paper Reinforced with Nano-TiO2, J. Nanomater. 2013 (2013) 1–7.

[21] W.T. Shugg, Handbook of Electrical and Electronic Insulating Materials, IEEE, 1995.

[22] B. Epstein, H. Brooks, The Theory of Extreme Values and Its Implications in the Study of the Dlelectnc Strength of Paper Capacitors, J. App. Phys. 19 (1948) 544–550.

[23] I.O. Wilson, Magnesium oxide as a high-temperature insulant, IEE Proc. 128 (1981) 159–164.

[24] B. Xu, H.Y. Sohn, Y. Mohassab, Y. Lan, Structures, preparation and applications of titanium suboxides, RSC Adv. 6 (2016) 79706–79722.

[25] Megger, “ A Stitch in Time ...” The Complete Guide to Electrical Insulation Testing, 2006.

[26] Standard Test Methods for Film-Insulated Magnet Wire, ASTM Int. (2017) 1–36.

[27] S. Ait-Amar, D. Roger, G. Vélu, M. Ben Fatallah, A. Habas, J.P. Habas, P. Notingher, P. Frezel, Dielectric parameters study of insulation wire free of volatile organic compound, Annu. Rep. - Conf. Electr. Insul. Dielectr. Phenomena, CEIDP. (2012) 866–869.

[28] T.J. Stueber, C. Mundson, Evaluation of Kapton Pyrolysis, Arc Tracking, and Flashover on

SiOx-Coated Polyimide Insulated Samples of Flat Flexible Current Carriers for SSF, 1993.
[29] Professional Plastics, Electrical Properties of Plastic, n.d.
[30] R.C. Dorf, The electrical engineering handbook, CRC Press, 1997.
[31] J. Beatty, An advanced arc track resistance airframe wire, St. Augustine, 1995.
[32] A complete range of wire & cable solutions for aerospace applications, (2013) 1–340.
[33] D.H. Han, H.G. Cho, S.W. Han, Effects of alumina trihydrate on the electrical insulation properties of HTV silicone rubber, in: Proc. 7th Int. Conf. Prop. Appl. Dielectr. Mater., IEEE, 2003: pp. 381–384.
[34] A. Choudhury, A.K. Bhowmick, C. Ong, M. Soddemann, Effect of Various Nanofillers on Thermal Stability and Degradation Kinetics of Polymer Nanocomposites, J. Nanosci. Nanotechnol. 10 (2010) 5056–5071.
[35] C. Chen, H. Wang, Y. Xue, Z. Xue, H. Liu, X. Xie, Y.-W. Mai, Structure, rheological, thermal conductive and electrical insulating properties of high-performance hybrid epoxy/nanosilica/AgNWs nanocomposites, Compos. Sci. Technol. 128 (2016) 207–214.
[36] Y. Xie, J. Wang, Y. Yu, W. Jiang, Z. Zhang, Enhancing breakdown strength and energy storage performance of PVDF-based nanocomposites by adding exfoliated boron nitride, Appl. Surf. Sci. 440 (2018) 1150–1158.
[37] L. Zhang, H. Deng, Q. Fu, Recent progress on thermal conductive and electrical insulating polymer composites, Compos. Commun. 8 (2018) 74–82.
[38] Y. Hu, G. Du, N. Chen, A novel approach for Al_2O_3/epoxy composites with high strength and thermal conductivity, Compos. Sci. Technol. 124 (2016) 36–43.
[39] Ceramawire, Ceramawire High Temperature Magnet Wire Technical Specifications, (n.d.) 1–3.
[40] CGP, VERY HIGH TEMPETATURE CERAFIL® Technical specifications, n.d.
[41] H. Metals, Selection and Use Directions for Magnet Wire Magnet Wire, (n.d.) 1–30.
[42] L.J. Payette, Solderable wire enamel, IEEE Electr. Insul. Mag. 6 (1990) 8–12.
[43] J. Powell, Arlyn, S., How copper cable is made - Cabling Install, Cabling Install. Maint. (1997).
[44] P. Yimsiri, M.R. Mackley, Spin and dip coating of light-emitting polymer solutions: Matching experiment with modelling, Chem. Eng. Sci. 61 (2006) 3496–3505.
[45] DuPont^{TM} Kapton® Polyimide film, Motor and Magnet Wire Technical Bulletin, 2016.
[46] K. Fukumoto, C. Kinoshita, S. Maeda, K. Nakai, The mechanism of radiation-resistance of $MgO \cdot nAl_2O_3$ through the formation process of defect clusters under irradiation, Nucl. Inst. Methods Phys. Res. B. 91 (1994) 252–257.
[47] E. Celik, I.H.H. Mutlu, H. Okuyucu, Y.S.S. Hascicek, Electrical characterization of ceramic insulation coatings for magnet technology, IEEE Trans. Appl. Supercond. 11 (2001) 2881–2884.
[48] O. Cakiroglu, High Voltage Breakdown Testing of Sol-Gel MgO-ZrO2 Iinsulation Coatings Under Various Compressions At 298 K and 77 K, Mold. J. Phys. Sci. 4 (2005) 49–53.
[49] M. Yao, W. Shan, Dielectric behavior of alumina thin film under high DC electric field prepared by sol–gel method, J. Adv. Dielectr. 3 (2013) 1–5.
[50] N. Braithwaite, G. Weaver, Electronic materials, Open University, 1990.
[51] Y. Liang, S. Sun, T. Deng, H. Ding, W. Chen, Y. Chen, The Preparation of TiO_2 Film by the Sol-Gel Method and Evaluation of Its Self-Cleaning Property., Materials (Basel). 11 (2018) 1–12.
[52] J.-Y. Zhang, B. Lim, I.W. Boyd, Thin tantalum pentoxide films deposited by photo-induced CVD, Thin Solid Films. 336 (1998) 340–343.
[53] A. Anders, Deposition rates of high power impulse magnetron sputtering: Physics and economics, Cit. J. Vac. Sci. Technol. A. 28 (2010) 783.
[54] U. Helmersson, M. Lattemann, J. Bohlmark, A.P. Ehiasarian, J.T. Gudmundsson, Ionized physical vapor deposition (IPVD): A review of technology and applications, Thin Solid Films. 513 (2006) 1–24.
[55] B.C. Mohanty, H.R. Choi, Y.M. Choi, Y.S. Cho, Thickness-dependent fracture behaviour of flexible ZnO : Al thin films, J. Phys. D. Appl. Phys. 44 (2011) 1–6.
[56] M. Thomas, John, The extraordinary impact of Michael Faraday on chemistry and related subjects, Chem. Commun. 53 (2017) 9179–9184.
[57] W. Crookes, On Radiant Matter, Pop. Sci. Mon. . 16 (1897).
[58] W. Crookes, Experiments on the Dark Space in Vacuum Tubes, Proc. Roy. Soc. 79 (1907) 98–117.
[59] J.E. Greene, Review Article: Tracing the recorded history of thin-film sputter deposition: From the 1800s to 2017, J. Vac. Sci. Technol. A Vacuum, Surfaces, Film. 35 (2017) 1–60.

[60] R. Baragiola, Sputtering: survey of observations and derived principles, Phil. Trans. R. Soc. Lond. A. 362 (2004) 29–53.

[61] K. Wasa, Sputtering Phenomena, in: Handb. Sputtering Technol., William Andrew Publishing, 2012: pp. 41–75.

[62] J.T. Gudmundsson, A. Hecimovic, Foundations of DC plasma sources, Plasma Sources Sci. Technol. 26 (2017) 1–20.

[63] D.M. Mattox, Physical Sputtering and Sputter Deposition (Sputtering), Handb. Phys. Vap. Depos. Process. (2010) 237–286.

[64] R. Behrisch, W. Eckstein, Introduction and Overview, in: Sputtering by Part. Bombard., 2006: pp. 1–19.

[65] A. Kavitha, R. Kannan, S. Rajashabala, Effect of target power on the physical properties of Ti thin films prepared by DC magnetron sputtering with supported discharge, Mater. Sci. 35 (2017) 173–180.

[66] S. Muhl, A. Pérez, The use of hollow cathodes in deposition processes: A critical review, Thin Solid Films. 579 (2015) 174–198.

[67] D.M. Mattox, Fundamentals of Ion Plating, J. Vac. Sci. Technol. 10 (1973) 47–52.

[68] D.M. Mattox, Ion plating — past, present and future, Surf. Coatings Technol. 133–134 (2000) 517–521.

[69] S. Swann, Magnetron sputtering, Phys. Technol. 19 (1988) 67–76.

[70] F. Cemin, G. Abadias, T. Minea, C. Furgeaud, F. Brisset, D. Solas, D. Lundin, Benefits of energetic ion bombardment for tailoring stress and microstructural evolution during growth of Cu thin films, Acta Mater. 141 (2017) 120–130.

[71] J. Kovac, H.-R. Stock, H.-W. Zoch, Influence of Substrate Bias Voltage on the Properties of Sputtered Aluminum-Scandium Thin Sheets, J. Surf. Eng. Mater. Adv. Technol. 2 (2012) 115–119.

[72] P.J. Kelly, R.D. Arnell, Control of the structure and properties of aluminum oxide coatings deposited by pulsed magnetron sputtering, J. Vac. Sci. Technol. A Vacuum, Surfaces, Film. 17 (1999) 945–953.

[73] M. Chandra Sekhar, P. Kondaiah, S.V. Jagadeesh Chandra, G. Mohan Rao, S. Uthanna, Effect of substrate bias voltage on the structure, electric and dielectric properties of TiO2 thin films by DC magnetron sputtering, Appl. Surf. Sci. 258 (2011) 1789–1796.

[74] J.M. Schneider, W.D. Sproul, A.A. Voevodin, A. Matthews, Crystalline alumina deposited at low temperatures by ionized magnetron sputtering, J. Vac. Sci. Technol. A. 15 (1997) 1084–1088.

[75] W.D. Sproul, D.J. Christie, D.C. Carter, Control of reactive sputtering processes, Thin Solid Films. 491 (2005) 1–17.

[76] P.J. Kelly, P.S. Henderson, R.D. Arnell, G.A. Roche, D. Carter, Reactive pulsed magnetron sputtering process for alumina films, J. Vac. Sci. Technol. A Vacuum, Surfaces, Film. 18 (2000) 2890–1448.

[77] D.M. Mattox, A Short History: Magnetron Sputter Deposition, 2015.

[78] I. Safi, Recent aspects concerning DC reactive magnetron sputtering of thin films: a review, Surf. Coatings Technol. 127 (2000) 203–219.

[79] S. Schiller, U. Heisig, K. Steinfelder, J. Strümpfel, R. Voigt, R. Fendler, G. Teschner, On the investigation of d.c. plasmatron discharges by optical emission spectrometry, Thin Solid Films. 96 (1982) 235–240.

[80] G.S. Chen, C.C. Lee, H. Niu, W. Huang, R. Jann, T. Schütte, Sputter deposition of titanium monoxide and dioxide thin films with controlled properties using optical emission spectroscopy, Thin Solid Films. 516 (2008) 8473–8478.

[81] R. Cremer, K. Reichert, D. Neuschütz, G. Erkens, T. Leyendecker, Sputter deposition of crystalline alumina coatings, Surf. Coatings Technol. 163–164 (2003) 157–163.

[82] W.D. Westwood, Sputter Deposition Processes, Third Edit, Elsevier Ltd., 1988.

[83] C.R. Lin, D.H. Wei, C.K. Chang, W.H. Liao, Optical Properties of Diamond-like Carbon Films for Antireflection Coating by RF Magnetron Sputtering Method, Phys. Procedia. 18 (2011) 46–50.

[84] J. Borges, N. Martin, N.P. Barradas, E. Alves, D. Eyidi, M.F. Beaufort, J.P. Riviere, F. Vaz, L. Marques, Electrical properties of AlNxOy thin films prepared by reactive magnetron sputtering, Thin Solid Films. 520 (2013) 6709–6717.

[85] M. Meissner, T. Tolg, P. Baroch, J. Musil, Elimination of Arcing in Reactive Sputtering of Al_2O_3 Thin Films Prepared by DC Pulse Single Magnetron, Plasma Process. Polym. 8 (2011) 500–504.

[86] J.A. Thornton, High rate thick film growth, 1977.

[87] D.C. Carter, R.L. Arent, D.J. Christie, Sputter Process enhancement through Pulsed-dc Power, Vacuum. 505 (2007) 210–215.

[88] D. Carter, H. Walde, G. Mcdonough, G. Roche, Parameter Optimization in Pulsed DC Reactive Sputter Deposition of Aluminum Oxide, Coaters. 505 (2002) 570–577.

[89] J. Sellers, Asymmetric bipolar pulsed DC: the enabling technology for reactive PVD, Surf. Coat. Technol. 98 (1998) 1245–1250.

[90] A. Belkind, A. Freilich, J. Lopez, Z. Zhao, W. Zhu, K. Becker, Characterization of pulsed dc magnetron sputtering plasmas, New J. Phys. 7 (2005) 1–16.

[91] D. Depla, S. Mahieu, J.E. Greene, Sputter Deposition Processes, William Andrew Publishing, 2010.

[92] A.P. Ehiasarian, R. New, W.-D. Münz, L. Hultman, U. Helmersson, V. Kouznetsov, Influence of high power densities on the composition of pulsed magnetron plasmas, Vacuum. 65 (2002) 147–154.

[93] J.T. Gudmundsson, The high power impulse magnetron sputtering discharge as an ionized physical vapor deposition tool, Vacuum. 84 (2010) 1360–1364.

[94] G. Eichenhofer, I. Fernandez, A. Wennberg, Industrial Use of HiPIMS up to Now and a Glance into the Future, A Review by a Manufacturer Introduction of the hiP-V hiPlus Technology, Univers. J. Phys. Appl. 11 (2017) 73–79.

[95] P.D. Davidse, L.I. Maissel, Dielectric Thin Films through rf Sputtering, J. Appl. Phys. 37 (1966) 574–579.

[96] C.S. Bhatia, Alumina films by sputter deposition with Ar/O2: Preparation and characterization, J. Vac. Sci. Technol. A Vacuum, Surfaces, Film. 7 (1989) 1298–1302.

[97] N. Reddy, P. Bera, V.R. Reddy, N. Sridhara, A. Dey, C. Anandan, A.K. Sharma, XPS study of sputtered alumina thin films, Ceram. Int. 40 (2014) 11099–11107.

[98] Q. Qiu, Q. Li, J. Su, Y. Jiao, J. Finley, Influence of operating parameters on target erosion of rectangular planar DC magnetron, IEEE Trans. Plasma Sci. 36 (2008) 1899–1906.

[99] J.S. Chapin, Sputtering process and apparatus, 1974.

[100] P.J. Kelly, R.D. Arnell, Magnetron sputtering : a review of recent developments and applications, Vacuum. 56 (1999) 159–172.

[101] R. Constantin, B. Miremad, Performance of hard coatings, made by balanced and unbalanced magnetron sputtering, for decorative applications, Surf. Coatings Technol. 120–121 (1999) 728–733.

[102] P.J. Clarke, Flat magnetron, 2004.

[103] K. Ganesan, S. Ilango, M. Shanmugam, M. Farrokh Baroughi, M. Kamruddin, A.K. Tyagi, Pre- and post-breakdown electrical studies in ultrathin Al_2O_3 films by conductive atomic force microscopy, Curr. Appl. Phys. 13 (2013) 1865–1869.

[104] F.-C. Chiu, A Review on Conduction Mechanisms in Dielectric Films, Adv. Mater. Sci. Eng. 2014 (2014) 1–18.

[105] Y. Sun, S.A. Boggs, R. Ramprasad, The intrinsic electrical breakdown strength of insulators from first principles, Appl. Phys. Lett. 101 (2012) 1–5.

[106] G. Dearnaley, A.M. Stoneham, D V Morgans, Electrical phenomena in amorphous oxide films, Reports Prog. Phys. Rep. Prog. Phys. 33 (1970) 1129–1191.

[107] J.J. O’Dwyer, The theory of avalanche breakdown in solid dielectrics, J. Phys. Chem. Solids. 28 (1967) 1137–1144.

[108] D.R. Wolters, J.J. Van Der Schoot, Dielectric breakdown in MOS devices part 1: Defect-related and intrinsic breakdown, Philips J. Res. 40 (1985) 115–136.

[109] S. Kremmer, C. Teichert, E. Pischler, H. Gold, F. Kuchar, M. Schatzmayr, Characterization of silicon gate oxides by conducting atomic force microscopy, Surf. Interface Anal. 33 (2002) 168–172.

[110] C.L. Wadhwa, High Voltage Engineering, 2nd ed., New Age International, 2007.

[111] N. Klein, Electrical Breakdown in Thin Dielectric Films, J. Electrochem. Soc. 116 (1969) 963–972.

[112] S. Hirano, A. Kishimoto, Thermal-Electrical Breakdown of Disordered Conductor Insulator composites, Jpn. J. Appl. Phys. 38 (1999) L662–L663.

[113] G. Sawa, Dielectric Breakdown in Solid Dielectrics, IEEE Trans. Electr. Insul. EI-21 (1986) 841–846.

[114] S. Tajima, Luminescence, breakdown and colouring of anodic oxide films on aluminium, Electrochim. Acta. 22 (1977) 995–1011.

[115] L. Li, Dielectric properties of aged polymers and nanocomposites, 2011.

[116] J. Martínez-Perdiguero, L. Mendizabal, M.C. Morant-Miñana, I. Castro-Hurtado, A. Juarros, R. Ortiz, A. Rodriguez, Electrical insulation and breakdown properties of SiO_2 and Al_2O_3 thin multilayer films deposited on stainless steel by physical vapor deposition, Thin Solid Films. 595 (2015) 171–175.

[117] Q. Yang, Y. Jin, W. Sima, M. Liu, Effect of the electrode material on the breakdown voltage and space charge distribution of propylene carbonate under impulse voltage, AIP Adv. 6 (2016) 1–8.

[118] B. Chen, M. Kollosche, M. Stewart, J. Busfield, F. Carpi, Electrical breakdown of an acrylic dielectric elastomer: effects of hemispherical probing electrode's size and force, Int. J. Smart Nano Mater. 6 (2015) 290–303.

[119] M.D. Groner, J.W. Elam, F.H. Fabreguette, S.M. George, Electrical characterization of thin Al_2O_3 films grown by atomic layer deposition on silicon and various metal substrates, Thin Solid Films. 413 (2002) 186–197.

[120] K. Ganesan, S. Ilango, S. Mariyappan, M. Farrokh Baroughi, M. Kamruddin, A.K. Tyagi, Conductive atomic force microscopy studies on dielectric breakdown behavior of ultrathin Al_2O_3 films, Appl. Phys. Lett. 98 (2011) 1–3.

[121] H. Bartzsch, D. Glöß, B. Böcher, P. Frach, K. Goedicke, Properties of SiO_2 and Al_2O_3 films for electrical insulation applications deposited by reactive pulse magnetron sputtering, Surf. Coatings Technol. 174 (2003) 774–778.

[122] Q. Feng, M. Yao, Z. Su, X. Yao, Significantly enhanced energy density of amorphous alumina thin films via silicon and magnesium co-doping, Ceram. Int. 44 (2018) 11160–11165.

[123] J.G. Simmons, Conduction in thin dielectric films, J. Phys. D. Appl. Phys. 4 (1971) 613–657.

[124] E. Lim, R. Ismail, Conduction Mechanism of Valence Change Resistive Switching Memory: A Survey, Electronics. 4 (2015) 586–613.

[125] E. Atanassova, N. Novkovski, A. Paskaleva, M. Pecovska-Gjorgjevich, Oxygen annealing modification of conduction mechanism in thin rf sputtered Ta2O5 on Si, Solid State Ionics. 46 (2002) 1887–1898.

[126] M. Lenzlinger, E.H. Snow, Fowler-Nordheim Tunneling into Thermally Grown SiO_2, J. Appl. Phys. 40 (1969) 278–283.

[127] X.W. Zhang, Y.J. Zou, H. Yan, B. Wang, G.H. Chen, S.P. Wong, Electrical properties and annealing effects on the stress of RF-sputtered c-BN films, Mater. Lett. 45 (2000) 111–115.

[128] R.L. Angle, H.E. Talley, Electrical and Charge Storage Characteristics of the Tantalum Oxide-Silicon Dioxide Device, IEEE Trans. Electron Devices. 25 (1978) 1277–1283.

[129] G.S. Oehrlein, A. Reisman, Electrical properties of amorphous tantalum pentoxide thin films on silicon, J. Appl. Phys. 54 (1983) 6502–2538.

[130] T.G.A. Malik, R.M. Abdel-Latif, Ohmic and space-charge limited conduction in cobalt phthalocyanine thin films, Thin Solid Films. 305 (1997) 336–340.

[131] W. Zhu, T.P. Chen, Y. Liu, S. Fung, Conduction mechanisms at low-and high-resistance states in aluminum/anodic aluminum oxide/aluminum thin film structure, J. Appl. Phys. 112 (2012) 1–5.

[132] Y.F. Chang, B. Fowler, Y.C. Chen, Y.T. Chen, Y. Wang, F. Xue, F. Zhou, J.C. Lee, Intrinsic SiOx-based unipolar resistive switching memory. II. Thermal effects on charge transport and characterization of multilevel programing, J. Appl. Phys. 116 (2014) 1–12.

[133] C. Chaneliere, J.L. Autran, R.A.B. Devine, B. Balland, Tantalum pentoxide (Ta2O5) thin films for advanced dielectric applications, Mater. Sci. Eng. R22 (1998) 269–322.

[134] S. Suyama, A. Okamoto, T. Serikawa, H. Tanigawa, Electrical Conduction and dielectric breakdown in sputter-deposited silicon dioxide films on silicon, Silicon Nitride Film. J. Appl. Phys. 62 (1987) 2360–2363.

[135] S. Ezhilvalavan, T.Y. Tseng, Preparation and properties of tantalum pentoxide (Ta2O5) thin films for ultra large scale integrated circuits (ULSIs) application ± A review, J. Mater. Sci. Mater. Electron. 10 (1999) 9–31.

[136] F.-C. Chiu, J.-J. Wang, J. Ya-min Lee, S. Chuan Wu, Leakage currents in amorphous Ta2O5 thin films, J. Appl. Phys. 81 (1997).

[137] D.M. Mattox, A Short History: Adhesion, Interface Formation, and Stress in PVD Coatings, 2016.

[138] V.A.C. Haanappel, H.D. van Corbach, T. Fransen, P.J. Gellings, Properties of alumina films prepared by low-pressure metal-organic chemical vapour deposition, Surf. Coatings Technol. 72 (1995) 13–22.

[139] M. Pletea, W. Brückner, H. Wendrock, R. Kaltofen, Stress evolution during and after sputter deposition of Cu thin films onto Si (100) substrates under various sputtering pressures, J. Appl.

Phys. 97 (2005) 1–7.

[140] A. Al-Masha'al, A. Bunting, R. Cheung, Evaluation of residual stress in sputtered tantalum thin-film, Appl. Surf. Sci. 371 (2016) 571–575.

[141] V. Bhatt, S. Chandra, S. Kumar, S. Rauthan, P.N. Dixit, Stress evaluation of RF sputtered silicon dioxide films for MEMS, Indian J. Pure Appl. Phys. 45 (2007) 377–381.

[142] S. Shinzato, T. Sumomogi, S. Kofune, K. Kuwahara, Internal stress in sputter-deposited Al_2O_3 films, Thin Solid Films. 97 (1982) 333–337.

[143] F. Ramos, M.T. Vieira, Adhesion improvement of RF-sputtered alumina coatings as determined by the scratch test, J. Adhes. Sci. Technol. 7 (1993) 801–811.

[144] S.J. Bull, Failure modes in scratch adhesion testing, Surf. Coatings Technol. 50 (1991) 25–32.

[145] A. Aryasomayajula, N.X. Randall, M.H. Gordon, D. Bhat, Tribological and mechanical properties of physical vapor deposited alpha alumina thin film coating, Thin Solid Films. 517 (2008) 819–823.

[146] J.-H. Huang, C.-H. Ma, H. Chen, Effect of Ti interlayer on the residual stress and texture development of TiN thin films deposited by unbalanced magnetron sputtering, Surf. Coatings Technol. 201 (2006) 3199–3204.

[147] K.-D. Bouzakis, S. Hadjiyiannis, G. Skordaris, I. Mirisidis, N. Michailidis, K. Efstathiou, E. Pavlidou, G. Erkens, R. Cremer, S. Rambadt, I. Wirth, The effect of coating thickness, mechanical strength and hardness properties on the milling performance of PVD coated cemented carbides inserts, Surf. Coatings Technol. 177–178 (2004) 657–664.

[148] B. Peng, D. Gong, W. Zhang, J. Jiang, L. Shu, Y. Zhang, Effects of sputtering parameters on AlN film growth on flexible hastelloy tapes by two-step deposition technique, Materials (Basel). 9 (2016) 1–9.

[149] D. Miao, H. Hu, A. Li, S. Jiang, S. Shang, Fabrication of porous and amorphous TiO2 thin films on flexible textile substrates, Ceram. Int. 41 (2015) 9177–9182.

[150] S.H. Jen, J.A. Bertrand, S.M. George, Critical tensile and compressive strains for cracking of Al_2O_3 films grown by atomic layer deposition, J. Appl. Phys. 109 (2011) 1–11.

[151] J. Musil, J. Sklenka, R. Čerstvý, Protection of brittle film against cracking, Appl. Surf. Sci. 370 (2016) 306–311.

[152] A. Moridi, H. Ruan, L.C. Zhang, M. Liu, Residual stresses in thin film systems: Effects of lattice mismatch, thermal mismatch and interface dislocations, Int. J. Solids Struct. 50 (2013) 3562–3569.

[153] H. Holleck, V. Schier, Multilayer PVD coatings for wear protection, Surf. Coatings Technol. 76–77 (1995) 328–336.

[154] M. Hu, X. Gao, L. Weng, J. Sun, W. Liu, The microstructure and improved mechanical properties of Ag/Cu nanoscaled multilayer films deposited by magnetron sputtering, Appl. Surf. Sci. 313 (2014) 563–568.

[155] O.S. Heavens, Some factors influencing the adhesion of films produced by vacuum evaporation, J. Phys. Radium. 11 (1950) 355–360.

[156] P. Benjamin, C. Weaver, Measurement of Adhesion of Thin Films, Proc. R. Soc. A Math. Phys. Eng. Sci. 254 (1960) 163–176.

[157] S.J. Bull, Failure mode maps in the thin film scratch adhesion test, Tribol. Int. 30 (1997) 491–498.

[158] J.H. Scofield, A. Duda, D. Albin, B.L. Ballardb, P.K. Predeckib, Sputtered molybdenum bilayer back contact for copper indium diselenide-based polycrystalline thin-film solar cells, Thin Solid Films. 260 (1995) 26–31.

[159] C. Haanappel, D. Vendel, H.S. C Metselaar, H.D. van Corbach, T. Fransen, P.J. Gellings, The mechanical properties of thin alumina films deposited by metal-organic chemical vapour deposition, Thin Solid Films. 254 (1995) 53–63.

[160] R.A. Erck, Pin-pull adhesion measurements of copper films on ion-bombarded alumina, Thin Solid Films. 253 (1994) 362–366.

[161] K.L. Mittal, Adhesion Measurement of Thin Films, Electrocompon. Sci. Technol. 3 (1976) 21–42.

[162] S. Suzuki, Y. Hayashi, K. Suzuki, E. Ando, Measurement of the adhesion strength of metal oxide and metal nitride thin films sputtered onto glass by the direct pull-off method, J. Adhes. Sci. Technol. 11 (2012) 1137–1147.

[163] H. Huang, F. Spaepen, Tensile testing of free-standing Cu, Ag and Al thin films and Ag/Cu multilayers, Acta Mater. 48 (2000) 3261–3269.

[164] Y.-W. Cheng, D.T. Read, J.D. Mccolskey, J.E. Wright, A tensile-testing technique for micrometer-sized free-standing thin films, Thin Solid Films. 484 (2005) 426–432.

[165] P. Nguyen, J.-M. Desmarres, C. Seguineau, J. Alexis, T. Masri, A comparative study of microscratch and microtensile adhesion tests for nickel coatings on various substrates, in: 2014 Symp. Des. Test, Integr. Packag. MEMS/MOEMS, IEEE, 2014: pp. 1–5.

[166] C. Xie, W. Tong, Cracking and decohesion of a thin Al_2O_3 film on a ductile Al-5%Mg substrate, Acta Mater. 53 (2005) 477–485.

[167] T. Jörg, D. Music, F. Hauser, M.J. Cordill, R. Franz, H. Köstenbauer, J. Winkler, J.M. Schneider, C. Mitterer, Deformation behavior of Re alloyed Mo thin films on flexible substrates: In situ fragmentation analysis supported by first-principles calculations, Sci. Rep. 7 (2017) 1–10.

[168] Z. Suo, E.Y. Ma, H. Gleskova, S. Wagner, Bending experiment on pentacene field-effect transistors on plastic films, Cit. Appl. Phys. Lett. 74 (1999) 1177–1179.

[169] A.R. Lansdown, Sputtering and other physical processes, in: Molybdenum Disulphide Lubr., 1967: pp. 153–178.

[170] D.M. Mattox, Surface effects on the growth, adhesion and properties of reactively deposited hard coatings, Surf. Coatings Technol. 81 (1996) 8–16.

[171] J.D. Lim, P.M. Lee, D.M.W. Rhee, K.C. Leong, Z. Chen, Effect of surface treatment on adhesion strength between magnetron sputtered copper thin films and alumina substrate, Appl. Surf. Sci. 355 (2015) 509–515.

[172] Z.T. Yao, M.S. Xia, P.K. Sarker, T. Chen, A review of the alumina recovery from coal fly ash, with a focus in China, Fuel. 120 (2014) 74–85.

[173] R.N. Lumley, Fundamentals of aluminium metallurgy : production, processing and applications, Woodhead Pub, 2011.

[174] B. Block, Y. Kim, D.K. Shetty, Dielectric Breakdown of Polycrystalline Alumina: A Weakest-Link Failure Analysis, J. Am. Ceram. Soc. 96 (2013) 3430–3439.

[175] F. Talbi, F. Lalam, D. Malec, Dielectric breakdown characteristics of alumina, in: Proc. 2010 Int. Conf. Solid Dielectr., 2010: pp. 1–4.

[176] R.G. Frieser, Phase Changes in Thin Reactively Sputtered Alumina Films, J. Electrochem. Soc. 113 (1966) 357–360.

[177] I.N. Reddy, V.R. Reddy, N. Sridhara, V.S. Rao, M. Bhattacharya, P. Bandyopadhyay, S. Basavaraja, A.K. Mukhopadhyay, A.K. Sharma, A. Dey, Pulsed rf magnetron sputtered alumina thin films, Ceram. Int. 40 (2014) 9571–9582.

[178] R.A. Gardner, Stability of rf-sputtered aluminum oxide, J. Vac. Sci. Technol. 14 (1977) 1139–1145.

[179] F.O. Ogundare, I.O. Olarinoye, He+ induced changes in the surface structure and optical properties of RF-sputtered amorphous alumina thin films, J. Non. Cryst. Solids. 432 (2016) 292–299.

[180] A.C.M. Esther, N. Sridhara, S. V. Sebastian, P. Bera, C. Anandan, S.T. Aruna, D. Rangappa, A.K. Sharma, A. Dey, Optical and RF transparent protective alumina thin films, J. Mater. Sci. Mater. Electron. 26 (2015) 9707–9716.

[181] R. Järvinen, T. Mäntylä, P. Kettunen, Improved adhesion between a sputtered alumina coating and a copper substrate, Thin Solid Films. 114 (1984) 311–317.

[182] P. Vuoristo, T. Mäntylä, P. Kettunen, Properties of magnetron-sputtered electrically insulating Al_2O_3 coatings on copper, J. Mater. Sci. 27 (1992) 4985–4996.

[183] B.G. Segda, M. Jacquet, J.P. Besse, Elaboration, characterization and dielectric properties study of amorphous alumina thin films deposited by r.f. magnetron sputtering, Vacuum. 62 (2001) 27–38.

[184] M.K. Olsson, K. Macák, U. Helmersson, B. Hjörvarsson, High rate reactive dc magnetron sputter deposition of films, Cit. J. Vac. Sci. Technol. A. 16 (1998) 639.

[185] J. Kohout, E. Bousser, T. Schmitt, R. Vernhes, O. Zabeida, J. Klemberg-Sapieha, L. Martinu, O.Z. Ji rí Kohout, Etienne Bousser, Thomas Schmitt, Richard Vernhes, L.M. Jolanta Klemberg-Sapieha, Stable reactive deposition of amorphous Al_2O_3 films with low residual stress and enhanced toughness using pulsed dc magnetron sputtering with very low duty cycle, Vacuum. 124 (2016) 96–100.

[186] F.C. Carreri, R. Bandorf, H. Gerdes, M. Vergöhl, G. Bräuer, Highly insulating alumina films by a bipolar reactive MF sputtering process with special arc handling, Surf. Coatings Technol. 290 (2016) 82–86.

[187] J. Liebault, J. Vallayer, D. Goeuriot, D. Treheux, F. Thevenot, How the trapping of charges can explain the dielectric breakdown performance of alumina ceramics, J. Eur. Ceram. Soc. 21 (2001) 389–397.

[188] J. Kolodzey, E.A. Chowdhury, T.N. Adam, G. Qui, I. Rau, J.O. Olowolafe, J.S. Suehle, Y.

Chen, Electrical conduction and dielectric breakdown in aluminum oxide insulators on silicon, IEEE Trans. Electron Devices. 47 (2000) 121–128.

[189] M. Voigt, M. Sokolowski, Electrical properties of thin rf sputtered aluminum oxide films, Mater. Sci. Eng. B. 109 (2004) 99–103.

[190] P. Ball, Silicon seduced from silica, Nat. News. (2003).

[191] W.-F. Wu, B.-S. Chiou, Properties of radio frequency magnetron sputtered silicon dioxide films, Appl. Surf. Sci. 99 (1996) 237–243.

[192] W. Guogang, C. Qiang, Preparation Methods and Application of Silicon Oxide Films, in: Int. Conf. Mechatronics, Electron. Ind. Control Eng., 2014: pp. 479–483.

[193] S.-H. Jeong, J.-K. Kim, B.-S. Kim, S.-H. Shim, B.-T. Lee, Characterization of SiO2 and TiO2 films prepared using rf magnetron sputtering and their application to anti-reflection coating, Vacuum. 76 (2004) 507–515.

[194] L.-N. He, J. Xu, Properties of amorphous SiO2 films prepared by reactive RF magnetron sputtering method, Vacuum. 68 (2002) 197–202.

[195] S.-I. Jun, T.E. McKnight, A.V. Melechko, M.L. Simpson, P.D. Rack, Characterisation of reactively sputtered silicon oxide for thin-film transistor fabrication, Electron. Lett. 41 (2005) 1–2.

[196] H. Ohsaki, Y. Tachibana, J. Shimizu, T. Oyama, High-rate deposition of SiO2 by modulated DC reactive sputtering in the transition mode without a feedback system, Thin Solid Films. 281–282 (1996) 213–217.

[197] R.R. Willey, Stability in the Deposition of Silicon Dioxide, 2015.

[198] S. Habermehl, R.T. Apodaca, Dielectric breakdown and Poole–Frenkel field saturation in silicon oxynitride thin films, Appl. Phys. Lett. 86 (2005) 1–3.

[199] A. García-Alonso, J. Artázcoz, E. Castaño, I. Obieta, F.J. Gracia, Mechanical and electrical properties Of SiO2thin films r.f. sputtered on non-silicon substrates for mechanical sensors, Sensors Actuators A. Phys. 37–38 (1993) 57–60.

[200] Z.A. Weinberg, Poole-Frenkel-effect as dominating current mechanism in thin oxide films-An illusion?, J. Vac. Sci. Technol. B Microelectron. Nanom. Struct. Process. 53 (1982) 5052–5056.

[201] D.J. Dumin, J.R. Cooper, J.R. Maddux, R.S. Scott, D.-P. Wong, Low-level leakage currents in thin silicon oxide films, Cit. J. Appl. Phys. 76 (1994) 319–327.

[202] T. Babeva, E. Atanassova, J. Koprinarova, Optical characteristics of thin rf sputtered Ta2O5 layers, Phys. Status Solidi. 202 (2005) 330–336.

[203] K.J. Kumar, N.R.C. Raju, A. Subrahmanyam, Properties of pulsed reactive DC magnetron sputtered tantalum oxide (Ta2O5) thin films for photocatalysis, Surf. Coatings Technol. 205 (2011) S261–S264.

[204] G.S. Oehrlein, A. Reisman, Electrical properties of amorphous tantalum pentoxide thin films on silicon, J. Appl. Phys. 54 (1983) 6502–6508.

[205] C. Mannequin, T. Tsuruoka, T. Hasegawa, M. Aono, Identification and roles of nonstoichiometric oxygen in amorphous Ta2O5 thin films deposited by electron beam and sputtering processes, Appl. Surf. Sci. 385 (2016) 426–435.

[206] S. Seki, T. Unagami, O. Kogure, B. Tsujiyama, Formation of high-quality, magnetron-sputtered Ta 2 O 5 films by controlling the transition region at the Ta 2 O 5 /Si interface, Cit. J. Vac. Sci. Technol. A. 5 (1987) 1771–1774.

[207] C. Corbella, M. Vives, A. Pinyol, I. Porqueras, C. Person, E. Bertran, Influence of the porosity of RF sputtered Ta 2 O 5 thin films on their optical properties for electrochromic applications, Solid State Ionics. 165 (2003) 15–22.

[208] K. Chen, M. Nielsen, G.R. Yang, E.J. Rymaszewski, T. Lu, Study of Amorphous Ta2O5 Thin Films by DC Magnetron Reactive Sputtering, J. Electron. Mater. 26 (1997) 397–401.

[209] G. Sethi, M. Olszta, J. Sloppy, M.W. Horn, E.C. Dickey, M.T. Lanagan, Structure and dielectric properties of amorphous tantalum pentoxide thin film capacitors, in: 2007 Annu. Rep. - Conf. Electr. Insul. Dielectr. Phenom., 2007: pp. 815–818.

[210] S.W. Smith, K.G. McAuliffe, J.F. Conley, Atomic layer deposited high-k nanolaminate capacitors, Solid. State. Electron. 54 (2010) 1076–1082.

[211] Y.K. Ezhovskii, a I. Klusevich, Fabrication and Dielectric Properties, 39 (2003) 1062–1066.

[212] C.-C. Lee, C.-J. Tang, TiO2-Ta2O5 composite thin films deposited by radio frequency ion-beam sputtering, Appl. Opt. 45 (2006) 9125–9131.

[213] K. Bewilogua, D. Hofmann, History of diamond-like carbon films — From first experiments to worldwide applications, Surf. Coatings Technol. 242 (2014) 214–225.

[214] T. Ishikawa, J. Choi, The effect of microstructure on the tribological properties of a-C:H films, Diam. Relat. Mater. 89 (2018) 94–100.

[215] J. Vetter, 60 years of DLC coatings: Historical highlights and technical review of cathodic arc processes to synthesize various DLC types, and their evolution for industrial applications, Surf. Coatings Technol. 257 (2014) 213–240.

[216] N.A. Sánchez, C. Rincón, G. Zambrano, H. Galindo, P. Prieto, Characterization of diamond-like carbon (DLC) thin films prepared by r.f. magnetron sputtering, Thin Solid Films. 373 (2000) 247–250.

[217] H. Decho, H.-R. Stock, C. Winkelmann, W. Lang, Development of hydrogenated amorphous carbon thin film with high electrical resistance for use in embedded sensors in abrasive environment, J. Intell. Mater. Syst. Struct. 24 (2012) 2197–2203.

[218] S. Chowdhury, M.T. Laugier, I.Z. Rahman, Characterization of DLC coatings deposited by rf magnetron sputtering, J. Mater. Process. Technol. 153–154 (2004) 804–810.

[219] R.D. Mansano, M. Massi, L.S. Zambom, P. Verdonck, P.M. Nogueira, H.S. MacIel, C. Otani, Effects of the methane content on the characteristics of diamond-like carbon films produced by sputtering, Thin Solid Films. 373 (2000) 243–246.

[220] M.I. Jones, I.R. McColl, D.M. Grant, K.G. Parker, T.L. Parker, Haemocompatibility of DLC and TiC–TiN interlayers on titanium, Diam. Relat. Mater. 8 (1999) 457–462.

[221] H.J. Pei, S.Y. Kuan, M.C. Liu, J.C. Huang, Tensile behavior of amorphous/nanocrystalline ZrCu/Cu multilayered films with graded interfaces, Intermetallics. 31 (2012) 191–195.

[222] T.E. O'Connor, Synthesis of Boron Nitride, J. Am. Chem. Soc. 84 (1962) 1753–1754.

[223] R.T. Paine, C.K. Narulat, Synthetic Routes to Boron Nitride, Chem. Rev. 90 (1990) 73–91.

[224] Y. Hattori, T. Taniguchi, K. Watanabe, K. Nagashio, Layer-by-Layer Dielectric Breakdown of Hexagonal Boron Nitride, ACS Nano. 9 (2015) 916–921.

[225] D.J. Kester, K.S. Ailey, D.J. Lichtenwalner, R.F. Davis, K.S. Ailey, Growth and characterization of cubic boron nitride thin films Raman spectroscopy investigation of size effects in cubic boron nitride Growth and characterization of cubic boron njtride thin films, J. Vac. Sci. Technol. A Vacuum, Surfaces, Film. 12 (1994) 3074–3081.

[226] A. Schütze, K. Bewilogua, H. Lüthje, S. Kouptsidis, S. Jäger, Cubic boron nitride films prepared by reactive r.f. and d.c. sputtering from different boron containing targets, Surf. Coatings Technol. 74–75 (1995) 717–722.

[227] N. Puychevrier, M. Menoret, Synthesis of III–V semiconductor nitrides by reactive cathodic sputtering, Thin Solid Films. 36 (1976) 141–145.

[228] M.D. Wiggins, C.R. Aita, F.S. Hickernell, Radio frequency sputter deposited boron nitride films, J. Vac. Sci. Technol. A Vacuum, Surfaces, Film. 21 (1984) 2646–2843.

[229] H. Saitoh, H. Morino, Y. Ichinose, Deposition Rate of Boron Nitride Films Using Plasma Jet Technique, Jpn. J. Appl. Phys. 32 (1993) L1684–L1687.

[230] D. Jin-Xiang, Z. Xiao-Kang, Y. Qian, W. Xu-Yang, C. Guang-Hua, H. De-Yan, Optical properties of hexagonal boron nitride thin films deposited by radio frequency bias magnetron sputtering, Chinese Phys. B. 18 (2009) 4013–4018.

[231] K.H. Seidel, K. Reichelt, W. Schaal, H. Dimigen, The preparation of cubic boron nitride films by reactive diode sputtering, Thin Solid Films. 151 (1987) 243–249.

[232] X.. Z. Ding, X.. T. Zeng, H. Xie, Cubic boron nitride films deposited by unbalanced RF magnetron sputtering and pulsed DC substrate bias, Thin Solid Films. 429 (2003) 22–27.

[233] D.A. Evans, A.G. McGlynn, B.M. Towlson, M. Gunn, D. Jones, T.E. Jenkins, R. Winter, N.R.J. Poolton, Determination of the optical band-gap energy of cubic and hexagonal boron nitride using luminescence excitation spectroscopy, J. Phys. Condens. Matter. 20 (2008) 1–7.

[234] M. Keunecke, E. Wiemann, K. Weigel, S.T. Park, K. Bewilogua, Thick c-BN coatings – Preparation, properties and application tests, Thin Solid Films. 515 (2006) 967–972.

[235] T.B. Wang, C.C. Jin, J. Yang, C.F. Hu, T. Qiu, Physical and mechanical properties of hexagonal boron nitride ceramic fabricated by pressureless sintering without additive, Adv. Appl. Ceram. 114 (2015) 273–276.

[236] H. Jensen, U.M. Jensen, G. Sorensen, Deposition of boron-nitride films by nitrogen sputtering from a boron-metal target, Cit. Appl. Phys. Lett. 66 (1995) 1489–1491.

[237] T.-S. Yang, T.-H. Tsai, C.-H. Lee, C.-L. Cheng, M.-S. Wong, Deposition of carbon-containing cubic boron nitride films by pulsed-DC magnetron sputtering, Thin Solid Films. 398 (2001) 285–290.

[238] A. Prakash, K.B. Sundaram, Studies on Electrical Properties of RF Sputtered Deposited Boron Carbon Nitride Thin Films, ECS J. Solid State Sci. Technol. 4 (2015) 25–29.

[239] W. Zhou, J. Zuo, X. Zhang, A. Zhou, Thermal, electrical, and mechanical properties of hexagonal boron nitride–reinforced epoxy composites, J. Compos. Mater. 48 (2013) 2517–2526.

[240] H. Fang, S.-L. Bai, C.P. Wong, “White graphene” – hexagonal boron nitride based polymeric composites and their application in thermal management, Compos. Commun. 2 (2016) 19–24.

[241] L. Yu, H. Zhao, J. Xu, Mechanical, tribological and corrosion performance of WBN composite films deposited by reactive magnetron sputtering, Appl. Surf. Sci. 315 (2014) 380–386.

[242] D.R.M. Crooks, G. Cagnoli, M.M. Fejer, G. Harry, J. Hough, B.T. Khuri-Yakub, S. Penn, R. Route, S. Rowan, P.H. Sneddon, I.O. Wygant, G.G. Yaralioglu, Experimental measurements of mechanical dissipation associated with dielectric coatings formed using SiO2, Ta2O5 and Al_2O_3, Class. Quantum Grav. 23 (2006) 4953–4965.

[243] P. Hidnert, H.S. Krider, Thermal Expansion of Aluminum and Some Aluminum Alloys, J. Res. Natl. Bur. Stand. (1934). 48 (1952) 209–220.

[244] W. Paszkowicz, J.B. Pelka, M. Knapp, T. Szyszko, S. Podsiadlo, Lattice parameters and anisotropic thermal expansion of hexagonal boron nitride in the 10-297.5 K temperature range, Appl. Phys. A Mater. Sci. Process. 75 (2002) 431–435.

[245] R. Jones, An Incomplete History and Timeline of the Electric Telegraph and the CD 731 Compromise Insulator, 2010.

[246] Fiberglass Braiding Process, Vetrotex. (n.d.) 1.

[247] B. Stuart, M. Gimeno-Fabra, J. Segal, I. Ahmed, D.M. Grant, Preferential sputtering in phosphate glass systems for the processing of bioactive coatings, Thin Solid Films. 589 (2015) 534–542.

[248] B. Probyn, Sputtering of insulators in an RF discharge, Vacuum. 18 (1968) 253–257.

[249] K.-I. Onisawa, M. Fuyama, K. Tamura, K. Taguchi, T. Nakayama, Y.A. Ono, Dielectric properties of rf-sputtered Y2O3 thin films, J. Appl. Phys. 68 (1990) 719–723.

[250] G.A.A. Battiston, R. Gerbasi, M. Porchia, R. Bertoncello, F. Caccavale, Chemical vapour deposition and characterization of gallium oxide thin films, Thin Solid Films. 279 (1996) 115–118.

[251] D. Stender, R. Frison, K. Conder, J.L.M. Rupp, B. Scherrer, J.M. Martynczuk, L.J. Gauckler, C.W. Schneider, T. Lippert, A. Wokaun, Crystallization of zirconia based thin films, Phys. Chem. Chem. Phys. 17 (2015) 18613–18620.

[252] P.H. Giauque, H.B. Cherry, M.-A. Nicolet, Thermal stability of amorphous thin films: Ti3Si1O8 vs. TiO2 and mictamict compounds, Thin Solid Films. 394 (2001) 136141.

[253] G. Beyer, Flame Retardant Properties of EVA-nanocomposites and Improvements by Combination of Nanofillers with Aluminium Trihydrate, Fire Mater. 25 (2001) 193–197.

[254] J. Balaji, M.G. Sethuraman, Improved corrosion resistance by forming multilayers over a copper surface by electrodeposition followed by a novel sol–gel coating method, RSC Adv. 6 (2016) 95396–95404.

[255] L. Ma, Q. Lei, Enhanced thermal and electrical insulation properties of polyimide films determined via a two-dimensional layered double hydroxide-potassium perfluorooctane sulfonate material, J. Appl. Polym. Sci. 135 (2018) 1–8.

[256] M. Mackey, A. Hiltner, E. Baer, L. Flandin, M.A. Wolak, J.S. Shirk, Enhanced breakdown strength of multilayered films fabricated by forced assembly microlayer coextrusion, J. Phys. D. Appl. Phys. 42 (2009) 1–12.

[257] E. Kar, N. Bose, S. Das, N. Mukherjee, S. Mukherjee, Enhancement of electroactive β phase crystallization and dielectric constant of PVDF by incorporating GeO2 and SiO2 nanoparticles, Phys. Chem. Chem. Phys. 17 (2015) 22784–22798.

[258] F. Bian, S. Yan, C. Xu, Z. Liu, X. Chen, C. Mao, F. Cao, J. Bian, G. Wang, X. Dong, Enhanced breakdown strength and energy density of antiferroelectric Pb,La(Zr,Sn,Ti)O3 ceramic by forming core-shell structure, J. Eur. Ceram. Soc. 38 (2018) 3170–3176.

[259] Z. An, C. Men, Z. Xu, P.K. Chu, C. Lin, Electrical properties of AlN thin films prepared by ion beam enhanced deposition, Surf. Coat. Technol. 196 (2005) 130–134.

[260] R. Khazaka, M. Bechara, S. Diaham, M.-L. Locatelli, Parameters affecting the DC breakdown strength of parylene F thin films, in: 2011 Annu. Rep. Conf. Electr. Insul. Dielectr. Phenom., IEEE, 2011: pp. 740–743.

[261] M.A. Wolak, A.S. Wan, J.S. Shirk, M. Mackey, A. Hiltner, E. Baer, Imaging the effect of dielectric breakdown in a multilayered polymer film, J. Appl. Polym. Sci. 123 (2012) 2548–2557.

[262] O. Knotek, F. Löffler, G. Krämer, Process and advantage of multicomponent and multilayer PVD coatings, Surf. Coatings Technol. 59 (1993) 14–20.

[263] T. Hori, Gate dielectrics and MOS ULSIs : principles, technologies, and applications, Springer, 1997.

[264] P. Barquinha, L. Pereira, G. Gonçalves, D. Kuscer, M. Kosec, A. Vilà, A. Olziersky, J.R.

Morante, R. Martins, E. Fortunato, Low-temperature sputtered mixtures of high-κ and high bandgap dielectrics for GIZO TFTs, J. Soc. Inf. Disp. 18 (2010) 762–772.

[265] W.K. Choi, C.K. Choo, Y.F. Lu, Electrical characterization of rapid thermal annealed radio frequency sputtered silicon oxide films, J. Appl. Phys. 80 (1996) 5837–5842.

[266] F.K. Shan, G.X. Liu, W.J. Lee, G.H. Lee, I.S. Kim, B.C. Shin, Structural, electrical, and optical properties of transparent gallium oxide thin films grown by plasma-enhanced atomic layer deposition, J. Appl. Phys. 98 (2005) 1–6.

[267] H. Kattelus, M. Ylilammi, J. Saarilahti, J. Antson, S. Lindfors, Layered tantalum-aluminum oxide films deposited by atomic layer epitaxy, Thin Solid Films. 225 (1993) 296–298.

[268] M. Yao, R. Xiao, Y. Peng, J. Chen, B. Hu, X. Yao, The influence of titanium doping on the electric properties of amorphous alumina films prepared by sol-gel technology, J. Sol-Gel Sci. Technol. 74 (2015) 39–44.

[269] P. Zou, M. Yao, J. Chen, Y. Peng, X. Yao, Leakage current and dielectric breakdown in lanthanum doped amorphous aluminum oxide films prepared by sol–gel, Ceram. Int. 42 (2016) 4120–4125.

[270] J.J. Ortega, A.A. Ortiz-Hernández, J. Berumen-Torres, R. Escobar-Galindo, V.H. Méndez-García, J.J. Araiza, Ag-N dual acceptor doped p-type ZnO thin films by DC reactive magnetron co-sputtering, Mater. Lett. 181 (2016) 12–15.

[271] C. Yung-I, D. Jenq-Gong, Conductive and transparent Al — doped ZnO thin films prepared by rf magnetron sputtering, Mater. Chem. Phys. 27 (1991) 427–439.

[272] W. Khan, Q. Wang, X. Jin, T. Feng, The Effect of Sputtering Parameters and Doping of Copper on Surface Free Energy and Magnetic Properties of Iron and Iron Nitride Nano Thin Films on Polymer Substrate., Materials (Basel). 10 (2017) 1–20.

[273] H.-C. Chen, P.-W. Cheng, K.-T. Huang, Biaxial stress and optoelectronic properties of Al-doped ZnO thin films deposited on flexible substrates by radio frequency magnetron sputtering, Appl. Opt. 56 (2017) C163–C167.

[274] H. Tamagaki, Y. Ikari, N. Ohba, Roll-to-roll sputter deposition on flexible glass substrates, Surf. Coatings Technol. 241 (2014) 138–141.

[275] N. Palavesam, S. Marin, D. Hemmetzberger, C. Landesberger, K. Bock, C. Kutter, Roll-to-roll processing of film substrates for hybrid integrated flexible electronics, Flex. Print. Electron. 3 (2018) 1–18.

[276] N. Kumar, Cylindrical magnetron sputtering system, 1991.

[277] U. Floegel-Delor, T. Riedel, D. Wippich, B. Goebel, R. Rothfeld, P. Schirrmeister, F.N. Werfel, A. Usoskin, A. Rutt, Reel-to-Reel Copper Electroplating on Pulse Laser Deposition Coated Conductor, IEEE Trans. Appl. Supercond. 21 (2011) 2984–2987.

[278] T. Olding, M. Sayer, D. Barrow, Ceramic sol–gel composite coatings for electrical insulation, Thin Solid Films. 398 (2001) 581–586.

[279] A.A. Dameron, S.D. Davidson, B.B. Burton, P.F. Carcia, R.S. Mclean, S.M. George, Gas Diffusion Barriers on Polymers Using Multilayers Fabricated by Al_2O_3 and Rapid SiO_2 Atomic Layer Deposition, J. Phys. Chem. C. 112 (2008) 4573–4580.

[280] H.E. Hallam, H. 39, Infrared and Raman Spectra of Inorganic Compounds, R. Inst. Chem., Rev. 1 (1968) 39–61.

[281] R. Minnes, M. Nissinmann, Y. Maizels, G. Gerlitz, A. Katzir, Y. Raichlin, Using Attenuated Total Reflection-Fourier Transform Infra-Red (ATR-FTIR) spectroscopy to distinguish between melanoma cells with a different metastatic potential., Sci. Rep. 7 (2017) 1–7.

[282] P. Atkins, J. De Paula, Atkins' Physical chemistry 9th edition, Chemistry (Easton). 9 (2009) 700–886.

[283] A. Monshi, M.R. Foroughi, M.R. Monshi, Modified Scherrer Equation to Estimate More Accurately Nano-Crystallite Size Using XRD, World J. Nano Sci. Eng. 2 (2012) 154–160.

[284] M.P. Seah, A review of the analysis of surfaces and thin films by AES and XPS, Vacuum. 34 (1984) 463–478.

[285] R. Lizárraga, E. Holmström, S.C. Parker, C. Arrouvel, Structural characterization of amorphous alumina and its polymorphs from first-principles XPS and NMR calculations, Phys. Rev. B. 83 (2011) 1–9.

[286] A.J. Gonzales, E.M. Philofsky, Applications of scanning electron microscopy to thin film studies on semiconductor devices, Proc. IEEE. 59 (1971) 1429–1433.

[287] D.C. Joy, Scanning Electron Microscopy, in: Mater. Sci. Technol., Wiley-VCH Verlag GmbH & Co. KGaA, Weinheim, Germany, 2006: pp. 222–248.

[288] L.A. Giannuzzi, J.L. Drown, S.R. Brown, R.B. Irwin, F.A. Stevie, Applications of the FIB lift-out technique for TEM specimen preparation, Microsc. Res. Tech. 41 (1998) 285–290.

[289] N.D. Klein, K.R. Hurley, Z.V. Feng, C.L. Haynes, Dark Field Transmission Electron Microscopy as a Tool for Identifying Inorganic Nanoparticles in Biological Matrices, Anal. Chem. 87 (2015) 4356‒4362.

[290] D. Rugar, P. Hansma, Atomic Force Microscopy, Phys. Today . (1990) 23–30.

[291] L.A.S.A. Prado, M. Sriyai, M. Ghislandi, A. Barros-Timmons, K. Schulte, Surface modification of alumina nanoparticles with silane coupling agents, J. Braz. Chem. Soc. 21 (2010) 2238–2245.

[292] R. Katamreddy, R. Inman, G. Jursich, A. Soulet, C. Takoudis, ALD and characterization of aluminum oxide deposited on Si (100) using tris(diethylamino) aluminum and water vapor, J. Electrochem. Soc. 153 (2006) C701–C706.

[293] M. Kaltchev, W.T. Tysoe, An infrared spectroscopic investigation of thin alumina films: measurement of acid sites and surface reactivity, Surf. Sci. 430 (1999) 29–36.

[294] E.S. Andrés, A. Del Prado, F.L. Martínezmartínez, I. Mártil, D. Bravo, F.J. López, Rapid thermal annealing effects on the structural properties and density of defects in and films deposited by electron cyclotron resonance, Cit. J. Appl. Phys. 87 (2000) 1187.

[295] D. Saygin-Hinczewski, K. Koc, I. Sorar, M. Hinczewski, F.Z. Tepehan, G.G. Tepehan, Optical and structural properties of Ta2O5–CeO2 thin films, Sol. Energy Mater. Sol. Cells. 91 (2007) 1726–1732.

[296] J. Liu, B. Xu, H. Wang, X. Cui, L. Zhu, G. Jin, Effects of film thickness and microstructures on residual stress, Surf. Eng. 32 (2015) 178–184.

[297] Y. Wang, H. Li, L. Ji, F. Zhao, X. Liu, Q. Kong, Y. Wang, W. Quan, H. Zhou, J. Chen, The effect of duty cycle on the microstructure and properties of graphite-like amorphous carbon films prepared by unbalanced magnetron sputtering, J. Phys. D. Appl. Phys. 43 (2010) 1–8.

[298] Y.C. Lin, J.Y. Li, W.T. Yen, Low temperature ITO thin film deposition on PES substrate using pulse magnetron sputtering, Appl. Surf. Sci. 254 (2008) 3262–3268.

[299] J. Wang, Y.-H. Yu, S.. Lee, Y.-W. Chung, Tribological and optical properties of crystalline and amorphous alumina thin films grown by low-temperature reactive magnetron sputter-deposition, Surf. Coatings Technol. 146–147 (2001) 189–194.

[300] Magnetron Performance Optimization Guide, Kurt J. Lesker Company. (n.d.) 1.

[301] Sputtering Yield Rates, Semicore. (n.d.) 1.

[302] D.R. Baer, M.H. Engelhard, A.S. Lea, P. Nachimuthu, T.C. Droubay, J. Kim, B. Lee, C. Mathews, R.L. Opila, L. V. Saraf, W.F. Stickle, R.M. Wallace, B.S. Wright, Comparison of the sputter rates of oxide films relative to the sputter rate of SiO2, J. Vac. Sci. Technol. A Vacuum, Surfaces, Film. 28 (2010) 1060–1072.

[303] N.D. Madsen, B.H. Christensen, S. Louring, A.N. Berthelsen, K.P. Almtoft, L.P. Nielsen, J. Bøttiger, Controlling the deposition rate during target erosion in reactive pulsed DC magnetron sputter deposition of alumina, Surf. Coatings Technol. 206 (2012) 4850–4854.

[304] H. Takatsuji, S. Tsuji, K. Kuroda, H. Saka, The influence of cooling water flowing in the sputtering target on aluminum based thin film nariostructure deposited on glass substrates, Thin Solid Films. 343–344 (1999) 465–468.

[305] L. Yu-Ran, Bond dissociation energies, 2010.

[306] M.P.P. Seah, T.S.S. Nunney, Sputtering yields of compounds using argon ions, J. Phys. D. Appl. Phys. (2010) 1–24.

[307] H.L. Brown, S.A. Thornley, S.J. Wakeham, M.J. Thwaites, R.J. Curry, M.A. Baker, The impact of substrate bias on a remote plasma sputter coating process for conformal coverage of trenches and 3D structures, J. Phys. D. Appl. Phys. 48 (2015) 1–10.

[308] P.J. Kelly, A.A. Onifade, Y. Zhou, G.C.B. Clarke, M. Audronis, J.W. Bradley, The Influence of Pulse Frequency and Duty on the Deposition Rate in Pulsed Magnetron Sputtering, Plasma Process. Polym. 4 (2007) 246–252.

[309] D. Sudha, S. Dhanapandian, C. Manoharan, A. Arunachalam, Structural, morphological and electrical properties of pulsed electrodeposited CdIn2Se4 thin films, Results Phys. 6 (2016) 599–605.

[310] M.K. Gunde, Optical Effects in IR Spectroscopy: Thickness-Dependent Positions of Absorbance Lines in Spectra of Thin Films, Appl. Spectrosc. 46 (2005) 365–372.

[311] K. Koski, J. Hölsä, P. Juliet, Surface defects and arc generation in reactive magnetron sputtering of aluminium oxide thin films, Surf. Coatings Technol. 115 (1999) 163–171.

[312] S. Diaham, S. Zelmat, M. Locatelli, S. Dinculescu, M. Decup, T. Lebey, Dielectric Breakdown of Polyimide Films : Area , Thickness and Temperature Dependence, IEEE Trans. Dielectr. Electr. Insul. 17 (2010) 18–27.

[313] A. Evtukh, O. Yilmazoglu, V. Litovchenko, M. Semenenko, O. Kyriienko, H.L. Hartnagel, D. Pavlidis, Peculiarities of the photon-assisted field emissions from GaN nanorods, J. Vac. Sci.

Technol. B, Nanotechnol. Microelectron. Mater. Process. Meas. Phenom. 28 (2010) C2A72-C2A76.

[314] S.J.S. Bull, Techniques for Improving Thin Film Adhesion, Vacuum. 43 (1992) 517–520.

[315] G.E. Stan, C.O. Morosanu, D.A. Marcov, I. Pasuk, F. Miculescu, G. Reumont, Effect of annealing upon the structure and adhesion properties of sputtered bio-glass/titanium coatings, Appl. Surf. Sci. 255 (2009) 9132–9138.

[316] K. Kajihara, H. Kamioka, M. Hirano, T. Miura, L. Skuja, H. Hosono, Interstitial oxygen molecules in amorphous SiO2. III. Measurements of dissolution kinetics, diffusion coefficient, and solubility by infrared photoluminescence, J. Appl. Phys. 98 (2005) 1–7.

[317] R. Nakamura, T. Toda, S. Tsukui, M. Tane, M. Ishimaru, T. Suzuki, H. Nakajima, Diffusion of oxygen in amorphous Al_2O_3, Ta_2O_5 and Nb_2O_5, J. Appl. Phys. 116 (2014) 1–8.

[318] X. Wu, G. Shao, S. Cui, L. Wang, X. Shen, Synthesis of a novel Al_2O_3–SiO_2 composite aerogel with high specific surface area at elevated temperatures using inexpensive inorganic salt of aluminum, Ceram. Int. 42 (2016) 874–882.

[319] J.W. Ma, W.J. Lee, J.M. Bae, K.S. Jeong, S.H. Oh, J.H. Kim, S.H. Kim, J.H. Seo, J.P. Ahn, H. Kim, M.H. Cho, Carrier Mobility Enhancement of Tensile Strained Si and SiGe Nanowires via Surface Defect Engineering, Nano Lett. 15 (2015) 7204–7210.

[320] W. Hu, L. Zou, C. Gao, Y. Guo, D. Bao, High speed and multi-level resistive switching capability of Ta2O5 thin films for nonvolatile memory application, J. Alloys Compd. 676 (2016) 356–360.

[321] J. Kwon, J.M. Ducéré, P. Alphonse, M. Bahrami, M. Petrantoni, J.-F. Veyan, C. Tenailleau, A. Estève, C. Rossi, Y.J. Chabal, Interfacial Chemistry in Al/CuO Reactive Nanomaterial and Its Role in Exothermic Reaction, ACS Appl. Mater. Interfaces. 5 (2013) 605–613.

[322] M.T. Wang, Y.C. Lin, M.C. Chen, Barrier Properties of Very Thin Ta and TaN Layers Against Copper Diffusion, J. Electrochem. Soc. 145 (1998) 2538–2545.

[323] A.P. Huang, S.L. Xu, M.K. Zhu, B. Wang, H. Yan, T. Liu, Crystallization control of sputtered Ta2O5 thin films by substrate bias, Appl. Phys. Lett. 83 (2003) 3278–3280.

[324] C. Lee, Y.-L. Kuo, The Evolution of Diffusion Barriers in Copper Metallization, JOM J. Miner. Met. Mater. Soc. 59 (2007) 44–49.

[325] Y. Zhao, G. Lu, First-principles simulations of copper diffusion in tantalum and tantalum nitride, Phys. Rev. B . (79AD) 1–8.

[326] Y. Qin, Y. Yang, R. Scholz, E. Pippel, X. Lu, M. Knez, Unexpected Oxidation Behavior of Cu Nanoparticles Embedded in Porous Alumina Films Produced by Molecular Layer Deposition, Nano Lett. 11 (2011) 2503–2509.

[327] A.L. Salaün, A. Mantoux, E. Blanquet, E. Djurado, ESD and ALD Depositions of Ta_2O_5 Thin Films Investigated as Barriers to Copper Diffusion for Advanced Metallization Figure 1. Phase diagrams of a O-Ta-Si and b Ta-Cu-O from FactSage, J. Electrochem. Soc. 156 (2009) 311–315.

[328] I.S. Park, K.M. Ryu, J. Jeong, J. Ahn, Dielectric stacking effect of Al_2O_3 and HfO2 in metal-insulator-metal capacitor, IEEE Electron Device Lett. 34 (2013) 120–122.

[329] O.S. Gefle, S.M. Lebedev, V.Y. Uschakov, The mechanism of the barrier effect in solid dielectrics, J. Phys. D Appl. Phys. 30 (1997) 3267–3273.

[330] D.M. Mattox, Adhesion and Deadhesion, Handb. Phys. Vap. Depos. Process. (2010) 439–474.

[331] B. Zhang, Z. Li, M. Ren, J. Liu, T. Moran, B. Huey, L. Sun, Y. Cao, A superior nanolaminate dielectric barrier coating for high breakdown strength, in: 2017 IEEE Conf. Electr. Insul. Dielectr. Phenom., IEEE, 2017: pp. 461–464.

[332] M. Ren, J. Liu, L. Sun, Y. Cao, Enhancing dielectric property of polymer films with nanoclay coatings, in: 2016 IEEE Conf. Electr. Insul. Dielectr. Phenom., IEEE, 2016: pp. 651–654.

[333] H.J. Quah, K.Y. Cheong, Effects of annealing time on the electrical properties of the Y2O3 gate on silicon, J. Exp. Nanosci. 10 (2015) 19–28.

[334] B.V.T. Hanby, B.W. Stuart, C. Grant, J. Moffat, J. Blissett, C. Gerada, M. Gimeno-Fabra, D.M. Grant, Dielectric breakdown of alumina thin films produced by pulsed direct current magnetron sputtering, Thin Solid Films. 662 (2018) 145–154.

[335] O. Knotek, R. Elsing, G. Kramer, F. Jungblutt, On the origin of compressive stress in PVD coatings - an explicative model, Surf. Coatings Technol. 46 (1991) 265–274.

[336] P. V Patil, R.K. Puri, V. Puri, Comparison of adhesion and intrinsic stress of chopped and non-chopped ZnS thin films, Mater. Chem. Phys. 49 (1997) 156–159.

[337] P. V. Patil, U. V. Nerle, V. Puri, R.K. Puri, Adhesion improvement and intrinsic stress decrease in cerium oxide thin films by chopping, J. Adhes. Sci. Technol. 10 (1996) 151–159.

[338] J.S. Park, S. Kim, H. Shin, H.S. Jung, K.S. Hong, Residual stress evolution in multilayer

ceramic capacitors corresponding to layer increase and its correlation to the dielectric constant, J. Appl. Phys. 97 (2005) 1–5.

[339] H. Shin, J.-S. Park, K. Sun Hong, H. Suk Jung, J.-K. Lee, K. Yop Rhee, Physical origin of residual thermal stresses in a multilayer ceramic capacitor Influence of thickness and number of dielectric layers on residual stresses in micromultilayer ceramic capacitors, Cit. J. Appl. Phys. 101 (2007) 1–5.

[340] K. Chu, Y.G. Shen, Mechanical and tribological properties of nanostructured TiN/TiBN multilayer films, Wear. 265 (2008) 516–524.

[341] A. Ouis, M. Cailler, Journal of Adhesion Science and Effects of substrate bias voltage on adhesion of DC magnetron-sputtered copper films on E24 carbon steel : investigations by Auger electron spectroscopy, J. Adhes. Sci. Technol. 27 (2013) 37–41.

[342] V.A.C. Haanappel, D. v.d. Vendel, H.D. van Corbach, T. Fransen, P.J. Gellings, The effect of thermal annealing on the properties of thin alumina films prepared by low pressure metal-organic chemical vapour deposition, Thin Solid Films. 256 (1995) 8–12.

[343] R. Ali, M. Renzelli, M. Khan, M. Sebastiani, E. Bemporad, Effects of Residual Stress Distribution on Interfacial Adhesion of Magnetron Sputtered AlN and AlN/Al Nanostructured Coatings on a (100) Silicon Substrate, Nanomaterials. 8 (2018) 1–16.

[344] X.C. Zhang, B.S. Xu, F.Z. Xuan, S.T. Tu, Analysis on multiple cracking in film/substrate systems with residual stresses, J. Appl. Phys. 103 (2008) 1–9.

[345] N.E. Jansson, Y. Leterrier, J.-A.E. Månson, Modeling of multiple cracking and decohesion of a thin film on a polymer substrate, Eng. Fract. Mech. 73 (2006) 2614–2626.